UNIVERSITÀ DEGLI STUDI DI MILANO

Scuola di Dottorato in Fisica, Astrofisica e Fisica Applicata

Dipartimento di Fisica

Corso di Dottorato in Fisica, Astrofisica e Fisica Applicata

Ciclo XXXVI

Microscopic theory of infinite nuclear matter and non-empirical energy functionals

Settore Scientifico Disciplinare FIS/04

Supervisore: Prof. Gianluca Colò

Co-Supervisore: Prof. Francesco Pederiva

Coordinatore: Prof. Roberta Vecchi

Tesi di Dottorato di:

Francesco Marino

Anno Accademico 2022-2023

Referees of the thesis:

Prof. Alexandros Gezerlis
Department of Physics, University of Guelph, Guelph, Ontario N1G 2W1, Canada

Dr. Jérôme Margueron
Université Lyon, Université Claude Bernard Lyon 1, CNRS/IN2P3, IP2I Lyon, UMR 5822, F-69622, Villeurbanne, France

Commission of the final examination:

Prof. Gianluca Colò
Dipartimento di Fisica, Università degli Studi di Milano, Milano, Italy

Prof. Laura Elisa Marcucci
Department of Physics "E. Fermi", University of Pisa, I-56127 Pisa, Italy

Dr. Vittorio Somà
IRFU, CEA, Université Paris-Saclay, 91191 Gif-sur-Yvette, France

Final examination:

Date: 19^{th} December 2023

Dipartimento di Fisica, Università degli Studi di Milano, 20133 Milano, Italy

MIUR subject:
FIS/04 - Nuclear and subnuclear physics

PACS:
21.60.Jz, 21.65.Mn, 21.60.Ka

Abstract

Nuclear density functional theory (DFT) and *ab initio* theory are complementary approaches to nuclear structure. DFT can be applied to the whole nuclear chart, but relies on empirical energy density functionals (EDFs). As a consequence, predictions in regions where experimental data are lacking, e.g. in neutron-rich nuclei close to the driplines, are subject to significant uncertainties. In contrast, *ab initio* theory allows to draw predictions with controlled uncertainties, but there are difficulties in extending these methods to heavy nuclei or e.g. far from magic numbers. The purpose of this thesis is to combine DFT and *ab initio* by grounding the nuclear EDFs into *ab initio* theoretical predictions, specifically on infinite nuclear matter calculations.

The *ab initio* Quantum Monte Carlo (QMC) and Self-consistent Green's functions (SCGF) methods are employed to study nuclear matter. An extension of SCGF based on the algebraic diagrammatic construction (ADC-SCGF) is developed to include Gorkov pairing correlations. The *ab initio* equations of state (EOS) are used to construct EDFs based on the local density approximation and gradient approximation, which are applied to magic nuclei. Then, the static response of nuclear matter is tackled with both DFT and QMC, and a study of the constraints that can be set on the EDF surface terms from *ab initio* is reported.

This thesis outlines a new strategy to ground nuclear EDFs into *ab initio* and implements some of its pillars. A critical discussion of the difficulties encountered is given. Future developments include the study of nuclear matter from a microscopic perspective, e.g. extending ADC-SCGF to tackle the dynamic response and superfluid matter.

Contents

List of Figures

List of Tables

Introduction

The study of the structure of atomic nuclei poses formidable challenges. The nucleus is an interacting quantum many-particle system, and sophisticated methods are required for its understanding. An additional difficulty is that the interaction between nucleons is rather complex and known only approximately. No 'standard model' exists that allows to study all nuclear phenomena, but different approaches and models are applicable at different scales [1, 2]. These include macroscopic approaches, such as the liquid drop model [3], and microscopic methods such as the interacting shell model [4], density functional theory (DFT) [5, 6] and the family of *ab initio* methods [7, 8].

The *ab initio* program aims at solving the many-nucleon Schrödinger equation with an exact or systematically improvable quantum many-body method, using as input a realistic model of the nuclear Hamiltonian in the vacuum [7–9]. A central goal of *ab initio* is to provide predictions of nuclear observables with controlled theoretical uncertainties [10, 11]. Examples of *ab initio* methods include the no-core shell model [12], coupled-cluster theory (CC) [13, 14], in-medium similarity renormalization group [15], many-body perturbation theory (MBPT) [16], Quantum Monte Carlo (QMC) [17, 18] and Self-consistent Green's functions (SCGF) [19, 20]. The task of *ab initio* is very complex and requires very large computational resources, that have limited for a long time its range of applicability to light nuclei. Nevertheless, simultaneous developments in many-body theory and nuclear force models have made it possible to achieve important results in recent years, that have allowed extending *ab initio* theory to medium- [21–23] and even heavy-mass nuclides [24, 25], as well as to open-shell nuclei [16, 26, 27]. A few milestones include the calculation of nuclear densities in the Sn and Xe chains [28], predictions for the neutron driplines [22], and a detailed analysis of ^{208}Pb [25]. Other notable applications are infinite nuclear matter (see e.g. Refs. [20, 29]) and lepton-nucleus scattering processes [30, 31].

While these advances are impressive, it must be noted that such calculations remain rather demanding and are by no means routine. Also, *ab initio* theory still has limitations in dealing with nuclei far from magicity, where strong static correlations are important [7, 16, 19]. That is the case, for instance, of doubly open-shell nuclei that show significant deformation [19]. The only microscopic method that can be applied to the whole nuclear chart with good accuracy, with the partial exception of very light nuclei, is the DFT approach [5, 6, 32, 33]. DFT translates the problem of interacting nucleons to a single-particle (s.p.) self-consistent (s.c.) problem that is based on the concept of an energy density functional (EDF). The EDF represents a map between the total energy of a given fermion system and its (generalized) densities, and minimizing it allows to determine the exact ground state (g.s.) of the interacting system. The existence of the EDF is guaranteed by the Hohenberg-Kohn theorems [34], which prove that DFT is formally an exact theory for the g.s. Additionally, DFT has been extended to allow to treat also excited states and dynamical phenomena [5, 35]. Its countless applications in nuclear physics include giant resonances [36, 37], infinite nuclear matter [38], clustered matter in neutron stars [39] and fission processes [40, 41].

DFT allows to handle the complexity of the many-nucleon problem. However, the form of the EDF is not known exactly, and thus DFT turns out to be an approximate, albeit very powerful, method. In particular, most relativistic [6, 42] and non-relativistic [5, 6, 32, 33] nuclear EDFs are designed in an empirical manner. A reasonable ansatz for the functional form is chosen and its actual parameters are fitted on experimental observables such as radii and masses of finite nuclei, or pseudo-observables such as the saturation density of symmetric nuclear matter [6, 43]. The available EDFs are overall successful [5, 44], e.g. the experimental binding energies are reproduced on average within 1-2 MeV and charge radii within 0.02-0.03 fm.

However, limitations affect the current EDFs. While the agreement of the existing EDFs with the experiment is generally satisfactory close to the stability valley, where they have been fitted, uncontrolled extrapolations affect the EDF predictions in the region of unstable nuclei. A strong model dependence, for example, has been observed in the prediction of proton and especially neutron driplines [45–47]; also, discrepancies tend to increase with the mass number [5]. Thus, current EDFs have limited reliability close to the limits of the nuclear chart, which are at the center of experimental research and still are, to a large extent, out of reach of *ab initio* theory. For instance, in Ref. [22] neutron driplines could be computed only up to $Z = 28$.

In addition, it turns out that empirical EDFs are difficult to further improve. The somewhat pessimistic conclusion of the UNEDF [48] project was that enriching the dataset and improving the fitting method may be insufficient to obtain substantial improvements, and new directions beyond the traditional EDFs should be pursued. A careful analysis of the limitations of current nuclear EDFs is also advocated e.g. in Ref. [49], in light of the tension between theoretical calculations and experimental measurements of the parity-violating asymmetry and the dipole polarizabilities even in two stable and very much studied nuclei, ^{48}Ca and ^{208}Pb (see [49–51] and references therein).

Thus, the current status of nuclear DFT, as well as the strong experimental interest in exotic and neutron-rich nuclei, has motivated studies into alternative directions, and the simultaneous developments in *ab initio* theory have made research on grounding DFT on more fundamental theories one of the timely subjects in the field [5, 52–55]. Several approaches have been put forward, and some of them are briefly mentioned here. In Refs. [56–58], the density matrix expansion has been used to incorporate the contributions of the pion exchanges, which determine the long-range physics in chiral forces, into the EDF. In Ref. [59], the EDF method is linked to the *ab initio* projected generator coordinate method (PGCM). Non-empirical EDFs inspired by the unitary Fermi gas have been proposed in Refs. [60, 61], and a power counting for nuclear EDFs has been discussed in e.g. Ref. [62–64]. In Refs. [53, 65], the possibility of determining the coupling constants of the EDF on the *ab initio* metadata obtained by perturbing finite nuclei has been investigated.

The idea of developing non-empirical EDFs has a long tradition in electronic DFT, where it has been advocated and developed to a large extent by Perdew and collaborators [34, 66, 67]. The so-called 'Jacob's ladder' program consists of constructing a hierarchy of EDFs of increasing complexity, where at each rung of the ladder one tries to impose as many exact conditions as possible, while using a limited amount of empirical input [66]. Essential is the theory of the homogeneous electron gas to guide the development of the EDF.

In this thesis, a new research program for grounding nuclear EDFs into *ab initio* is pursued. The proposed strategy is inspired by the Jacob's ladder in two respects [68]. First, it is aimed at constructing a series of increasingly more refined EDFs. Second, the main constraints to the EDFs are to come from *ab initio* calculations of model systems, and in particular infinite nuclear matter. The first rung of the ladder is well established and is the so-called Local Density Approximation (LDA). LDA maps the equation of state (EOS) of homogeneous nuclear matter into an EDF that is function of the number densities, and in the context of nuclear physics it has been explored e.g. in Refs. [69–71].

LDA is not sufficient, though, and it is known that surface terms, such as gradients of the density and spin-orbit contributions, are essential to describe finite nuclei. The following rung of the DFT ladder is called Gradient Approximation (GA) in this work. There is no obvious way on how to implement the GA. The generalized gradient approximation (GGA) of electronic DFT, which includes e.g. the extremely popular PBE functional [72], is based on analytical properties specific to Coulomb systems, which cannot be straightforwardly migrated to nuclear physics. Also, since surface terms simply vanish in uniform matter, a different inhomogeneous system must be found to provide information on the terms beyond LDA. Confined nuclear matter, such as neutron and neutron-proton drops, has been suggested as a means to gain additional information on the EDF [73].

A different possibility is considered in this work, which consists of studying nuclear matter subject to an external static potential. This so-called static response problem has been tackled from an *ab initio* perspective by Gezerlis and collaborators in neutron matter [74–76], thus paving the way to the study of this property in nuclear physics. The study of infinite nuclear matter, both in its homogeneous state and under the effect of an external perturbation, is thus one of the pillars of this work. The other pillar is to find a way to exploit the *ab initio* nuclear matter information for constructing the EDF.

QMC has been extensively used to tackle the static response problem (see e.g. [75, 77, 78]), and provides a quite natural way to introduce external potentials. In particular, the Auxiliary field Diffusion Monte Carlo (AFDMC) [17] technique is employed here to study perturbed nuclear matter. Since AFDMC (as well as several other *ab initio* methods) simulate the infinite system using a finite number of nucleons, with the purpose of matching the *ab initio* predictions with the EDF ones in a consistent way, following Refs. [76, 79], a finite-A DFT approach for both homogeneous and perturbed matter has been developed [80], and it has been applied to infer the parameters of the EDF from the *ab initio* data.

However, limitations of AFDMC, such as its computational complexity and difficulties in using fully realistic interactions, have led us to consider other methods. A significant portion of this thesis is devoted to the development and extension of SCGF, and in particular the variant based on the algebraic diagrammatic construction (ADC) scheme [26, 81, 82], for nuclear matter. ADC-SCGF is a state-of-the-art approach for finite nuclei (see [19] and references therein), and it has been adapted to infinite matter in Refs. [82, 83], where ADC at third order in Dyson-SCGF, i.e. based on a Hartree-Fock reference state (in short, Dyson-ADC(3)), has been proposed. In this work, the first full implementation of Dyson-ADC(3) with chiral interactions is presented. Moreover, the method has been extended by including Gorkov pairing correlations [84].

This thesis is structured as follows. In Ch. 1, a general introduction to the key concepts of the work is provided, concerning the simulations of infinite nuclear matter, the theory of the static response, and the

essential notions of the nuclear interaction. The following three chapters delve into the different theoretical methods employed in this work. Ch. 2 is devoted to DFT. After a general introduction to this approach, original developments are presented, namely the construction of *ab initio*-constrained LDA and GA EDFs and the solution of the perturbed matter problem. Ch. 3 reviews the *ab initio* QMC method and details how it has been applied to both homogeneous and perturbed nuclear matter. The subject of Ch. 4 is Self-consistent Green's functions for infinite nuclear matter. In particular, the implementation of the Dyson-ADC(3) approach and its extension to incorporate Gorkov correlations are discussed. In the second part of the thesis, results are shown. In Ch. 5, the nuclear matter EOS obtained with the *ab initio* methods are presented, and Dyson-ADC is accurately discussed. In Ch. 6, the LDA EDFs based on the *ab initio* EOS are constructed and applied to magic nuclei. Also, a preliminary study of the gradient terms is performed. In Ch. 7, perturbed nuclear matter calculations are performed with the DFT approach. Then, Ch. 8 is devoted to developing *ab initio*-based GA EDFs. In particular, the static response is computed with AFDMC, and a protocol to constrain the gradient terms by matching the DFT and AFDMC predictions for perturbed nuclear matter is discussed. Finally, conclusions and perspectives to this work are given in Ch. 9. Further details are provided in the Appendixes. App. A gives an overview of chiral interactions and their applications in infinite matter studies. App. B complements the discussion on the static response theory. App. C provides details on DFT calculations. Finally, in App. D technical aspects of SCGF are discussed.

CHAPTER 1

Theoretical background and motivation

In this chapter, we aim to provide a general introduction to the key concepts of this thesis. The general motivation and an outline of this work are given in Sec. 1.1. Then, a brief introduction to the nuclear interactions and their use in *ab initio* theory is given in Sec. 1.2. Additional details on chiral forces are presented in App. A. In Sec. 1.3 we define infinite nuclear matter and detail how it can be simulated using a finite number of particles. These concepts are the essential background for the nuclear matter studies we conduct with AFMDC, SCGF and DFT. Finally, in Sec. 1.4 we discuss the theory of the response of infinite matter to an external static perturbation and explain how it can be computed; this section is complemented by App. B.

1.1 Purpose of this work

This Section is meant to explain the purpose of this work and give an overview of its main themes. Our essential motivation is to lay the first steps for the construction of fully *ab initio*-constrained EDFs. This is a highly timely subject in nuclear theory [5, 53, 55], that stems from the necessity to extend the accuracy of nuclear DFT towards the regions of neutron-rich nuclei, that are at the edge of current experimental research, and the parallel recognition that it is difficult to find breakthroughs within the framework of traditional empirical EDFs [48]. In this respect, the rapid developments of *ab initio* theory suggest that the latter may help surpass the limitations that affect the phenomenological EDFs. *Ab initio* can provide information to understand the impact of the different terms of the EDFs, suggest new functional forms, and allow to set constraints on the EDF parameters, such as the isovector or spin terms [73, 85].

Our strategy takes inspiration from condensed matter DFT, and in particular from the non-empirical "Jacob's ladder" approach [34, 66], from which we adopt two general principles. First, we aim to construct a hierarchy of EDFs of increasing complexity and accuracy, starting from simple approximations and then introducing more complex ones. Second, at each "rung" of the construction we favor the use of *ab initio* calculations, instead of experimental data, to fix the parameters and the structure of the EDF. More specifically, the theory of infinite nuclear matter (the analog of the homogeneous electron gas) is our pillar. Fig. 1.1 shows a schematic representation of our approach. The simplest approximation is the local density approximation (LDA), which maps the EOS of homogeneous nuclear matter into an EDF that is a function of the number densities only. LDA assumes that the energy density of finite nuclei can be approximated at each point by that of infinite matter, that is, in LDA finite systems are assimilated to the homogeneous system, and surface effects are not explicitly considered in the EDF. However, while the LDA is well-known in both condensed matter [34, 66] and nuclear physics [71], there is not a clear way to improve upon it. Surface terms, such as density-gradient terms and spin-orbit contributions, are essential to properly describe nuclei (and in general finite systems). However, they trivially vanish in uniform systems, and thus homogeneous matter cannot provide any information on them. To go beyond LDA, it is thus necessary to study *inhomogeneous* systems. The simplest way to induce a density fluctuation in nuclear matter is to introduce an external potential. While in the past harmonically confined droplets have been suggested to tune the EDF parameters [73, 86], in this thesis we explore nuclear matter perturbed by a weak monochromatic potential, the so-called static response problem. The work by Gezerlis and collaborators [74–76] has opened the way to an *ab initio* approach to perturbed matter, which, at variance with droplets, offers a clear connection to uniform matter.

To carry out our program, we must be able to study both uniform and perturbed nuclear matter within the frameworks of both DFT and *ab initio*. Few *ab initio* methods have been used to study the response of infinite matter. Quantum Monte Carlo, employed in Refs. [75, 76] as well as in condensed matter [77, 78] for the static response, offers a somewhat natural way to incorporate external potentials. Thus, AFDMC is extended and then applied extensively in this work to generate *ab initio* pseudodata. Since AFDMC (as several other *ab initio* techniques) employs a finite number of nucleons to simulate the infinite system, in order to be able to properly match the *ab initio* and DFT descriptions of perturbed matter we have developed, extending Refs. [76, 79], a finite-A DFT method specific for this problem [80].

Unfortunately, AFDMC suffers from some limitations. Large computational resources and care are needed to properly treat the tensor and spin-orbit operators of the nuclear interaction: while in PNM it is a leading

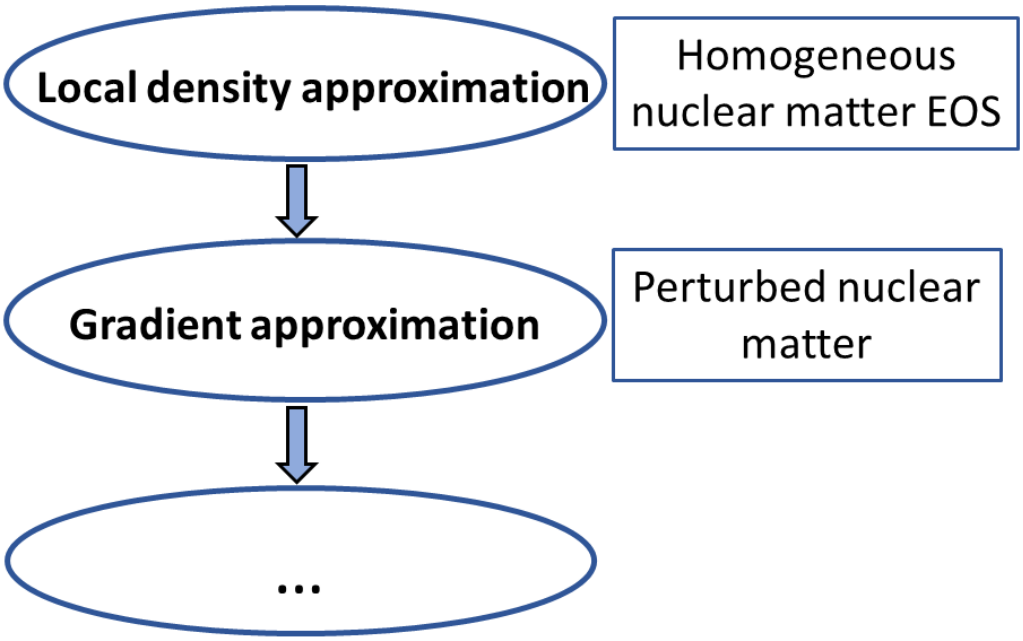

Figure 1.1: Schematic representation of our "ladder" of *ab initio*-based nuclear EDFs. The first two rungs are shown, while the dots denote future developments. The local density approximation requires as *ab initio* input the equation of state of homogeneous nuclear matter. The gradient approximation involves studying nuclear matter perturbed by an external weak potential, both in the *ab initio* and DFT frameworks.

technique, AFDMC has found relatively few applications in SNM [87, 88]. Since both PNM and SNM are essential for our program, in this exploratory study we have considered a simplified model of the nuclear interaction, namely the Argonne 4 force [89]. This is suited for development purposes, as some of the technical difficulties above are avoided. Another limit to be mentioned is that so far, except for a few exploratory studies [90, 91], AFDMC has been limited only to some specific chiral interactions (the so-called local forces) [92]. Many of the most accurate chiral forces, therefore, are inaccessible to AFDMC.

Thus, it has proved important to consider different *ab initio* approaches, and in particular we have focused on the Self-consistent Green's function (SCGF) method [19, 20]. SCGF allows to study both SNM and PNM and can employ all chiral interactions naturally. Initially, existing EOS calculations performed with the established finite-temperature SCGF formalism based on the ladder approximation for the self-energy [20] (Finite-T SCGF from now on) have been used. A significant portion of this thesis is devoted to the development of a different variant of Green's function method. Indeed, the so-called algebraic diagrammatic construction (ADC) is a leading approach in the *ab initio* theory of finite nuclei [19]. Its applications to infinite matter have been initiated in Refs. [82, 83], and full-fledged ADC-SCGF calculations for homogeneous are presented in this work. Green's functions theory is well suited, in principle, for studying the (both dynamical and static) response. However, this is a challenging project on its own and is left for future studies.

To summarize, homogeneous nuclear matter is studied in this work with the *ab initio* AFDMC and SCGF approaches, and LDA EDFs are constructed and tested based on the resulting EOS. A thorough presentation of the ADC-SCGF method is one of the novelties presented in this work. The static response of perturbed matter is tackled both within DFT and AFDMC. Finally, a preliminary study of GA EDFs constrained by the *ab initio* response is presented.

1.2 Nuclear interactions

In this Section, we give an overview of the nuclear interactions used in *ab initio* nuclear theory. The subject is discussed in detail e.g. in Refs. [1, 17, 92–94]

At low energies, nuclear systems can be described assuming the nucleons as degrees of freedom and modeling their interactions through a non-relativistic Hamiltonian, which includes two- (NN) and three-nucleon (3N) (and possibly many-nucleon) potential terms:

$$\hat{H} = \hat{T} + \hat{V} + \hat{W} + ..., \tag{1.1}$$

where $\hat{V}$ and $\hat{W}$ denote the NN and 3N interactions, respectively. The qualitative properties of the NN interaction are well-known [1, 17, 92, 95]. As the binding energy per nucleon of finite nuclei is roughly constant,

one deduces that the interaction between nucleons must be short-ranged. An attractive component at ~ 1 fm coexists with a repulsive core at a very short distance, which makes nuclear systems relatively dilute. Also, the fact that the deuteron is the only two-nucleon system that admits a (shallow) bound state implies that the nuclear force must depend on spin and isospin. In particular, it is stronger in the isoscalar channel, with proton and neutron coupled to total isospin $T = 0$ and total spin $S = 1$. Moreover, since the deuteron has a non-vanishing quadrupole moment, the NN force must contain non-central terms. The basic model by Yukawa, which describes the nuclear interaction in terms of the exchange of a pion, is successful in explaining its long-range properties. Additional two-pion-exchange contributions explain the intermediate-range attraction. The NN force alone, however, overbinds the triton, and 3N interactions are then needed to provide the missing repulsive contribution.

Despite our understanding of its general properties, finding nuclear interactions that are quantitatively accurate is still an active area of research, see e.g. [96], but realistic models of the nuclear force, that are fitted to reproduce accurately two- or few-body observables (e.g. NN scattering phase shift or the binding energy of the deuteron) do exist. Interactions are constructed in a phenomenological way [17, 89, 94], or by making use of chiral EFTs [93, 96–99]. Potentials extracted directly from lattice Quantum Chromodynamics (QCD) calculations are still in their infancy [10, 100, 101] and will not be discussed. Chiral forces are derived in an order-by-order, low-momentum expansion consistent with the QCD symmetries. They are defined in momentum space, although coordinate-space versions of the so-called local forces have been put forward [92, 102, 103]. Since they are naturally cut off at high momenta by regulators [104], they elude the problem of handling the hard core, i.e. the strongly repulsive short-range behavior of the phenomenological potentials [19]. In this sense, chiral forces are considered "soft" interactions, in contrast with the "hard" phenomenological forces. Phenomenological interactions postulate the form of the interactions combining symmetry arguments and elements of meson-exchange theory [17, 89]. The calculations performed in this work make use of the chiral NNLO$_{\rm sat}$ [105] and ΔNNLO$_{\rm go}$ [106] and the phenomenological AV4′+UIX$_c$ interactions [89]. App. A is devoted to chiral forces, and details several aspects of their form and their use in infinite matter calculations. The remainder of this section is dedicated to phenomenological forces.

The most general structure of the phenomenological interactions that are commonly used comprises 18 operators [17]. Of those, 14 are charge independent, while of the remaining four, three are charge dependent and one is a charge symmetry breaking term [17]. Argonne interactions are widely employed phenomenological potentials [17, 89, 94]. The highly accurate Argonne 18 (AV18) model [94] includes all the terms in full. The dominant contributions are the first eight operators, that enter the widely used Argonne 8 (AV8′) [89] and chiral interactions at NNLO. Sticking to the notation used for coordinate space potential, $\hat{V}$ reads

$$\hat{V} = \sum_{i\neq j} v_{ij} = \sum_{i\neq j}\sum_{p=1}^{18} v_p(r_{ij}) O_{ij}^p, \tag{1.2}$$

where

$$O_{ij}^{p=1,8} = [\mathbb{1}, \sigma_i\cdot\sigma_j, S_{ij}, \mathbf{L}_{ij}\cdot\mathbf{S}_{ij}] \otimes [\mathbb{1}, \tau_i\cdot\tau_j], \tag{1.3}$$

$$O_{ij}^{p=9,14} = [\mathbf{L}_{ij}^2, \mathbf{L}_{ij}^2\sigma_i\cdot\sigma_j, (\mathbf{L}_{ij}\cdot\mathbf{S}_{ij})^2] \otimes [\mathbb{1}, \tau_i\cdot\tau_j]. \tag{1.4}$$

In the previous equation, σ_i and τ_i are spin and isospin Pauli matrices, respectively, $\mathbf{S}_{ij} = \frac{1}{2}(\sigma_i + \sigma_j)$ is the total spin of the nucleon pair, $\mathbf{L}_{ij}$ is the relative angular momentum operator,

$$\mathbf{L}_{ij} = -\frac{i}{2}(\mathbf{r}_i - \mathbf{r}_j)\times(\nabla_i - \nabla_j). \tag{1.5}$$

and S_{ij} is the tensor operator,

$$S_{ij} = 3\sigma_i\cdot\mathbf{r}_{ij}\sigma_j\cdot\mathbf{r}_{ij} - \sigma_i\cdot\sigma_j. \tag{1.6}$$

AV18 is very complex and computationally demanding, and some terms cannot be included in all *ab initio* methods. Simplified versions, more amenable to many-body calculations, have been devised [89]. Denoted as AVn′, these interactions contain a subset of n operators and are refitted in order to reproduce as many two-nucleon properties as possible. Together with the NN interaction, a three-nucleon force (3NF) has to be introduced to reproduce the spectrum of light nuclei and saturation properties of infinite nucleonic matter [107]. In Refs. [108, 109] it was found that the simple AV4′, which comprises only four operators:

$$O_{ij}^{p=1,..,4} = [1, \sigma_i\cdot\sigma_j] \otimes [1, \tau_i\cdot\tau_j]\,, \tag{1.7}$$

complemented with the central term of the Urbana IX 3N interaction (UIX$_c$), yields reasonable ground-state energies of light and medium-mass nuclei — the binding energies deviate by about 10% from the experiment.

AV4′+UIX$_c$ is therefore interesting for this exploratory work since it allows to carry out accurate Monte Carlo studies of nuclear matter (both PNM and SNM) and of nuclei as large as ^{90}Zr. Moreover, the fact that AV4′ does not contain tensor or spin-orbit operators greatly simplifies the solution of the many-body problem with the AFDMC method.

The NNLO$_{\rm sat}$ [105] force, as well as the more recent ΔNNLO$_{\rm go}$ model [106], are widespread chiral forces that are successful in reproducing the bulk properties of nuclei (binding energies, radii, and densities [28]) in a wide mass range and at the same time yielding a SNM saturation point compatible with empirical constraints. This is a non-trivial achievement that has been made possible by including in the fitting protocol of the interaction information on light nuclei and constraints on infinite nuclear matter [105, 106, 110]. Some drawbacks persist, e.g. the symmetry energy around and above saturation is underestimated in NNLO$_{\rm sat}$ [111], spectroscopic properties are not so accurately described, and the quality in the reproduction of scattering observables deteriorates [112], especially in Δ-full models. Still, these potentials remain among the most used and (for bulk properties) successful chiral Hamiltonians, see e.g. Refs. [113, 114].

1.3 Infinite nuclear matter

In this Section, an introduction to infinite nuclear matter is given. We present the essential notions about nuclear matter and outline the approach to simulate homogeneous matter with a finite number of particles.

Nuclear matter is an infinite system of nucleons that interact through the strong interaction only [38, 115]. While it is an idealized system, it bears connections to the nuclear physics of finite nuclei [38, 116, 117], the astrophysics of neutron stars and gravitational waves [39, 118–120], and the physics of cold Fermi gases [29, 121]. For this reason, nuclear matter is an active subject of research from multiple perspectives. In this work, we focus on the microscopic description of nuclear matter from a many-body theory perspective and do not aim at a study of neutron stars. We do not consider other degrees of freedom, such as hyperons, that are expected to appear in the neutron star core [39], and focus instead on the purely nucleonic EOS. The modeling of the (inhomogeneous) neutron star crust is reviewed e.g. in Refs. [118, 122]. We concentrate on zero-temperature and spin-unpolarized matter, that is characterized by the proton and neutron densities ρ_n, ρ_p, or equivalently by the total density

$$\rho_0 = \rho_n + \rho_p \tag{1.8}$$

and the isospin asymmetry

$$\beta = \frac{\rho_n - \rho_p}{\rho_0}. \tag{1.9}$$

We anticipate that we will focus, to a large extent, on the limiting cases of SNM ($\rho_n = \rho_p = \rho_0/2$) and PNM ($\rho_p$=0, $\rho_n = \rho_0$), although extensions are straightforward. The fundamental property of homogeneous matter is the EOS

$$e(\rho, \beta) = E(\rho, \beta)/A, \tag{1.10}$$

where E is the total energy of the system and e is the energy per nucleon. A typical example of EOS is shown in Fig. 1.2, where the energy is plotted as a function of the density for several values of the asymmetry. PNM and SNM are shown as thick lines, while intermediate β's are represented with dashed lines. The essential property of SNM is that it saturates, i.e. the EOS admits an empirical minimum at density $\rho_{sat} \approx 0.16$ fm^{-3} and energy per particle $E_{sat} \approx -16$ MeV [38]. The PNM EOS, instead, is a monotonically increasing function of ρ, since the the kinetic energy is dominant compared to the potential energy. Indeed, the nuclear interaction is rather weak among neutrons, but strong between protons and neutrons in the $T = 0$ isospin channel. In between, asymmetric nuclear matter (ANM) saturates or not according to the value of the asymmetry and the specific model used to compute the EOS. Works on ANM include Refs. [38, 87, 123].

Some theoretical approaches attack nuclear matter directly in the thermodynamic limit (TL). These include nuclear DFT [38, 124] and *ab initio* methods such as e.g. Brückner-Hartree-Fock [39], Finite-T SCGF (Sec. 4.5) [20] and frameworks based on many-body perturbation theory (MBPT) [123, 125]. Most *ab initio* techniques, though, simulate infinite matter by using a finite number of particles (see e.g. Refs. [14, 126, 127]). Among them is AFDMC [17, 128], see Chapter 3, that has been used extensively not only for the nuclear matter EOS, but also for inhomogeneous matter, namely neutron drops [73, 129], as well as for the neutron matter response [74–76]. The coupled-cluster method [13] has been applied to nuclear matter [126, 130] using a finite number of particles, and it has become an important tool in fitting nuclear forces (see e.g. Refs. [105, 106]). A variant of SCGF that exploits the state-of-the-art ADC approximation scheme is also based on a finite model space, and Chapter 4 is devoted to it. DFT, too, can be formulated with a finite nucleon number, as proposed in Ref. [79] and further developed in [80] and in this work (Sec. 2.3).

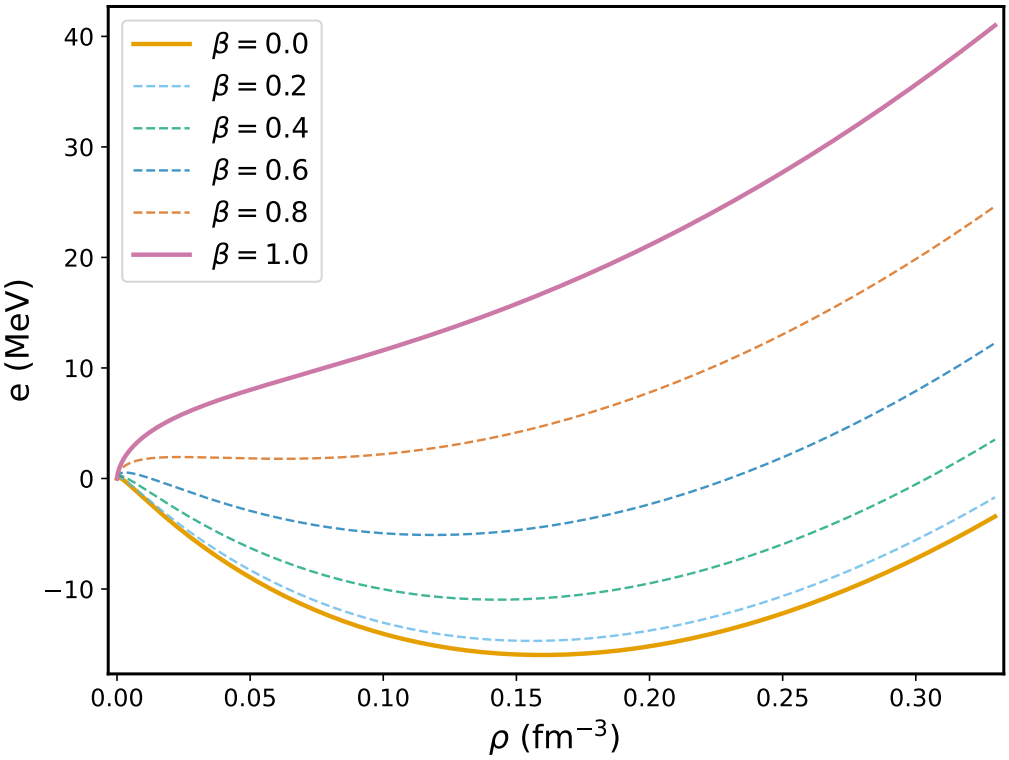

Figure 1.2: Equation of state at various isospin asymmetries. The energy per particle is shown as a function of the density for several values of β. The limiting cases of PNM ($\beta = 1$) and SNM ($\beta = 0$) are represented by thick lines. Results have been obtained with the Sly4 EDF [43] in the thermodynamic limit.

The standard technique adopted in most studies [14, 128] involves considering A fermions enclosed in a cubic box of size L and volume $\Omega = L^3$ and imposing periodic boundary conditions (PBCs) on the wave function. (See below for a different choice.) The cell size is chosen such as the density of the system is a fixed and constant $\rho_0 = A/\Omega$. In this framework, the TL corresponds to the limit in which both A and L go to infinity while keeping ρ_0 fixed [115]. The use of PBCs is suggested by the fact that, in a uniform infinite medium, all physical properties must be invariant under translation [115]. Intuitively, PBCs allow us to simulate the homogeneous system by reducing it to a single "unit cell" that repeats itself in space (Fig. 1.3). The free gas (FG), that is the starting point for studying the interacting matter, is described in terms of momentum eigenstates $|\mathbf{k}, s, t\rangle$, where $\mathbf{k}$ is the wave number, s the spin projection and t the isospin projection of the nucleon. In coordinate space, the $|\mathbf{k}\rangle$ states are represented by plane waves,

$$\psi_{\mathbf{k}}(\mathbf{x}) = \langle \mathbf{x}|\mathbf{k}\rangle = \frac{e^{i\mathbf{k}\cdot\mathbf{x}}}{\sqrt{\Omega}}. \tag{1.11}$$

The wave number is quantized as a consequence of PBCs, $\psi_{\mathbf{k}}(\mathbf{x}) = \psi_{\mathbf{k}}(\mathbf{x} + L\mathbf{n})$, i.e.

$$\mathbf{k} = \frac{2\pi}{L}\mathbf{n}, \tag{1.12}$$

where $\mathbf{n}$ is a three-component vector of integer numbers. The kinetic energy of these states is given by

$$\epsilon_{\mathbf{k}} = \frac{\hbar^2\mathbf{k}^2}{2m} = \frac{\hbar^2}{2m}\left(\frac{2\pi}{L}\right)^2 \mathbf{n}^2. \tag{1.13}$$

Since the energy depends on $\mathbf{k}^2$ and thus on $\mathbf{n}^2$, a "momentum space" shell structure emerges, with different energy levels being labeled by n^2 and being degenerate. The g.s. of the FG is obtained by occupying the first A lowest-energy states. Momentum space "magic numbers" correspond to completely filling a given number of shells. The first few of them are given by A/g =1, 7, 19, 27, 33 etc. [14], where g is spin/isospin degeneracy (2 for spin-saturated PNM, 4 for spin-saturated SNM). In Tab. 1.1 the lowest momentum space shells and magic numbers are shown. Typically, the number of fermions in a calculation is selected to correspond to a shell closure of the FG. This choice simplifies calculations in finite-A methods since it allows to use a single, uniquely defined Slater determinant as a starting point. In contrast, in open-shell configurations only a subset of degenerate orbitals is occupied, and the choice of this subset is not unique [131].

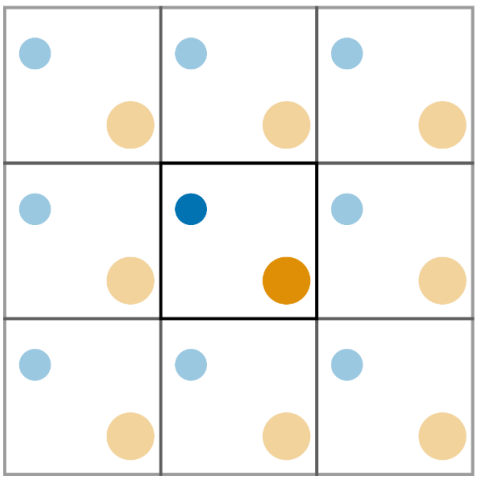

Figure 1.3: A pictorial (two-dimensional) example of periodic boundary conditions. A repeated lattice of cells is used to model the homogeneous system (e.g. a solid or nuclear matter). Particles in the main cells are allowed to interact with the adjacent cells, and thus the extended system can be better simulated. Taken from https://pythoninchemistry.org/sim_and_scat/important_considerations/pbc.html.

n^2	N. states	States	Tot.
0	1	(0,0,0)	1
1	6	$(\pm1,0,0),(0,\pm1,0),(0,0,\pm1)$	7
2	12	$(\pm1,\pm1,0),(\pm1,0,\pm1),(0,\pm1,\pm1)$	19
3	8	$(\pm1,\pm1,\pm1)$	27
4	6	$(\pm2,0,0),(0,\pm2,0),(0,0,\pm2)$	33
5	24	$(\pm2,\pm1,0),(0,\pm2,\pm1),(\pm2,0,\pm1)$ $(\pm1,\pm2,0),(0,\pm1,\pm2),(\pm1,0,\pm2)$	57

Table 1.1: Momentum space states of the FG are listed. The states are organized in momentum shells labeled by $n^2 = n_x^2 + n_y^2 + n_z^2$, where n_i are three integer numbers. The states in the shell and their number are shown in the second and third columns, respectively. Lastly, the total number of particles needed to fill the shells up to a given n^2 (included) is reported.

Simulating a finite system is different from studying a homogeneous system in the TL. These discrepancies are called finite-size (FS) effects. It is well-known that simulations with $33g$ fermions are usually a good choice for minimizing the FS effects on the EOS [126], as the kinetic energy of the finite systems is, for this specific particle number, rather close to the TL value (Fig. 1, Ref. [75]). In nuclear physics, $N = 66$ neutrons are routinely used in PNM; in SNM, $A = 132$ nucleons are used when feasible, e.g. in coupled-cluster [126], but sometimes, e.g. in AFDMC with fully realistic interaction [88], this may be too demanding computationally.

FS effects on the static response function (Sec. 1.4), instead, are rather strong, as it has been discussed in the context of the electron gas [77, 132, 133] and in PNM [75, 76]. The free FG response itself fluctuates significantly as the particle number changes (see Fig. 7.3), as a consequence of the discrete momentum shell structure of the finite system [80, 133], see also Ch. 7. As only discrete momenta are allowed in the finite system, the finite-A response looks rather different from the continuous TL response and exhibits a peculiar non-monotonic behavior at low q. The convergence to the TL is slow, as seen in cases where the TL response is available analytically, such as the free FG [80] and Skyrme-like EDFs [79, 80]. These considerations have motivated proposals to extrapolate the finite-A calculations of the interacting system to the TL. Recipes have been proposed in the context of Monte Carlo simulations of the static response, see e.g. Refs. [76, 77, 133]. For our program of matching DFT and *ab initio*, it is fundamental to be able to perform the calculations in the two frameworks as consistently as possible. As explained above, the EOS poses no substantial problems, but the situation concerning the static response, which is related to the gradient terms of the EDFs, is challenging. Thus, we are faced with a choice. A possibility is to work in the TL. However, the accuracy of the formulas to extrapolate from the *ab initio* calculations for the finite systems to the TL is uncertain. The other route, first explored by Gezerlis and collaborators [76, 79], consists in developing a finite-A DFT approach for perturbed matter (Sec. 2.3) that can be compared more directly to the outcomes of *ab initio* methods that adopt the same basic scheme and particle numbers [80]. In our work, we choose the second approach.

A way to improve the convergence of many-body calculations towards the TL has been proposed in replacing PBCs with more general boundary conditions, named twist-averaged boundary conditions (TABC) [83, 126, 134, 135]. The idea of TABC is that of breaking the multiplicity that characterizes the PBC momentum

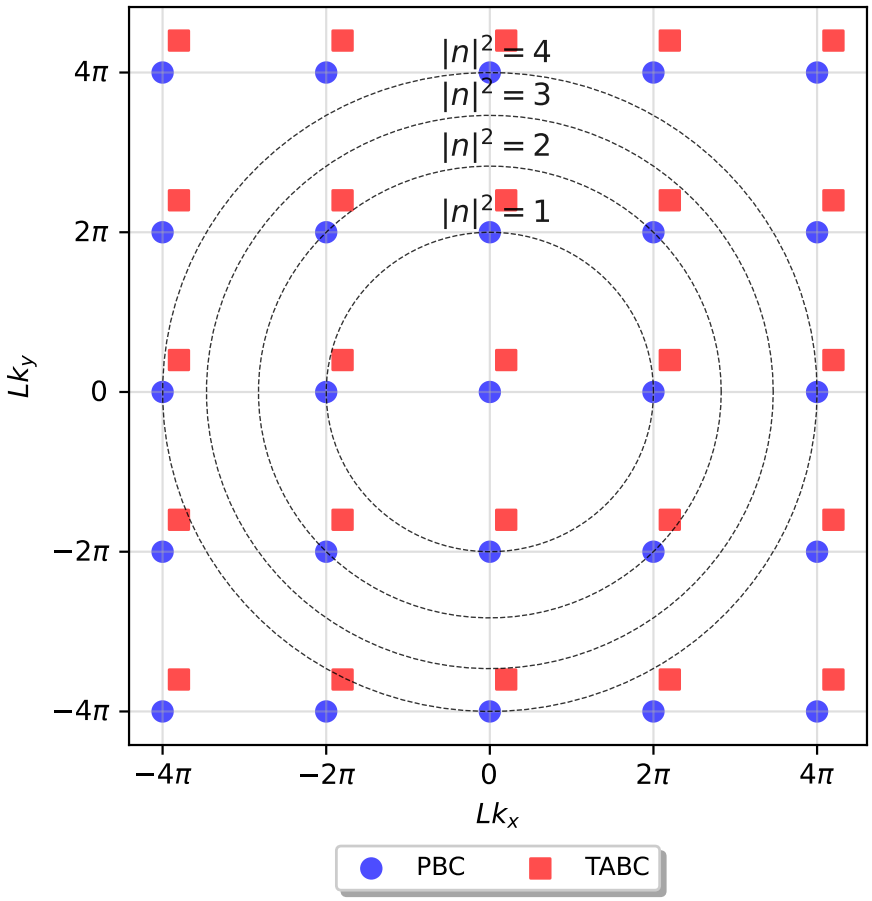

Figure 1.4: Two-dimensional example of momentum eigenstates with PBC and TABC. PBC states (circles) have coordinates $L\mathbf{k} = 2\pi(n_x, n_y)$, while TABC states are located at $L\mathbf{k} = 2\pi(n_x, n_y) + (\theta_x, \theta_y)$, with twist angles θ_x and θ_y between 0 and π. Dashed circles denote the sets of $\mathbf{k}$ points that satisfy $|\mathbf{k}|^2 = \frac{(2\pi)^2}{L^2}|\mathbf{n}|^2$ with $|\mathbf{n}|^2 = n_x^2 + n_y^2$. Note that several PBC $\mathbf{k}$ points lie on each of the circles, i.e. they are degenerate in energy. By contrast, TABC momenta have all different magnitudes, i.e. they are non-degenerate. See also text.

states (1.12). A larger set of $\mathbf{k}$ points is thus obtained, and a closer approximation to the continuum limit can be found for quantities such as the momentum distribution, the kinetic energy, and the total energy. The formal motivation behind TABC is that, in general, a periodic wave function need not be invariant under translation, but can acquire a constant phase factor, i.e. $\psi_{\mathbf{k}}(\mathbf{x}) = e^{i\theta_i}\psi_{\mathbf{k}}(\mathbf{x} + L\hat{\mathbf{e}}_i)$, where $\hat{\mathbf{e}}_i$ are the unit vector and θ_i three arbitrary angles. Under this condition, the momentum eigenstates are given by

$$\mathbf{k} = \frac{1}{L}\left(2\pi\mathbf{n} + \boldsymbol{\theta}\right). \tag{1.14}$$

In general, $-\pi \leq \theta_i < \pi$, but for time-reversal-invariant systems, $0 \leq \theta_i < \pi$ [126]. Momentum states under PBCs and TABCs are shown for simplicity in the two-dimensional case in Fig. 1.4. The momentum states (1.14) are in general non-degenerate if the three angles are different. This allows to treat in principle a different number of particles for each spin-isospin species in the system, and it has been exploited e.g. to study the spin susceptibility in PNM for arbitrary spin polarizations [135]. Importantly, by averaging over the twist angles shell effects are much reduced for both the free FG [133] and interacting fermion systems [126], and a smoother convergence to the TL is achieved ([135], Fig. 1). Moreover, a smaller number of particles is necessary to simulate the infinite system. In QMC methods, there is a distinct advantage, since sampling the twist angles is a relatively cheap operation [135]. In basis expansion methods such as coupled-cluster [126] or SCGF [83], TABCs are costly because many separate calculations must be performed and averaged. A possibility is to run a single TABC calculation with a specific choice of twist angles. This procedure is called special point TABC (sp-TABC). The optimal angle is determined e.g. minimizing the discrepancy between the HF energy computed in the TL and the HF energy of the finite-A system as a function of $\boldsymbol{\theta}$ [83, 126], and has proved effective in approaching the TL when compared to full TABC averages [126]. TABCs will be further discussed in Chapter 4 for SCGF.

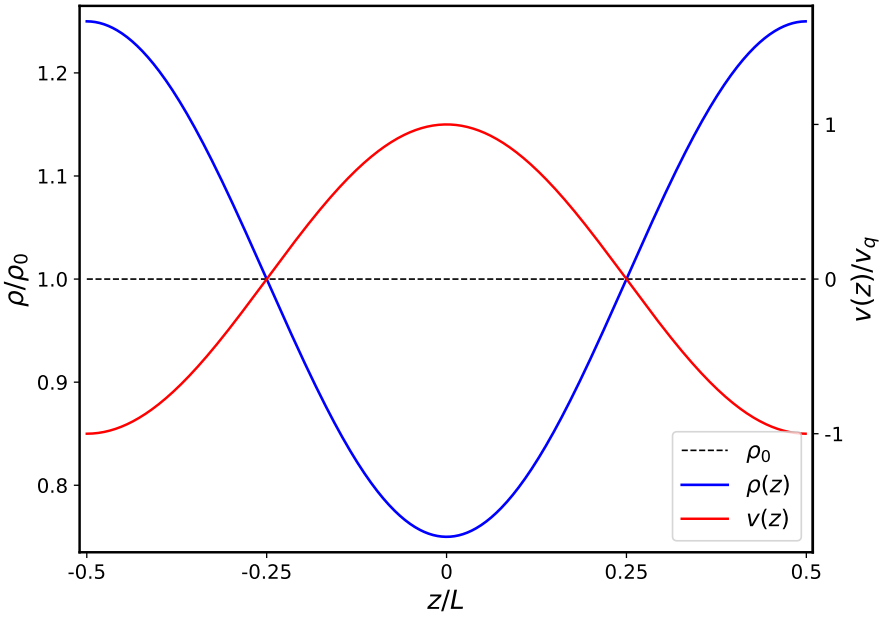

Figure 1.5: Pictorial representation of perturbed nuclear matter simulated with a finite box. The external potential (red) and the density profile (blue) are shown in normalized units ($v(z)/v_q$ and $\rho(z)/\rho_0$, respectively) as a function of the position (in units of the box size, z/L). The wave number is given by $q = 2\pi/L$, i.e. both the potential and the density complete one period inside the box. The density of the homogeneous system is represented by the dashed horizontal line. Peaks in the external potential are associated with depletions in the density and vice versa. See text for details.

1.4 Static response of infinite matter

In this Section, the theory of the response of homogeneous matter to an external static perturbation is introduced. References on the subject include Refs. [34, 75, 77, 78, 136] and our paper [80]. App. B complements this discussion.

The physical picture of the static response problem is to understand how a many-particle system reacts when an external perturbing potential is applied [77–79]. In particular, we consider a sinusoidal (monochromatic) potential coupled to the density that acts on a homogeneous system. As a consequence, a density fluctuation is induced, as shown in a pictorial representation in Fig. 1.5. Perturbed matter is realized experimentally in cold atomic systems [137, 138]. Perturbed nuclear matter is a theoretical model, that however potentially contains information on inhomogeneous phases of nucleonic matter such as those found in the inner crust of neutron stars [29, 75, 120]. Besides its intrinsic interest as a many-body system, information on the static response can be used as an ingredient to construct EDFs that include gradient corrections based on *ab initio* theory, as we discuss in Sec. 2.2.

A more formal description of the response problem is now given. Let us consider a system with uniform g.s. density ρ_0, described either by a Hamiltonian $\hat{H}$ or an EDF. We denote the g.s. by $|\Psi_0\rangle$. A static potential $v(\mathbf{x})$ coupled to the total density is then turned on. In order to satisfy the PBCs, $v(\mathbf{x})$ is taken periodic. The density and energy of the g.s. of the perturbed system are called $\rho_v(\mathbf{x})$ and $E[v]$, respectively. We highlight the functional dependence of both the total energy and the density on the external potential. If the potential is weak enough, its effect can be treated perturbatively [34]. The density fluctuation induced by $v(\mathbf{x})$, in particular, is linear in the external potential and is written as follows:

$$\delta\rho(\mathbf{x}) = \rho_v(\mathbf{x}) - \rho_0 = \int d\mathbf{x}'\chi(\mathbf{x},\mathbf{x}')v(\mathbf{x}'). \tag{1.15}$$

The static response function $\chi(\mathbf{x},\mathbf{x}')$ has been introduced. This can also be found as the zero-frequency limit of the density-density retarded correlation function or dynamical response function $\chi(\mathbf{x},\mathbf{x}',\omega)$, that is defined as the Fourier transform of the real-time response function $\chi(\mathbf{x},\mathbf{x}',t-t')$ [34, 115], namely

$$\chi(\mathbf{x},\mathbf{x}',\omega) = \int dt e^{+i\omega t}\chi(\mathbf{x},\mathbf{x}',t), \tag{1.16}$$

where

$$\chi(\mathbf{x},\mathbf{x}',t-t') = -\frac{i}{\hbar}\theta(t-t')\,\langle\Psi_0|[\hat{\rho}(\mathbf{x},t),\hat{\rho}(\mathbf{x}',t')]|\Psi_0\rangle\,. \tag{1.17}$$

In the previous relation, $\hat{\rho}$ is the density operator, $|\Psi_0\rangle$ is the wave function of the unperturbed system, θ is the step function [$\theta(t) = 1$ if $t > 0$ and zero otherwise] and $[,]$ denotes the commutator of two operators. We stress that χ depends exclusively on the properties of the unperturbed system. In homogeneous matter, the response is a function only of $\mathbf{x} - \mathbf{x}'$, i.e. $\chi(\mathbf{x}, \mathbf{x}') = \chi(\mathbf{x} - \mathbf{x}')$. Standard second-order perturbation theory implies that χ is a negative quantity.

While a generic periodic function $v(\mathbf{x})$ is a superposition of plane waves, in the following, we consider without loss of generality a monochromatic potential oscillating at a given wave number $\mathbf{q}$, namely

$$v(\mathbf{x}) = v_q e^{i\mathbf{q}\cdot\mathbf{x}} + c.c. = 2v_q \cos(\mathbf{q}\cdot\mathbf{x}) . \tag{1.18}$$

Thus the density fluctuation induced by the perturbation (1.18) is monochromatic too and is given by

$$\delta\rho(\mathbf{x}) = 2\rho_q \cos(\mathbf{q}\cdot\mathbf{x}) , \tag{1.19}$$

where the amplitude ρ_q is linear in v_q, i.e.

$$\rho_q = \chi(q) v_q, \tag{1.20}$$

and $\chi(q)$ is the Fourier transform of $\chi(\mathbf{x}, \mathbf{x}')$, see Eq. (B.8). As an effect of applying the external potential of the type (1.18), the density of the system assumes a sinusoidal profile with the same periodicity as that of the static perturbation. Due to Eq. (1.20) and $\chi(q) < 0$, maxima in the potential correspond to depletions in the density profile, and vice versa, as shown also in Fig. 1.5. The energy of the perturbed system is quadratic in the external potential. In App. B, we derive that the energy per particle is given by [77]

$$\delta e_v = e_v - e_0 = \frac{\chi(q)}{\rho_0} v_q^2. \tag{1.21}$$

The question is now how to compute the response function in practice. For generalized Skyrme EDFs [124] and Gogny and Nakada EDFs [139], for example, the response in the TL can be determined analytically (App. C.3). An alternative for studying $\chi(q)$ is provided by exploiting Eqs. (1.20) or (1.21). The strategy to determine $\chi(q)$ for a uniform system at a given density ρ_0, and with a given particle number, is the following. For a given (quantized) momentum q, multiple calculations of the g.s. of the perturbed system are performed for different values of the strength v_q of the external potential (1.18). Then $\chi(q)$ can be extracted from the amplitude of the density fluctuations [Eq. (1.20)] or from the energies [Eq. (1.21)] as a function of v_q, for sufficiently small v_q. This strategy has been applied in several contexts, e.g. Refs. [75, 77, 78, 140], and provides a relatively straightforward way to determine the static response function numerically.

In the following, we will extract $\chi(q)$ by interpolating energies with the more general formula [75, 133]

$$\delta e_v = e_v - e_0 = \frac{\chi(q)}{\rho_0} v_q^2 + C_4 v_q^4 \tag{1.22}$$

which takes into account higher-order contributions. In App. B.5, we discuss the extraction of $\chi(q)$ from fits of the density fluctuations via Eq. (1.20). Therein, we also show and explain why very close results are found using the two techniques.

Second-order perturbation theory, or equivalently the spectral representation of the dynamical density response $\chi(\mathbf{q}, \omega)$, can be employed to derive a formula that relates $\chi(q)$ to the excited states of the homogeneous system [34, 115]. For the case of the spin- and isospin-saturated A-fermion FG, the response $\chi_{0,\mathrm{A}}$ at zero temperature is given by [34, 133]

$$\chi_{0,\mathrm{A}}(q) = -\frac{4mg}{\hbar^2\Omega} \sum_{\substack{\mathbf{k}\,\mathrm{occ} \\ \mathbf{k}+\mathbf{q}\,\mathrm{unocc}}} \frac{1}{(\mathbf{k}+\mathbf{q})^2 - \mathbf{k}^2}, \tag{1.23}$$

where the sum extends over the occupied momentum states $\mathbf{k}$, and one must include only terms for which $\mathbf{k} + \mathbf{q}$ is unoccupied. Consistently with the assumptions of Sec. 1.3, we write $\mathbf{k} = \frac{2\pi}{L}\mathbf{n}$ and take $\mathbf{q}$ quantized and parallel to the z direction, i.e. $\mathbf{q} = q\hat{\mathbf{z}} = \frac{2\pi}{L} p\,\hat{\mathbf{z}}$, with p integer. Then Eq. (1.23) is expressed as

$$\chi_{0,\mathrm{A}}(q) = -\frac{mg}{L\pi^2\hbar^2} \sum_{\mathbf{n}\,\mathrm{occ}} \frac{1}{p^2 + 2pn_z}. \tag{1.24}$$

This formula is straightforward to evaluate: we determine the occupied states of the A-particle FG g.s. once and then, for each value of q, we simply perform a sum over these states. In the TL, $n_{\mathbf{k}} = \theta(q_F - k)$, $\frac{1}{\Omega}\sum_{\mathbf{k}} \longrightarrow$

$\int \frac{d\mathbf{k}}{(2\pi)^3}$ [115] and the static response becomes the well-known Lindhard function at zero-frequency [141]

$$\chi_0(q) = -g\frac{mq_F}{2(\hbar\pi)^2} f\left(\frac{q}{2q_F}\right), \tag{1.25}$$

$$f(k) = \frac{1}{2}\left(1 + \frac{1-k^2}{2k}\log\left|\frac{1+k}{1-k}\right|\right). \tag{1.26}$$

The $f(k)$ function (1.26) has the following notable limits:

$$f(k \longrightarrow 0) = 1,\ f(k \longrightarrow 1) = 1/2,\ f(k \longrightarrow +\infty) = 0. \tag{1.27}$$

CHAPTER 2

Density functional theory

Density functional theory (DFT) is one of the leading approaches in nuclear structure, that stands out for its versatility and for being applicable to the whole nuclear chart [5, 6, 32]. In the Kohn-Sham (KS) scheme, DFT maps the many-particle problem to a single-particle (s.p.) self-consistent (s.c.) problem that is based on the concept of an Energy Density Functional (EDF), i.e. on expressing the total energy of a generic system as a functional of its (generalized) densities [5, 6, 142]. DFT is rather efficient from a computational point of view and allows to study large systems that would be out of reach of *ab initio* techniques. Originally introduced for electronic systems and targeted to the g.s. [34, 142, 143], it has found countless application in quantum chemistry [144–146], cold atoms [137] and nuclear physics [5, 6, 32, 35, 44, 69]. In the latter case, it represents the only microscopic approach that allows to cover almost the whole nuclear chart [5, 6, 44], with the partial exception of very light nuclei, and to study both the g.s. and excited states. Giant resonances, for example, can be studied with the random phase approximation (RPA) method and its extensions built on top of a DFT description, see Refs. [36, 37] and references therein. Time-dependent DFT is presented in Refs. [35, 147]. Nuclear fission studies conducted with DFT are reviewed in Refs. [40, 41], and the impact of DFT predictions on r-process nucleosynthesis is discussed in e.g. Refs. [148, 149]. DFT is also applied to infinite nuclear matter [38] and is the only microscopic approach that can be used to study clustered matter in neutron stars [39, 122].

In principle, DFT provides an exact formulation of the many-body problem based on the Hohenberg-Kohn theorems [44, 144, 150], which state that all observables, starting from the total energy, can be expressed in a unique way as a functional of the one-body density. (Actually, in practice the EDF is written in terms of a few generalized densities, such as spin densities and kinetic densities [151].) However, these theorems give no hints about the actual form of the EDF. Hence, in practice, DFT turns out to be an approximate, albeit very powerful, method. In particular, most relativistic [42] and non-relativistic [5, 6, 32] nuclear EDFs are designed empirically. A reasonable ansatz for the functional form is chosen and its actual parameters are fitted on experimental observables such as radii and masses of finite nuclei, or pseudo-observables such as the saturation density of symmetric nuclear matter [6, 43]. The available EDFs are overall successful [5, 44], e.g. the experimental binding energies are reproduced on average within 1-2 MeV and charge radii within 0.01-0.02 fm. However, it is unclear how to further improve the performance of traditional EDFs [48, 55]. Existing EDFs are affected by uncontrolled extrapolation errors when applied to systems for which scarce data are available, like neutron-rich nuclei or superheavy nuclei [5, 45, 54]. The motivation of this work is to try to overcome these limitations by exploring a new strategy for constructing nuclear EDFs constrained by *ab initio* theory (Sec. 1.1).

This Chapter is structured as follows. In Sec. 2.1, we present the general framework of nuclear DFT. Original developments are presented in the next two sections. In Sec. 2.2, we describe our research on constructing *ab initio*-based EDFs. Sec. 2.2.1 describes local density approximation (LDA) EDFs. Gradient terms constrained *ab initio* are introduced in Sec. 2.2.2, and the gradient approximation (GA) EDFs are discussed. Then, in Sec. 2.3, the solution of the DFT equations for perturbed nuclear matter simulated in a finite box is presented. Further details and derivations are given in App. C.

2.1 Overview of nuclear DFT

In this section, we give an overview of nuclear DFT [5, 6, 32]. DFT is a powerful method for tackling the quantum many-particle problem, as in this framework an interacting system is described not in terms of its full many-body wave function, but in in terms of the density or, in nuclear physics, a few generalized densities. These are functions of the three spatial coordinates and are thus much simpler objects. Specifically, DFT is based on the Hohenberg-Kohn theorems, which state that the total energy of a generic system can be expressed as a functional of the density, and the exact g.s. is determined by minimizing the energy functional. In the Kohn-Sham (KS) scheme [5, 142], DFT boils down to solving a set of s.c. s.p. Schrödinger equations. This is a significant advance both from a computational perspective, as solving s.p. equations is greatly faster than dealing with many-particle equations, and from a physical point of view, as a picture of independent particles moving in a (s.c.) mean field is retrieved. The complexity of the many-body problem, however, cannot disappear, and indeed it emerges in the fact that the EDF, i.e. the functional map between the densities

and the total energy, is not known exactly, and it has to be approximated somehow. This is a difficult task in Coulomb systems, and even more so in nuclear physics, as the complexity of the nuclear force and of the solution of the nuclear many-body problem give little analytical constraints on the form of the EDF.

The nuclear EDF approach, nonetheless, has been rather successful for decades, since the pioneering work of Vautherin and Brink [152]. The perspective introduced in [152] is to describe nuclear problems at the mean-field level, i.e. Hartree-Fock (HF) or Hartree-Fock-Bogoliubov (HFB), using an *effective* interaction, that is tailored for this kind of methods and is meant to describe the interactions between nucleons in the medium. The connection with the bare force is somewhat left out; in particular, it turns out that introducing a density dependence in the interaction is essential to obtain a good description of nuclei. The interaction then is essentially a tool for generating the HF(B) energy expectation value, which is then identified with the EDF $E[\rho]$. Several phenomenological forces have been invented over the years, such as the Skyrme zero-range interaction and the Gogny and Nakada finite-range potentials, as well as covariant models [153], that describe nuclear systems in terms of nucleons, effective mesons and their interactions, see e.g. Refs. [5, 6, 32]. In fact, in a modern perspective these mean-field approaches are formulated in the DFT framework, and the focus has shifted to the construction of the EDF, rather than on the construction of the effective two-body interaction [43, 48]. Such models are phenomenological and must be fitted on observables, such as radii and masses of stable nuclei [5, 6].

From now on, we consider the specific case of non-relativistic EDFs and, in particular, we study quasi-local (or Skyrme-like) EDF models [6], i.e. EDFs that can be written as the integral of an energy density $\mathcal{E}(\mathbf{x})$ which is a function of the local densities and their gradients. This is equivalent to adopting zero-range, density-dependent NN interactions. Moreover, we specialize to time-reversal-invariant systems, such as even-even nuclei and spin-saturated nuclear matter, and neglect pairing. Thus, applications shall be limited to magic nuclei and some closed-subshell ones. Under these assumptions, the total energy of a generic system is written as a functional of number density $\rho_t(\mathbf{x})$, kinetic density $\tau_t(\mathbf{x})$ and spin-orbit density $\mathbf{J}_t(\mathbf{x})$ [6, 32] with $t = 0, 1$ labeling isoscalar ($\rho_0 = \rho_n + \rho_p$) and isovector ($\rho_1 = \rho_n - \rho_p$) quantities, and has the following structure:

$$E = \int d\mathbf{x}\, \mathcal{E}(\mathbf{x}) = E_{kin} + E_{pot} + E_{Coul} + E_{ext}, \tag{2.1}$$

which comprises the kinetic energy, a nuclear potential energy term, a Coulomb energy term, and possibly an external potential contribution,

$$E_{kin} = \int d\mathbf{x}\, \mathcal{E}_{kin}(\mathbf{x}) = \int d\mathbf{x}\, \frac{\hbar^2}{2m} \tau_0(\mathbf{x}), \tag{2.2}$$

$$E_{pot} = \int d\mathbf{x}\, \mathcal{E}_{pot}(\mathbf{x}), \tag{2.3}$$

$$E_{ext} = \sum_{t=0,1} \int d\mathbf{x}\, \rho_t(\mathbf{x}) v_t(\mathbf{x}). \tag{2.4}$$

The Coulomb contribution E_{Coul} is treated in the standard local Slater approximation [154]. (E_{Coul} is neglected in nuclear matter calculations.) The most general form of the potential term is reported in Eqs. (48-49) of Ref. [32]. Throughout this work $\mathcal{E}_{pot}$ has the form [68]

$$\begin{aligned} \mathcal{E}_{pot}(\mathbf{x}) = &\sum_{\gamma} \left(c_{\gamma,0} + c_{\gamma,1}\beta^2\right) \rho_0^{\gamma+1} \\ &+ \sum_{t=0,1} \left(C_t^{\tau} \rho_t \tau_t + C_t^{\Delta\rho} \rho_t \Delta\rho_t + C_t^{J} \mathbf{J}_t^2 + C_t^{\nabla J} \rho_t \nabla \cdot \mathbf{J}_t \right) \end{aligned} \tag{2.5}$$

with $\beta = \rho_1/\rho_0$. This structure has been introduced in Ref. [68] and represents a generalization of the typical Skyrme-like functionals, that includes a richer density dependence. We will discuss more on this in Sec. 2.2.1. The coefficients of the different terms are all, in principle, functions of the density, but they are set to constant values in Eq. 2.5, as commonly done [6]. We adopt the KS scheme [5, 142], in which a description in terms of independent particles is adopted. In practice, a set of s.p. orbitals $\psi_j(\mathbf{x})$ is introduced, the kinetic energy term is equal to that of a non-interacting Fermi system, and the densities are expressed as functions of the orbitals (see App. C.2.3). The variational principle for the EDF $\delta E = 0$, is translated into a variation w.r.t. the orbitals and the KS-DFT equations are found by minimizing the EDF w.r.t $\psi_j^*(\mathbf{x})$ with the constraint of orthonormality between the wave functions [6, 155]. The KS equations read for protons and neutrons ($q = n, p$) [6]

$$\begin{aligned} \Big[&-\nabla \cdot \frac{\hbar^2}{2m_q^*(\mathbf{x})} \nabla + U_q(\mathbf{x}) + U_{Coul}(\mathbf{x})\delta_{q,p} + v_q(\mathbf{x}) + \\ &\mathbf{W}_q(\mathbf{x}) \cdot (-i)\,(\nabla \times \sigma) \Big] \psi_j(\mathbf{x}) = \epsilon_j \psi_j(\mathbf{x}) \end{aligned} \tag{2.6}$$

where the fields entering the equations are defined as

$$U_q = \frac{\delta E_{pot}}{\delta \rho_q} \qquad \frac{\hbar^2}{2m_q^*} = \frac{\delta E}{\delta \tau_q} \qquad \mathbf{W}_q = \frac{\delta E}{\delta \mathbf{J}_q}. \tag{2.7}$$

$m_q^*(\mathbf{x})$, $U_q(\mathbf{x})$, and $\mathbf{W}_q(\mathbf{x})$ are called effective mass, mean field and spin-orbit potential, respectively. $v_q = \frac{\delta E_{ext}}{\delta \rho_q}$ is the external potential. These are in essence s.p. Schrödinger equations. Because the fields are functions of the densities, the KS equation must be solved iteratively. The solution of the KS-DFT equations in finite nuclei is well-known [6], and is performed with the skyrme_rpa code [154]. Note that the KS orbitals and eigenvalues do not have, strictly speaking, a physical meaning, and must be thought of as auxiliary quantities [142].

In infinite nuclear matter (Sec. 1.3), uniformity leads to important simplifications of Eq. (2.1). The s.p. orbitals are simple plane waves, and the number and kinetic densities are uniform and related by [156]

$$\tau_q = \frac{3}{5} k_{F,q}^2 \rho_q = \frac{3}{5} \left(3\pi^2\right)^{2/3} \rho_q^{5/3}. \tag{2.8}$$

Moreover, the spin-orbit densities $\mathbf{J}_q$, as well the derivatives of the density ($\nabla\rho_q = \Delta\rho_q = 0$), vanish. Thus only the ρ and $\rho\tau$ terms contribute to the nuclear matter energy, while the gradient ($\rho\Delta\rho$), spin-orbit ($\rho\nabla\cdot\mathbf{J}$) and tensor ($\mathbf{J}^2$) terms are non-vanishing in non-uniform systems only, such as nuclei, neutron drops or semi-infinite matter.

These considerations suggest the following regrouping of the potential density $\mathcal{E}_{pot}$ for a generic nuclear system [68]

$$\mathcal{E}_{pot} = \mathcal{E}_{bulk} + \mathcal{E}_{surf}, \tag{2.9}$$

where

$$\mathcal{E}_{bulk} = \sum_{\gamma} \left(c_{\gamma,0} + c_{\gamma,1}\beta^2\right) \rho_0^{\gamma+1} + \sum_{t=0,1} C_t^{\tau} \rho_t \tau_t \tag{2.10}$$

and

$$\mathcal{E}_{surf} = \sum_{t=0,1} \left(C_t^{\Delta\rho} \rho_t \Delta\rho_t + C_t^{J} \mathbf{J}_t^2 + C_t^{\nabla J} \rho_t \nabla\cdot\mathbf{J}_t\right). \tag{2.11}$$

These terms are called here bulk and surface contributions, respectively. Infinite matter probes only the bulk contributions, while surface terms are active in non-uniform systems.

2.2 Construction of the EDFs

In this Section, the construction of *ab initio*-based EDFs is detailed. Sec. 2.2.1 describes our LDA EDFs; attention is devoted to the parametrization of the *ab initio* EOS. In Sec. 2.2.2, surface terms are added on top of LDA. The key equations of the resulting GA EDFs are presented, and our strategy for constraining the gradient terms using perturbed nuclear matter is discussed.

2.2.1 Parametrization of the EOS and local density approximation

The simplest way to define an EDF based on the infinite matter EOS is the Local Density Approximation (LDA) [68, 69, 71, 142]. In LDA, one assumes that the same expression of the potential energy density valid in infinite matter holds for non-uniform densities $\rho_q(\mathbf{x})$ too. The only input to LDA is the EOS of homogeneous matter, and thus information on infinite matter is directly mapped to finite systems. This approximation is well-suited in particular for slowly varying density distributions, so that each small region of a generic (finite or infinite) system can be treated as a piece of bulk matter [142].

As a preliminary step, a suitable parametrization for the EOS as a function of the densities must be determined. First of all, it is convenient to represent the energy per particle $e(\rho,\beta)$ as the sum of the kinetic energy per particle of the Fermi gas $t(\rho,\beta)$ and of a potential term $v(\rho,\beta)$ [157, 158], consistently with the EDF structure (2.1):

$$e(\rho,\beta) = t(\rho,\beta) + v(\rho,\beta). \tag{2.12}$$

The kinetic energy per particle is given in the TL by [43],

$$t(\rho,\beta) = \frac{\hbar^2}{2m\rho} \sum_{q=p,n} \tau_q = \frac{3\hbar^2}{10m} \left(\frac{3\pi^2}{2}\right)^{2/3} \frac{1}{2} \left[(1+\beta)^{\frac{5}{3}} + (1-\beta)^{\frac{5}{3}}\right] \rho^{2/3}. \tag{2.13}$$

In the finite-A system, instead, it is given

$$t_A = \frac{1}{A} \frac{\hbar^2}{2m} \sum_{\mathbf{k}\,\mathrm{occ}} \mathbf{k}^2, \tag{2.14}$$

where the sum is extended over the occupied states of the finite-A Fermi gas. The kinetic energy density τ_q is given in Eq. (2.8), and we have used

$$\rho_n = \frac{1+\beta}{2}\rho_0, \qquad \rho_p = \frac{1-\beta}{2}\rho_0. \tag{2.15}$$

We anticipate that in Ref. [68] we used the TL kinetic energy (2.13), while in the new fits presented in Chs. 5 and 8 we use the prescription (2.14).

Next, an ansatz for the expression of the potential energy per particle $v(\rho,\beta)$ as a function of both ρ and β must be chosen. We follow here our previous work, Ref. [68]. Due to the isospin invariance of the nuclear force, odd powers of β vanish. Moreover, neglecting terms in β^4 is deemed accurate for densities close to saturation even for large asymmetries [38]. This quadratic dependence is adopted here, too. Presently, *ab initio* methods are mostly applied to PNM ($\beta = 1$) and SNM ($\beta = 0$). Hence, the dependence on β must be extrapolated from the limiting cases $\beta = 0$ and $\beta = 1$.

As far as the ρ-dependence is concerned, one can reasonably expect that a limited number of powers of ρ should suffice for reproducing the theoretical EoS, see e.g. Refs. [88, 157]. While a Taylor expansion in powers of the density is simple and useful [71, 157], we argue that a better option is to postulate that the potential term be a polynomial of the Fermi momentum k_F, or equivalently of $\rho^{1/3}$ [158, 159]. Heuristic motivations are the following: from a practical perspective, it grants greater flexibility than a ρ-expansion, to which it may eventually reduce as a special case. Also, it is known on an empirical basis that local EDFs need fractional powers of the density to get satisfactory predictions of the nuclear incompressibility [32, 160], thus using k_F instead of ρ as an expansion variable is also in keeping with this latter necessity. Lastly, if the EOS is thought as arising from a diagrammatic expansion, then powers of the Fermi momentum should appear naturally [158, 161].

Combining the above assumptions, one can then write

$$v(\rho,\beta) = \sum_{\gamma=1/3\ldots 6/3} c_\gamma(\beta)\rho^\gamma = \sum_{\gamma=1/3\ldots 6/3} \left[c_{\gamma,0} + c_{\gamma,1}\beta^2\right]\rho^\gamma \tag{2.16}$$

where $c_{\gamma,0} \equiv c_\gamma(\beta=0)$ and $c_{\gamma,1} \equiv c_\gamma(\beta=1) - c_\gamma(\beta=0)$. Up to this point, the model is still quite general. The only condition is that γ's have to be of the form integer/3. Now, we do not choose the potential a priori [158], but, in order to determine how many terms and which powers should enter the potential, we perform a model selection procedure. In practice, we consider all possible polynomials with at most six terms and γ not larger than 6 (Eq. (2.16)), fit each model to the data, and finally select the function that best reproduces the *ab initio* data. The following convention is employed: each model is identified by the exponents of the powers of k_F or $\rho^{\frac{1}{3}}$ it contains. For example, we refer to the polynomial $c_{\frac{2}{3}}\rho^{\frac{2}{3}} + c_{\frac{5}{3}}\rho^{\frac{5}{3}} + c_2\rho^2$ by $(2,5,6)$. Each model is fitted on the SNM and PNM data points and the optimal parameters are determined by minimizing the mean squared error (MSE) [162, 163]

$$\sigma^2\left(c_{\gamma,0}, c_{\gamma,1}\right) = \frac{1}{N_{data}}\sum_{i=1}^{N_{data}}\Big[e(\rho_i,\beta_i) - e_i\Big]^2. \tag{2.17}$$

Cross-validation is used to evaluate the out-of-sample error [163, 164], which we use to rank the different models. This is a more robust measure of goodness than the fit MSE or χ^2 [162]. The statistical analysis has been performed with the scikit-learn [165] and Minuit [166, 167] libraries.

Once we have interpolated the nuclear EOS, LDA provides the following expression for the bulk energy density $\mathcal{E}_{bulk}(\mathbf{x})$:

$$\mathcal{E}_{bulk}\left[\rho(\mathbf{x}),\beta(\mathbf{x})\right] = \rho(\mathbf{x})v\left[\rho(\mathbf{x}),\beta(\mathbf{x})\right]. \tag{2.18}$$

The LDA EDFs read

$$E_{LDA} = E_{kin} + E_{bulk} + E_{Coul} \tag{2.19}$$

and Eq. (2.6) simplifies, as $m^* = m$, $\mathbf{W}(\mathbf{x}) = 0$ and $U_q(\mathbf{x}) = U_q^{bulk}(\mathbf{x})$, where

$$U_q^{bulk}(\mathbf{x}) = \frac{\delta E_{bulk}}{\delta\rho_q(\mathbf{x})} = \tag{2.20}$$
$$\sum_\gamma\Big[\left(\gamma+1\right)c_{\gamma,0} + \big(\left(\gamma-1\right)\beta(\mathbf{x}) + 2\tau_z\big)\beta(\mathbf{x})\,c_{\gamma,1}\Big]\rho^\gamma(\mathbf{x}),$$

for the potential term (2.16) and $\tau_z = +1$ for neutron and $\tau_z = -1$ for protons. See App. C.1.1 for the derivation. App. C.1.3 is devoted to the concept of rearrangement energy of the EDF.

We anticipate that it is known that LDA is not sufficient to accurately describe nuclear systems [69]. Even for electronic DFT, where LDA is a solid starting point, it is understood that gradient terms are necessary

for quantitatively accurate predictions [144]. As shown in Ref. [68] and Sec. 6.1, the LDA EDFs based on our chosen Hamiltonians give rather different outcomes. Hence, to better gauge the LDA, we also perform a preliminary analysis of a set of EDFs that include surface terms. These so-called gradient approximation (GA) functionals are the subject of the next section.

2.2.2 Gradient approximation

In the previous section, we discussed how to use the LDA scheme to define an EDF based on *ab initio* calculations of the EOS of homogeneous nuclear matter. The LDA EDF is only dependent on the number densities, but for a realistic description of nuclei it is essential to include surface terms that are a function of the gradients of the density, as well as spin-orbit contributions. However, in uniform matter $\nabla\rho$ and $\mathbf{J}$ vanish, and only contribute to inhomogeneous systems. Empirical EDFs directly use experimental data of stable nuclei as data set to constrain the surface term. In this work we explore an alternative path, in which perturbed nuclear matter is studied *ab initio* and employed as a source of information to fix the GA EDFs (see Sec. 1.1). First, the key expression for the GA functionals is shown; then, we further motivate our approach to constrain the GA EDFs *ab initio*.

Our GA EDFs have the following form:

$$E_{GA} = E_{LDA} + E_{surf}, \tag{2.21}$$

where

$$E_{surf} = \int d\mathbf{x} \left[\sum_{t=0,1} \left(C_t^{\Delta\rho} \rho_t \Delta\rho_t + C_t^{\nabla J} \rho_t \nabla \cdot \mathbf{J}_t \right) \right]. \tag{2.22}$$

The parameters C_0^{Δ}, C_1^{Δ}, $C_0^{\nabla J}$ and $C_1^{\nabla J}$ are introduced and are all assumed to be density-independent constants. These parameters are measured in MeV fm^5; from now on, for simplicity, the dimension is omitted. Note that in [68] we used a one-parameter spin-orbit contribution and a slightly different notation. The expressions of Ref. [68] are easily recovered by setting $C_0^{\Delta\rho} = -\frac{3}{4}W_0$ and $C_1^{\Delta\rho} = -\frac{1}{4}W_0$. We have decided not to include effective mass ($\rho\tau$) terms. Indeed, in homogeneous matter they cannot be distinguished from powers of the density, see Eq. (2.8). The mean field equations (2.6) hold, with $m^* = m$ and $U_q(\mathbf{x}) = U_q^{bulk}(\mathbf{x}) + U_q^{surf}(\mathbf{x})$, where

$$\mathbf{W}_q(\mathbf{x}) = \frac{\delta E_{surf}}{\delta \mathbf{J}(\mathbf{x})} = -\left(C_0^{\nabla J} \nabla\rho_0 + C_1^{\nabla J} \nabla\rho_1\tau_z \right), \tag{2.23}$$

$$U_q^{surf}(\mathbf{x}) = \frac{\delta E_{surf}}{\delta \rho_q} = \\ = (2C_0^{\Delta\rho}\Delta\rho_0 + 2C_1^{\Delta\rho}\Delta\rho_1\tau_z) + (C_0^{\nabla J}\nabla\cdot\mathbf{J}_0 + C_1^{\nabla J}\nabla\cdot\mathbf{J}_1\tau_z) \tag{2.24}$$

and U_q^{surf} is derived in App. C.1.2.

Surface terms are essential to achieve a realistic description of nuclei improving upon LDA. In Ref. [68], we have performed a preliminary analysis of the GA EDFs. To tune the surface terms, a grid search on the three parameters C_0^{Δ}, C_1^{Δ} and W_0 is carried out, although full-fledged fits will be necessary in later works. To benchmark the quality of the EDF predictions, the root mean square (rms) errors of the binding energies and the charge radii for the GA EDFs,

$$\sigma_E(C_0^{\Delta}, C_1^{\Delta}, W_0) = \sqrt{\frac{\sum_{k=1}^{n_E} \left(E_k^{th} - E_k^{exp}\right)^2}{n_E}}, \tag{2.25a}$$

$$\sigma_{r_{ch}}(C_0^{\Delta}, C_1^{\Delta}, W_0) = \sqrt{\frac{\sum_{k=1}^{n_r} \left(r_k^{th} - r_k^{exp}\right)^2}{n_r}}. \tag{2.25b}$$

are evaluated with respect to the experimental radii of ^{40}Ca, ^{48}Ca, ^{132}Sn and ^{208}Pb and the binding energies of ^{40}Ca, ^{48}Ca, ^{90}Zr, ^{132}Sn and ^{208}Pb [168].

We now motivate our strategy for constraining the GA EDF *ab initio*. The simplest inhomogeneous model system one can study is obtained by perturbing a reference homogeneous system by an external perturbation. Neutron drops, i.e. systems of neutrons confined by a harmonic or Woods-Saxon trap, have been studied with QMC in e.g. Refs. [73, 129, 138]. It has been suggested that the energies of these systems may provide constraints on the isovector gradient terms of the nuclear EDF [73]. We remember that, in general, inhomogeneous nuclear matter is relevant for understanding the inner crust of neutron stars, where a lattice of neutron-rich nuclei coexists with a superfluid neutron gas [29, 138]. However, droplets strongly break the translational invariance of homogeneous matter. Plane waves are no longer a good starting point for describing the system,

and the reference Slater determinant must be built out of spherically symmetric orbitals. Instead, applying a small sinusoidal perturbation to homogeneous matter induces a density fluctuation, but at the same time, it involves a minimal breaking of translational invariance and is the model system that offers the closest connection to uniform matter. App. B.2 presents a formal argument, which was contained in essence already in the original paper by Hohenberg and Kohn [150], that relates the gradient expansion of the EDF to the static response function of uniform matter.

Also, there are several examples in the literature that show the relevance of the static response to connect a first-principle description of many-body systems to an EDF description, or more generally to find reliable EDFs. In Ref. [137], for example, an EDF for the bosonic ^{4}He liquid is introduced, and it is constrained to reproduce not only the EOS, but also the static response at low momentum, that for this system could be accessed experimentally. A significant improvement in the description of inhomogeneous systems, such as helium droplets or surfaces, is thus achieved. In Ref. [169], a QMC study of the unitary Fermi gas subject to a periodic perturbation has been performed. General arguments essentially fix the expression of the EDF for this system [170, 171]. Then, the free parameters are constrained using the QMC calculations, and the resulting EDF is applied to predict the energies of systems of trapped unitary fermions. Again, the importance of the static response in fixing the long-wavelength properties of the EDF is highlighted. The electron gas at finite temperature in the regime of warm dense matter (WDM) has been studied extensively with both Monte Carlo techniques and DFT in recent years, see e.g. Refs. [78, 133, 172–174]. The static and dynamic response of the homogeneous gas has been computed, and parametrizations of the local field factor in a range of conditions have been determined and employed as input to DFT models [78, 172]. These works extend the seminal results at zero temperature by Moroni *et al.* [77, 132]. In nuclear physics, the study of the static response of PNM has been pioneered using the AFDMC and DFT methods by Gezerlis *et al.* [74–76, 79]. While it was suggested to use the *ab initio* response to modify the isovector gradient terms of the EDF [75], more in-depth studies were not pursued.

To motivate the interest in using the information coming from the *ab initio* static response to constrain the surface terms of the EDF, and thus build *ab initio*-based EDFs beyond LDA. An important point to tackle is that the available *ab initio* calculations of the response have been performed with AFDMC and use a finite number of particles. To constrain the nuclear EDF, two alternatives are possible. One choice is to extrapolate the response to the thermodynamic limit. The other possibility is to match DFT calculations in the finite-A system with the *ab initio* pseudodata. (We remind, as already mentioned, that an implicit assumption is that gradient terms are relatively insensitive to the FS effects, and thus they can be reliably extracted in this way.)

The first choice would allow easing the fit procedure significantly, as analytical formulas for the TL response of Skyrme-like functionals are known [124] (App. C.3). However, despite the efforts in developing extrapolation formulas [75, 76] and their overall success in electron gas calculations [77, 78] (see also App. B.3), the accuracy of a given approximation scheme remains difficult to gauge in the nuclear matter case. For example, one could perform calculations at different particle numbers and check whether the extrapolated results are indeed roughly independent on A, as it has been shown e.g. for WDM [78, 133]. However, the computational cost of AFDMC and the small maximum number of nucleons that are accessible make such benchmarks rather demanding, and so far they have not been performed. Also, the nuclear interaction is much more complicated than the Coulomb force, and it is not obvious that considerations that hold for electronic systems may be directly translated to nuclear systems. Therefore, we have decided to stick to the second choice, and a DFT approach for simulating infinite matter in a finite box is detailed in Sec. 2.3.

In short, there exist physically motivated recipes for extrapolating the static response to the TL [75, 76], but their reliability is not known at the moment. Therefore, we deem that a more robust strategy is to calculate perturbed nuclear matter with *ab initio* and with DFT using consistent schemes, i.e. using the same discretization of the continuum based on using a finite number of particles in a box and PBCs.

We mention in passing that another possibility to control FS effects would be to employ TABC. This has been done for example in Refs. [135] to study the spin susceptibility of PNM. While technically involved and even more demanding computationally, it would provide possibly the most elegant solution to the problem. We consider this as an interesting project for the future.

2.3 Solution of DFT in a periodic box

In this Section, we discuss in detail the solution of the DFT problem for a finite number of nucleons enclosed in a cubic box subject to PBCs (see Sec. 1.3). This presentation is largely based on our paper Ref. [80]. Further details can be found in App. C.2.

We focus on spin-saturated PNM and SNM, which are the most important cases for nuclei and neutron stars [38]. Moreover, SNM and PNM can be treated as two-component (spin up/down) fermionic systems in a unified way. The case of asymmetric matter ($\rho_n \neq \rho_p$, N $\neq$ Z) would require some limited extensions of the formalism and is left for future studies. From now on, for the sake of simplicity in the notation the isospin labels (q or t) are suppressed. Our method extends the one introduced in Ref. [79], which was limited to PNM

and neglected spin-orbit terms.

We consider an external potential $v(z)$ that is a function of the z coordinate only. Thus, translational invariance is broken in the z direction but still holds in the xy plane. To respect PBCs, $v(z)$ must be periodic as well. Moreover, we adopt the spin- and isospin-independent sinusoidal potential

$$v(z) = 2v_q \cos(qz), \tag{2.26}$$

with q being an integer multiple of $q_{min} = 2\pi/L$. The s.p. wave functions (in 2-spinor notation), then, have the following structure:

$$\psi_{\mathbf{n},\lambda}(\mathbf{x}) = \frac{e^{ik_x x}}{\sqrt{L}} \frac{e^{ik_y y}}{\sqrt{L}} \begin{pmatrix} \phi_{\mathbf{n},\lambda}(z,\uparrow) \\ \phi_{\mathbf{n},\lambda}(z,\downarrow). \end{pmatrix} \tag{2.27}$$

PBCs imply that k_x and k_y are quantized in units of $2\pi/L$, i.e. $k_x = \frac{2\pi}{L} n_x$ and $k_y = \frac{2\pi}{L} n_y$, and $\phi_{\mathbf{n},\lambda}(z)$ is periodic, i.e. $\phi_{\mathbf{n},\lambda}(z+L) = \phi_{\mathbf{n},\lambda}(z)$. The states are labeled by the three integer numbers $\mathbf{n}$, plus a spin quantum number $\lambda = \pm 1$ whose precise meaning will be discussed below.

The general DFT equations (2.6) are now specialized to our case. We first note that the fields are functions of the z coordinate only: $m^* = m^*(z)$, $U = U(z)$ and $\mathbf{W} = W(z)\hat{\mathbf{z}}$. (The detailed expressions of the EDF and the fields are reported in App. C.2.1.) For later convenience, we define the transverse momentum as

$$\mathbf{k}_{n_x n_y} = k_x \hat{\mathbf{x}} + k_y \hat{\mathbf{y}} = \frac{2\pi}{L} (n_x \hat{\mathbf{x}} + n_y \hat{\mathbf{y}}), \tag{2.28}$$

whose magnitude is given by

$$k_{n_x n_y} = \sqrt{k_x^2 + k_y^2} = \frac{2\pi}{L} \sqrt{n_x^2 + n_y^2}. \tag{2.29}$$

Now, we discuss the spin-orbit term of Eq. (2.6) with the help of $\frac{\partial \psi_{\mathbf{n},\lambda}}{\partial x} = ik_x \psi_{\mathbf{n},\lambda}$ and $\frac{\partial \psi_{\mathbf{n},\lambda}}{\partial y} = ik_y \psi_{\mathbf{n},\lambda}$:

$$\begin{aligned} &\mathbf{W}(\mathbf{x}) \cdot (-i) (\nabla \times \sigma) \psi_{\mathbf{n},\lambda}(\mathbf{x}) = \\ &W(z) (-i) (\partial_x \sigma_y - \partial_y \sigma_x) \psi_{\mathbf{n},\lambda}(\mathbf{x}) = \\ &W(z) (k_x \sigma_y - k_y \sigma_x) \psi_{\mathbf{n},\lambda}(\mathbf{x}) = \\ &W(z) K_{n_x,n_y} \psi_{\mathbf{n},\lambda}(\mathbf{x}). \end{aligned} \tag{2.30}$$

In the last equality, we have introduced the spin matrix $K_{n_x,n_y} = k_x \sigma_y - k_y \sigma_x$, which reads explicitly as

$$K_{n_x,n_y} = \begin{pmatrix} 0 & -i(k_x + ik_y) \\ i(k_x - ik_y) & 0 \end{pmatrix}. \tag{2.31}$$

Since K_{n_x,n_y} is not diagonal, it is clear that the states $\psi_{\mathbf{n},\lambda}$ cannot be eigenstates of σ_z. While one possibility would be to solve the coupled DFT equation for the spin-up and -down components, a better choice is to take the ψ's to be eigenstates of K_{n_x,n_y}, as suggested in Ref. [175]. It is easy to verify that K_{n_x,n_y} has eigenvalues $\pm k_{n_x n_y}$. Thus we impose

$$K_{n_x,n_y} \psi_{\mathbf{n},\lambda}(\mathbf{x}) = \lambda k_{n_x n_y} \psi_{\mathbf{n},\lambda}(\mathbf{x}), \tag{2.32}$$

where $\lambda = \pm 1$. Importantly, since K_{n_x,n_y} is independent of the position, Eq. (2.32) implies that the orbitals (2.27) can be decomposed into the product of a single spatial orbital, function of the position z, and a constant spinor, namely

$$\psi_{\mathbf{n},\lambda}(\mathbf{x}) = \frac{e^{ik_x x}}{\sqrt{L}} \frac{e^{ik_y y}}{\sqrt{L}} \phi_{\mathbf{n},\lambda}(z) \chi_{n_x,n_y,\lambda}. \tag{2.33}$$

The spinors $\chi_{n_x,n_y,\lambda}$ satisfy

$$K_{n_x,n_y} \chi_{n_x,n_y,\lambda} = \lambda k_{n_x n_y} \chi_{n_x,n_y,\lambda}, \tag{2.34}$$

where

$$\chi_{n_x,n_y,\lambda} = \frac{1}{\sqrt{2}} \begin{pmatrix} 1 \\ \lambda e^{i\phi} \end{pmatrix}. \tag{2.35}$$

In the last expression, the angle ϕ is given by $\phi = \arctan(n_y/n_x)$.

Physically, the states $\psi_{\mathbf{n},\lambda}$ have a definite spin projection in the direction of the transverse momentum (2.28), which is not fixed but depends on the numbers n_x, n_y. The label λ thus can be interpreted as a spin projection or helicity quantum number.

The kinetic term can be manipulated along the same lines and is discussed in App. C.2.2. Finally, applying Eqs. (C.23), (2.30) and (2.32) to Eq. (2.6), we find the following one-dimensional equations for the spatial orbital $\phi_{\mathbf{n},\lambda}(z)$:

$$-\frac{d}{dz}\left(\frac{\hbar^2}{2m^*(z)}\phi'_{\mathbf{n},\lambda}(z)\right)+ \left(U(z)+v(z)+\lambda k_{n_x n_y}W(z)+\frac{\hbar^2}{2m^*(z)}k^2_{n_x n_y}\right)\phi_{\mathbf{n},\lambda}(z)= \epsilon_{\mathbf{n},\lambda}\phi_{\mathbf{n},\lambda}(z). \tag{2.36}$$

These are s.p. state-dependent Schrödinger equations that must be solved self-consistently due to the density-dependence of the fields. For a given set of quantum numbers n_x,n_y and λ, n_z labels the eigensolutions ordered by increasing s.p. energies ϵ. The z coordinate is restricted to the symmetric interval $\left[-\frac{L}{2},\frac{L}{2}\right]$.

We note that due to time-reversal invariance, that holds if we consider the spin-independent potential (2.26), the eigenvalues $\epsilon_{\mathbf{n},+1}$ and $\epsilon_{\mathbf{n},-1}$ are degenerate, while the $\lambda=\pm1$ spatial orbitals are different. In the special case of homogeneous matter ($v=0$ and $\rho(z)=\rho_0$), though, the spin-orbit field $W(z)$ vanishes [see Eq. (C.20)], and thus the equations for the spin-orbit partners $\lambda=\pm1$ are identical and so are the orbitals, namely $\phi_{\mathbf{n},+1}=\phi_{\mathbf{n},-1}$. As a consequence, the spin-orbit density vanishes too [Eq. (C.26)] and thus uniform matter is insensitive to spin-orbit. In passing, we also observe that the energy of a spin-saturated and closed-shell system is invariant when the sign of the spin-orbit coefficient is flipped, $C^{\nabla J}\longrightarrow -C^{\nabla J}$. Indeed, the effect of this transformation is that of swapping the $\lambda=1$ and $\lambda=-1$ states in Eq. (2.36) and, if an equal number of spin states is occupied, all the densities, including $J(z)$, remain unchanged, and so does the total energy.

We now describe how the Schrödinger equation (2.36) is solved, how the many-particle g.s. of the system is constructed, and how the s.c. the loop is dealt with. Due to the intrinsic periodicity of the systems under study, expanding Eq. (2.36) in the plane waves basis (see e.g. Refs. [142, 176]) allows solving the problem very efficiently. Few tens of plane waves are typically enough to find converged results even for moderately strong perturbations (see Fig. 7.6); by contrast, the finite-difference approach used in Ref. [79] requires a mesh of several hundred points at least and a much more time-consuming diagonalization. The orbitals are Fourier-expanded as $\phi(z)=\frac{1}{\sqrt{L}}\sum_k c_k e^{ikz}$ where again $k=\frac{2\pi}{L}n$ and the Schrödinger equation is recast into matrix form, namely

$$\sum_{k'}\left(\tilde{h}_{\mathbf{n},\lambda}\right)_{k,k'}c_{k'}=\epsilon_{\mathbf{n},\lambda}c_k, \tag{2.37}$$

where $\left(\tilde{h}_{\mathbf{n},\lambda}\right)_{k,k'}$ is the Hamiltonian matrix in the plane waves basis and is derived in App. C.2.4.

Nuclear DFT is based on an independent-particle picture and the many-particle g.s. configuration is found by occupying the lowest A energy levels of the system. To determine them, Eqs. (2.36) are solved for several different combinations (n_x,n_y), and separately for the two spin states λ [79]. Then, the solutions are collated and the lowest-energy states are filled up with $A/2$ spin-up and $A/2$ spin-down particles. (We remind that the discussion is limited to spin-saturated systems.) Energy levels are degenerate, since n_x and n_y only enter Eq. (2.36) in the combination $k_{n_x n_y}\propto n_x^2+n_y^2$, so that inverting the sign of n_x, n_y or both, or exchanging the two numbers, leaves the equation invariant. Such degeneracy g_{n_x,n_y} can be exploited to reduce the computational load of the method, since we can restrict ourselves to the pairs (n_x,n_y) with $0\le n_x\le n_y\le n_{max}$. It is good practice to choose at first a large value for n_{max}, though the following argument, which generalizes that of Ref. [79], allows to stop the search over the (n_x,n_y) pairs sooner. Indeed, we observe that $k_{n_x n_y}$ enters Eq. (2.36) in the combination $\lambda k_{n_x n_y}W(z)+\frac{\hbar^2}{2m^*(z)}k^2_{n_x n_y}$. This contribution is positive when $k_{n_x n_y}$ satisfies the inequality

$$k_{n_x n_y}>\bar{k}_{n_x n_y}=\max_z\left(-\lambda\frac{2m^*(z)W(z)}{\hbar^2}\right). \tag{2.38}$$

Then, provided that $k_{n_x n_y}>\bar{k}_{n_x n_y}$, the lowest eigenvalue of Eqs. (2.36) increases as $k_{n_x n_y}$ increases. Now, while one is iterating over the combinations (n_x,n_y) (which must have been sorted according to increasing values of $n_x^2+n_y^2$), and separately for $\lambda=+1$ and -1, one checks whether the lowest eigenvalue $\epsilon_{n_x,n_y,0,\lambda}$ is greater than the energy of the first $A/2$ lowest-energy states found so far. In that case, the cycle can be stopped, since we are guaranteed by Eq. (2.38) that the many-nucleon g.s does not receive contributions from higher $n_x^2+n_y^2$.

Once the occupied orbitals and the corresponding s.p. energies have been found, the total energy and the densities (App. C.2.3) of the system are computed. The total energy is evaluated in two ways, i.e. as an integral of the energy density,

$$E=L^2\int_{-L/2}^{L/2}dz\mathcal{E}(z), \tag{2.39}$$

and using

$$E = \frac{1}{2}\left(T + \sum_j \epsilon_j\right) + E_{rea}. \tag{2.40}$$

The rearrangement energy E_{rea} and the energy density $\mathcal{E}(z)$ are given in App. C.2.1. The expressions (2.39) and (2.40) must match when they are evaluated on the g.s. and this provides a strong check on the correctness of the method and its convergence.

A crucial aspect of DFT is that the potential is itself a functional of the densities. Therefore, a s.c. solution to the problem must be looked for [6]. At each iteration i of the s.c. loop, the densities are determined for the current values of the fields, as described above. Then new fields are generated by linearly mixing the old fields with the ones evaluated on the newly obtained densities $\rho^{(i)}$ [154], namely

$$U^{(i+i)} = \alpha U^{(i)} + (1-\alpha)\, U\left[\rho^{(i)}\right] \tag{2.41}$$

and similar relations for W and $\hbar/(2m^*)$. α is a mixing parameter; to achieve convergence, it is safe to be rather conservative, e.g. we choose $\alpha = 0.8 - 0.9$ at the beginning and then gradually decrease it as iterations go by. At the beginning ($i = 0$), the densities are initialized at the uniform matter values $\rho(z) = \rho_0$, $\tau(z) = \frac{3}{5}\rho_0 q_F^2$ and $J(z) = 0$ and the fields are determined accordingly.

The s.c. procedure is stopped if two conditions are met: the energies between iterations i and $i-1$ and, at the same time, the two formulas (2.40) and (2.39) for the energy at iteration i, agree within a chosen tolerance. Thresholds of the order of 0.1-1 keV per nucleon can be obtained usually in a few tens of iterations. Combining linear mixing and two convergence conditions makes our approach rather robust.

CHAPTER 3

Quantum Monte Carlo methods

Quantum Monte Carlo (QMC) methods are a prominent class of *ab initio* many-body approaches [17, 18, 177–180]. The common ground of all QMC variants is that they are stochastic methods, which employ Monte Carlo sampling techniques to reduce the computational cost needed to solve the many-particle Schrödinger equation. All Monte Carlo observables are characterized by statistical error bars, and the possibility of drawing theoretical predictions with controlled uncertainties is provided.

QMC is rather general and has been widely employed to study a variety of many-body systems. A few representative systems that have been studied with QMC include the homogeneous electron gas at zero- [77, 181] and finite-temperature [78], atoms and molecules [182], the unitary Fermi gas [138, 169] and, in nuclear physics, both finite nuclei and infinite nuclear matter [17, 18, 179]. Many other examples are reported e.g. in Refs. [8, 17, 77, 180, 183, 184]. Among the variety of QMC algorithms, we concentrate on the coordinate-space Variational Monte Carlo (VMC) and Diffusion Monte Carlo (DMC) for fermions in real space and outline their use in nuclear theory. In VMC, an ansatz for the ground state (g.s.) wave function is chosen and its parameters are optimized by minimizing the expectation value of the Hamiltonian; Monte Carlo quadrature techniques are used to evaluate the multidimensional integrals. The variational principle ensures that an upper bound to the g.s. energy is found. On the other hand, DMC is an exact method that allows in principle to find the true g.s. of the system, which is obtained starting from a trial state using a stochastic imaginary-time evolution [17, 177]. Crucial aspects of DMC are implementing a propagation scheme that makes it possible to converge to the g.s. efficiently, as well as determining suitable initial wave functions for the problem at hand, which are often optimized in preliminary VMC calculations. Also, it is important to understand that, while DMC for bosons is indeed exact, DMC for fermionic systems is affected by the "sign problem" [177, 180], that would lead, if left uncured, to a diverging variance on the energy. Techniques to mitigate this issue do exist, but are approximate and introduce a dependence on the trial wave function. Thus, DMC can be considered in practice as a rather effective variational technique [180]. In recent years, VMC has attracted a renewed interest in nuclear physics in conjunction with neural network wave functions, see e.g. Refs. [185–187]. While this approach is very promising, the well-established DMC techniques are still the state of the art in nuclear QMC.

In general, the complexity of the nuclear Hamiltonian and its dependence on the spin and isospin degrees of freedom make nuclear DMC methods rather complex and more computationally demanding than the corresponding approaches for e.g. Coulomb systems. Two DMC variants have been devised that differ in the way they treat the spin-isospin degrees of freedom, namely the Green's function Monte Carlo (GFMC) and the auxiliary field diffusion Monte Carlo (AFDMC) methods [17, 18]. In GFMC, explicit sums over the spin and isospin components of the wave function are performed. GFMC is very accurate, but limited by its rather high computational cost to light nuclei up to $A \approx 12$. Indeed, the number of spin-isospin states increases exponentially as a function of the number of nucleons. AFDMC has been developed to mitigate this issue, in that a clever technique based on the Hubbard-Stratonovich transformation is exploited to allow to sample not only the spatial coordinates of the particles, but also their spin-isospin components. At the price of using somewhat less sophisticated trial wave functions, AFDMC achieves a polynomial scaling of the computational cost ($\sim A^3$) and thus allows to study larger nuclei and nuclear matter. AFDMC, in particular, is one of the state-of-the-art *ab initio* methods for nuclei [18, 29, 179] and pure neutron matter. The status of AFDMC for PNM is summarized in Refs. [29, 127, 128, 188]. Somewhat fewer studies have been conducted in symmetric nuclear matter [87, 88, 108, 189, 190].

Coordinate space QMC techniques, which are the subject of this chapter, can deal with hard interactions without difficulty. In fact, several phenomenological potentials, such as the Argonne forces [89, 94], have been devised for use with QMC. However, there are difficulties in treating the propagation of derivative operators, and most calculations have been performed with local chiral interactions, which, after the Fourier transformation to real space, depend only on the relative distance between nucleons, but not on their gradients [128]. Efforts have been taken in this direction, and local chiral forces have been developed [18, 92, 191] and applied to nuclei [102, 103, 192, 193] and nuclear matter [88]. The use of non-local chiral interactions in GFMC has been investigated in Refs. [90, 91]. Also, non-local interactions are accessible to a different variant of DMC, the so-called configuration interaction Monte Carlo (CIMC) [23, 194, 195]. This is a diffusion method where the

propagation takes place in configuration space and so far has been applied only to PNM. In the following, we will touch only briefly on CIMC and focus on AFDMC.

In this work, AFDMC will be used for both nuclei and infinite matter. The relatively simple Argonne 4 (AV4′) interaction [89] is used (Sec. 1.2), which allows to bypass some of the difficulties that affect QMC calculations with fully realistic nuclear forces. Interestingly, we have been able to study closed-shell nuclei up to ^{90}Zr [68], which is an unusually large mass number. As far as nuclear matter is concerned, it is very important for our work that AFDMC allows to study both homogeneous and perturbed nuclear matter. The equation of state and the static response function [75] are thus the main targets for our AFDMC calculations.

This Chapter is structured as follows. In Sec. 3.1, coordinate-space QMC methods are introduced, and their application to nuclear systems is detailed. In Sec. 3.2, the AFDMC approach for nuclear physics is presented. Finally, Sec. 3.3 is devoted to the trial wave functions that are used in AFDMC calculations of nuclei and nuclear matter.

3.1 Quantum Monte Carlo methods in nuclear physics

In this Section, an overview of QMC methods in the context of nuclear physics is provided. The essential aspects of QMC are summarized, while we refer to the in-depth discussion on this subject contained in Refs. [17, 18, 177, 179] for details. An introductory section on the general features of QMC is followed by Sec. 3.1.1, where the basic steps of the DMC algorithm are listed, and Sec. 3.1.2, on the fermion sign problem and the importance sampling techniques. Finally, in Sec. 3.1.3 we briefly describe how densities are evaluated.

The principle of DMC methods [17, 177] is to determine the ground state $|\Psi_0\rangle$ of a many-body system by evolving a starting trial state $|\Psi_T\rangle$ in imaginary time:

$$|\Psi_0\rangle \propto \lim_{\tau\to+\infty} |\Psi(\tau)\rangle = \lim_{\tau\to+\infty} e^{-(H-E_T)\tau} |\Psi_T\rangle \,, \tag{3.1}$$

where $\hat{H}$ is the Hamiltonian, τ is the imaginary time and E_T is a parameter that controls the normalization [103]. Provided $|\Psi_T\rangle$ has a non-zero overlap with $|\Psi_0\rangle$, the operator $e^{-(H-E_T)\tau}$ projects the initial state into the exact g.s. This is easily understood decomposing $|\Psi_T\rangle$ on the basis of the eigenstates of $\hat{H}$, $|\Psi_n\rangle$. Then, the action of the evolution operator is given by

$$e^{-(H-E_T)\tau} |\Psi_T\rangle = e^{-(H-E_T)\tau} \sum_{n=0}^{+\infty} \langle\Psi_n|\Psi_T\rangle |\Psi_n\rangle = \sum_{n=0}^{+\infty} e^{-(E_n-E_T)} \langle\Psi_n|\Psi_T\rangle |\Psi_n\rangle = \tag{3.2}$$

$$e^{-(E_0-E_T)} \left[\langle\Psi_0|\Psi_T\rangle |\Psi_0\rangle + \sum_{n\geq 1} e^{-(E_n-E_0)} \langle\Psi_n|\Psi_T\rangle |\Psi_n\rangle \right] .$$

Excited states are thus damped faster than the g.s. component, and in the long-time limit only the g.s. component survives. As $e^{-(H-E_T)\tau}$ is not unitary, the wave function is not normalized. Generally, E_T should be an estimate of the true g.s. energy E_0. $|\Psi_T\rangle$ and E_T are typically optimized in a preliminary VMC calculation, before being used in DMC [177]. Note that Eq. (3.1) has the form of a diffusion equation, hence the name of these approaches. The pillars of DMC are the choice of the trial wave function, the implementation of the diffusion process, and the evaluation of observables. A discussion of trial states is postponed to Sec. 3.3. In this section, the other two key aspects are analyzed in the context of coordinate-space DMC. In the following, we will denote the generalized coordinates of the nucleons as $X = (R, S)$, where $R = \{\mathbf{r}_1, \mathbf{r}_2 ... \mathbf{r}_A\}$ are the positions and $S = \{s_1, t_1; s_2, t_2 ... s_A, t_A\}$ the spin-isospin projections of the A nucleons.

The time evolution cannot be performed directly for large finite times, as we do not know how to evaluate the action of $e^{-(H-E_T)\tau}$ on a state vector. However, the solution comes in breaking down the diffusion into a series of many small time steps $\delta\tau$, according to the path integral perspective. Indeed, by inserting a completeness relation in Eq. (3.1), we can write

$$\Psi(X, \tau+\delta\tau) = \int dX' G(X, X', \delta\tau)\Psi(X', \tau) \tag{3.3}$$

where

$$\Psi(X, \tau) = \langle X|\Psi(\tau)\rangle \,, \tag{3.4}$$

$$G(X, X', \delta\tau) = \langle X|e^{-(H-E_T)\delta\tau}|X'\rangle \tag{3.5}$$

are the wave function and the short-time propagator, respectively. $\Psi(X, \tau)$ can be seen as a function of the position and a vector in the spin-isospin space. Similarly, $G(X, X', \delta\tau)$ acts as a matrix on the spin-isospin

components. The integral in Eq. (3.3) must be understood as an integration over R' and a sum over the spin-isospin states S'. For vanishing $\delta\tau$, the propagator (3.5) can be indeed evaluated as follows. Using the Trotter-Suzuki formula [1], G is conveniently broken down into the product of the free propagator (G_0) and a term that depends on the potential (G_V), namely

$$G(X, X', \delta\tau) \approx G_0(X, X', \delta\tau) G_V(X, X', \delta\tau), \tag{3.7}$$

where

$$G_0(X, X', \delta\tau) = \langle X | e^{-T\delta\tau} | X' \rangle = \left(\frac{m}{2\pi\hbar^2\delta\tau}\right)^{\frac{3A}{2}} e^{-\frac{m(R-R')^2}{2\hbar^2\delta\tau}} \delta(S - S'), \tag{3.8}$$

$$G_V(X, X', \delta\tau) = \langle X | e^{-(V-E_T)\delta\tau} | X' \rangle . \tag{3.9}$$

The free propagator is exact and amounts to a multidimensional Gaussian distribution in the spatial coordinates with standard deviation $\sigma^2 = \hbar^2\delta\tau/m$. For spin-isospin dependent interactions, G_V is further decomposed as follows [103]:

$$\begin{aligned} G_V(X, X', \delta\tau) &= \langle S | e^{-(V(R)-E_T)\delta\tau} | S' \rangle \, \delta(R - R') \\ &\approx \prod_{i<j} \langle S | e^{-(V(r_{ij})-E_T)\delta\tau} | S' \rangle \, \delta(R - R'). \end{aligned} \tag{3.10}$$

Note that so far we have considered only NN forces, but later on we will comment on how 3N forces are taken care of. From Eqs. (3.8) and (3.10), it is apparent that G_V is a matrix in spin-isospin space, while G_0 is function only of the coordinates.

The number of coordinates grows quickly with the number of particles A, and an accurate evaluation of this integral in such a high-dimensional space quickly becomes infeasible with standard quadrature methods. Thus, the essential idea of DMC is to use Monte Carlo techniques to evaluate the diffusion integral stochastically. It is well-known that the numerical error that affects an integral evaluated using Monte Carlo is a statistical error that scales like $1/\sqrt{N_{samples}}$, where $N_{samples}$ is the number of samples used to approximate the integral. Crucially, the error is independent of the dimensionality of the integral [177]. The spatial coordinates R are sampled in the integral of Eq. (3.3) in all DMC variants, while two choices are possible in nuclear physics to treat the spin-isospin degrees of freedom. In GFMC [17], full sums over the spin-isospin coordinates are performed. As the number of spin-isospin components grows exponentially $\sim 2^A \binom{A}{Z}$ with the number of nucleons, GFMC, while very accurate, is limited to light nuclei up to $A \approx 12$. The alternative is to sample also the spin-isospin coordinates, as is done in the AFDMC approach [18]. In this way, a polynomial scaling of the computational cost with the number of particles is achieved, and AFDMC is the leading method for medium-mass nuclei and infinite nuclear matter [17, 18]. In Sec. 3.2 we discuss the main technical aspects of AFDMC.

3.1.1 DMC algorithm

We now describe how the diffusion integral (3.3) is solved using the Monte Carlo technique. A crucial point to understand is that in DMC the wave function is represented by a discrete set of sampling configurations $\{X\}$, called walkers. We never have direct access to the wave function, but we possess a set of walkers that are distributed approximately according to the wave function itself (not its modulus squared!) [178]. The walkers are evolved in imaginary time and are used to evaluate the expectation values of in principle any observable. The essential steps of the general DMC algorithm are listed below, while some of the modifications needed by AFDMC will be detailed in Sec. 3.2 [18, 109]:

1. An initial population of walkers is sampled from the trial state $\Psi_T(X) = \langle X | \Psi_T \rangle$, and a trial energy E_T is chosen. Typically, this may come from a variational calculation, and then could be readjusted as iterations go by. E_T should be reasonably close to the true g.s. energy E_0, so to avoid large fluctuations in the normalization of the wave function, i.e. the number of walkers in the population.

2. At each time step, the walkers are evolved. As dictated by the free propagator G_0, Eq. (3.8), the spatial coordinates are updated by drawing random displacements ξ from a $3A$-dimensional Gaussian distribution with variance $\sigma^2 = \hbar^2\delta\tau/m$ and zero average,

$$R = R' + \xi. \tag{3.11}$$

[1] For simplicity, in our presentation of DMC we use the lowest-order version of the formula,

$$e^{(\hat{A}+\hat{B})\delta\tau} = e^{\hat{A}\delta\tau} e^{\hat{B}\delta\tau} + \mathcal{O}(\delta\tau^2). \tag{3.6}$$

The Trotter formula at order $\mathcal{O}(\delta\tau^3)$ is often employed in actual implementations of the method, see e.g. Ref. [103].

This corresponds to a Brownian motion, i.e. a free diffusion of classical particles. In AFDMC, spin-isospin components are also sampled similarly, see Sec. 3.2, while in GFMC the matrix-vector product between the propagator and the wave function [Eq. (3.3)] is performed, i.e.

$$\Psi_\alpha(R,\tau+\delta\tau)=\sum_\beta G_{\alpha\beta}(R,R',\delta\tau)\Psi_\beta(R',\tau), \tag{3.12}$$

where α and β label the spin-isospin components.

3. The effect of the interactions is encoded in the G_V factor and is implemented in the diffusion algorithm by assigning a weight W to each configuration. In the basic DMC procedure,

$$W=G_V(X,X',\delta\tau). \tag{3.13}$$

These factors are employed in two ways: they are used to weight the contribution of each configuration to the expectation values, and they are in used in the branching or birth/death algorithm, in which w determines the number of copies of the walker that survive to the next time step [109, 177]. The statistical population for the following iteration is made up of an integer number of copies of each configuration X' in the current population, which is determined by the formula

$$N_{new}=\mathrm{INT}\left(\eta+\mathrm{W}\right), \tag{3.14}$$

where η is a random number uniformly distributed between 0 and 1 and INT denotes the integer part of a real number. If $w<1$, i.e. the potential energy of the configuration is higher than the trial energy, the walker can either survive or die. If $w\geq 1$, instead, the walker is guaranteed to survive and possibly multiply.

4. After a large enough number of iterations, the configurations X shall be distributed according to a probability density $\Psi(X,\tau)$, which should be close to the desired g.s. wave function $\Psi_0(X)$, and expectation values can be estimated. If an operator $\hat{O}$ commutes with the Hamiltonian, then its expectation value $\langle O(\tau)\rangle$ is evaluated as the mixed matrix element [17]

$$\langle O(\tau)\rangle=\frac{\langle\Psi_T|\hat{O}|\Psi(\tau)\rangle}{\langle\Psi_T|\Psi(\tau)\rangle}. \tag{3.15}$$

Indeed, as $\hat{O}$ commutes with $\exp\Big\{-(\hat{H}-E_T)\tau\Big\}$, Eq. (3.15) is equal to

$$\langle O(\tau)\rangle=\frac{\langle\Psi(\tau/2)|\hat{O}|\Psi(\tau/2)\rangle}{\langle\Psi(\tau/2)|\Psi(\tau/2)\rangle}, \tag{3.16}$$

which in the long-time limit yields the g.s. expectation value

$$\langle O\rangle=\frac{\langle\Psi_0|\hat{O}|\Psi_0\rangle}{\langle\Psi_0|\Psi_0\rangle}. \tag{3.17}$$

The action of $\hat{O}$ on the trial wave function can be directly evaluated, and Eq. (3.15) is easily implemented as

$$\langle O(\tau)\rangle=\frac{\sum_i(O\Psi_T^*)(X_i)w_i}{\sum_i\Psi_T^*(X_i)w_i}, \tag{3.18}$$

where the sum is extended over the walkers in the population and w_i is the weight associated with each configuration. To evaluate other quantities that do not commute with the time evolution, e.g. the density, linear extrapolations are used [17]. In particular, the following formula is employed:

$$O(\tau)=2\frac{\langle\Psi_T|\hat{O}|\Psi(\tau)\rangle}{\langle\Psi_T|\Psi(\tau)\rangle}-\frac{\langle\Psi_T|\hat{O}|\Psi_T\rangle}{\langle\Psi_T|\Psi_T\rangle}. \tag{3.19}$$

The second term is the VMC expectation value. If the trial wave function is accurate, the extrapolation error is small. That is the case in our work. However, we mention that in general extra care has to be taken when evaluating quantities other than the energy, e.g. the radii in open-shell nuclei [103].

3.1.2 Sign problem and importance sampling

This is the most basic version of the DMC algorithm. So far, however, two aspects have been neglected. First, the infamous "sign problem" that plagues projection methods for fermions has to be discussed. Second, the efficiency of the elementary DMC algorithm is rather poor, and importance sampling techniques [177] are used to drastically improve it.

Importance sampling consists in sampling in the diffusion process, instead of $\Psi(X,\tau)$, the product $\Psi_I(X)\Psi(X,\tau)$ between the wave function and a suitably chosen positive-definite importance function $\Psi_I(X)$. Typically, $\Psi_I = \Psi_T$. Eq. (3.3) is easily rearranged in terms of $\Psi_I\Psi$ as

$$\begin{aligned}\Psi_I(X)\Psi(X,\tau+\delta\tau) &= \int dX' \frac{\Psi_I(X)}{\Psi_I(X')} G(X,X',\delta\tau)\, \Psi_I(X')\Psi(X',\tau) \\ &= \int dX' G_I(X,X',\delta\tau)\, \Psi_I(X')\Psi(X',\tau),\end{aligned} \tag{3.20}$$

and the walkers are sampled using the modified propagator

$$G_I(X,X',\delta\tau) = \frac{\Psi_I(X)}{\Psi_I(X')} G(X,X',\delta\tau). \tag{3.21}$$

The formula (3.18) must be modified as well, and reads

$$\langle O(\tau)\rangle = \frac{\sum_i O_L(X_i) W_i}{\sum_i W_i}, \tag{3.22}$$

where the so-called local observable $O_L(X)$ has been defined as

$$O_L(X) = \frac{\langle \Psi_T|\hat{O}|X\rangle}{\langle \Psi_T|X\rangle}. \tag{3.23}$$

The additional factor $\frac{\Psi_I(X)}{\Psi_I(X')}$ in Eq. (3.21) penalizes moves that lead to configurations X where the importance wave function is small. By contrast, compared to the free propagator (3.5), moves that increase the probability Ψ_I are accepted with a higher rate. In this sense, the imaginary-time evolution is guided by the importance function [177]. If a reasonable approximation of the g.s. wave function can be found, a much faster convergence of the algorithm to the g.s. can be achieved. Moreover, the local energy

$$E_L(X) = \frac{\langle \Psi_T|\hat{H}|X\rangle}{\langle \Psi_T|X\rangle} \tag{3.24}$$

would be equal to E_0 if $\Psi_T = \Psi_0$. Thus, for a good trial function E_L remains close to the g.s. energy and fluctuates mildly [177]. Therefore, estimates of the g.s. energy are affected by a smaller uncertainty thanks to importance sampling.

An issue intrinsically inherent to all DMC methods for fermionic systems is the sign problem [177, 180]. DMC makes sense only if $\Psi(X,\tau)$ can be interpreted as a probability distribution for the walkers, and in particular $\Psi(X,\tau)$ must be positive. However, many-fermion wave functions must be antisymmetric in order to comply with the Pauli principle, and thus must necessarily change sign. The mathematical ground state, towards which the imaginary time evolution leads, is a symmetric (bosonic) state, and the fermionic g.s. is, in a sense, an excited state of the Hamiltonian [177]. The expectation values [Eq. (3.15)] involve overlaps between $\Psi(X,\tau)$ and the fermionic trial state, and so the desired fermionic component of $\Psi(X,\tau)$ is projected out. Indeed, if we decompose Ψ as $\Psi^{(S)} + \Psi^{(A)}$ and use $\langle \Psi^{(S)}|\Psi_T\rangle = 0$ that holds for symmetry reasons, we immediately see that $\langle \Psi_T|\hat{O}|\Psi(\tau)\rangle = \langle \Psi_T|\hat{O}|\Psi^{(A)}(\tau)\rangle$ and only the fermionic part $\Psi^{(A)}$ survives. However, this cancellation property does not hold for the variance, and the statistical error grows exponentially with τ, as well as with the particle number [18]. If left uncured, therefore, the sign problem would quickly lead to diverging uncertainties. A solution would come in limiting the walker propagation to regions where $\Psi(X,\tau)$ is positive. As the true wave function is unknown, one must resort to using an approximate guiding wave function to control the diffusion process [177]. For real Hamiltonians, the fixed-node approximation is a popular choice, in which moves that lead to a change in the sign of the trial state Ψ_T are rejected and the corresponding walkers killed [177, 180]. In AFDMC, the constrained path technique is employed [18, 127], see Sec. 3.2. In any case, all approaches to face the sign problem are approximate and introduce some kind of bias. While DMC is exact (affected only by statistical uncertainties) for bosonic systems, in fact systematic uncertainties are unavoidable in fermionic DMC [180].

3.1.3 Calculation of the number densities

We now describe how number densities are computed with QMC, see e.g. [17, 18]. We concentrate on the case of spherical nuclei, where the density $\rho_q(r)$ ($q = p, n$) is a function of the radial distance r from the center of mass of the system. The strategy to evaluate $\rho_q(r)$ is to first subdivide a sufficiently large interval $0 < r < r_{\max}$ in a certain number of bins centered at $\bar{r}_i$ and having width δr. Then, the density is related to the number of walkers lying in the radial shell $\bar{r}_i < r < \bar{r}_i + \delta r$, namely

$$\langle \rho_q(\bar{r}_i) \rangle = \frac{1}{\Omega_i} \sum_{j:\bar{r}_i < r_j < \bar{r}_i + \delta r} W_j, \tag{3.25}$$

where we sum over walkers j (with weight W_j) that lie in the shell centered around $\bar{r}_i$ and Ω_i is the volume

$$\Omega_i = \frac{4\pi}{3} \left((\bar{r}_i + \delta r)^3 - \bar{r}_i^3 \right) \approx 4\pi \bar{r}_i^2 \delta r. \tag{3.26}$$

The procedure is essentially the same for both VMC and DMC. Since the density does not commute with the Hamiltonian, its expectation value is estimated by combining the VMC and DMC expectation values as [103]

$$\langle \rho_q(r) \rangle = 2 \langle \rho_q(r) \rangle_{DMC} - \langle \rho_q(r) \rangle_{VMC} , \tag{3.27}$$

where the DMC (VMC) subscript refers to the first (second) term in Eq. (3.19).

We now turn to the case of infinite nuclear matter, and in particular to the case of perturbed matter under the effect of an external perturbation which is a function of z only (Sec. 1.4), that will be studied thoroughly in Ch. 8. As the translational symmetry is preserved on the xy plane, the relevant density is $\rho_q(z)$. In this case, we bin the z direction of the simulation box, with $-L/2 \leq z < L/2$. Then,

$$\langle \rho_q(\bar{z}_i) \rangle = \frac{1}{\Omega_i} \sum_{j:\bar{z}_i < z_j < \bar{z}_i + \delta z} W_j, \tag{3.28}$$

where the volume is given by $\Omega_i = L^2 \delta z$ and $\bar{z}_i$ and δz denote the centers and the width of the bins, respectively.

3.2 Auxiliary field diffusion Monte Carlo

A thorough introduction to DMC methods has been presented in Sec. 3.1. The present Section is meant to discuss in particular the AFDMC method for nuclear physics. Essential references on this subject are Refs. [17, 18, 103, 179].

Nuclear physics is made complicated by the need to treat the spin and isospin degrees of freedom. In GFMC, the spatial coordinates are diffused, while full summations over the spin-isospin components are performed [17]. This is rather demanding computationally due to the exponential growth of the number of spin-isospin states as a function of the number of particles. As a simple example, the spin part of three-particle systems is described by an 8-component spinor [109]:

$$|\psi\rangle_{A=3} = \begin{pmatrix} a_{\uparrow\uparrow\uparrow} \\ a_{\uparrow\uparrow\downarrow} \\ a_{\uparrow\downarrow\uparrow} \\ a_{\uparrow\downarrow\downarrow} \\ a_{\downarrow\uparrow\uparrow} \\ a_{\downarrow\downarrow\uparrow} \\ a_{\downarrow\uparrow\downarrow} \\ a_{\downarrow\downarrow\downarrow} \end{pmatrix} \qquad a_{\uparrow\uparrow\downarrow} = \langle \uparrow\uparrow\downarrow | \psi \rangle_{A=3} . \tag{3.29}$$

Symmetries reduce the number of states only mildly. AFDMC mitigates the computational burden of GFMC by representing the spin-isospin states as tensor products of single-particle spinors [18],

$$|S\rangle = |s_1\rangle \otimes |s_2\rangle \otimes ... \otimes |s_A\rangle , \tag{3.30}$$

where $|s_i\rangle$ denotes the four-component vectors

$$|s_i\rangle = a_{i,\uparrow,p} |\uparrow, p\rangle + a_{i,\downarrow,p} |\downarrow, p\rangle + a_{i,\uparrow,n} |\uparrow, n\rangle + a_{i,\downarrow,n} |\downarrow, n\rangle . \tag{3.31}$$

The states $\langle S|\Psi\rangle$ are fully represented by $4A$ complex amplitudes, instead of the factorial number of coefficients of the GFMC states. To keep the computational advantage, it is crucial to maintain the product representation throughout the calculation. However, the basis (3.30) is not closed under the action of spin-isospin quadratic operators. For example,

$$\begin{aligned}&\boldsymbol{\sigma}_1\cdot\boldsymbol{\sigma}_2[|s_1\rangle\otimes|s_2\rangle\otimes|s_3\rangle] = (2P_{12}-1)[|s_1\rangle\otimes|s_2\rangle\otimes|s_3\rangle] = \\ &2\,|s_2\rangle\otimes|s_1\rangle\otimes|s_3\rangle - |s_1\rangle\otimes|s_2\rangle\otimes|s_3\rangle\,,\end{aligned} \tag{3.32}$$

where P_{12} is the operator that flips the spin-isospin states 1 and 2. It is clear from Eq. (3.32) that quadratic operators mix up different states of the basis (3.30). As a consequence, the single-particle representation is broken by the nuclear potential, and the number of components of the wave function tends to grow quickly as iterations go by, with a loss of any advantage over GFMC. By contrast, operators acting on a single particle leave the product structure intact. The action of exponential operators of the type $e^{-iO_j\lambda}$, in particular, simply amounts to rotating one of the spinors:

$$\begin{aligned}&e^{-iO_j\lambda}\,|S\rangle = e^{-iO_j\lambda}[|s_1\rangle\otimes\ldots|s_j\rangle\otimes\ldots\otimes|s_A\rangle] = |s_1\rangle\otimes\ldots e^{-iO_j\lambda}\,|s_j\rangle\ldots\otimes|s_A\rangle = \\ &|s_1\rangle\otimes\ldots|\tilde{s}_j\rangle\otimes\ldots\otimes|s_A\rangle\,,\end{aligned} \tag{3.33}$$

where $|\tilde{s}_j\rangle = e^{-iO_j\lambda}\,|s_j\rangle$. The key intuition of AFDMC is therefore to linearize the action of the quadratic operators using the Hubbard-Stratonovich transformation

$$e^{-\frac{1}{2}O^2\lambda} = \int\frac{dx}{\sqrt{2\pi}}e^{-\frac{x^2}{2}+\sqrt{-\lambda}xO}. \tag{3.34}$$

At the cost of introducing an auxiliary variable x for each quadratic operator, one can obtain expressions in which exponentials of linear operators enter the propagator. The action of the original quadratic operator is recovered on average by sampling these auxiliary fields from the Gaussian distributions in Eq. (3.34), as we now detail.

We discuss how these concepts are applied to a nuclear Hamiltonian of the form of Eq. (1.2). Its first six terms, that we label V_{NN}^6 for short, are conveniently decomposed in the sum of spin-isospin-independent (V_{SI}) and spin-isospin-dependent terms (V_{SD}). We shall comment on how spin-orbit and 3N interactions are treated later on. Our goal is to rewrite the propagator so that Eq. (3.34) can be applied. For a given position R, the potential $V_{SD}(R)$ can be written in terms of matrices in the spin-isospin space [103],

$$V_{SD}(R) = \frac{1}{2}\sum_{i\neq j}A_{ij}^{(\tau)}\boldsymbol{\tau}_i\cdot\boldsymbol{\tau}_j + \frac{1}{2}\sum_{i\neq j}\sum_{\alpha\beta}A_{i\alpha j\beta}^{(\sigma)}\sigma_i^\alpha\sigma_j^\beta + \frac{1}{2}\sum_{i\neq j}\sum_{\alpha\beta}A_{i\alpha j\beta}^{(\sigma\tau)}\boldsymbol{\tau}_i\cdot\boldsymbol{\tau}_j\sigma_i^\alpha\sigma_j^\beta. \tag{3.35}$$

The indexes i and j are used for the particles in the system, while Greek indeces denote the Cartesian components. $A_{ij}^{(\tau)}$, $A_{i\alpha j\beta}^{(\sigma)}$ and $A_{i\alpha j\beta}^{(\sigma\tau)}$ are real and symmetric matrices of dimensions $A\times A$, $3A\times 3A$ and $3A\times 3A$, respectively. Their expressions are given e.g. in Refs. [103, 109]. If these matrices are diagonalized, a new set of operators defined in terms of the eigenvectors $\psi_n^{(\tau)}$, $\psi_n^{(\sigma)}$, $\psi_n^{(\sigma\tau)}$ and eigenvalues $\lambda_n^{(\tau)}$, $\lambda_n^{(\sigma)}$, $\lambda_n^{(\sigma\tau)}$ of the A matrices can be introduced, such that $V_{SD}(R)$ can be recast as a sum of quadratic operators:

$$V_{SD}(R) = \frac{1}{2}\sum_{\alpha=1}^{3}\sum_{n=1}^{A}\lambda_n^{(\tau)}(\mathcal{O}_{n\alpha}^{(\tau)})^2 + \frac{1}{2}\sum_{n=1}^{A}\lambda_n^{(\sigma)}(\mathcal{O}_n^{(\sigma)})^2 + \frac{1}{2}\sum_{\alpha=1}^{3}\sum_{n=1}^{A}\lambda_n^{(\sigma\tau)}(\mathcal{O}_{n\alpha}^{(\sigma\tau)})^2, \tag{3.36}$$

where

$$\mathcal{O}_n^{(\sigma)} = \psi_n^{(\sigma)}\sigma = \sum_{i\alpha}\psi_{n,i\alpha}^{(\sigma)}\sigma_{i\alpha} \tag{3.37}$$

and similarly for the (τ) and $(\sigma\tau)$ operators. A diagonalization of the potential matrices has to be performed for each new configuration R. This is the driving factor in the computational cost of AFDMC and it scales as $\sim A^3$. It is now possible to apply the transformation (3.34) to the propagator of the V_{NN}^6 interaction. We use an index n to label the $15A$ operators and corresponding eigenvalues that appear in Eq. (3.36). Following Ref. [103], we write

$$\begin{aligned}&e^{-V_{NN}^6\delta\tau}\,|RS\rangle = e^{-V_{SI}(R)\delta\tau}e^{-V_{SD}(R)\delta\tau}\,|S\rangle = \\ &e^{-V_{SI}(R)\delta\tau}\prod_{n=1}^{15A}\int\frac{dx_n}{\sqrt{2\pi}}\,e^{-\frac{x_n^2}{2}}e^{+x_n\sqrt{-\lambda_n\delta\tau}\mathcal{O}_n}\,|S\rangle = |RS'\rangle\,.\end{aligned} \tag{3.38}$$

In the previous expression, $\mathcal{O}_n$ stands for the $15A$ operators $\mathcal{O}_n^{(\tau)}$, $\mathcal{O}_n^{(\sigma)}$ and $\mathcal{O}_n^{(\sigma\tau)}$, and exponentials of sums of operators have been approximated as products of exponentials. The tensor-product basis is closed under the action of the propagator in Eq. (3.38), although this is not apparent yet. But, this can be understood by noting that the $\mathcal{O}_n$ operators are linear superpositions of σ, τ and $\sigma\tau$ matrices acting on single particles j, see Eq. (3.37). Therefore, the action of $e^{+x_n\sqrt{-\lambda_n\delta\tau}\mathcal{O}_n}$ consists in a product of independent rotations, each one acting on a single spin-isospin state j. For the case of the $\mathcal{O}_n^{(\sigma)}$ operators, for example, one finds the following expression:

$$
\begin{aligned}
e^{x_n\sqrt{-\lambda_n\delta\tau}\mathcal{O}_n^{(\sigma)}}\,|S\rangle &= \prod_{j=1}^{A} e^{x_n\sqrt{-\lambda_n\delta\tau}\sum_\alpha \psi^{(\sigma)}_{n,j\alpha}\sigma_{j\alpha}}\,|s_1\rangle\otimes\ldots\otimes|s_A\rangle \\
&= \prod_{j=1}^{A}\left[e^{x_n\sqrt{-\lambda_n\delta\tau}\sum_\alpha \psi^{(\sigma)}_{n,j\alpha}\sigma_{j\alpha}}\,|s_j\rangle\right] = |\tilde{s}_1\rangle\otimes\ldots\otimes|\tilde{s}_A\rangle\,,
\end{aligned}
\tag{3.39}
$$

where

$$
|\tilde{s}_j\rangle = e^{x_n\sqrt{-\lambda_n\delta\tau}\sum_\alpha \psi^{(\sigma)}_{n,j\alpha}\sigma_{j\alpha}}\,|s_j\rangle\,. \tag{3.40}
$$

Again, the sum over j in the exponent has been translated into a product of exponential, each function of a single j index. The product representation is thus conserved, as proved by Eq. (3.39). The new spin-isospin state $|S'\rangle$ is now a function of the auxiliary fields $\{x_n\} = \mathcal{X}$, $S' = S'(\mathcal{X})$. Thus, the imaginary-time propagation of the spin-isospin state can now be performed by sampling the auxiliary fields from the Gaussian to approximate the integral in Eq. (3.34). The updated spinors are determined with

$$
|S'\rangle = \prod_{n=1}^{15A} e^{\bar{x}_n\sqrt{-\lambda_n\delta\tau}\mathcal{O}_n}\,|S\rangle\,, \tag{3.41}
$$

where $\bar{x}_n$ are the sampled values of the auxiliary fields. Therefore, in AFDMC the spin-isospin coordinates are evolved stochastically through the auxiliary fields.

Some modifications must be made to the basic DMC method described in Sec. 3.1. In particular, the branching process is slightly different, and a specialized technique is used to deal with the sign problem. In the recent implementation of AFDMC [18, 127], the "plus and minus" procedure introduced in Ref. [87] is used in the propagation. Besides the $3A$ displacements of Eq. (3.11), in each diffusion step $15A$ field χ are sampled from normalized Gaussians. Eq. (3.41) is then used to obtain the new spin-isospin vector rotating the initial components. Then, four weights, corresponding to separately flipping the sign of the spatial moves and spin-isospin rotations, are evaluated:

$$
w_i = \frac{\Psi_T(\pm R, S(\pm\mathcal{X})}{\Psi_T(R', S')}. \tag{3.42}
$$

Only one of the four new configurations is kept, sampling it with the normalized weights w_i/W where $W = 1/4\sum_{i=1}^{4} w_i$ is the cumulative weight. Then, a global weight is assigned to the selected walker, and used for branching and evaluating observables as in standard DMC [2] :

$$
W = \left(\frac{1}{4}\sum_{i=1}^{4} w_i\right) e^{-(V_{SI}(R)-E_T)\delta\tau}. \tag{3.43}
$$

It has been shown that in this way the dependence of the results on the time step $\delta\tau$ is reduced, as linear terms in the exponentials (3.38) cancel out [18].

The constrained path (CP) method is used to control the sign problem. The weights (3.42) are evaluated with

$$
\frac{\Psi_T(X)}{\Psi_T(X')} \longrightarrow \mathrm{Re}\left(\frac{\Psi_T(X)}{\Psi_T(X')}\right), \tag{3.44}
$$

and if the ratio is negative, the weight is set to zero [18]. Unlike the fixed-node approximation [177], the CP approximation, which is adapted to complex wave functions, is not variational, i.e. it is not guaranteed to provide an upper bound to the true g.s. energy. Moreover, the use of an approximate state to guide the

[2] To understand the logic, remind how the importance-sampling propagator is defined, Eq. (3.21), and that both the kinetic energy and the spin-isospin dependent terms of V are used in the propagation. Thus, only the spin-independent potential V_{SI} is left out to weight the configurations.

evolution causes a bias in the results, so that the exact g.s. may not be approached. While the induced bias is mild for simple Hamiltonians, the most sophisticated AFDMC calculations need to be corrected by performing, after the CP, an unconstrained propagation (UC) [18, 196], where the constraint above is released and the diffusion is performed using the positive-definite importance function

$$\Psi_G(X) = |\mathrm{Re}\,\Psi_T(X)| + \alpha|\mathrm{Im}\,\Psi_T(X)|, \tag{3.45}$$

where typically $0.1 < \alpha < 0.5$. While the variance on the energy increases quickly with τ, the data can be fitted with an exponential function and extrapolated to $\tau \longrightarrow +\infty$ to find E_0 [18]. The importance of UC to properly treat interactions that include spin-orbit terms has been highlighted e.g. in Refs. [103, 127]. For the Hamiltonians used in this work, CP is a good approximation [127].

The discussion of the AFDMC propagator has been limited so far to NN forces that comprise the first six operators of Eq. (1.3). The propagation of the spin-orbit potential $\mathbf{L}\cdot\mathbf{S}$ is not trivial due to the presence of gradient terms, and a solution is described in Refs. [103, 197]. The inclusion of 3N forces is discussed in Refs. [103, 109]. Terms that involve only quadratic spin and isospin operators can be readily included in AFDMC. The remaining terms are approximated as two-body operators, and the difference is not propagated, but only evaluated in perturbation theory.

We stress again that AFDMC is significantly cheaper than GFMC: while in GFMC one has to sum over all spin-isospin components of the system, in AFDMC the propagation of the spin-isospin degrees of freedom is achieved at the cost of diagonalizing the potential matrices and performing several rotations of the $4A$ spin-isospin vector. Of course, AFDMC has also some limitations. The additional samplings make it somewhat less accurate than GFMC. Also, AFDMC trial functions must have a single-particle representation, so that they can not be as complex as those employed in VMC or GFMC (Sec. 3.3). Moreover, some terms of the nuclear interaction, such as the cubic spin-isospin operators entering 3N forces [103], or isospin-dependent spin-orbit contributions [68], can not be treated with the Hubbard-Stratonovich transformation, yet.

3.3 Trial wave functions

The subject of this Section is to describe the trial wave functions that we employ in our AFDMC calculations of infinite nuclear matter and finite nuclei. Finding a good ansatz $|\Psi_T\rangle$ requires a careful understanding of the properties of the system under study. The trial wave function is crucial for DMC for several reasons. The most obvious one is that if the initial state is already a reasonable approximation to the true g.s., then the diffusion process converges much more quickly to Ψ_0. Also, Ψ_T is used to guide the time evolution in DMC with importance sampling. A more subtle reason is that the trial function is essential in controlling the sign problem. In the standard DMC with some form of constrained propagation, the results of calculations are biased by the choice of the guiding function [180]. Thus, a bad choice for $|\Psi_T\rangle$ can negatively affect the final results.

We now come to discuss the AFDMC wave functions. The trial state is commonly expressed as the product of a reference state $|\Phi\rangle$ that encodes the long-range properties of the system and of two- and three-body correlations. For this work, we will use trial wave functions with the following Jastrow-like structure [87, 103]:

$$|\Psi_T\rangle = \prod_{i<j} f^c_{ij} \prod_{i<j<k} f^c_{ijk} \left(1 + \sum_{i<j} F_{ij} + \sum_{i<j<k} F_{ijk}\right) |\Phi\rangle\,, \tag{3.46}$$

where

$$F_{ij} = \sum_{p=2}^{6} f^p_{ij} O^p_{ij}. \tag{3.47}$$

f^c_{ij} and f^c_{ijk} are scalar correlation functions, while F_{ij} and F_{ijk} are linear spin-isospin-dependent correlations. The O^p_{ij} operators are those entering the nuclear interaction, see Eq. (1.3). The ansatz (3.46) contains a set of parameters that are determined minimizing the expectation value of the Hamiltonian on $|\Psi_T\rangle$,

$$E_T = \frac{\langle\Psi_T|\hat{H}|\Psi_T\rangle}{\langle\Psi_T|\Psi_T\rangle} \geq E_0. \tag{3.48}$$

Dedicated algorithms, such as the stochastic reconfiguration or the linear method, are used to efficiently optimize the energy [127, 178, 184].

The spinor-product structure forces AFDMC trial wave functions to be somewhat simpler than those employed in VMC or GFMC. The typical AFDMC ansatz (3.46) only includes linearized spin-isospin two-body correlations, where only one pair of nucleons is correlated at a time. More refined wave functions with

quadratic correlations, that are still compatible with the Hubbard-Stratonovich transformation, have been explored in some studies, e.g. Refs. [88, 103]. These are cheaper to evaluate, but less accurate than the GFMC and VMC trial functions that include correlations between all pairs of nucleons. Also, linear two-body correlations violate the cluster property [18, 127], which makes them somewhat inaccurate for large nuclei. Actually, for the calculations performed with the simple AV4′ interaction, that does not include tensor or spin-orbit operators, satisfying results can be obtained using just the scalar correlations, as done in our work [68] consistently with Refs. [108, 198]. Linear correlations, however, are extremely important for interactions that include the tensor potential [127]. Indeed, the tensor term is rather weak in the $T = 1$ channel, but strong in proton-neutron pairs coupled to isospin $T = 0$. However, its expectation value vanishes when only scalar correlations are included in the wave function. As a consequence, it is mandatory to include operator correlations in systems other than PNM [87, 88].

In finite nuclei, the reference state $|\Phi\rangle$ is made of a superposition of Slater determinants, each built from single-particle orbitals $|nljm_j\rangle$, coupled together to reproduce the quantum numbers (total angular momentum, total isospin, and parity) of the nuclear state of interest [17, 18]. The s.p. orbitals read in general

$$\phi_\alpha(x_i) = R_{nl}(r_i)Y_{lm_l}(\hat{r}_i)\chi_{\frac{1}{2}s}(\sigma_i)\chi_{\frac{1}{2}t}(\tau_i) \tag{3.49}$$

where $R_{nl}(r)$ is the radial function, $Y_{lm_l}(\hat{r})$ is the spherical harmonic, and $\chi_{\frac{1}{2}s}(\sigma)$ and $\chi_{\frac{1}{2}t}(\tau)$ are the complex spinors describing the spin and isospin of the s.p. state [18]. Typical choices consist in using the eigenfunctions of Woods-Saxon potential or mean-field orbitals obtained from DFT calculations.

In QMC, infinite matter is simulated using a finite number of particles with PBC, as described in Sec. 1.3. The particle number is chosen to correspond to a shell closure of the FG, whose eigenstates are plane waves with quantized wave numbers $\mathbf{k} = 2\pi/L\,\mathbf{n}$. In homogeneous matter, the natural choice for $|\Phi\rangle$ is to use the Slater determinant made of the first A occupied momentum eigenstates. When perturbed matter is studied, a better ansatz consists in employing a mean field state that is aware of the translational symmetry breaking induced by the external potential. Solutions of the one-body Schrödinger equation for the potential (2.26), i.e.

$$-\frac{\hbar^2}{2m}\psi''(z) + 2v_q\cos(qz)\,\psi(z) = \epsilon\psi(z), \tag{3.50}$$

the so-called Mathieu orbitals, have been employed as a starting point for both the electron gas [77, 132] and PNM [75, 76]. We have implemented the Mathieu wave functions in our QMC code and verified that this ansatz allows to to lower the variational energy of the inhomogeneous interacting system.

CHAPTER 4

Self-consistent Green's functions

Green's functions provide a unifying language to tackle the quantum many-body problem [115, 199]. The approach known as the Self-consistent Green's functions (SCGF) method plays a prominent role in *ab initio* nuclear theory, with wide-ranging applications to finite nuclei and infinite nuclear matter [19, 20, 82, 200]. SCGF can be applied to both closed-shell and open-shell nuclei using the Dyson and Gorkov formulations, respectively. The state-of-the-art SCGF method used to study finite nuclei is the so-called algebraic diagrammatic construction (ADC) at order n [ADC(n)], which provides a class of systematically improvable approximation to the self-energy [19, 82]. ADC has been developed up to third order [ADC(3)] in Dyson- [81, 82] and, recently, Gorkov-SCGF [201]. Infinite matter calculations have been performed so far with a different variant of SCGF, which is based on a finite-temperature (Finite-T) formalism and approximates the self-energy at the level of ladder diagrams [20]. ADC(3) has been applied to nuclear matter for the first time in Ref. [82] using a simplified interaction and further developed in Ref. [83]. One of the purposes of this work is to present the first full implementation of the ADC(3) method for nuclear matter with chiral interactions.

The Chapter is structured as follows. Sec. 4.1 presents an overview of the general Green's function formalism. In Sec. 4.2, the ADC method is presented in the context of the Dyson formalism. Then, in Sec. 4.3 we describe how the method has been extended to incorporate Gorkov pairing correction at first order on top of Dyson-ADC(3). In Sec. 4.4, we detail how ADC-SCGF is applied to infinite nuclear matter. Finally, in Sec. 4.5 a summary of the Finite-T SCGF approach for nuclear matter is reported. Further technical aspects and details on SCGF can be found in App. D.

4.1 SCGF formalism

This Section is devoted to introducing the SCGF method. For the general theory of Green's functions we will refer to the standard books Refs. [115, 199, 202]. SCGF is described in detail in Refs. [19, 26, 82, 84, 200, 201].

SCGF is based on the second quantization formulation of quantum theory. Greek letters shall be used to denote the states of a generic single-particle (s.p.) basis, that could include either a discrete or continuous spectrum. c_α and $c^\dagger_\beta$ will denote the annihilation and creation operators, respectively, and a nuclear Hamiltonian H comprising two-body (2B) ($\hat{V}$) and three-body (3B) interactions ($\hat{W}$) is assumed,

$$H = \hat{T} + \hat{V} + \hat{W}. \tag{4.1}$$

We also anticipate a partitioning of H into the sum of a reference uncorrelated Hamiltonian $H_0 = \hat{T} + \hat{U}$ and the residual interaction $H_1 = -\hat{U} + \hat{V} + \hat{W}$, where we have introduced a mean field one-body (1B) potential $\hat{U}$. In terms of the antisymmetrized 2B (3B) matrix elements $\bar{v}_{\alpha\beta,\gamma\delta}$ ($\bar{w}_{\alpha\beta\gamma,\delta\epsilon\zeta}$), these read

$$H_0 = \sum_{\alpha\beta} h^{(0)}_{\alpha\beta} c^\dagger_\alpha c_\beta = \sum_{\alpha\beta} (t_{\alpha\beta} + u_{\alpha\beta}) c^\dagger_\alpha c_\beta, \tag{4.2}$$

$$H_1 = -\sum_{\alpha\beta} u_{\alpha\beta} c^\dagger_\alpha c_\beta + \frac{1}{4} \sum_{\alpha\beta\gamma\delta} \bar{v}_{\alpha\beta,\gamma\delta} c^\dagger_\alpha c^\dagger_\beta c_\delta c_\gamma + \frac{1}{36} \sum_{\alpha\beta\gamma\delta\epsilon\zeta} \bar{w}_{\alpha\beta\gamma,\delta\epsilon\zeta} c^\dagger_\alpha c^\dagger_\beta c^\dagger_\gamma c_\zeta c_\epsilon c_\delta. \tag{4.3}$$

The concept of Green's functions (GF) or propagators lies at the heart of the SCGF method. The 1B propagator, in particular, is defined as

$$g_{\alpha\beta}(\omega) = \int dt\, e^{i\omega t} g_{\alpha\beta}(t) = \tag{4.4}$$
$$-\frac{i}{\hbar} \int dt\, e^{i\omega t} \left\langle \Psi^A_0 \right| T[c_\alpha(t) c^\dagger_\beta(0)] \left| \Psi^A_0 \right\rangle,$$

where c_α and $c^\dagger_\beta$ are evolved in the Heisenberg representation (i.e. with respect to H), and $T[\ldots]$ is the time-ordering operator. We introduce also a specific 2B propagator g^{II} as [203]

$$g^{II}_{\alpha\beta,\gamma\delta}(t-t') = -\frac{i}{\hbar}\left\langle \Psi^A_0 \middle| T[c_\beta(t)c_\alpha(t^+)c^\dagger_\gamma(t')c^\dagger_\delta(t'^+)] \middle| \Psi^A_0 \right\rangle . \tag{4.5}$$

The eigenstates of the Hamiltonian are denoted in general as the solutions to

$$H\left|\Psi^A_n\right\rangle = E^A_n \left|\Psi^A_n\right\rangle . \tag{4.6}$$

In particular, $\left|\Psi^A_0\right\rangle$ is the exact ground state of the A-particle system. The physical content of the propagator is manifest in its Lehmann or spectral representation [202]. In short, this is obtained unfolding the T-product,

$$T[c_\alpha(t)c^\dagger_\beta(0)] = \theta(t)c_\alpha(t)c^\dagger_\beta(0) - \theta(-t)c^\dagger_\beta(0)c_\alpha(t), \tag{4.7}$$

then inserting the completeness relation for the $A+1$ and $A-1$ Hilbert spaces in the first and second term, respectively, and finally performing the Fourier transform to the frequency space in Eq. (4.4). Then, one finds the following expression [82]:

$$g_{\alpha\beta}(\omega) = \sum_n \frac{(\mathcal{X}^n_\alpha)^* \mathcal{X}^n_\beta}{\hbar\omega - \epsilon^+_n + i\eta} + \sum_k \frac{\mathcal{Y}^k_\alpha (\mathcal{Y}^k_\beta)^*}{\hbar\omega - \epsilon^-_k - i\eta} \tag{4.8}$$

where the (experimentally observable) one-nucleon addition and removal energies ϵ^+_n and ϵ^-_k and the spectroscopic amplitudes $\mathcal{X}^n_\alpha$ and $\mathcal{Y}^k_\alpha$ have been defined as

$$\epsilon^+_n = E^{A+1}_n - E^A_0, \tag{4.9}$$
$$\epsilon^-_k = E^A_0 - E^{A-1}_k, \tag{4.10}$$
$$(\mathcal{X}^n_\alpha)^* = \left\langle \Psi^A_0 \middle| c_\alpha \middle| \Psi^{A+1}_n \right\rangle , \tag{4.11}$$
$$\mathcal{Y}^k_\alpha = \left\langle \Psi^{A-1}_k \middle| c_\alpha \middle| \Psi^A_0 \right\rangle , \tag{4.12}$$

respectively. The GF has (first-order) poles at the exact excitation energies of the interacting system, and the amplitudes are related to the residues at such poles.

In the standard (Dyson) formulation, the one-body propagator (4.4) is completely determined by solving the Dyson equation,

$$g_{\alpha\beta}(\omega) = g^{(0)}_{\alpha\beta}(\omega) + \sum_{\gamma\delta} g^{(0)}_{\alpha\gamma}(\omega)\Sigma^{(\star)}_{\gamma\delta}(\omega)g_{\delta\beta}(\omega), \tag{4.13}$$

where $g^{(0)}_{\alpha\beta}(\omega)$ and $g_{\alpha\beta}(\omega)$ denote the initial reference propagator, associated with H_0, and the full correlated propagator, respectively. Unless stated otherwise, for the present discussion a Hartree-Fock (HF) reference state is adopted (Dyson-SCGF). Extensions to Hartree-Fock-Bogoliubov (HFB) reference states have been developed in the so-called Gorkov-SCGF formalism, which allows to tackle open-shell superfluid systems, see e.g. Refs. [26, 84, 201]. In Sec. 4.3, we discuss a procedure to include partial Gorkov-ADC(3) corrections to Dyson-SCGF.

States occupied (unoccupied) in the HF reference state are denoted as hole (particle) s.p. states in the following. The non-linear equation (4.13) defines the irreducible self-energy $\Sigma^{(\star)}(\omega)$, in which medium effects on the propagation of the fermions are included [81]. The physical meaning of the self-energy is that of a non-local, frequency-dependent 1B potential that is felt by the particles in the system due to the interactions with the many-body environment [82]. Although Eq. (4.13) is exact, in practice $\Sigma^{(\star)}(\omega)$ must be approximated by keeping selected classes of Feynman diagrams, as will be discussed below. The specific approximation scheme we adopt is presented in Sec. 4.2.

The power of Green's function method lies in the wealth of quantities that can be accessed in a single calculation. Besides the quasiparticle (addition/removal) energies and the spectroscopic factors [200], the 1B GF allows to determine all the 1B observables and (with some caveats) the ground state energy. We first define the particle and hole spectral functions by taking the imaginary part of Eq. (4.8):

$$S^p_{\alpha\beta}(\omega) = \sum_n (\mathcal{X}^n_\alpha)^* \mathcal{X}^n_\beta \delta\left(\hbar\omega - \epsilon^+_n\right), \tag{4.14}$$
$$S^h_{\alpha\beta}(\omega) = \sum_k \mathcal{Y}^k_\alpha \left(\mathcal{Y}^k_\beta\right)^* \delta\left(\hbar\omega - \epsilon^-_k\right). \tag{4.15}$$

Then, the 1B density matrix can be related to the hole spectral function as [82]

$$\begin{aligned}\rho_{\alpha\beta} &= \left\langle \Psi_0^A \middle| c_\beta^\dagger c_\alpha \middle| \Psi_0^A \right\rangle \\ &= \int_{-\infty}^{\epsilon_0^-} S^h_{\alpha\beta}(\omega) d(\hbar\omega) = \sum_k \mathcal{Y}^k_\alpha \left(\mathcal{Y}^k_\beta\right)^* . \end{aligned} \tag{4.16}$$

From the density matrix, the expectation value of any 1B operator on the correlated ground state $\left|\Psi_0^A\right\rangle$ can be computed in terms of the $\mathcal{Y}$ amplitudes:

$$\begin{aligned}\left\langle O^{1B} \right\rangle &= \sum_{\alpha\beta} O^{1B}_{\alpha\beta} \left\langle c_\alpha^\dagger c_\beta \right\rangle = \sum_{\alpha\beta} O^{1B}_{\alpha\beta} \rho_{\beta\alpha} \\ &= \sum_k \sum_{\alpha\beta} \left(\mathcal{Y}^k_\alpha\right)^* O^{1B}_{\alpha\beta} \mathcal{Y}^k_\beta . \end{aligned} \tag{4.17}$$

Importantly, while in general finding the expectation value of a n-body observable requires knowing the n-body propagator, the total energy can also be determined with the 1B GF - exactly, when there are only 2B interactions; approximately, when the Hamiltonian contains also 3B interactions. This is achieved using the so-called generalized Koltun sum rule [203]

$$E_0^A = \frac{1}{2} \sum_{\alpha\beta} \int_{-\infty}^{\epsilon_0^-} d(\hbar\omega) \left[t_{\alpha\beta} + \omega \delta_{\alpha\beta} \right] S^h_{\beta\alpha} - \frac{1}{2} \left\langle W \right\rangle , \tag{4.18}$$

where $\langle W \rangle$ denotes the expectation value of the 3B interaction. In most cases, $\langle W \rangle$ is a perturbative correction, much smaller than the other contributions to the energy. Thus, it can be approximated with good accuracy at lowest-order using the Hartree-Fock formula in terms of three correlated 1B density matrices [82, 203]:

$$\left\langle W \right\rangle \approx \frac{1}{6} \sum_{\alpha\beta\gamma\lambda\mu\nu} W_{\alpha\beta\gamma,\lambda\mu\nu} \rho_{\lambda\alpha} \rho_{\mu\beta} \rho_{\nu\gamma} . \tag{4.19}$$

Many-body interactions can be treated by means of a perturbative expansion as a power series in H_1. We refer the reader to textbooks [115, 202] or reviews [82, 200] for the theory of propagators and Feynman diagrams, and summarize only some key notions relevant for the discussion. For the 1B propagator, the expansion reads

$$g_{\alpha\beta}(t_\alpha, t_\beta) = -\frac{i}{\hbar} \sum_{n=0}^{+\infty} \left(-\frac{i}{\hbar}\right)^n \frac{1}{n!} \int dt_1 ... \int dt_n \times \tag{4.20}$$

$$\left\langle \Phi_0^A \middle| T \left[H_1(t_1) ... H_A(t_A) c^I_\alpha(t_\alpha) c^{I\dagger}_\beta(t_\beta) \right] \middle| \Phi_0^A \right\rangle_{conn} , \tag{4.21}$$

where operators are now evolved in the interaction picture with respect to the unperturbed Hamiltonian H_0, $\left|\Phi_0^A\right\rangle$ is the A-particle g.s. of H_0, and only connected diagrams have to be considered when using the Wick theorem.

The Dyson equation (4.13) leads to a first reorganization of the diagrammatic expansion. Indeed, the self-energy in practice collects only the one-particle irreducible (1PI) diagrams, i.e. those graphs that cannot be disconnected by cutting a single fermion line. A further simplification is achieved by expressing the self-energy as a functional of the *dressed* GFs. This reduces the set of diagrams to the so-called *skeleton* ones, and gives rise to a self-consistent formulation of the Green's functions approach. Skeletons are defined as those diagrams that do not contain any portion that can be disconnected by cutting a fermion line twice in two different points, i.e. they do not contain any self-energy insertion [203]. Any reference to unperturbed states is dropped at the skeleton level, and the Dyson equation is written only in terms of the full GF $g(\omega)$. This is the essence of the SCGF method. Such reorganization is convenient for several reasons, see [203]. For example, the number of diagrams to evaluate is significantly reduced. Also, artificial dependencies on the reference state and auxiliary potential $\hat{U}$ are absent.

When 3B interactions are included, the number of diagrams in the perturbative expansion of the self-energy grows (factorially) in an uncontrolled way. In order to reduce this complexity, a strategy has been proposed in Ref. [203], which is based on the concepts of effective 1B and 2B interaction and interaction-irreducible diagrams. The interaction Hamiltonian is recast as

$$\tilde{H}_1 = \tilde{U} + \tilde{V} + \hat{W} \tag{4.22}$$

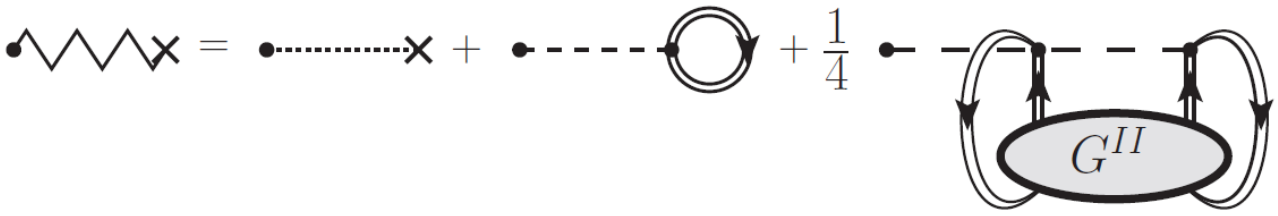

Figure 4.1: Diagrammatic representation of the effective one-body interaction, Eq. (4.23). The 1B interaction receives contributions from the original 1B external potential, from the 2B force contracted with one 1B GF and from the 3B interaction contracted with the 2B GF. Taken from Ref. [203].

Figure 4.2: Diagrammatic representation of the effective two-body interaction, Eq. (4.24). The contributions from the bare 2B interaction and from the 3B interaction contracted with a 1B GF are shown. Taken from Ref. [203].

where the explicit expressions of the matrix elements of the effective operators are given by

$$\tilde{u}_{\alpha\beta} = -u_{\alpha\beta} + \sum_{\gamma\delta} \bar{v}_{\alpha\gamma,\beta\delta}\rho_{\delta\gamma} + \frac{1}{4}\sum_{\gamma\delta\epsilon\zeta} \bar{w}_{\alpha\gamma\delta,\beta\epsilon\zeta}\Gamma_{\epsilon\zeta,\gamma\delta}, \tag{4.23}$$

$$\tilde{v}_{\alpha\beta,\gamma\delta} = \bar{v}_{\alpha\beta,\gamma\delta} + \sum_{\epsilon\zeta} \bar{w}_{\alpha\beta\epsilon,\gamma\delta\zeta}\rho_{\zeta\epsilon}, \tag{4.24}$$

and the 2B density matrix can be computed exactly from the 2B propagator,

$$\Gamma_{\epsilon\zeta,\gamma\delta} = \left\langle \Psi_0^A \middle| c_\gamma^\dagger c_\delta^\dagger c_\zeta c_\epsilon \middle| \Psi_0^A \right\rangle = +i\hbar \lim_{t\to 0^-} g^{II}_{\epsilon\zeta,\gamma\delta}(t). \tag{4.25}$$

The diagrammatic representations of $\tilde{U}$ and $\tilde{V}$ are shown in Figs. 4.1 and 4.2. In evaluating the contribution to the 1B effective potential stemming from the 3B forces, g^{II} is in practice treated in the approximation of two dressed, but non-interacting nucleons [82], namely

$$g^{II}_{\epsilon\zeta,\gamma\delta}(t) \approx i\hbar g_{\epsilon\gamma}(t)g_{\zeta\delta}(t) - i\hbar g_{\epsilon\delta}(t)g_{\zeta\gamma}(t), \tag{4.26}$$

that implies approximating Γ as the product of two correlated 1B densities,

$$\Gamma_{\epsilon\zeta,\gamma\delta} \approx \rho_{\epsilon\gamma}\rho_{\zeta\delta} - \rho_{\epsilon\delta}\rho_{\zeta\gamma}. \tag{4.27}$$

Thus, in practical calculations $\tilde{U}$ (4.23) is computed as

$$\tilde{u}_{\alpha\beta} = -u_{\alpha\beta} + \sum_{\gamma\delta} \bar{v}_{\alpha\gamma,\beta\delta}\rho_{\delta\gamma} + \frac{1}{2}\sum_{\gamma\delta\epsilon\zeta} \bar{w}_{\alpha\gamma\delta,\beta\epsilon\zeta}\rho_{\epsilon\gamma}\rho_{\zeta\delta}. \tag{4.28}$$

These effective interactions, in essence, are obtained by averaging the bare forces over the correlated 1B density matrices. In this way, part of the many-body correlations is already included at the level of the Hamiltonian [82]. In particular, the effects of the 3B interactions are incorporated to some extent into $\tilde{U}$ and $\tilde{V}$. This scheme is similar in spirit to normal-ordering techniques [14, 126]. However, it improves upon it, since the correlated density matrices of the system are used, while normal-ordering is based on the HF density matrices. It has been shown in Ref. [203] that the perturbation expansion in terms of H_1 and irreducible diagrams is equivalent to performing an expansion in terms of $\tilde{H}_1$ provided that only the subclass of *interaction-irreducible* diagrams is resummed. An interaction vertex is said to be reducible if the whole diagram can be disconnected in two parts by cutting the vertex itself. Equivalently, a diagram is interaction-reducible if there exists a group of isolated fermion lines (either interacting among themselves or not) that leaves one interaction vertex and eventually all return to it. In the following, 1PI, skeleton, and interaction-irreducible diagrams will be considered in the expansion of the self-energy. Diagrams are expressed as function of the correlated GF, and effective interactions are used.

The self-energy can be decomposed as the sum of static and frequency-dependent contributions as follows:

$$\Sigma^{(\star)} = -U + \Sigma^{(\infty)} + \tilde{\Sigma}(\omega), \tag{4.29}$$

where $\Sigma^{(\infty)}$ is the frequency-independent part of the self-energy, while $\tilde{\Sigma}(\omega)$ collects the dynamical contributions that appear starting from the second order in the diagrammatic expansion. When only skeletons are considered, $\Sigma^{(\infty)}$ stems from first-order diagrams. Without self-consistency, higher-order terms must be included, see Ref. [81]. $\Sigma^{(\infty)}$ plays the role of a static mean field and generalizes the HF potential to correlated densities, in the same way as the effective interactions (4.23) and (4.24) generalize the standard normal-ordering approximation. Since it does not propagate any intermediate excitation, it receives contributions only from diagrams where incoming and outgoing lines are attached to the same interaction vertex [82], and satisfies

$$\begin{aligned}\Sigma^{(\infty)} = \tilde{U} + U &= \sum_{\gamma\delta} \bar{v}_{\alpha\gamma,\beta\delta}\rho_{\delta\gamma} + \frac{1}{4}\sum_{\gamma\delta\epsilon\zeta} \bar{w}_{\alpha\gamma\delta,\beta\epsilon\zeta}\Gamma_{\epsilon\zeta,\gamma\delta} \\ &\approx \sum_{\gamma\delta} \bar{v}_{\alpha\gamma,\beta\delta}\rho_{\delta\gamma} + \frac{1}{2}\sum_{\gamma\delta\epsilon\zeta} \bar{w}_{\alpha\gamma\delta,\beta\epsilon\zeta}\rho_{\epsilon\gamma}\rho_{\zeta\delta}.\end{aligned} \tag{4.30}$$

Note that bare 2B and 3B matrix elements are being used in Eq. (4.30). The expression of the dynamical self-energy, instead, depends on the specific approximation scheme that one adopts, as will be discussed in connection to the algebraic diagrammatic construction in Sec. 4.2.

4.2 Algebraic diagrammatic construction

The algebraic diagrammatic construction (ADC) is a Green's function method that has found widespread application in quantum chemistry [204, 205] and nuclear physics [81, 201]. In this section, we discuss ADC in the framework of Dyson-SCGF; an effective way to include pairing correlations on top of a Dyson description is the subject of Sec. 4.3.

ADC defines a hierarchy of approximations of the irreducible self-energy at different orders n [ADC(n)], and is systematically improvable, in the sense that in the limit $n \longrightarrow +\infty$ the exact self-energy would be recovered. The key principle of ADC is to construct a class of approximate self-energies that have the same analytical structure as the exact $\Sigma^{(\star)}$. Indeed, similarly to the one-body propagator, the self-energy admits a Lehmann representation that dictates that only first-order poles should appear. Moreover, causality implies that the poles should be shifted from the real axis by imaginary factor $\pm i\eta$, with $\eta \longrightarrow 0^+$. Without loss of generality, the exact and ADC self-energies have the following non-diagonal matrix structure

$$\begin{aligned}\Sigma^{(\star)}(\omega) &= -U + \Sigma^{(\infty)} + \tilde{\Sigma}(\omega) \\ &= -U + \Sigma^{(\infty)} + M^\dagger \frac{1}{\hbar\omega\mathbb{1} - (E^> + C) + i\eta} M + N \frac{1}{\hbar\omega\mathbb{1} - (E^< + D) - i\eta} N^\dagger.\end{aligned} \tag{4.31}$$

The self-energy carries two s.p. states indexes, i.e. $\Sigma^{(\star)} = (\Sigma^{(\star)}_{\alpha\beta})$. M and N are called coupling matrices and connect s.p. states to intermediate state configurations (ISCs) consisting of 2-particle-1-hole (2p1h), 3p2h... (forward configurations, labeled by r) and 2h1p, 3h2p... s.p. states (backward configurations, s), respectively. Thus, M and N are matrices of the type $(M_{r\alpha})$ and $(N_{\alpha s})$, respectively. $E^>$ ($E^<$) represent the energies of the unperturbed ISCs and are diagonal matrices of dimension $N_{fw} \times N_{fw}$ ($N_{bk} \times N_{bk}$), with N_{fw} and N_{bk} counting the number of forward and backward ISCs in the model space, respectively. $\mathbb{1}$ is the identity matrix in the space of either forward or backward configurations. Lastly, $C = (C_{rr'})$ [$D = (D_{ss'})$] are called interaction matrices and connect two different ISCs. They appear starting from ADC(3) and their effect is to shift the position of the self-energy poles. As we discuss below, non-vanishing C and D matrices imply a resummation of an infinite number of diagrams [82]. Both coupling and interaction matrices are made antisymmetric with respect to the permutation of any two particle or two hole indexes [81].

We give the general idea of how the ADC matrices are determined, as the details can be found elsewhere, e.g. in Refs. [81, 82, 201, 205]. The key step to define the ADC(n) self-energy is to expand all the matrices in Eq. (4.31) in power series of the interaction Hamiltonian and keep terms up to order n in the resulting self-energy. The coupling matrices M and N can contain terms of any order in H_1 or, equivalently, $\tilde{H}_1$, i.e.

$$M = M^{(1)} + M^{(2)} + ..., \quad N = N^{(1)} + N^{(2)} + ... \tag{4.32}$$

The coupling matrices C and D, instead, can only be of first order [81]. To expand the energy denominators, the formula

$$\frac{1}{A-B} = \frac{1}{A} + \frac{1}{A}B\frac{1}{A-B} = \frac{1}{A} + \frac{1}{A}B\frac{1}{A} + \frac{1}{A}B\frac{1}{A}B\frac{1}{A} + ... \tag{4.33}$$

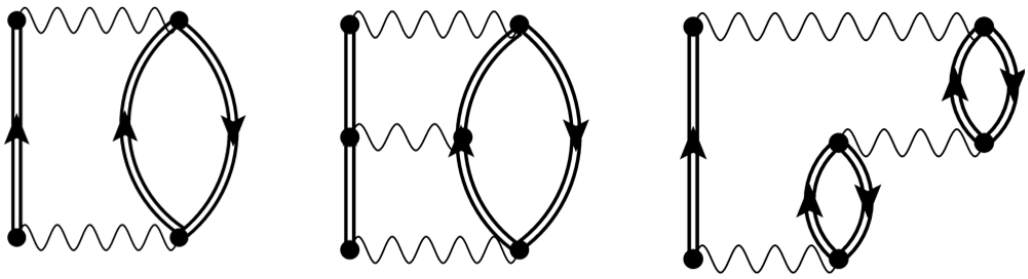

Figure 4.3: Feynman diagrams contributing to the ADC(3) working equation for the self-energy. From left to right: second-order contribution, third-order ring diagram, third-order ladder diagram. One-particle irreducible, skeleton, and interaction-irreducible diagrams that propagate only 2p1h or 2h1p ISCs are shown. The wiggly lines denote the effective 2B interaction. Dressed propagators are used.

is exploited. We now use these relations and retain terms up to order n. Performing such expansion up to $n = 3$, for example, gives [82]

$$\begin{aligned}\Sigma^{(\star)} = &- U + \Sigma^{(\infty)} \\ &+ M^{(1)\dagger} \frac{1}{\hbar\omega\mathbb{1} - E^{>} + i\eta} M^{(1)} + N^{(1)} \frac{1}{\hbar\omega\mathbb{1} - E^{<} - i\eta} N^{(1)\dagger} \\ &+ M^{(2)\dagger} \frac{1}{\hbar\omega\mathbb{1} - E^{>} + i\eta} M^{(1)} + N^{(2)} \frac{1}{\hbar\omega\mathbb{1} - E^{<} - i\eta} N^{(1)\dagger} \\ &+ M^{(1)\dagger} \frac{1}{\hbar\omega\mathbb{1} - E^{>} + i\eta} M^{(2)} + N^{(1)} \frac{1}{\hbar\omega\mathbb{1} - E^{<} - i\eta} N^{(2)\dagger} \\ &+ M^{(1)\dagger} \frac{1}{\hbar\omega\mathbb{1} - E^{>} + i\eta} C \frac{1}{\hbar\omega\mathbb{1} - E^{>} + i\eta} M^{(1)} \\ &+ N^{(1)} \frac{1}{\hbar\omega\mathbb{1} - E^{<} - i\eta} D \frac{1}{\hbar\omega\mathbb{1} - E^{<} - i\eta} N^{(1)\dagger}\end{aligned} \tag{4.34}$$

In order to determine the unknown matrices, ADC asks to evaluate all possible self-energy diagrams up to order n explicitly and compare them to the previous formal expansion to identify the minimal expression of the different matrices. ADC(n), then, contains all the n-th order self-energy diagrams, but also incorporates some higher-order diagrams, and automatically implies an all-orders resummation of specific classes of diagrams, such as rings and ladders [81]. This can be understood by Eq. (4.33), which generates an infinite number of intermediate contributions from the energy denominators. ADC is thus a non-perturbative approach, that allows to construct an approximate self-energy operator that includes selected classes of relevant diagrams and is consistent with the essential analytic structure of the exact $\Sigma^{(\star)}$.

The full theory of ADC(3) with 3B interaction has been developed in the framework of Dyson-SCGF in Ref. [81]. However, this work (as most nuclear physics calculations so far) treats the 3B forces at the level of the 2B effective interaction (4.24). In ADC(2) and ADC(3) with only two-body forces, only 2p1h and 2h1p configurations appear. When 3N interactions are included, a coupling to 3p2h and 3h2p states is induced as well [81]. The numerical cost of including 3p2h ISCs, though, is very large, and these contributions are expected to be small. As a consequence, numerical calculations have been performed with 2p1h and 2h1p configurations [113]. Under these assumptions, forward and backward ISCs are given by the triplets of s.p. states $r = (n_1 < n_2, k_3)$ and $s = (k_1 < k_2, n_3)$, with n and k referring to particle and hole states, respectively. The Feynman diagrams that define the ADC(3) scheme with 2B effective interactions are shown in Fig. 4.3. From left to right, these are the second-order self-energy diagram, that defines ADC(2), the third-order ring diagram, and the third-order ladder diagram. The second-order term generates only coupling matrices that are of order 1 in the interaction, $M^{(1)}$ and $N^{(1)}$. The ladder and ring diagrams contribute to both second-order coupling matrices and to the interaction matrices. The different contributions are labelled as $M^{(2,pp)}$, $N^{(2,hh)}$, $C^{(pp)}$ and $D^{(hh)}$, for the ladder term, and $M^{(2,ph)}$, $N^{(2,ph)}$, $C^{(ph)}$ and $D^{(ph)}$, for the ring term. Indeed, the ring term propagates particle-hole excitations, while the ladder diagram involves particle-particle and hole-hole excitations.

Below we list all the contributions to the ADC(3) matrices, following Refs. [81, 82]. We first define the following 2p2h amplitudes $t_{n_1 n_2, k_1 k_2}$:

$$t_{n_1 n_2, k_1 k_2} = \sum_{\substack{\alpha\beta \\ \gamma\delta}} \frac{\mathcal{X}^{n_1}_{\alpha} \mathcal{X}^{n_2}_{\beta} \tilde{v}_{\alpha\beta,\gamma\delta} \mathcal{Y}^{k_1}_{\gamma} \mathcal{Y}^{k_2}_{\delta}}{\epsilon^{-}_{k_1} + \epsilon^{-}_{k_2} - \epsilon^{+}_{n_1} - \epsilon^{+}_{n_2}}. \tag{4.35}$$

$t_{n_1 n_2, k_1 k_2}$ are functions of the amplitudes and poles of the propagator (4.4). If an unperturbed reference state is used in Eq. (4.35), they reduce to the $t^{(0)}$ amplitudes used in the coupled-cluster method [14, 126] and in MBPT (App. D.3). In the following equations, a sum over the repeated Greek indices is implicit. $\tilde{v}_{\alpha\beta,\gamma\delta}$ refers to the matrix elements of either the effective 2B interaction (4.24) (if 3N forces are included), or the bare NN interaction (if 3N forces are neglected).

The ADC(3) forward-in-time matrices are now given:

$$M^{(1)}_{r\alpha} = \mathcal{X}^{n_1}_{\mu} \mathcal{X}^{n_2}_{\nu} \mathcal{Y}^{k_3}_{\lambda} \tilde{v}_{\mu\nu,\alpha\lambda}, \tag{4.36}$$

$$M^{(2,pp)}_{r\alpha} = \sum_{k_4<k_5} t_{n_1 n_2, k_4 k_5} \tilde{v}_{\mu\nu,\alpha\lambda} \left(\mathcal{Y}^{k_4}_{\mu} \mathcal{Y}^{k_5}_{\nu}\right)^* \mathcal{Y}^{k_3}_{\lambda}, \tag{4.37}$$

$$\begin{aligned} M^{(2,ph)}_{r\alpha} = \sum_{k_5 n_6} \Big(& t_{n_2 n_6, k_3 k_5} \tilde{v}_{\mu\nu,\alpha\lambda} \mathcal{X}^{n_1}_{\mu} \left(\mathcal{Y}^{k_5}_{\nu} \mathcal{X}^{n_6}_{\lambda}\right)^* \\ & - t_{n_1 n_6, k_3 k_5} \tilde{v}_{\mu\nu,\alpha\lambda} \mathcal{X}^{n_2}_{\mu} \left(\mathcal{Y}^{k_5}_{\nu} \mathcal{X}^{n_6}_{\lambda}\right)^* \Big), \end{aligned} \tag{4.38}$$

$$C^{(pp)}_{rr'} = \mathcal{X}^{n_1}_{\alpha} \mathcal{X}^{n_2}_{\beta} \tilde{v}_{\alpha\beta,\gamma\delta} \left(\mathcal{X}^{n_1'}_{\gamma} \mathcal{X}^{n_2'}_{\delta}\right)^* \delta_{k_3 k_3'}, \tag{4.39}$$

$$\begin{aligned} C^{(ph)}_{rr'} = & \mathcal{X}^{n_1}_{\alpha} \mathcal{Y}^{k_3}_{\beta} \tilde{v}_{\alpha\delta,\beta\gamma} \left(\mathcal{X}^{n_1'}_{\gamma} \mathcal{Y}^{k_3'}_{\delta}\right)^* \delta_{n_2 n_2'} - \mathcal{X}^{n_2}_{\alpha} \mathcal{Y}^{k_3}_{\beta} \tilde{v}_{\alpha\delta,\beta\gamma} \left(\mathcal{X}^{n_1'}_{\gamma} \mathcal{Y}^{k_3'}_{\delta}\right)^* \delta_{n_1 n_2'} \\ & - \mathcal{X}^{n_1}_{\alpha} \mathcal{Y}^{k_3}_{\beta} \tilde{v}_{\alpha\delta,\beta\gamma} \left(\mathcal{X}^{n_2'}_{\gamma} \mathcal{Y}^{k_3'}_{\delta}\right)^* \delta_{n_1' n_2} + \mathcal{X}^{n_2}_{\alpha} \mathcal{Y}^{k_3}_{\beta} \tilde{v}_{\alpha\delta,\beta\gamma} \left(\mathcal{X}^{n_2'}_{\gamma} \mathcal{Y}^{k_3'}_{\delta}\right)^* \delta_{n_1 n_1'}, \end{aligned} \tag{4.40}$$

$$E^{>}_{rr'} = \mathrm{diag}\left(\epsilon^{+}_{\mathrm{n}_1} + \epsilon^{+}_{\mathrm{n}_2} - \epsilon^{-}_{\mathrm{k}_3}\right). \tag{4.41}$$

The ADC(3) backward-in-time matrices read:

$$N^{(1)}_{\alpha,s} = \tilde{v}_{\alpha\lambda,\mu\nu} \mathcal{Y}^{k_1}_{\mu} \mathcal{Y}^{k_2}_{\nu} \mathcal{X}^{n_3}_{\lambda}, \tag{4.42}$$

$$N^{(2,hh)}_{\alpha,s} = \sum_{n_4<n_5} \tilde{v}_{\alpha\lambda,\mu\nu} \mathcal{X}^{n_3}_{\lambda} \left(\mathcal{X}^{n_4}_{\mu} \mathcal{X}^{n_5}_{\nu}\right)^* t_{n_4 n_5, k_1 k_2}, \tag{4.43}$$

$$\begin{aligned} N^{(2,ph)}_{\alpha,s} = \sum_{n_4 k_5} \Big(& t_{n_4 n_3, k_5 k_2} \tilde{v}_{\alpha\beta,\gamma\delta} \mathcal{Y}^{k_1}_{\mu} \left(\mathcal{X}^{n_4}_{\nu} \mathcal{X}^{n_5}_{\lambda}\right)^* \\ & - t_{n_4 n_3, k_5 k_1} \tilde{v}_{\alpha\beta,\gamma\delta} \mathcal{Y}^{k_2}_{\mu} \left(\mathcal{X}^{n_4}_{\nu} \mathcal{X}^{n_5}_{\lambda}\right)^* \Big), \end{aligned} \tag{4.44}$$

$$D^{(hh)}_{ss'} = -\left(\mathcal{Y}^{k_1}_{\alpha} \mathcal{Y}^{k_2}_{\beta}\right)^* \tilde{v}_{\alpha\beta,\gamma\delta} \mathcal{Y}^{k_1'}_{\gamma} \mathcal{Y}^{k_2'}_{\delta} \delta_{n_3 n_3'}, \tag{4.45}$$

$$\begin{aligned} D^{(ph)}_{ss'} = & -\left(\mathcal{Y}^{k_1}_{\alpha} \mathcal{X}^{n_3}_{\beta}\right)^* \tilde{v}_{\alpha\delta,\beta\gamma} \mathcal{Y}^{k_1'}_{\gamma} \mathcal{X}^{n_3'}_{\delta} \delta_{k_2 k_2'} + \left(\mathcal{Y}^{k_2}_{\alpha} \mathcal{X}^{n_3}_{\beta}\right)^* \tilde{v}_{\alpha\delta,\beta\gamma} \mathcal{Y}^{k_1'}_{\gamma} \mathcal{X}^{n_3'}_{\delta} \delta_{k_1 k_2'} \\ & + \left(\mathcal{Y}^{k_1}_{\alpha} \mathcal{X}^{n_3}_{\beta}\right)^* \tilde{v}_{\alpha\delta,\beta\gamma} \mathcal{Y}^{k_2'}_{\gamma} \mathcal{X}^{n_3'}_{\delta} \delta_{k_2 k_1'} - \left(\mathcal{Y}^{k_2}_{\alpha} \mathcal{X}^{n_3}_{\beta}\right)^* \tilde{v}_{\alpha\delta,\beta\gamma} \mathcal{Y}^{k_2'}_{\gamma} \mathcal{X}^{n_3'}_{\delta} \delta_{k_1 k_1'}, \end{aligned} \tag{4.46}$$

$$E^{<}_{ss'} = \mathrm{diag}\left(\epsilon^{-}_{\mathrm{k}_1} + \epsilon^{-}_{\mathrm{k}_2} - \epsilon^{+}_{\mathrm{n}_3}\right). \tag{4.47}$$

A series of approximations of intermediate complexity between ADC(2) and ADC(3) can be introduced. As interaction matrices are relatively inexpensive computationally, it has been suggested to extend ADC(2) using the ADC(3) C and D matrices, while keeping the ADC(2) coupling matrices. We use the notation ADC(i,c) to name these approximations, where the first term in brackets refers to the interaction matrices and the second

one to the coupling matrices, and we consider the ADC(2) ladder [ADC(ld,2)] approximation, in which we include the ladder C and D matrices, and the 2p1h Tamm-Dancoff approximation (TDA) [ADC(3,2)] [82], where both ring and ladder contributions to C and D are included. A further scheme we test is called ADC(ld,pp-hh), and consists in using only the pp (hh) terms in both the C and M (D and N) matrices, while ph contributions are neglected. In Tab. 4.1 the terms entering the different ADC approximations are listed. The ADC(ld,2) scheme, in particular, is strictly related to the coupled-cluster hole-hole and particle-particle ladder approximations [126, 130], as we discuss in App. D.4.3; this provides a useful test on several aspects of the implementation of ADC(3). We also mention extensions that add further correlations beyond the minimal prescription. An example is the Faddeev random phase approximation [82, 206, 207] which includes RPA correlations in the pp/hh and ph interaction channels. Another possibility is to replace the amplitudes that enter the ADC(3) coupling matrices with the corresponding coupled-cluster amplitudes obtained with the CCD method [82, 208]. This is a more complex method, as it requires to first solving the coupled-cluster equations and then the ADC(3) problem, which looks promising in early applications [82, 208].

Approximation	M	C	N	D
ADC(2)	$M^{(1)}$	0	$N^{(1)}$	0
ADC(ld,2)	$M^{(1)}$	$C^{(pp)}$	$N^{(1)}$	$D^{(hh)}$
ADC(3,2)	$M^{(1)}$	$C^{(pp)} + C^{(ph)}$	$N^{(1)}$	$D^{(hh)} + D^{(ph)}$
ADC(ld,pp-hh)	$M^{(1)} + M^{(2,pp)}$	$C^{(pp)}$	$N^{(1)} + N^{(2,hh)}$	$D^{(hh)}$
ADC(3)	$M^{(1)}+$ $M^{(2,pp)} + M^{(2,ph)}$	$C^{(pp)} + C^{(ph)}$	$N^{(1)}+$ $N^{(2,hh)} + N^{(2,ph)}$	$D^{(hh)} + D^{(ph)}$

Table 4.1: Approximations of the self-energy in Dyson-SCGF. The contributions to the coupling (M,N) and interaction matrices (C,D) are listed. Besides ADC(2) and ADC(3), three schemes of intermediate complexity are defined, that extend ADC(2) including (parts of) the ADC(3) interaction matrices. These are called ADC(ld,2), which includes the contributions to C and D from the ladder diagram (Fig. 4.3), ADC(3,2) (Tamm-Dancoff approximation), which also includes the ring diagrams, and ADC(ld,pp-hh), that includes pp and hh terms in both coupling and interaction matrices, but neglects ring contributions. See text for details.

Once an approximation for the self-energy has been determined, the Dyson equation (4.13) has to be solved in order to determine the dressed propagator. In the ADC method, it is convenient to cast the latter into an eigenvalue problem. The derivation can be found in Refs. [81, 82] and is also reported in App. D.1. The essential steps are summarized here. First, the propagator is written in terms of a general index i,

$$g_{\alpha\beta}(\omega) = \sum_i \frac{\mathcal{Z}^i_\alpha (\mathcal{Z}^i_\beta)^*}{\hbar\omega - \epsilon_i}, \tag{4.48}$$

where for $i = n$ (particle), $\mathcal{Z}^i_\alpha = (\mathcal{X}^n_\alpha)^*$ and $\epsilon_i = \epsilon^+_n$, and for $i = k$ (hole), $\mathcal{Z}^i_\alpha = \mathcal{Y}^k_\alpha$ and $\epsilon_i = \epsilon^-_k$. Then, auxiliary vectors $\mathcal{W}^i$ and $\mathcal{V}^i$ in the space of ISCs are introduced as

$$\mathcal{W}^i = \left(\omega - E^> - C\right)^{-1} M \mathcal{Z}^i, \tag{4.49}$$

$$\mathcal{V}^i = \left(\omega - E^< - D\right)^{-1} N^\dagger \mathcal{Z}^i. \tag{4.50}$$

Finally, it can be shown that in this way the Dyson equation can be turned into the following energy-independent eigenvalue problem:

$$\begin{pmatrix} T + \Sigma^{(\infty)} & M^\dagger & N \\ M & E^> + C & \\ N^\dagger & & E^< + D \end{pmatrix} \begin{pmatrix} \mathcal{Z}^i \\ \mathcal{W}^i \\ \mathcal{V}^i \end{pmatrix} = \epsilon_i \begin{pmatrix} \mathcal{Z}^i \\ \mathcal{W}^i \\ \mathcal{V}^i \end{pmatrix}. \tag{4.51}$$

A clear advantage of such an approach is that all poles and amplitudes are found in a single diagonalization of a Hermitian matrix and, despite the increased dimension of the matrix problem Eq. (4.51), it has proven to be much faster and numerically stable than using a root-finding algorithm to search for the poles individually [82]. A full diagonalization of Eq. (4.51) is a very demanding task from a computational point of view, but fortunately, it is generally not required to determine the full spectrum. The Lanczos algorithm is exploited to reduce the dimension of the backward and forward subspaces separately [209]. Then, the resulting much smaller matrix is fully diagonalized. Few tens or hundreds of Lanczos vectors are typically sufficient to get an accurate reproduction of the propagator. In particular, the Lanczos method is accurate in preserving the extremal (smallest or largest) eigenvalues of a matrix [176]. This is a rather important feature, since we are mostly interested in the poles that are closest to the Fermi surface, either from below (2h1p configurations) or from above (2p1h), as the strength of the propagator mostly concentrates there. Details are given in App. D.2.

The eigenvalue problem (4.51) is the key equation of the ADC method. The nature of SCGF requires to search for an iterative solution to the problem, since the self-energy at the same time is determined by and

determines the 1B GF. In principle, a fully self-consistent solution would work as follows: one should build the self-energy using an uncorrelated reference propagator, solve the equations to obtain a dressed Green's function $g(\omega)$, construct again the Dyson matrix using the new propagator and then repeat the procedure until the total energy converges. However, in most cases, this is infeasible from a computational point of view. This is due to the large cost of evaluating the self-energy matrices, and also to the fact that at each iteration the number of poles in the propagator would increase, as explained in [26]. Therefore, techniques have been developed over the years that elude the need for full self-consistency and allow to determine accurate, albeit approximate, solutions to the Dyson equation in a reasonable amount of time. The first important simplification, which is employed in most large-scale SCGF studies, consists of building the Dyson matrix out of an uncorrelated, but properly chosen, HF-like propagator. This allows to sum over a limited number of poles, with a significant reduction of computing time. The iterations are then carried out at two different levels, which we call "sc0" (to be contrasted to the fully self-consistent method, "sc") and optimized reference state (OpRS) methods.

The principle of the sc0 technique is that only the static self-energy is iterated in the Dyson equation. That is, the Dyson matrix is built from $g^{(0)}$, Lanczos-reduced and diagonalized. The resulting propagator is then used to evaluate the new $\Sigma^{(\infty)}$ [Eq. (4.30)], while the dynamical self-energy matrices are kept unchanged. The Dyson matrix which is obtained by updating only the upper corner in Eq. (4.51), then, is diagonalized and the process is repeated until convergence. This approximation, in which $\tilde{\Sigma}(\omega)$ is evaluated and stored just once and kept "frozen" afterward, is numerically inexpensive and has been shown to allow to recover a large fraction of the correlation energy [26].

A "higher level" of self-consistency is realized in the OpRS scheme. The concept of OpRS, originally introduced in Ref. [210], is discussed in detail in Ref. [201] and represents an effective way to include the correlations of the dressed propagator, while keeping the computational cost manageable. The idea is to determine an uncorrelated propagator g^{OpRS} of the HF type that allows to approximate the correlated propagator while using a small number of poles,

$$g^{OpRS}_{\alpha\beta}(\omega) = \sum_n \frac{(\psi^n_\alpha)^* \psi^n_\beta}{\hbar\omega - \epsilon^{OpRS}_n + i\eta} + \sum_k \frac{\psi^k_\alpha (\psi^k_\beta)^*}{\hbar\omega - \epsilon^{OpRS}_k - i\eta}. \tag{4.52}$$

Since we are mostly interested in reproducing the features of $g(\omega)$ close to the Fermi energy, the moments of the propagator with respect to the inverse powers of $E_F - \omega$ are introduced, namely

$$\begin{aligned} M^{(p)}_{\alpha\beta} &= \int d(\hbar\omega) \frac{S^h_{\alpha\beta}(\omega)}{(E_F - \hbar\omega)^p} = \\ &\sum_n \frac{(\mathcal{X}^n_\alpha)^* \mathcal{X}^n_\beta}{\left(E_F - \epsilon^+_n\right)^p} + \sum_k \frac{\mathcal{Y}^k_\alpha (\mathcal{Y}^k_\beta)^*}{\left(E_F - \epsilon^-_k\right)^p} = \\ &\sum_i \frac{\mathcal{Z}^i_\alpha (\mathcal{Z}^i_\beta)^*}{(E_F - \epsilon_i)^p}, \end{aligned} \tag{4.53}$$

and we ask that the moments of the optimized reference propagator match those of the true propagator resulting from the solution of the Dyson equation. Typically, we require that only the moments with $p = 0, 1$ be equal, i.e. $M^{(0)}_{\alpha\beta} = M^{(0,OpRS)}_{\alpha\beta}$ and $M^{(1)}_{\alpha\beta} = M^{(1,OpRS)}_{\alpha\beta}$. This allows to guarantee the reproduction of 1B observables and the total energy with a good accuracy [211]. In practice, after an sc0 cycle has been completed, the aforementioned conditions are imposed and exploited to determine the new s.p. energies ϵ^{OpRS}_i and the corresponding amplitudes of the reference propagator, and the full Dyson matrix is constructed again using the new uncorrelated propagator. An sc0 loop can then be started again. The workflow of SCGF calculations is depicted in Fig. 4.4 and summarized in the caption.

A further aspect that must be discussed concerns the Fermi energy. The chemical potential or Fermi energy is usually defined in finite systems as the average between the highest removal energy and lowest addition energy,

$$E_F = \frac{1}{2}\left(\epsilon^+_0 + \epsilon^-_0\right). \tag{4.54}$$

E_F separates quasi-particle states from quasi-hole states and enters the evaluation of all the observables, see formulas (4.18) and (4.17). Therefore, it is very important to determine the Fermi level accurately. An initial estimate of E_F, which is exact for an unperturbed reference state, is given by the average of the HF energies of the last occupied and first unoccupied levels. However, after each diagonalization of the Dyson equation the chemical potential has to be readjusted by imposing the auxiliary condition that the particle number be conserved. Indeed, the SCGF method is formulated in the Fock space and thus the particle number is not a

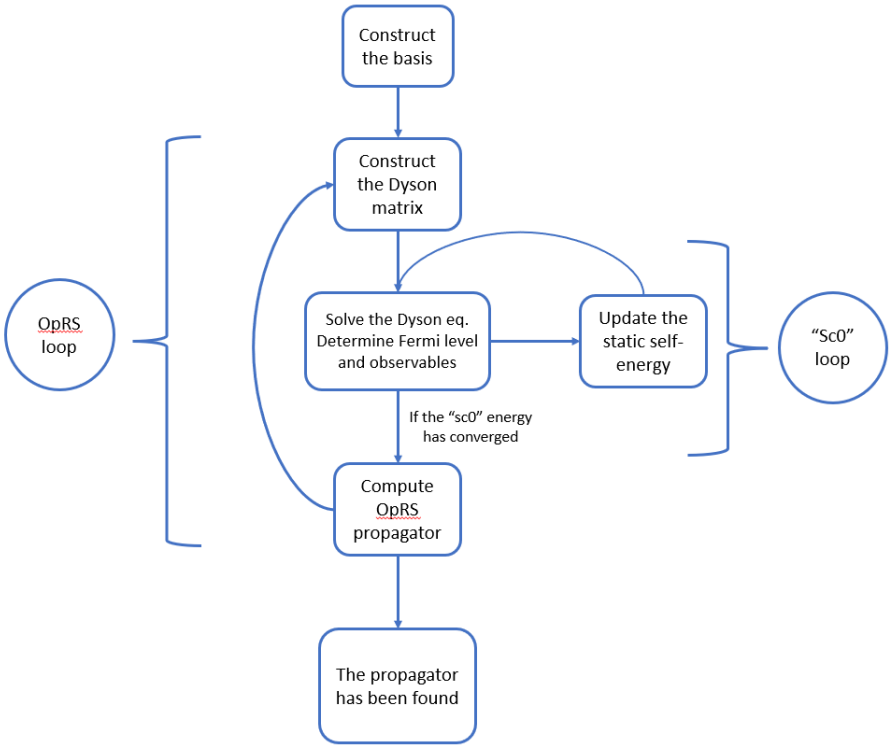

Figure 4.4: Schematic workflow of a SCGF calculation. The first step is always to construct the s.p. basis and determine the corresponding HF reference propagator and 2p1h/2h1p configurations. Then, the Dyson matrix is constructed using the reference propagator, Lanczos-reduced and stored. Afterward, the Dyson eigenvalue problem (4.51) is solved for the first time. The dressed propagator $g(\omega)$ is thus obtained. Then, the Fermi level is adjusted to conserve the particle number, and the total energy, the density matrix and the relevant one-body observables are computed. The static self-energy $\Sigma^{(\infty)}$ is evaluated using $g(\omega)$ and inserted in the Dyson matrix (while the dynamical self-energy is kept unchanged). This is the content of the sc0 loop, which is repeated until the total energy is converged from one iteration to the next within a chosen tolerance. Typically, about 10-15 iterations are sufficient for the sc0 loop. Once a sc0 cycle has converged, a new reference state, the so-called OpRS, is determined to approximate the dressed propagator. The OpRS GF in general is characterized by s.p. energies and amplitudes somewhat different from those of the HF propagator. Then, the whole Dyson matrix is built again from scratch using the new (uncorrelated) reference state, and the sc0 loop is started again. Convergence is typically achieved within 10 OpRS cycles (and often 5 iterations are enough).

fixed number, but rather an operator $\hat{A}_i$, with i denoting the different fermion species in the system. Thus, the number of particles A_i can be conserved only on average,

$$\left\langle \hat{A}_i \right\rangle = \sum_\alpha \rho_{\alpha\alpha} = \int_{-\infty}^{\epsilon_0^-} \sum_\alpha S^h_{\alpha\alpha}(\omega)\, d\omega = \sum_\alpha \sum_k \left| \mathcal{Y}^k_\alpha \right|^2, \tag{4.55}$$

by demanding $\left\langle \hat{A}_i \right\rangle = A_i$.

In [84], it has been shown (to second order) that ADC(n) is a so-called conserving approximation of the self-energy. That is, it was shown by Baym and Kadanoff [212, 213] that, if the self-energy can be derived from a certain functional $\Phi[g]$ of the dressed 1B propagator, then all basic conservation laws are satisfied by the corresponding many-body method [214, 215]. This is an important and non-trivial property that, however, is rigorously verified only if the observables are evaluated on the exact Green's function. However, since, as discussed above, only approximations to the true self-consistent solution of the Dyson equation are attainable in practical cases, a slight violation of the particle number is to be expected, usually in the range of 2-3%. In contrast, Gorkov-SCGF [26, 84] does not suffer from this issue, as the particle number is fixed exactly on average in this framework. This is one of the main motivations for introducing Gorkov corrections, as we describe in Sec. 4.3.

4.3 First-order Gorkov corrections

In this work, we do not implement a full Gorkov approach for infinite matter. However, we do study an approximation in which first-order Gorkov corrections are introduced on top of Dyson-ADC (Sec. 4.2).

Gorkov Green's functions theory has been developed to deal with superfluid systems [202]. The Gorkov-SCGF approach, in particular, has been developed to treat open-shell nuclei, see e.g. Refs. [19, 26]. From a physical point of view, as far as infinite nuclear matter is concerned, pairing is important to describe neutron matter at relatively low densities (k_F of the order of 1 fm^{-1}), such as those encountered in the inner crust of neutron stars [216, 217]. At these large interparticle distances, the neutrons mainly experience the attractive component of the nuclear interaction [217]. As ρ increases (at saturation density and above), the repulsive core of the nuclear force comes into play and tends to suppress pairing effects. This is manifest, for example, in the trends of the superfluid gaps as a function of the density, which have been investigated with effective forces [218] and microscopic interactions (see e.g. Refs. [104, 216, 219, 220]). These arguments hold for $T = 1$ pairing also in symmetric nuclear matter. In this case, however, the features and the impact of pairing in the $T = 0$ channel are still an open question [104, 221].

A superfluid extension of SCGF to study infinite matter is thus desirable. A complete Gorkov-ADC method is left for the future. The approach we propose here combines the dynamical Dyson-ADC(3) self-energy, to describe the fragmentation of s.p. states, and a first-order treatment of the pairing potentials (i.e. the anomalous self-energies).

From a technical point of view, calculations are made more stable when using the Gorkov framework. In low-density nuclear matter, zero-temperature calculations with normal propagators may fail to converge due to pairing instabilities [222]. (In Finite-T SCGF, such instabilities are lifted by using a sufficiently large temperature [20, 222].) Physically meaningful solutions can be found by introducing pairing corrections. In addition, in the Gorkov (or HFB) approach the particle number is conserved on average by construction. This is a very useful property since the small violations of the number of nucleons that affect Dyson Green's functions can be removed completely.

Some minimal notions of the Gorkov formalism are summarized following Refs. [26, 84, 201]. In Gorkov-SCGF, the reference state is chosen to be a symmetry-breaking Bardeen-Cooper-Schrieffer (BCS) state $|\Psi_0\rangle$ that is made out of a superposition of ground states of A, $A \pm 2$... -particle systems [84],

$$|\Psi_0\rangle = \sum_{A\,\mathrm{even}} c_A \left|\Psi_0^A\right\rangle . \tag{4.56}$$

Together with $|\Psi_0\rangle$, the grand-canonical Hamiltonian $\hat{\Omega}$ is introduced,

$$\hat{\Omega} = \hat{H} - \sum_i \mu_i \hat{A}_i, \tag{4.57}$$

where i sums over different particle types (protons and neutrons in our case). $|\Psi_0\rangle$ is the state that minimizes the expectation value of $\hat{\Omega}$,

$$\Omega_0 = \langle\Psi_0|\hat{\Omega}|\Psi_0\rangle , \tag{4.58}$$

under the constraints

$$A_i = \langle\Psi_0|\hat{A}_i|\Psi_0\rangle , \tag{4.59}$$

i.e. $|\Psi_0\rangle$ is not an eigenstate of $\hat{A}_i$, but has a fixed number of particles on average [84].

The (anti-unitary) time-reversal operator T is introduced. Given a s.p. state $|\alpha\rangle$, its time-reversed partner is denoted as $|\tilde{\alpha}\rangle$. Following the notation of Ref. [84], states $|\bar{\alpha}\rangle$ are also introduced, that differ from $|\tilde{\alpha}\rangle$ by a phase factor η_α:

$$|\bar{\alpha}\rangle = T\,|\alpha\rangle = \eta_\alpha\,|\tilde{\alpha}\rangle . \tag{4.60}$$

For our purposes, η_α is in practice chosen such that the time-reversal operator acts on the spin-projection eigenstates as follows:

$$T\,|\uparrow\rangle = |\downarrow\rangle , \qquad T\,|\downarrow\rangle = -\,|\uparrow\rangle . \tag{4.61}$$

For each "barred" state in a matrix element, a factor η_α has to be included. An example is

$$\bar{v}_{\alpha\bar{\beta},\gamma\bar{\delta}} = \eta_\beta \eta_\delta \bar{v}_{\alpha\tilde{\beta},\gamma\tilde{\delta}}. \tag{4.62}$$

The GF (4.4) must be generalized by introducing additional functions that account for the creation and de-

struction of pairs [84]. Four 1B propagators are defined with respect to the reference state as follows:

$$g^{11}_{\alpha\beta}(t) = -\frac{i}{\hbar}\left\langle \Psi_0 \right| T[c_\alpha(t) c^\dagger_\beta(0)] \left| \Psi_0 \right\rangle, \tag{4.63}$$

$$g^{12}_{\alpha\beta}(t) = -\frac{i}{\hbar}\left\langle \Psi_0 \right| T[c_\alpha(t)\, \bar{c}_\beta(0)] \left| \Psi_0 \right\rangle, \tag{4.64}$$

$$g^{21}_{\alpha\beta}(t) = -\frac{i}{\hbar}\left\langle \Psi_0 \right| T[\bar{c}^\dagger_\alpha(t)\, c^\dagger_\beta(0)] \left| \Psi_0 \right\rangle, \tag{4.65}$$

$$g^{22}_{\alpha\beta}(t) = -\frac{i}{\hbar}\left\langle \Psi_0 \right| T[\bar{c}^\dagger_\alpha(t) \bar{c}_\beta(0)] \left| \Psi_0 \right\rangle, \tag{4.66}$$

where field operators are evolved with respect to $\hat{\Omega}$. The four Gorkov propagators admit the following Lehmann representations [84]:

$$g^{11}_{\alpha\beta}(\omega) = \sum_q \frac{\mathcal{U}^q_\alpha (\mathcal{U}^q_\beta)^*}{\hbar\omega - \hbar\omega_q + i\eta} + \frac{(\bar{\mathcal{V}}^q_\alpha)^* \bar{\mathcal{V}}^q_\beta}{\hbar\omega + \hbar\omega_q - i\eta}, \tag{4.67}$$

$$g^{12}_{\alpha\beta}(\omega) = \sum_q \frac{\mathcal{U}^q_\alpha (\mathcal{V}^q_\beta)^* }{\hbar\omega - \hbar\omega_q + i\eta} + \frac{(\bar{\mathcal{V}}^q_\alpha)^* \bar{\mathcal{U}}^q_\beta}{\hbar\omega + \hbar\omega_q - i\eta}, \tag{4.68}$$

$$g^{21}_{\alpha\beta}(\omega) = \sum_q \frac{\mathcal{V}^q_\alpha (\mathcal{U}^q_\beta)^* }{\hbar\omega - \hbar\omega_q + i\eta} + \frac{(\bar{\mathcal{U}}^q_\alpha)^* \bar{\mathcal{V}}^q_\beta}{\hbar\omega + \hbar\omega_q - i\eta}, \tag{4.69}$$

$$g^{22}_{\alpha\beta}(\omega) = \sum_q \frac{\mathcal{V}^q_\alpha (\mathcal{V}^q_\beta)^* }{\hbar\omega - \hbar\omega_q + i\eta} + \frac{(\bar{\mathcal{U}}^q_\alpha)^* \bar{\mathcal{U}}^q_\beta}{\hbar\omega + \hbar\omega_q - i\eta}, \tag{4.70}$$

where q labels the sum over the excited states of $\hat{\Omega}$, $|\Psi_q\rangle$, and the spectroscopic amplitudes are defined as

$$\mathcal{U}^q_\alpha = \langle \Psi_0 | c_\alpha | \Psi_q \rangle, \tag{4.71}$$

$$\left(\mathcal{U}^q_\beta\right)^* = \langle \Psi_q | c^\dagger_\beta | \Psi_0 \rangle, \tag{4.72}$$

$$\left(\bar{\mathcal{V}}_\alpha\right)^* = \langle \Psi_q | c_\alpha | \Psi_0 \rangle, \tag{4.73}$$

$$\bar{\mathcal{V}}_\beta = \langle \Psi_0 | c^\dagger_\beta | \Psi_q \rangle. \tag{4.74}$$

The barred amplitudes satisfy [84]

$$\bar{\mathcal{U}}^q_\alpha = +\mathcal{U}^q_{\bar{\alpha}} = +\eta_\alpha \mathcal{U}^q_{\bar{\alpha}}, \tag{4.75}$$

$$\bar{\mathcal{V}}^q_\alpha = -\mathcal{V}^q_{\bar{\alpha}} = -\eta_\alpha \mathcal{V}^q_{\bar{\alpha}} \tag{4.76}$$

The poles ω_q are given by

$$\hbar\omega_q = \Omega_q - \Omega_0. \tag{4.77}$$

Note that solutions to the Gorkov equations come in pairs $+\omega_q, -\omega_q$, as is also visible in the Lehmann representation, which features poles at $\omega = \pm\omega_q$. In the sums, we will always consider $\omega_q > 0$. We also report a symmetry property of the anomalous GF for later use: $g^{12}_{\beta\alpha}(\omega) = -g^{12}_{\alpha\beta}(-\omega)$. In analogy with the GF, four self-energies are introduced, as discussed in [84]. The Koltun sum rule must be modified from the Dyson theory. If we define the negative-frequency normal spectral function

$$S^{11,-}_{\alpha\beta}(\omega) = \sum_q (\bar{\mathcal{V}}^q_\alpha)^* \bar{\mathcal{V}}^q_\beta\, \delta(\hbar\omega + \hbar\omega_q), \tag{4.78}$$

then the total g.s. energy is given by [84]

$$E^A_0 = \frac{1}{2}\int_{-\infty}^{0} d\omega\, (t_{\alpha\beta} + \omega\delta_{\alpha\beta} + \mu\delta_{\alpha\beta}) S^{11,-}_{\beta\alpha}(\omega) \tag{4.79}$$

From the propagators, the normal and anomalous density matrices are determined as

$$\rho_{\alpha\beta} = \langle \Psi_0 | c^\dagger_\beta c_\alpha | \Psi_0 \rangle = \sum_q \left(\bar{\mathcal{V}}^q_\alpha\right)^* \bar{\mathcal{V}}^q_\beta, \tag{4.80}$$

$$\tilde{\rho}_{\alpha\beta} = \langle \Psi_0 | \bar{c}_\beta c_\alpha | \Psi_0 \rangle = \sum_q \left(\bar{\mathcal{V}}^q_\alpha\right)^* \bar{\mathcal{U}}^q_\beta. \tag{4.81}$$

In terms of the energy-dependent self-energies, the Gorkov equations for the GF can be cast into matrix form as the following eigenvalue problem [84]:

$$\begin{pmatrix} T-\mu\mathbb{1}+\Sigma^{11}(\omega) & \Sigma^{12}(\omega) \\ \Sigma^{21}(\omega) & -(T-\mu\mathbb{1})+\Sigma^{22}(\omega) \end{pmatrix}\Bigg|_{\omega=\omega_q} \begin{pmatrix} \mathcal{U}^q \\ \mathcal{V}^q \end{pmatrix} = \hbar\omega_q \begin{pmatrix} \mathcal{U}^q \\ \mathcal{V}^q \end{pmatrix}. \tag{4.82}$$

The unknowns of the problem are the energies ω_q and the amplitudes $(\mathcal{U}^q, \mathcal{V}^q)$. The structure of Eq. (4.82) implies that eigenvalues come in pairs $(+\omega_q, -\omega_q)$ of opposite sign. Only the positive-energy solutions ($\omega_q > 0$) need to be computed, as the $\omega_q < 0$ ones are trivially related to the former. If the first-order expressions are used in all the self-energies, then one retrieves the well-known HFB equations [84]. Also, we mention that symmetry properties relate $\Sigma^{22}(\omega)$ to $\Sigma^{11}(\omega)$ and the anomalous self-energies at first order $\Sigma^{12(\infty)}$ and $\Sigma^{21(\infty)}$, namely

$$\Sigma^{22}_{\alpha\beta}(\omega) = -\Sigma^{11}_{\bar{\beta}\bar{\alpha}}(-\omega), \tag{4.83}$$

$$\Sigma^{22(\infty)}_{\alpha\beta} = -\Sigma^{11(\infty)}_{\bar{\alpha}\bar{\beta}}, \tag{4.84}$$

$$\Sigma^{12(\infty)} = \left(\Sigma^{21(\infty)}\right)^\dagger. \tag{4.85}$$

The full Gorkov SCGF theory would use dynamical self-energies in both the normal and anomalous sectors built out of an HFB reference state. That is the case of e.g. the Gorkov-ADC(2) [84] and Gorkov-ADC(3) [201] methods. The approach we develop here is a somewhat hybrid technique, in which Σ^{11} is treated dynamically at the level of the Dyson-ADC(3) theory, while Σ^{12} is included at first-order, i.e. the static $\Sigma^{12(\infty)}$ is employed in the off-diagonal part of the Gorkov matrix (4.82). This solution is an effective way of introducing pairing correlations, while requiring relatively little extensions to the Dyson ADC(3) method described in Sec. 4.2. The essential limitation of this hybrid method is that it is still based on an HF reference state, and not a true HFB state.

The key equations for the Gorkov corrections are now presented. The starting point is Eq. (4.82), where the off-diagonal anomalous self-energies are set to their static (first-order) expressions, given by

$$\begin{aligned}\Sigma^{11(\infty)}_{\alpha\beta} &= \sum_{\gamma\delta} \bar{v}_{\alpha\gamma,\beta\delta}\rho_{\delta\gamma} \\ &+ \frac{1}{2}\sum_{\gamma\delta\mu\nu} \bar{w}_{\alpha\gamma\mu,\beta\delta\nu}\rho_{\delta\gamma}\rho_{\nu\mu} + \frac{1}{4}\sum_{\gamma\delta\mu\nu} \bar{w}_{\alpha\bar{\mu}\nu,\beta\gamma\bar{\delta}}\tilde{\rho}_{\gamma\delta}\tilde{\rho}^*_{\mu\nu},\end{aligned} \tag{4.86}$$

$$\Sigma^{12(\infty)}_{\alpha\beta} = \frac{1}{2}\sum_{\gamma\delta} \bar{v}_{\alpha\bar{\beta},\gamma\bar{\delta}}\tilde{\rho}_{\gamma\delta} + \frac{1}{2}\sum_{\gamma\delta\mu\nu} \bar{w}_{\alpha\bar{\beta}\mu,\gamma\bar{\delta}\nu}\tilde{\rho}_{\gamma\delta}\rho_{\nu\mu}. \tag{4.87}$$

The normal component of the static self-energy, Eq. (4.86), presents, compared to the Dyson $\Sigma^{(\infty)}$ (4.30), an additional term that depends on the anomalous density and is shown in Fig. 4.5. The anomalous self-energy consists of two diagrams (Fig. 4.6) that both depend on $\tilde{\rho}$ (and thus it vanishes in a normal system). Contributions that involve the 3N interaction have been derived here following the rules discussed in Ref. [84].

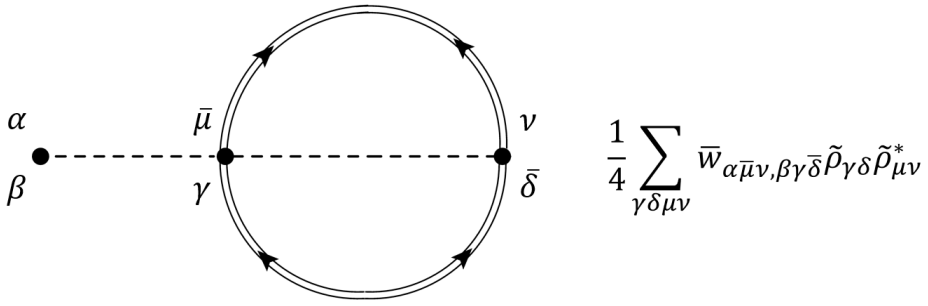

Figure 4.5: Contribution to the normal self-energy, Eq. (4.86), that depends on the anomalous density. The dashed line represents the antisymmetrized matrix elements of the 3N potential. The other two contributions to $\Sigma^{11(\infty)}_{\alpha\beta}$ are depicted in Fig. 4.1.

Then, the eigenvalue problem (4.82) is cast into an energy-independent form by introducing auxiliary vectors. The procedure can be found in Ref. [84] and is also summarized in App. D.1 for Dyson-ADC. We define

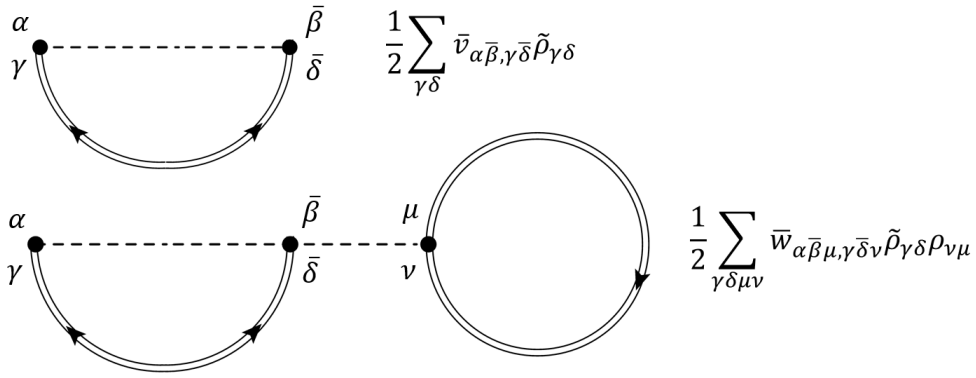

Figure 4.6: Contributions to the anomalous static self-energy, Eq. (4.87). Dashed lines denote the antisymmetrized matrix elements of the bare NN and 3N interactions.

the Dyson matrix $\mathcal{H}$ following Eq. (4.51), with the only change being that now in the upper corner $\Sigma^{11(\infty)}$ (4.86) has to be used. The M, N, C, and D matrices, that define the dynamical self-energy, are the same as in Dyson-ADC(3). Thus,

$$\mathcal{H} = \begin{pmatrix} T + \Sigma^{11(\infty)} & M^\dagger & N \\ M & E^> + C & \\ N^\dagger & & E^< + D \end{pmatrix}. \tag{4.88}$$

Finally, our Gorkov matrix reads

$$\mathcal{G}(\mu) = \begin{pmatrix} \mathcal{H} - \mu\mathbb{1} & \Sigma^{12(\infty)} \\ (\Sigma^{12(\infty)})^\dagger & -\left(\mathcal{H}^\dagger - \mu\mathbb{1}\right) \end{pmatrix}, \tag{4.89}$$

where we stress that $\mathcal{G}$ is a function of the chemical potential for the appropriate particle species. $\Sigma^{12(\infty)}$ acts only on the upper corner of $\mathcal{H}$. The Gorkov eigenvalue problem has the form

$$\mathcal{G}(\mu) \begin{pmatrix} \mathcal{A}^q \\ \mathcal{B}^q \end{pmatrix} = \hbar\omega_q \begin{pmatrix} \mathcal{A}^q \\ \mathcal{B}^q \end{pmatrix}, \tag{4.90}$$

where $\mathcal{A}^q$ and $\mathcal{B}^q$ are vectors in the extended space of the form

$$\mathcal{A}^q = \begin{pmatrix} \mathcal{U}^q_\alpha & \mathcal{W}^q_r & \mathcal{X}^q_s \end{pmatrix}, \tag{4.91}$$

$$\mathcal{B}^q = \begin{pmatrix} \mathcal{V}^q_\alpha & \mathcal{Y}^q_r & \mathcal{Z}^q_s \end{pmatrix}. \tag{4.92}$$

For each eigensolution q, the normalization condition $\sum_\alpha(|\mathcal{U}^q_\alpha|^2 + |\mathcal{V}^q_\alpha|^2) + \sum_r(|\mathcal{W}^q_r|^2 + |\mathcal{Y}^q_r|^2) + \sum_s(|\mathcal{X}^q_s|^2 + |\mathcal{Z}^q_s|^2) = 1$ is set. Our notation differs slightly from that of Ref. [84], and amounts essentially to a reshuffling of the different blocks within the Gorkov matrix. Note that in this form $\mathcal{G}$ resembles the HFB matrix closely, with the mean-field terms being replaced by Dyson matrices along the main diagonal. Eq. (4.89) has a clear physical interpretation. The s.p. Hamiltonians that describe the state α and its time-reversed state $\tilde{\alpha}$ are coupled together by the off-diagonal terms that describe the BCS pairing. Moreover, a numerical implementation is immediately suggested, as it is clear that the terms $\mathcal{H}$ can be evaluated just as in Dyson-ADC and then employed as building blocks for $\mathcal{G}$.

The iterative solution of this Gorkov problem requires modest changes to the scheme presented in Sec. 4.2, and the workflow remains essentially the one depicted in Fig. 4.4. We summarize the main steps. The Dyson matrix $\mathcal{H}$ is constructed and Lanczos-reduced. Then, the resulting small matrices of the dynamical self-energy are inserted into Eq. (4.89) and kept frozen afterwards. A guess for the 1B propagators is chosen, and the static normal and anomalous self-energies are evaluated based on this ansatz. Note that we must start with a particle-number-breaking GF to find non-vanishing off-diagonal pairing terms. If we just start from an HF propagator, we simply find two identical copies of the Dyson problem (see also App. D.6). $\mathcal{G}(\mu)$ is then repeatedly diagonalized for different values of the chemical potentials μ_i for all the particle species i in the system. This is a slightly more complex step than for the Dyson method and is detailed in App. D.5. After the Fermi surface has been determined, a new sc0 step can be performed in analogy with Dyson-ADC. The normal self-energy is updated inside the Dyson matrix $\mathcal{H}$ (4.88), as well as the anomalous term $\Sigma^{12(\infty)}$. Then, the chemical potential must be fixed again, and so on.

Once a sc0 cycle has finished, an optimized propagator is defined and a new OpRS cycle starts. The dressed GF is mapped back to an HF-like propagator, in analogy to the Dyson-SCGF case, and is used to build the new

dynamical self-energy matrices at the Dyson level [1]. We define the moments of the normal Gorkov spectral function S^{11} as

$$M^{(p)}_{\alpha\beta} = \sum_q (\hbar\omega_q)^p \left((\bar{\mathcal{V}}^q_\alpha)^* \bar{\mathcal{V}}^q_\beta - \mathcal{U}^q_\alpha (\mathcal{U}^q_\beta)^* \right). \tag{4.93}$$

We have explored two recipes. One uses $p = -1$ as in Dyson OpRS. However, we have also considered the possibility $p = 1$, where the centroid energy of the correlated Gorkov distribution is evaluated. See also Sec. 4.4.

4.4 Applications to infinite matter

We present the application of the Dyson-ADC(3) method (Sec. 4.2) and of the first-order Gorkov corrections (Sec. 4.3) to infinite nuclear matter. The groundwork has been laid in Refs. [82, 83], to which we refer.

The first great simplification that appears when the general ADC framework (Sec. 4.2) is specialized to infinite matter is that translational invariance imposes that the Dyson equation is diagonal in momentum space [82]. As a consequence, it is natural to adopt the momentum eigenstates as s.p. basis. In the following, states

$$|\alpha\rangle = |\mathbf{k}_\alpha, s_\alpha, t_\alpha\rangle \tag{4.94}$$

will be used, where s_α and t_α are the spin and isospin projection quantum numbers, respectively. We remind that the momenta are quantized, see Sec. 1.3, namely

$$\mathbf{k}_\alpha = \frac{2\pi}{L}\mathbf{n} \qquad \text{(PBC)}, \tag{4.95}$$

$$\mathbf{k}_\alpha = \frac{1}{L}(2\pi\mathbf{n} + \theta) \quad \text{(TABC)}. \tag{4.96}$$

The dimension of the s.p. space can be set by imposing a cutoff on the maximum momentum, $|\mathbf{k}| < k_{max}$, or requiring $|\mathbf{n}|^2 < N^2_{max}$ for a certain integer number N^2_{max}. A convergence study on the model space dimension is usually performed, where the cutoff is gradually increased until results (in particular the total energy) stabilize. The typical cutoff in our calculations is $N^2_{max} = 25$.

The states (4.94) are automatically HF states. HF states and energies can thus be characterized by a single label α, too:

$$\epsilon^{HF}_\alpha = \epsilon^{HF}(\mathbf{k}_\alpha, s_\alpha, t_\alpha) = t_\alpha + \sum_{h_1} \bar{v}_{\alpha h_1, \alpha h_1} + \frac{1}{2}\sum_{h_1 h_2} \bar{w}_{\alpha h_1 h_2, \alpha h_1 h_2} \tag{4.97}$$

with $t_\alpha = \hbar^2\mathbf{k}^2_\alpha/(2m)$ is the kinetic energy and h_1, h_2 are hole states. The corresponding HF propagator reads

$$g^{(0)}_\alpha(\omega) = \frac{1}{\hbar\omega - \epsilon^{HF}_\alpha \pm i\eta} \tag{4.98}$$

where the imaginary part is $+i\eta$ ($-i\eta$) if α is a particle (hole) state, and is characterized by a single pole for each α. The amplitudes reduce to delta functions, i.e. $\mathcal{X}^n_\alpha = \delta_{\alpha n}$ and $\mathcal{Y}^k_\alpha = \delta_{\alpha k}$, and thus also the evaluation of the dynamical self-energy matrices is drastically simplified when the HF propagator (4.98) is used.

The full propagator in momentum space reads [2]

$$g_\alpha(\omega) = \sum_j \frac{\left|\mathcal{Z}^j_\alpha\right|^2}{\hbar\omega - \epsilon_{\alpha,j}} = \sum_n \frac{|\mathcal{X}^n_\alpha|^2}{\hbar\omega - \epsilon^+_{\alpha,n} + i\eta} + \sum_k \frac{\left|\mathcal{Y}^k_\alpha\right|^2}{\hbar\omega - \epsilon^-_{\alpha,k} - i\eta}, \tag{4.99}$$

and correspondingly the spectral function is given by

$$S_\alpha(\omega) = \sum_j \left|\mathcal{Z}^j_\alpha\right|^2 \delta(\hbar\omega - \epsilon_{\alpha,j}) = \sum_n |\mathcal{X}^n_\alpha|^2 \delta(\hbar\omega - \epsilon^+_{\alpha,n}) + \sum_k \left|\mathcal{Y}^k_\alpha\right|^2 \delta(\hbar\omega - \epsilon^-_{\alpha,k}). \tag{4.100}$$

[1] We stress that in a full Gorkov SCGF approach the OpRS state would have the structure of a HFB propagator. In our scheme, instead, we search for an uncorrelated HF-like form of the Gorkov propagator.

[2] From the definition of the 1B GF, it is clear that to satisfy the momentum and charge conservation laws, the states α and β must carry the same momentum and isospin, otherwise the propagator vanishes. Perhaps, it is less obvious at first sight that $g(\omega)$ must be diagonal also in the spin projection index. We report a simple argument from Ref. [115]: the spin structure of the propagator is made out of the 2×2 identity matrix or by $\mathbf{k}\cdot\boldsymbol{\sigma}$, as $\mathbf{k}$ is the only available vector that can be combined with the Pauli matrices to generate a scalar. However, this quantity is a pseudoscalar under spatial reflections. Thus, if the system is invariant under parity, this term must vanish. Therefore $s_\alpha = s_\beta$, hence $\alpha = \beta$.

In particular, from Eq. (4.98) one finds that the HF spectral function reads

$$S_\alpha^{(0)}(\omega) = \sum_j \delta\left(\hbar\omega - \epsilon_\alpha^{HF}\right). \tag{4.101}$$

The Dyson equation decouples in the different momentum states:

$$g_\alpha(\omega) = g_\alpha^{(0)}(\omega) + g_\alpha^{(0)}(\omega)\Sigma_\alpha^{(\star)}(\omega)g_\alpha(\omega). \tag{4.102}$$

We stress that Eq. (4.102) can be solved in each $\mathbf{k}$ channel separately [82]. The notation $\epsilon_{\alpha,j}$ is used to denote the different energy poles j that are found solving the Dyson equation for the state α. Moreover, thanks to homogeneity we know that s.p. properties must be independent on the direction of the wave vector. In the case of spin-saturated matter, they are also independent of the spin projection. Therefore, s.p. states can be organized, for each particle species separately, in groups characterized by a given $|\mathbf{k}|$, and the Dyson equation has to be solved for just one representative state for each group [3].

The density matrix is diagonal too, i.e. $\rho_{\alpha\beta} = \delta_{\alpha\beta}\rho_\alpha$, where ρ_α represents the momentum distribution function of the system, and is given by

$$\rho_\alpha = \sum_j \left|\mathcal{Y}_\alpha^j\right|^2. \tag{4.103}$$

The static self-energy is evaluated with the formula (4.28)

$$\Sigma_\alpha^{(\infty)} = \sum_\mu \bar{v}_{\alpha\mu,\alpha\mu}\rho_\mu + \frac{1}{2}\sum_{\mu\nu}\bar{w}_{\alpha\mu\nu,\alpha\mu\nu}\rho_\mu\rho_\nu, \tag{4.104}$$

where the 2B and 3B interactions are averaged on the correlated density. The Koltun sum rule is also simpler in infinite matter and reads

$$E_0^A = \frac{1}{2}\sum_\alpha\left(t_\alpha\rho_\alpha + \sum_j \epsilon_{\alpha,j}\left|\mathcal{Y}_\alpha^j\right|^2\right) - \frac{1}{2}\langle W\rangle, \tag{4.105}$$

with

$$\langle W\rangle \approx \frac{1}{6}\sum_{\alpha\beta\gamma}\bar{w}_{\alpha\beta\gamma,\alpha\beta\gamma}\rho_\alpha\rho_\beta\rho_\gamma. \tag{4.106}$$

The OpRS propagator has the same structure of $g^{(0)}$, Eq. (4.98) and is thus characterized by a single pole with amplitude 1 for each α. The condition on the zeroth-order moment (4.53) of the spectral function is satisfied automatically, while the first-order condition reads

$$M_\alpha^{(1,OpRS)} = M_\alpha^{(1)} = \frac{1}{E_F - \epsilon_\alpha^{OpRS}} = \sum_j \frac{\left|\mathcal{Z}_\alpha^j\right|^2}{E_F - \epsilon_{\alpha,j}}, \tag{4.107}$$

and hence the OpRS energies are given by

$$\epsilon_\alpha^{OpRS} = E_F - \frac{1}{M_\alpha^{(1)}}. \tag{4.108}$$

As in the case of Dyson SCGF, in the Gorkov approach the propagators and the self-energies are diagonal in the momentum basis.

We now consider the case of Gorkov-SCGF. As in Dyson's theory, both the normal and anomalous propagators are diagonal in the momentum basis ($\alpha = \beta$). In fact, only pairs of time-reversed states can be created or destroyed. As a consequence, the density matrices and the self-energies are diagonal, too: $\rho_{\alpha\beta} = \delta_{\alpha\beta}\rho_\alpha$,

[3] A technical note: in the thermodynamic limit, indeed all s.p. properties are functions of $|\mathbf{k}|$. In a finite model space, when PBCs are used this is strictly true only for states $\mathbf{n}$ that are related by a permutation and/or sign change of the three components n_i, e.g. $(2,0,1)$ and $(0,-2,1)$. However, there also exist states that have the same value of $|\mathbf{n}|^2$, but are not related by such symmetry, e.g. the states $(3,0,0)$ and $(2,2,1)$. These states must be assigned to different groups, and slightly different results concerning e.g. the spectral function and the occupation number may be observed. Thus, isotropy is in fact mildly broken in calculations performed with discretized momenta. By contrast, when TABC are used $\mathbf{k}$ vector are non-degenerate (see Fig. 1.4 and related discussion).

$\tilde{\rho}_{\alpha\beta} = \delta_{\alpha\beta}\tilde{\rho}_\alpha$, $\Sigma^{11}_{\alpha\beta} = \delta_{\alpha\beta}\Sigma^{11}_\alpha$ and $\Sigma^{12}_{\alpha\beta} = \delta_{\alpha\beta}\Sigma^{12}_\alpha$. For convenience, we report the expression of the relevant elements of the propagators, densities and static self-energies:

$$g^{11}_\alpha(\omega) = \sum_q \frac{|\mathcal{U}^q_\alpha|^2}{\hbar\omega - \hbar\omega_{\alpha,q} + i\eta} + \frac{|\bar{\mathcal{V}}^q_\alpha|^2}{\hbar\omega + \hbar\omega_{\alpha,q} - i\eta}, \tag{4.109}$$

$$\rho_\alpha = \sum_q |\bar{\mathcal{V}}^q_\alpha|^2, \tag{4.110}$$

$$\tilde{\rho}_\alpha = \sum_q (\bar{\mathcal{V}}^q_\alpha)^* \bar{\mathcal{U}}^q_\alpha = -\sum_q (\mathcal{V}^q_\alpha)^* \mathcal{U}^q_\alpha, \tag{4.111}$$

$$\Sigma^{11(\infty)}_\alpha = \sum_\beta \bar{v}_{\alpha\beta,\alpha\beta}\rho_\beta + \frac{1}{2}\sum_{\beta\gamma} \bar{w}_{\alpha\beta\gamma,\alpha\beta\gamma}\rho_\beta\rho_\gamma + \frac{1}{4}\sum_{\beta\gamma} \bar{w}_{\alpha\bar{\beta}\beta,\alpha\gamma\bar{\gamma}}\tilde{\rho}^*_\beta\tilde{\rho}_\gamma, \tag{4.112}$$

$$\Sigma^{12(\infty)}_\alpha = \frac{1}{2}\sum_\beta \bar{v}_{\alpha\bar{\alpha},\beta\bar{\beta}}\tilde{\rho}_\beta + \frac{1}{2}\sum_{\beta\gamma} \bar{w}_{\alpha\bar{\alpha}\beta,\gamma\bar{\gamma}\beta}\rho_\beta\tilde{\rho}_\gamma. \tag{4.113}$$

The Koltun sum rule (4.79) in infinite matter reads

$$E^A_0 = \frac{1}{2}\sum_{\alpha q} (t_\alpha + \mu - \omega_{\alpha,q}) |\mathcal{V}^q_\alpha|^2 - \frac{1}{2}\langle W\rangle, \tag{4.114}$$

with $\langle W\rangle$ given by Eq. (4.106). The OpRS energies are generated from the Gorkov propagator either as centroids of the spectral function,

$$\epsilon^{OpRS}_\alpha = \sum_q \hbar\omega_{\alpha,q}\left(|\mathcal{V}^q_\alpha|^2 - |\mathcal{U}^q_\alpha|^2\right), \tag{4.115}$$

or averaging over the inverse power of the energy poles,

$$\frac{1}{\epsilon^{OpRS}_\alpha} = \sum_q \frac{1}{\hbar\omega_{\alpha,q}}\left(|\mathcal{V}^q_\alpha|^2 - |\mathcal{U}^q_\alpha|^2\right). \tag{4.116}$$

We will denote as Gorkov-Cen (Gorkov-Inv) the calculations performed with the Gorkov correction with OpRS energies generated with the recipe Eq. (4.115) [Eq. (4.116)].

To summarize, we describe the essential steps of the actual implementation of the Dyson-ADC method and the first-order Gorkov method of Sec. 4.3 in infinite nuclear matter as follows:

1. The s.p. basis is determined and organized in groups of states with the same momentum and particle species.
2. The ADC matrices of Sec. 4.2 are built using an unperturbed propagator (4.98). This boils down to replacing the $\mathcal{X}$ and $\mathcal{Y}$ amplitudes by Kronecker's δ's and using HF (or OpRS) energies in place of the excitation energies ϵ^+ and ϵ^- in Eqs. (4.35)-(4.41).
3. The matrices $E^> + C$ and $E^< + D$ are reduced with the Lanczos algorithm (App. D.2) separately. It is also convenient to diagonalize the resulting matrices, to write the self-energy in a simpler form.
4. The sc0 loop is performed. At each iteration, the Dyson (4.51) or Gorkov (4.90) eigenvalue problem is solved for a representative state in each of the groups in the s.p. basis. The amplitudes are used to evaluate the occupation numbers and the total energy using Eqs. (4.103) and (4.105) in Dyson-sc0, or (4.110) and (4.114) in Gorkov-sc0.
5. OpRS energies are generated using formula Eq. (4.108) in Dyson calculations, or with the recipes (4.115) or (4.116) in Gorkov calculations. The Dyson matrices are evaluated using the new s.p. energies, and the cycle is repeated.

4.5 Finite-temperature SCGF

Green's functions methods have been used to study infinite nuclear matter extensively in the past. SCGF based on the finite-temperature formalism (from now on "Finite-T SCGF") has been applied to homogeneous nuclear matter, as demonstrated by applications to asymmetric matter in a range of temperatures relevant for astrophysical scenarios [20, 111]. In this Section we limit ourselves to a brief overview of the method, which is described in detail in Refs. [20, 82, 200, 223].

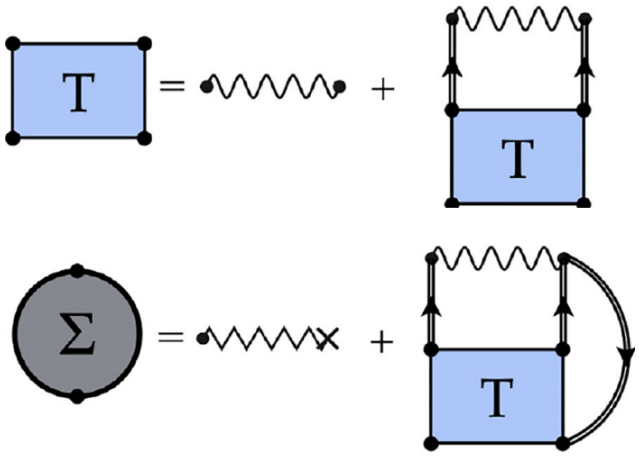

Figure 4.7: Diagrammatic representation of the ladder approximation to the self-energy in the Finite-T SCGF formalism. The self-consistent equation for the T-matrix (top) and the self-energy (bottom) are shown. The wiggly lines represent the effective 1B and 2B interactions shown in Figs. 4.1 and 4.2, respectively. Adapted from Ref. [20].

The Finite-T SCGF method is based on the so-called ladder approximation of the self-energy. The key ingredient of this approach is the T-matrix, which represents an in-medium, energy-dependent effective two-body interaction. The T-matrix satisfies a self-consistent Lippmann-Schwinger-like equation that allows effectively resum contributions from repeated scatterings of the particles and holes in the medium to all orders. The diagrams that define the equations for T and the self-energy are shown in Fig. 4.7. Since the formalism is expressed in the TL with continuous momenta, it allows us to capture the short-range correlations that are expected to dominate in (dilute) Fermi gases [20, 224]. Also, in Finite-T SCGF fully self-consistent solutions for the dressed propagator can be found [20]. By contrast, in ADC-SCGF self-consistency is realized approximately using the OpRS technique [210]. A consequence is that Finite-T SCGF is thermodynamically consistent, i.e. thermodynamical properties calculated microscopically coincide with the quantities calculated as derivatives of the free energy [20, 214]. A notable example is the chemical potential. Moreover, the ladder approximation is a conserving approximation, so that conservation laws are guaranteed to be satisfied by fully self-consistent calculations [20]. Studies that report applications of the Finite-T SCGF to calculations of EOS, momentum distributions and spectral functions include [20, 104, 111, 223, 225].

A comparison between the Finite-T and ADC formalism is in order. The first and most obvious is that ADC is strictly a zero-temperature method, whereas, in the other approach, calculations are performed at energies of at least 5 MeV. Temperature is effective in lifting the pairing instabilities that would emerge when at low matter densities the energy gap tends to vanish. This is a well-understood phenomenon, that nonetheless makes it difficult to converge calculations at low ρ in many-body methods based on HF reference states, such as Dyson SCGF and coupled-cluster [126], and is a clear manifestation of the need to use a multi-reference or BCS state, as e.g. in Gorkov SCGF [84]. The $T = 0$ limit is accessed using an extrapolation procedure (see e.g. [222]), such as a Sommerfeld expansion [226]. Such procedure is well understood and precise, and does not introduce any significant numerical error. Second, in ADC-SCGF calculations are performed in a finite model space, with a finite number of particles and a finite number of basis states, and the method is cast into a matrix eigenvalue problem. By contrast, Finite-T SCGF is formulated in the continuum and allows to access the TL directly. The treatment of the continuum is the most relevant difference with both ADC and coupled-cluster [126], where the k-space is discretized. Lastly, Finite-T SCGF includes the dominant ladder contributions, while ADC(3) also resums the ring diagrams. These are important in finite nuclei, where they determine the long-range physics, but their effect is modest in infinite matter. Moreover, ADC is a systematically improvable scheme. Also, the significant developments in both theory and algorithms of the Dyson and Gorkov methods that have occurred in the last years can be quite readily applied to infinite nuclear matter.

CHAPTER 5

Ab initio equations of state

In this Chapter, the *ab initio* equations of state of infinite nuclear matter are presented. The EOS have been interpolated with polynomials of the Fermi momentum, see Sec. 2.2.1, as a preliminary step before being employed to define the local density approximation EDFs (Ch. 6). We remind that a model selection procedure has been used to choose the set of powers $\{\gamma_i\}$ that allows to best fit the data. We refer to a model EOS listing the powers of $\rho^{1/3}$ it is made of. For example, (2,5,6) stands for $c_{\frac{2}{3}}\rho^{\frac{2}{3}} + c_{\frac{5}{3}}\rho^{\frac{5}{3}} + c_2\rho^2$.

This chapter is structured as follows. In Sec. 5.1 the EOS obtained with the AV4′+UIX$_c$ interaction and the AFMDC method (Ch. 3) is discussed. In Sec. 5.2, the Finite-T SCGF method, introduced in Sec. 4.5, is used to determine the EOS with the NNLO$_{\rm sat}$ potential. Since the methods are well consolidated, in these sections only the final results are shown. Sec. 5.3 is devoted to a study of the newly developed ADC-SCGF method for infinite matter (Ch. 4), which is thoroughly discussed and validated.

5.1 AFDMC

Calculations performed with the AFDMC method and the AV4′+UIX$_c$ interaction are reported in this Section. We present the results that have been obtained in PNM using $N = 66$ neutrons and in SNM with $A = 76$ and $A = 132$ nucleons for several densities up to 0.40 fm^{-3}. Part of these calculations have already been presented in Ref. [68] and are, to the best of our knowledge, the first application of AV4′+UIX$_c$ to nuclear matter. We will also use the short-hand notation "Argonne 4" to refer to this (NN+3N) interaction, when there is no ambiguity. The Argonne 4 potential represents a good choice for methodological purposes (Sec. 1.2). On the one hand, it has a simple operator structure that allows to perform reliable AFDMC calculations not only of PNM, but also of SNM and medium-mass nuclei [68]. On the other hand, it yields reasonable predictions for the binding energies of magic nuclei, see [108].

The QMC calculations are obtained using the constrained path approximation. Wave functions that include linear operator correlations are optimized in VMC and then used in the diffusion process. DMC runs employ about 2000 walkers. After about 100 blocks (each block consisting of 40 steps), convergence to the g.s. is typically achieved, and we start computing observables for at least 50 blocks. This blocking technique helps reduce the correlations between steps in the time evolution [178].

The energies per nucleon as a function of the density are reported with their statistical error bars in Fig. 5.1. As far as SNM is concerned (lower panel), the saturation point is located at an unusually high density ($\rho \approx 0.24$ fm^{-3}) and low (i.e. high in absolute value) energy, and the 3N contribution is instrumental in allowing the SNM EOS to saturate; in fact, AV4′ alone predicts no saturation before 0.50 fm^{-3} [190]. With $A = 76$ (diamonds), the saturation energy amounts to about -23.7 MeV, while with $A = 132$ (circles) it is roughly 2 MeV higher. Thus, Argonne 4 gives a realistic description of finite magic nuclei [68, 108] (Ch. 2.2), but in infinite matter predictions are farther from the empirical constraints.

The EOS have been fitted with the polynomial functions described in Sec. 2.2.1, using the finite-A kinetic energy (2.14) in Eq. (2.12). The model that best reproduces the *ab initio* EOS is the (2,5,6) polynomial, whose predictions are shown in Fig. 5.1 as dotted lines. Note that separate fits have been done for the SNM EOS with the two different nucleon numbers.

For later convenience, we have also considered the results for the AV8′ + UIX interaction ("Argonne 8" for short) obtained with AFDMC in Ref. [227] for PNM with 66 neutrons. This is the initial step for an analysis of perturbed neutron matter presented in Sec. 8.2. The optimal interpolation is given by the polynomial model (3,4,5,6), and is shown in Fig. 5.2 together with the *ab initio* data points.

5.2 Finite-T SCGF

We report the EOS computed in both SNM and PNM with the Finite-T SCGF method and the NNLO$_{\rm sat}$ interaction. Calculations have been originally performed in Ref. [111]; the zero-temperature EOS shown here is obtained as a controlled extrapolation of finite-temperature results.

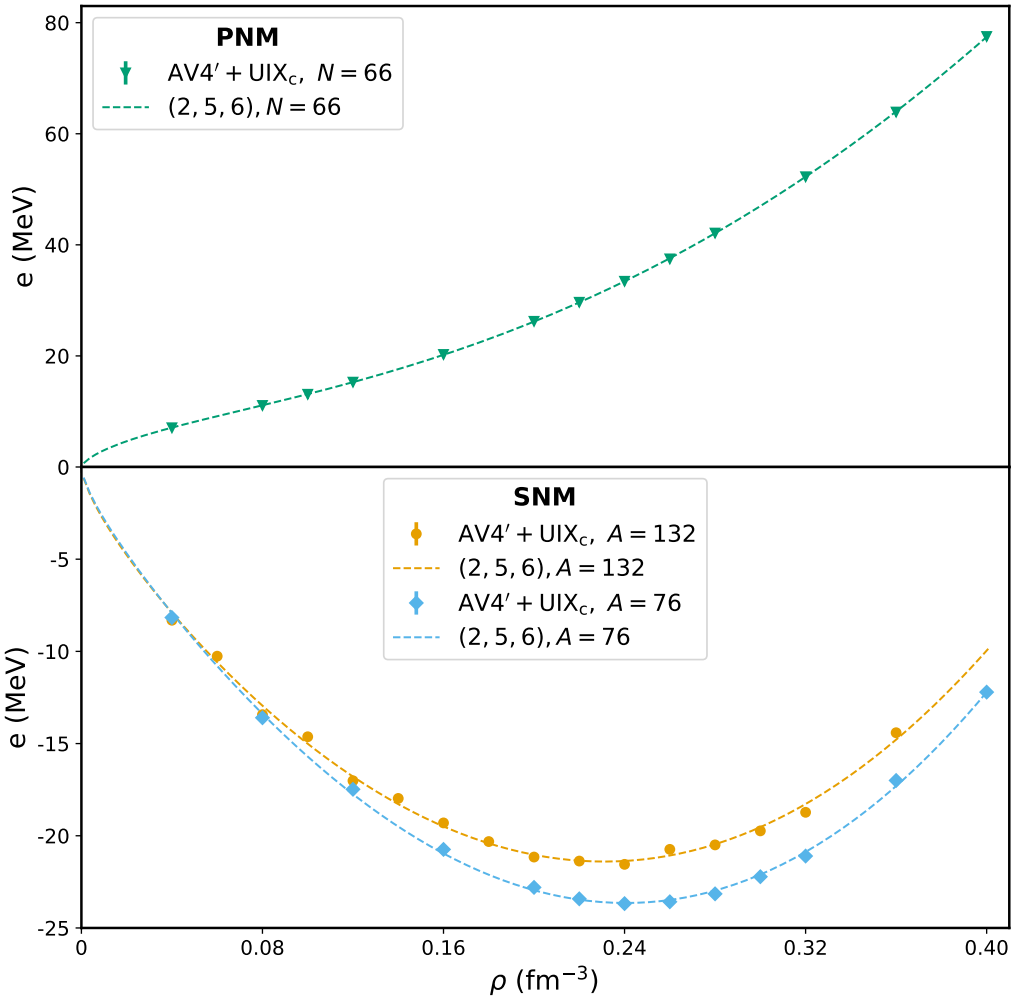

Figure 5.1: Equation of state computed with the AV4′+UIX$_c$ interaction and the AFDMC method in PNM with $N = 66$ neutrons (upper panel) and SNM (lower panel) with $A = 76$ (diamonds) and $A = 132$ nucleons (circles). Dashed lines denote fits performed with the model EOS (2,5,6) (see text for details).

We have considered simulations up to densities $\rho = 0.32$ fm^{-3}, as these are still compatible with the soft momentum cutoff of this interaction. The SNM EOS saturates at $\rho_{sat} = 0.15$ fm^{-3} and $\mathrm{E}_{sat} = -14.7$ MeV. Note that predicting a saturation point compatible with the empirical constraints is a non-trivial achievement that has contributed to the popularity of NNLO$_{\mathrm{sat}}$ [105]. As in Ref. [68], we performed fits on on a set of points equally spaced by 0.01 fm^{-3} following the parametrizations discussed in Sec. 2.2.1. A 5-fold cross-validation procedure was used to estimate the validation error and select the best model. The optimal choice is the polynomial $(2, 3, 4, 5, 6)$. This model is shown by the curves in Fig. 5.3 along with the complete *ab initio* dataset used in the fit.

In summary, representing the nuclear EOS as a polynomial of the Fermi momentum has proved an effective ansatz in all cases that we have examined. Such parametrizations are used in Ch. 6 as the building block of the *ab initio*-based EDFs.

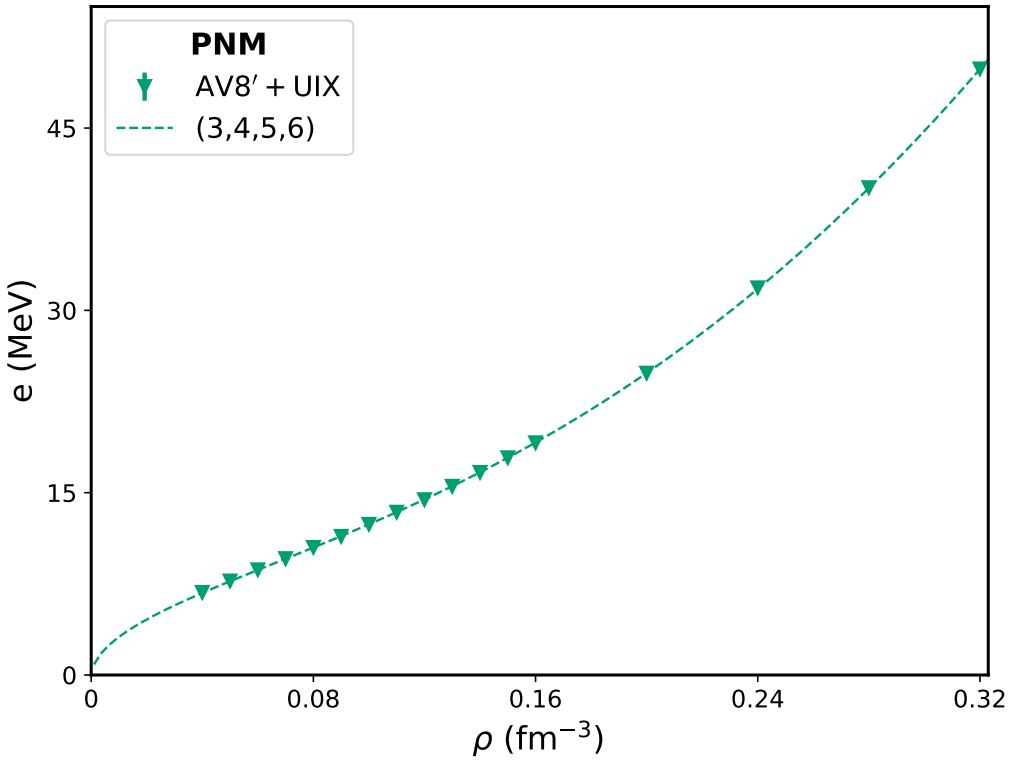

Figure 5.2: Equation of state computed with the AV8′+UIX interaction and the AFDMC method in PNM with $N = 66$ neutrons. Dashed lines denote fits performed with the model EOS (3,4,5,6). Data are taken from Ref. [227].

5.3 ADC-SCGF

In this Section, a study of the ADC-SCGF method for infinite nuclear matter (Sec. 4.2) is reported. When not stated otherwise, $N = 66$ neutrons and $A = 132$ nucleons are used in PNM and SNM, respectively, and PBCs are imposed. The $\text{NNLO}_{\text{sat}}\,(450)$ [105] and $\Delta\text{NNLO}_{\text{go}}\,(394)$ [106] chiral interactions are employed (Sec. 1.2). These potentials use non-local regulators in both the NN and 3N sectors; the number in parenthesis refers to their cutoff in MeV/c (see App. A). We perform calculations up to $\rho = 0.32\,\text{fm}^{-3}$. For finite nuclei, the region around the saturation density is most relevant. Also, as the chiral interactions are defined in a low-momentum expansion, we are aware that physically meaningful results can be expected only for densities such that $\hbar k_F \lesssim \Lambda$, with Λ being the cutoff of the potential. Fermi momenta for both PNM and SNM are reported in Tab. 5.1 for some representative densities. The reliability of the interactions at $\rho = 0.32\,\text{fm}^{-3}$ is questionable, especially for PNM, as $\hbar k_F$ becomes comparable with the cutoff. Yet, it is interesting to examine how the method behaves in the strongly-correlated high-density regime.

	$\rho\,(\text{fm}^{-3})$	$k_F\,(\text{fm}^{-1})$	$\hbar k_F\,(\text{MeV/c})$
PNM	0.08	1.333	263.041
	0.16	1.680	331.411
	0.24	1.923	379.371
	0.32	2.116	417.552
SNM	0.08	1.058	208.776
	0.16	1.333	263.041
	0.24	1.526	301.107
	0.32	1.680	331.411

Table 5.1: Fermi momentum (in fm^{-1} and in MeV/c) as a function of the number density in PNM and SNM.

As discussed in Secs. 4.2 and 4.3, in ADC-SCGF the particle number is conserved only on average. While in Gorkov-SCGF $\langle A \rangle = A$ is imposed by construction, a violation of the nucleon number is sometimes observed in Dyson-SCGF, especially in high-density SNM, where correlations are strong. In the following, the EOS are shown using the expectation value $\langle A \rangle$, and *not* the 'nominal' particle number A. That is, the EOS is to be understood as the energy per particle $E/\langle A \rangle$ versus the density $\langle A \rangle / \Omega$, with Ω being the quantization volume.

In basis expansion methods, it is necessary to study the convergence of the results as a function of the

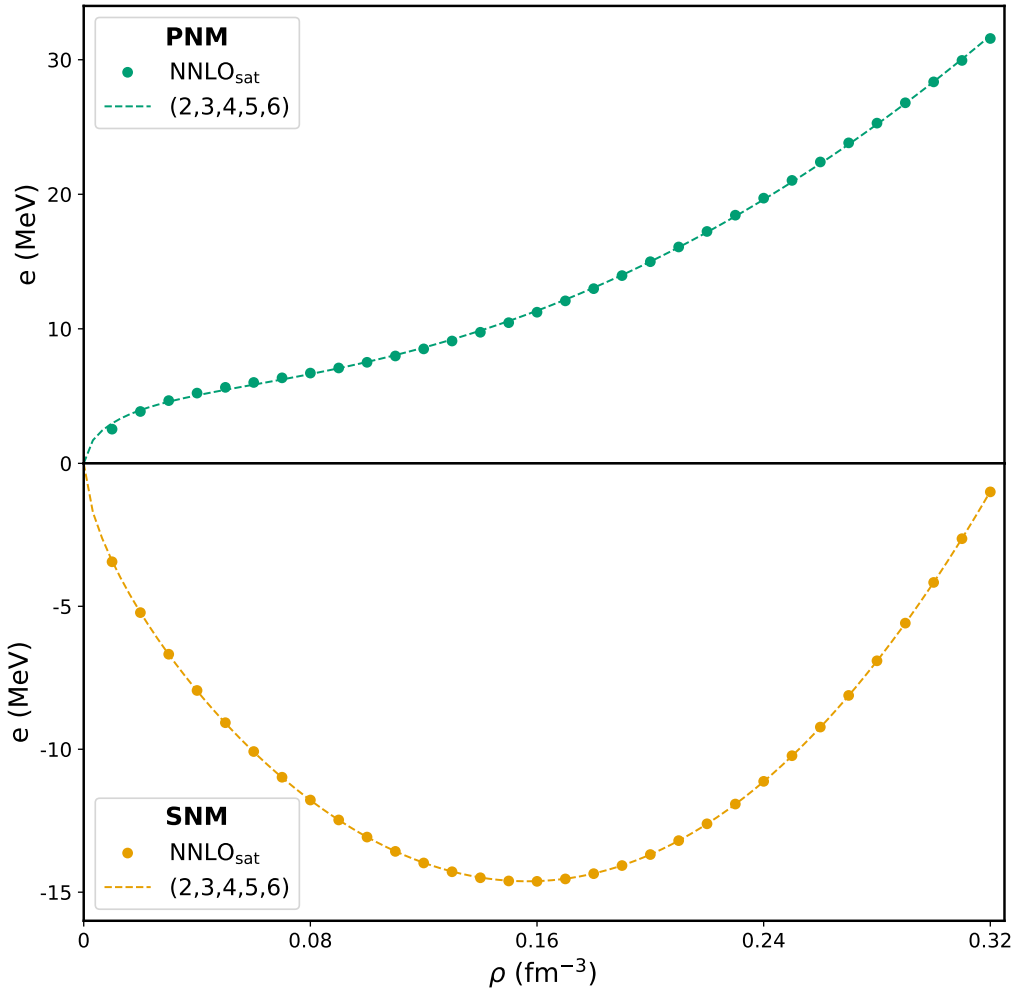

Figure 5.3: Equation of state computed with the $\mathrm{NNLO_{sat}}$ interaction and the Finite-T SCGF method in PNM (upper panel) and SNM (lower panel). Results have been extrapolated to the $T = 0$ limit. Dashed lines denote fits performed with the model EOS (2,3,4,5,6) (see text for details).

dimension of the s.p. basis. The parameter that controls the model space in infinite matter is N^2_{max}, i.e. the s.p. basis is made of the momentum eigenstates with $|\mathbf{n}|^2 < N^2_{max}$ (Sec. 4.4). First, the convergence of the MBPT(2) energies (see App. D.3) is reported in Fig. 5.4. PNM (SNM) calculations are shown in the upper (lower) panels at densities $\rho = 0.16$ fm^{-3} (left) and 0.32 fm^{-3} (right) for the two interactions, rewhichented by squares [$\mathrm{NNLO_{sat}}$ (450)] and circles [$\Delta\mathrm{NNLO_{go}}$ (394)]. The energies per particle are shown for N^2_{max} ranging between 4 and 30. The insets report the difference between the energy for a given cutoff and the value of the energy at $N^2_{max} = 30$, that is well-converged in all cases. As the s.p. basis is enlarged, the energy decreases monotonically. The trend is not smooth, though, and a few hints of 'plateaus' are observed. One can appreciate that PNM is more perturbative than SNM, and in turn the calculations with $\Delta\mathrm{NNLO_{go}}$, that is softer, i.e. has a lower cutoff, than $\mathrm{NNLO_{sat}}$, converge more quickly. We have observed that at the higher density, $\rho = 0.32$ fm^{-3}, where the system is more strongly correlated, convergence is faster as a function of N^2_{max}. This behavior might be explained as follows (see Ref. [83]). For a fixed number of particles, one can expect the calculations to be converged with respect to the s.p. basis for a maximum momentum, k_{max}, of the order of the Fermi momentum plus the cutoff of the potential, $\hbar k_{max} \approx \hbar k_F + \Lambda$. In turn, k_{max} is related to N^2_{max} and to the density as follows:

$$k_{max} \sim \frac{1}{L}\sqrt{N^2_{max}} \sim \rho^{1/3}\sqrt{N^2_{max}}. \tag{5.1}$$

As k_{max} varies mildly with the density (see Tab. 5.1), the maximum N^2_{max} required is expected to be smaller for larger densities. In PNM, already with $N^2_{max} = 20$ differences in energy from the largest model space considered amount to little more than 1 keV at most. In SNM, a similar convergence pattern is reached only for $N^2_{max} \approx 25$ in the $\mathrm{NNLO_{sat}}$ case. Interactions are indeed stronger in SNM than in PNM.

A convergence study of ADC is then performed for the case that manifests the slowest convergence pattern in MBPT(2), i.e. SNM at $\rho = 0.16$ fm^{-3} with $\mathrm{NNLO_{sat}}$. The ADC(3) approximation with Gorkov first-order

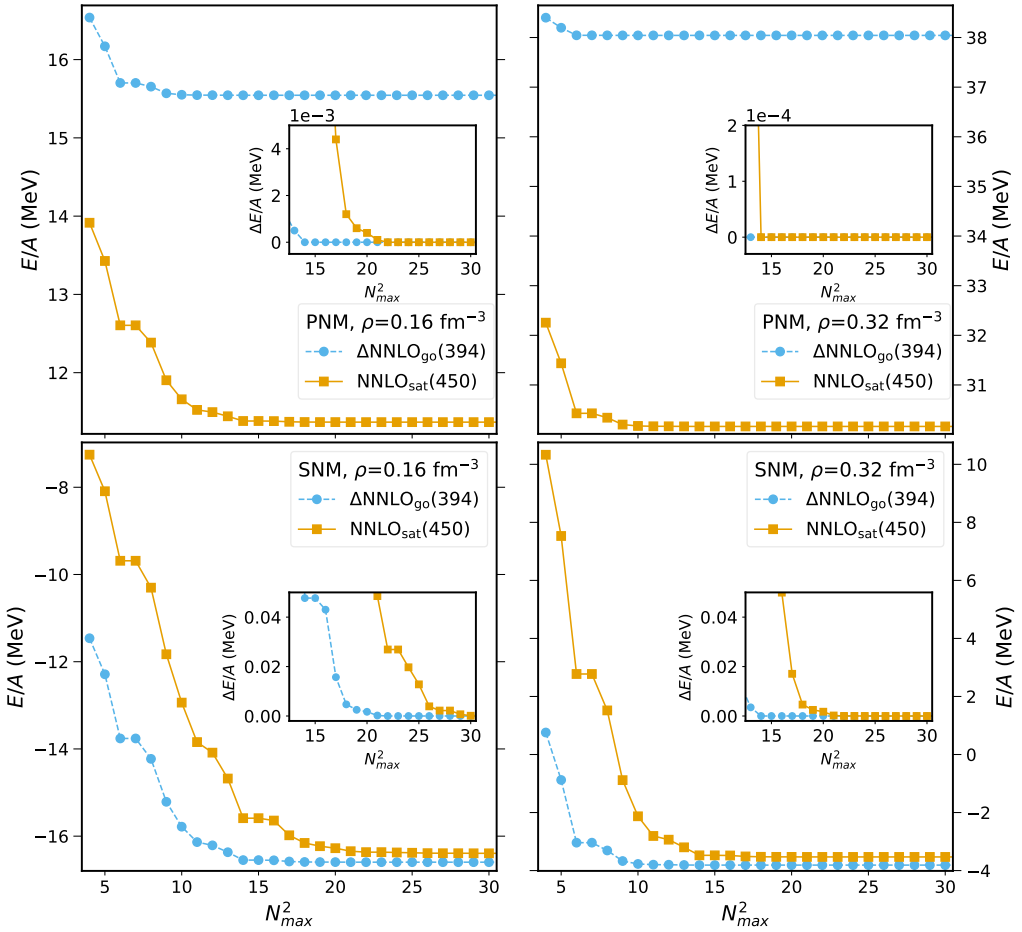

Figure 5.4: MBPT(2) energies per nucleon as a function of the cutoff N^2_{max} of the s.p. basis. Calculations are performed with the NNLO$_{\rm sat}$ (450) (squares) and ΔNNLO$_{\rm go}$ (394) (circles) interactions in both PNM (upper panels) and SNM (lower panels), at densities $\rho = 0.16$ fm^{-3} (left) and 0.32 fm^{-3} (right). Insets: differences $\Delta E/A$ between the energy for a given cutoff and the converged energies (obtained for $N^2_{max} = 30$). Lines are a guide to the eye.

corrections is adopted, and OpRS energies are determined as centroids of the spectral function using Eq. (4.115) (Gorkov-Cen for short). A convergence criterion of 10 keV/A is set for the energies of both the sc0 and OpRS cycles (see App. D.7). Calculations are reported for cutoffs up to $N^2_{max} = 28$ in Fig. 5.5. While the computing time is always manageable, the memory required to store the potential matrix elements and the Dyson matrix increases quickly and at present makes it difficult to access larger model spaces. In any case, the trend is clear, and in fact energies for $N^2_{max} = 24$ are within $\approx 20\,$keV/A from $N^2_{max} = 28$, as shown in the inset. All subsequent calculations will be done with a cutoff of $N^2_{max} = 25$, that we expect to be converged with respect to the model space truncation within the accuracy of the method.

A comparison of the different ADC approximations is then presented. We study the representative case of the NNLO$_{\rm sat}$ (450) potential, which is less perturbative and thus allows to emphasize beyond-mean-field effects. Also, the Gorkov-Cen method is used, as this has proved to be the most stable SCGF variant (see below). Besides ADC(2) and ADC(3), the ADC(ld,2) approximation, of intermediate complexity, is considered as well (Sec. 4.2). The results for the PNM and SNM EOS are shown in the upper and lower panel of Fig. 5.6, respectively, for densities between 0.04 and 0.32 fm^{-3}. In the insets, correlation energies per particle, $E_{corr} = E - E_{HF}$, are reported for the three ADC approximations and also for MBPT(2) (triangles). First, one can appreciate that correlation energies are much larger in SNM than in PNM, as expected. In neutron matter, most of E_{corr} is captured already at the MBPT(2) level, and the non-perturbative ADC calculations provide a small repulsive correction, that amounts at most to about 300 keV/A, for ADC(3) at $\rho = 0.16\,$fm^{-3}. A hierarchy is observed, since ADC(2), ADC(ld,2), and ADC(3) tend to give increasingly larger contributions to the correlation energy. It is interesting to note that discrepancies between the different schemes are most evident at intermediate densities around $\rho = 0.16\,$fm^{-3}, while they shrink in the low- and high-density limits. Again, we suggest that at high momenta close to the cutoff the strength of the interaction may be quenched. At variance with PNM, SNM is a strongly correlated system, and MBPT(2) energies range between approximately -5 and -15 MeV/A. The additional effect that ADC brings to MBPT(2) is of the order of 0.5-1 MeV/A and

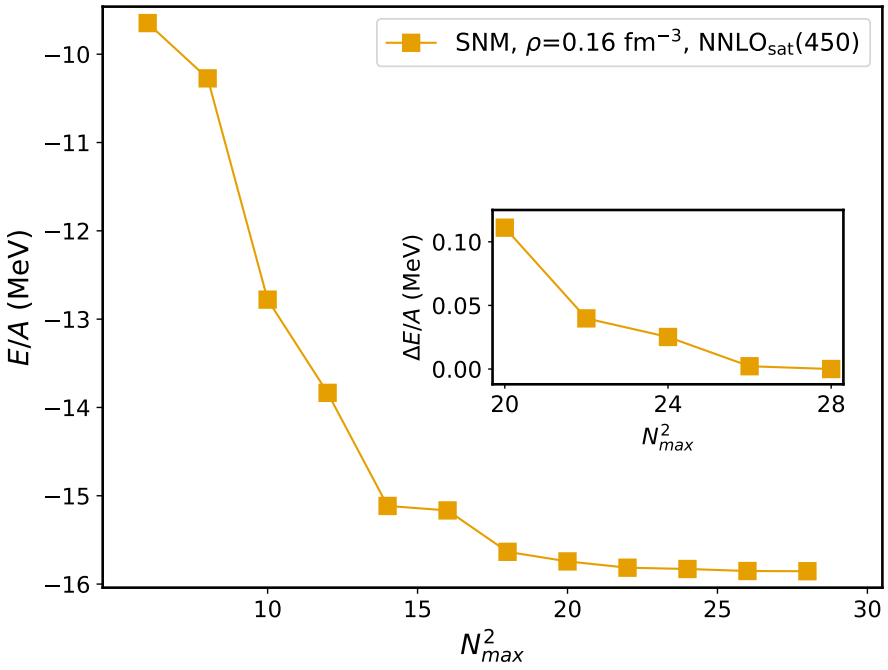

Figure 5.5: Convergence of the energy per nucleon as a function of N^2_{max} for SNM, $A = 132$, at density $\rho = 0.16$ fm^{-3}. Calculations are performed at the level of ADC(3) with Gorkov corrections. OpRS energies are determined as centroids of the spectral function, see Eq. (4.115) (Gorkov-Cen). Inset: difference between the energy per particle at a given cutoff and the one for $N^2_{max} = 28$. The NNLO$_{\rm sat}$ (450) interaction is employed.

is positive. In this case, ADC(2) typically provides more repulsion than ADC(3), with ADC(ld,2) lying in between.

The SNM and PNM EOS computed with ADC(3) are now discussed in detail. In Fig. 5.7, results obtained with NNLO$_{\rm sat}$ (450) (left) and ΔNNLO$_{\rm go}$ (394) (right) interactions are shown for PNM (top) and SNM (bottom). We compare in each panel Dyson-ADC(3) (triangles) with the calculations in which Gorkov corrections have been included. Two recipes for generating the OpRS energies are employed, Gorkov-Cen (diamonds) and Gorkov-Inv (stars), which are defined by Eqs. (4.115) and (4.116), respectively. In PNM, all three variants are essentially indistinguishable on this scale. This is not surprising, since neutron matter is relatively weakly correlated. Note that ΔNNLO$_{\rm go}$ (394) predicts larger energies than NNLO$_{\rm sat}$. Indeed, the latter is known to predict an extremely soft PNM EOS and to underestimate the symmetry energy [111], while the issue is mitigated by the other interaction [106]. In SNM, differences between various calculation schemes are more evident. Gorkov corrections bring in small repulsive contributions to the Dyson-ADC(3) energies. The Gorkov-Inv approach suffers from some uncontrolled fluctuations. Near the Fermi surface, i.e for small $|\omega_q|$, the delicate interplay in Eq. (4.116) of a small numerator, resulting from the cancellation between positive and negative terms, and a small denominator, indeed, is prone to numerical instabilities. Importantly, though, the Gorkov-Cen technique is rather stable and produces a regular EOS. This method converges easily at all densities up to $\rho = 0.36$ fm^{-3}, even when Dyson-ADC(3) fails, and allows to conserve the nucleon number on average in virtue of the Gorkov ansatz, while some violations can be seen in the Dyson case for both interactions. (Points for Dyson results can be located at slightly different densities than the corresponding Gorkov ones.) At the densities where converged results are available for both Dyson and Gorkov, a substantial agreement is observed, that hints at the fact that pairing effects are indeed small and the first-order treatment of Gorkov correlations is justified. We note in passing that Dyson and Gorkov-Inv energies are quite similar to each other, while Gorkov-Cen is typically somewhat more repulsive. To summarize, the Gorkov formalism (especially in the Gorkov-Cen OpRS variant) has proved to be rather effective in stabilizing ADC-SCGF calculations of infinite matter.

SCGF is not limited to the total energy, but can access much information, including the momentum distribution $\rho(k)$. Interactions induce a change in the occupation numbers, that is modified with respect to the Fermi-Dirac distribution of the free Fermi gas. At the HF level, states are either fully occupied or completely empty. In beyond-mean-field, a depletion is observed in the occupation of hole states, and correspondingly a high-momentum tail appears, which gives a small but finite occupation to states outside the Fermi sphere. In the TL, if an HF reference state is adopted, $\rho(k)$ is discontinuous at the Fermi momentum. In BCS theory and in methods built on top of a BCS state, the distributions are continuous across the Fermi surface [202]. In the finite-A system, only a finite number of k points is available, so that a discrete sample of the occupation func-

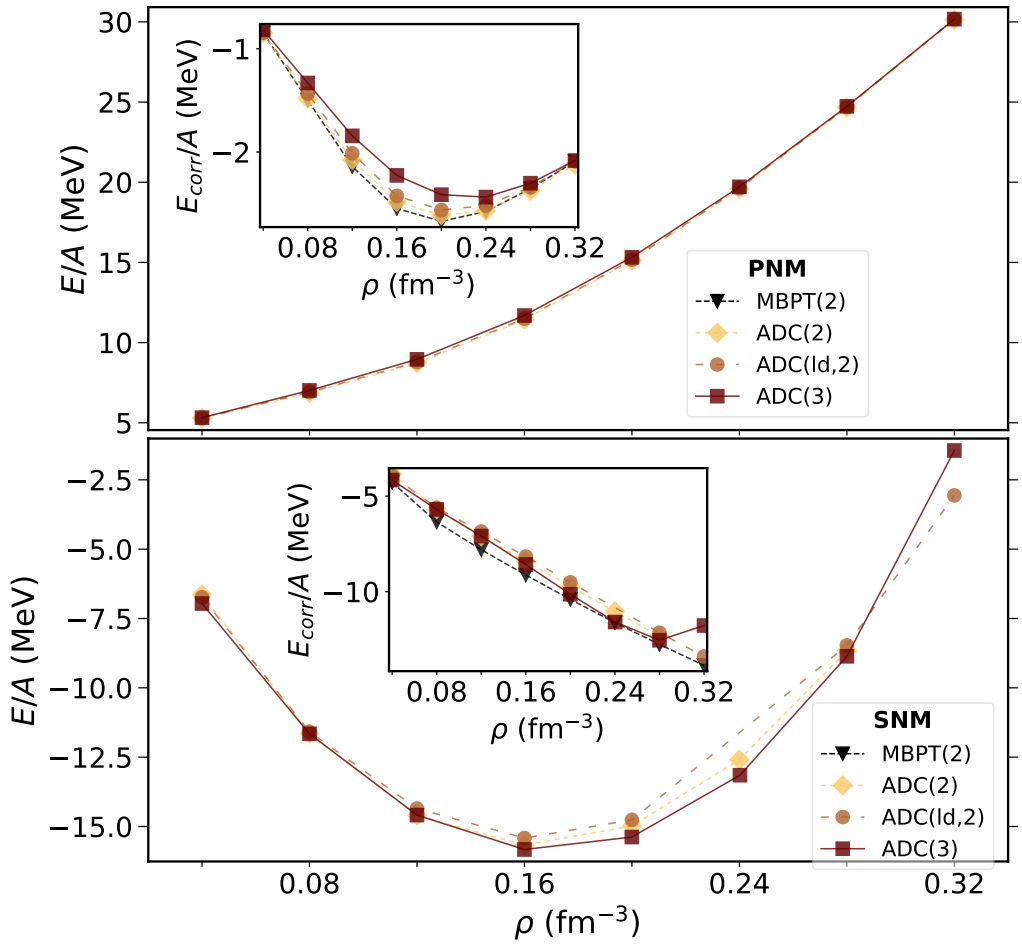

Figure 5.6: EOS of PNM (top) and SNM (bottom) computed with three ADC approximations: ADC(2) (diamonds), ADC(ld,2) (circles), and ADC(3) (squares). The $\mathrm{NNLO_{sat}}$ interaction is used, and calculations are performed including first-order Gorkov corrections with the Gorkov-Cen scheme. Insets: correlation energy per particle. Triangles denote MBPT(2) energies.

tions is provided. Results for $\rho(k)$ as a function of the wave number in units of the Fermi momentum, k/k_F, are shown in Fig. 5.8 for four densities ranging between 0.08 and 0.32 fm^{-3} in PNM for the $\mathrm{NNLO_{sat}}\,(450)$ (left) and $\Delta\mathrm{NNLO_{go}}\,(394)$ (right) potentials. The Gorkov-Cen variant of ADC(3) is employed. $\mathrm{NNLO_{sat}}\,(450)$ predicts an appreciable depletion that amounts to about 0.1 for the last occupied momentum state of the HF g.s. The occupation for the lowest-momentum particle state is smaller, 0.05 at most. As the density increases, the gap at the Fermi surface reduces, as it is expected due to the stronger correlations induced by the interactions at large ρ. The effect has been attributed predominantly to 3N forces [23]. For $\Delta\mathrm{NNLO_{go}}\,(394)$, changes to the uncorrelated momentum distribution are more modest, and amount to roughly one-half of those observed for $\mathrm{NNLO_{sat}}$. While this is consistent with the softness of the potential, we are unable at present to explain why the depletion is smaller above saturation density than below. In any case, these are very detailed effects that concern variations of less than 0.02 on $\rho(k)$.

The neutron occupation number in SNM is plotted in Fig. 5.9. Correlations strongly modify the HF picture. Momentum tails above k_F are more pronounced, and depletions at small k are larger than in PNM. However, the more interesting features of the SNM distributions appear near the Fermi momentum, where the occupation number of the outermost hole state is greatly altered. With the $\Delta\mathrm{NNLO_{go}}\,(394)$ potential, it is about 0.7 at or above saturation density, i.e. a 30% depletion is observed, and as low as 0.5 at $\rho = 0.08\,\mathrm{fm}^{-3}$. Deviations are even larger when $\mathrm{NNLO_{sat}}\,(450)$ is employed, however the trend of $\rho(k)$ is less regular in this case. These effects are induced by the pairing correlations. Tentatively, we suggest that a BCS-like distribution may emerge as a consequence of the Gorkov corrections. The closure of the discontinuity at the Fermi surface would be one of the distinctive signs of pairing, but, due to the quantization of momenta, it is difficult to verify in PBC calculations.

To further investigate the behavior of nuclear matter in the vicinity of the Fermi surface, we study the spectrum of the dressed propagator. Spectral functions are the heart of SCGF, and, although they are not observables, they encode the information on how the interactions in the many-body system affect the single-

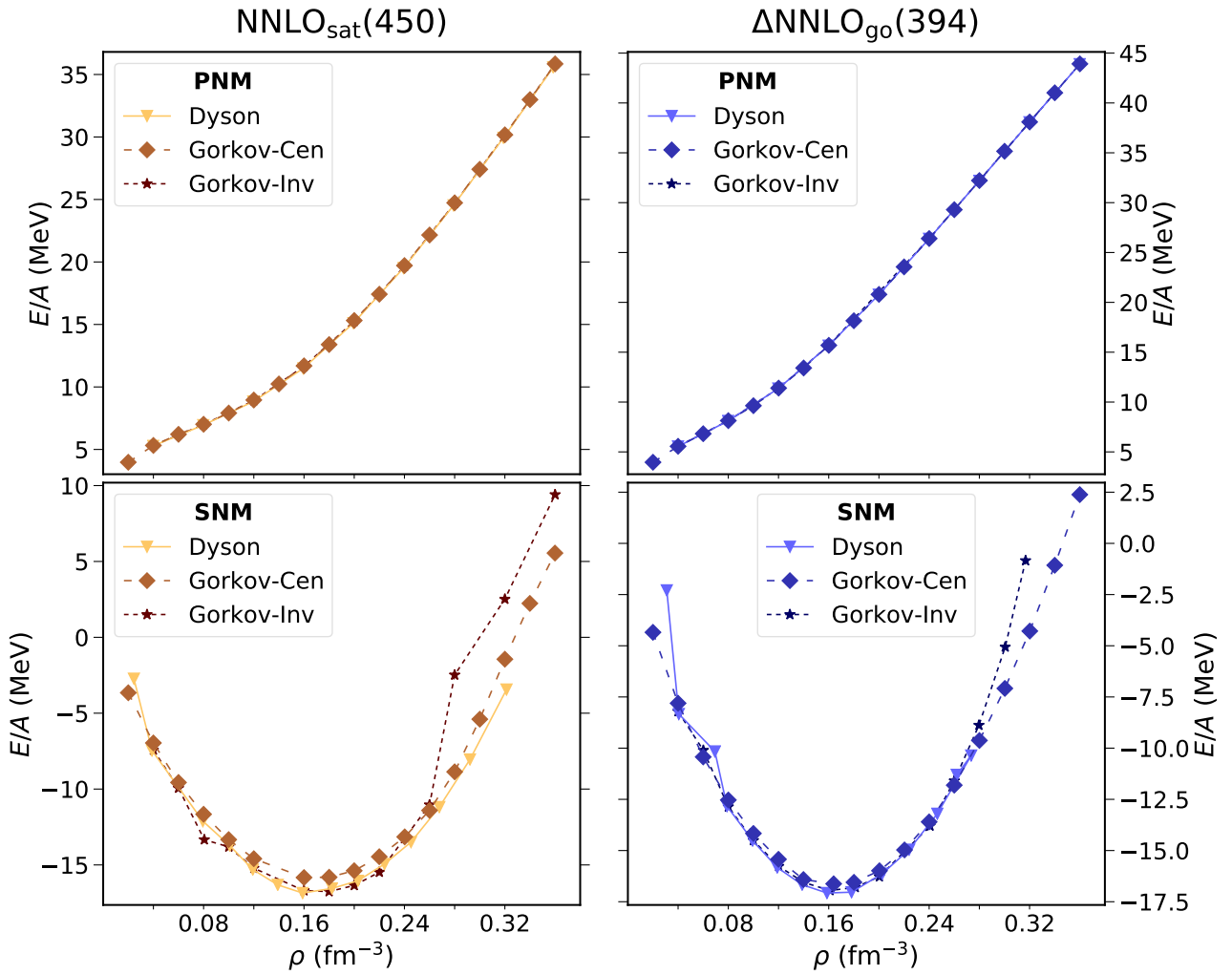

Figure 5.7: Equations of state in SNM (bottom panels) and PNM (top panels) with the NNLO$_{\rm sat}$ (450) (left) and ΔNNLO$_{\rm go}$ (394) (right) interactions. Triangles denote calculations performed with Dyson-ADC(3). Diamonds (stars) refer to the results obtained including the Gorkov corrections, with the OpRS energies defined as centroid energies (Gorkov-Cen), see Eq. (4.115) [averaging the inverse of the frequency poles (Gorkov-Inv), see (4.116)]. Lines are a guide to the eye.

particle states. We start with an illustrative example, before moving on to a more detailed analysis of SNM. In Fig. 5.10 we plot the spectral functions resulting from Dyson-ADC(3) calculations [1] in PNM at $\rho = 0.16$ fm^{-3} (left) and $\rho = 0.32$ fm^{-3} (right). Peaks are folded with a Lorentzian distribution for display purposes,

$$S_k(\omega) = \frac{\Gamma}{\pi} \sum_j \frac{\left|\mathcal{Z}_\alpha^j\right|^2}{\Gamma^2 + (\hbar\omega - \epsilon_{\alpha,j})^2}, \tag{5.2}$$

where we use a width of Γ=1.5 MeV. A 3D representation of the spectral function, previously discussed in Ref. [82], is adopted. Due to PBCs, momenta are quantized, while $S_k(\omega)$ is continuous as a function of the frequency ω. Each section of the curve is the strength function for a given k. The Fermi energy is shown as a dashed red line at a fixed frequency, and separates quasihole states (continuous lines) from quasiparticle states (dashed lines). In a weakly correlated system such as PNM, quasihole, and quasiparticle are in a one-to-one correspondence to the hole and particle states in the HF g.s., respectively. The HF spectral function (not shown) is characterized by an isolated peak of height 1 for each momentum, see Eq. (4.101). Interactions induce a fragmentation in the spectrum. The effect is largest for deeply bound neutrons and high-momentum states. In contrast, the distribution for states close to the Fermi momentum is dominated by a single peak (a Landau quasiparticle) and closely resembles the uncorrelated one. Indeed, on general grounds (see e.g. [199]) states close to the Fermi surface are expected to have a quasiparticle character. Qualitative features of the spectral function are similar at both densities, but the spectrum at $\rho = 0.32$ fm^{-3} splits up into a wealth of small peaks, while at saturation density there appear fewer, but larger, contributions.

[1] Results for Dyson and Gorkov ADC(3) in PNM are almost indistinguishable. Dyson spectral functions are shown here as they can be easily visualized with a 3D plot.

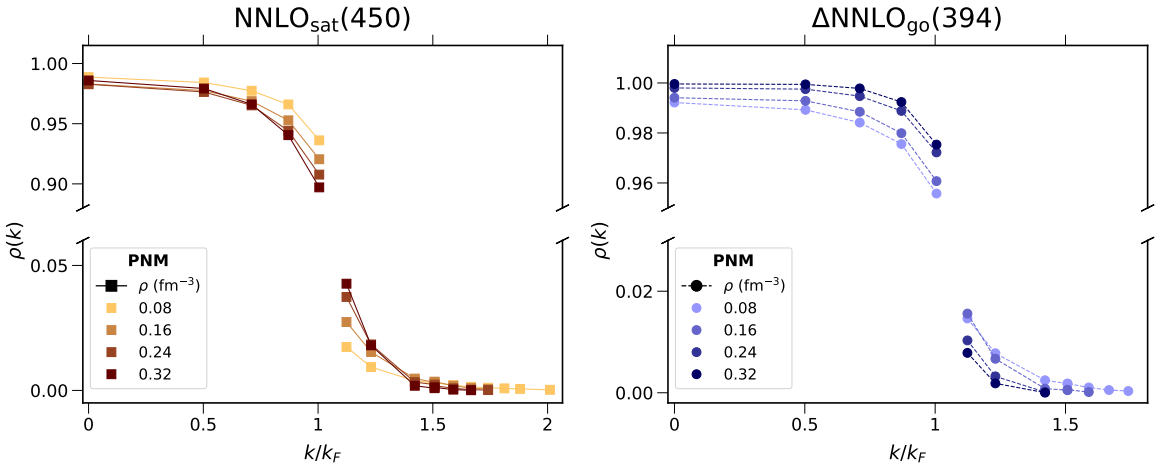

Figure 5.8: Momentum distributions $\rho(k)$ in PNM as a function of k/k_F for several densities with the NNLO$_{\rm sat}$ (450) (left) and ΔNNLO$_{\rm go}$ (394) (right) interactions. Calculations are performed with ADC(3) with Gorkov corrections, and OpRS energies are generated as centroids of the spectral function (Gorkov-Cen technique). Lines are a guide to the eye. Note that different scales are used for $k < k_F$ and $k > k_F$.

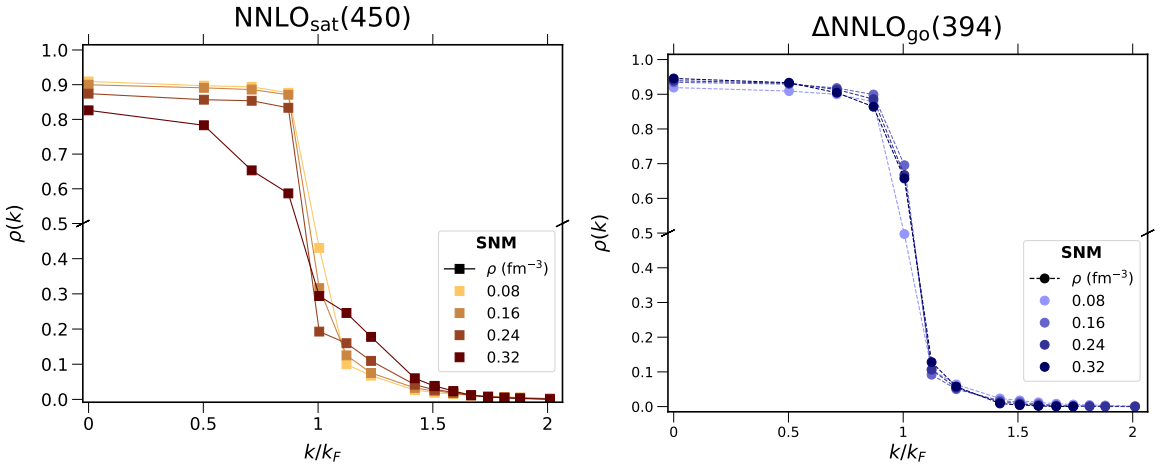

Figure 5.9: Same as Fig. 5.8, but for SNM. The momentum distribution for neutrons is shown.

The (normal) Gorkov spectral function

$$S^{11}_{\alpha}(\omega) = \sum_{q} \left|\bar{\mathcal{V}}^{q}_{\alpha}\right|^2 \delta(\hbar\omega + \hbar\omega_{\alpha,q}) + \left|\mathcal{U}^{q}_{\alpha}\right|^2 \delta(\hbar\omega - \hbar\omega_{\alpha,q}), \tag{5.3}$$

is conveniently represented as a two-dimensional map. Each panel of Fig. 5.11 shows a different SNM spectrum. Increasing densities ($\rho = 0.08, 0.16, 0.24, 0.32\,\mathrm{fm}^{-3}$) are shown from the top to the bottom for NNLO$_{\rm sat}$ (450) (left) and ΔNNLO$_{\rm go}$ (394) (right). On the horizontal (vertical) axis the wave number (energy) is reported. The Fermi momentum and the chemical potential are denoted by the dash-dotted (vertical) and dashed (horizontal) lines, respectively. The quasiparticle and quasihole energy poles, that are obtained from the frequencies as $\epsilon_{\alpha,q} = \mu + \hbar\omega_{\alpha,q}$ ($\epsilon_{\alpha,q} = \mu - \hbar\omega_{\alpha,q}$), have spectral strengths $|\mathcal{U}^{q}_{\alpha}|^2$ ($|\bar{\mathcal{V}}^{q}_{\alpha}|^2$). Color scales are reported next to each plot. Also, the HF energies are shown as crosses. States with momenta to the left of the Fermi momentum are occupied at the HF level, while states to the right ($k > k_F$) are empty. The HF Fermi energy lies between the last occupied and the first unoccupied states.

Self-consistent calculations lower the chemical potential with respect to HF. As a consequence, the last occupied state acquires a significant $|\mathcal{U}|^2$ strength. A robust feature, that can be observed in all plots of Fig. 5.11, is indeed the presence of a pair of poles close to chemical potential ($\omega_q \approx 0$) with $|\mathcal{U}|^2$ and $|\mathcal{V}|^2$ of roughly comparable magnitude. This is consistent with the BCS phenomenology [202, 217], and confirms the trends of the momentum distributions of Fig. 5.9. The dependence of the occupation numbers as a function of the density, instead, remains unclear, since pairing effects look rather strong at densities above saturation for NNLO$_{\rm sat}$, e.g. the highest occupied state is predominantly a quasiparticle ($|\mathcal{U}|^2 \gg |\mathcal{V}|^2$) and the second-to-highest has a mixed particle-hole character. In contrast, for the ΔNNLO$_{\rm go}$ (394) interaction the impact of

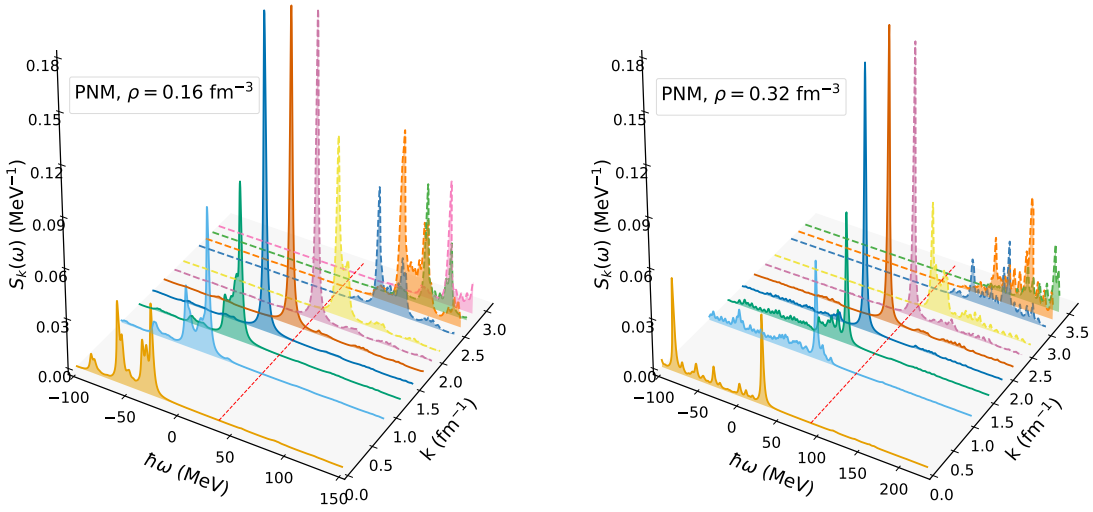

Figure 5.10: Three-dimensional representation of the PNM spectral functions at densities $\rho = 0.16\,\mathrm{fm}^{-3}$ (left) and $\rho = 0.32\,\mathrm{fm}^{-3}$ (right). Calculations are performed with the NNLO$_{\mathrm{sat}}$ (450) interaction using Dyson-ADC(3). Peaks are convoluted with a Lorentzian having a finite width $\Gamma = 1.5$ MeV for display purposes. The height represents the value of the spectral function for given momentum k and energy $\hbar\omega$. The vertical sections identify the groups of momentum k. Quasihole and quasiparticle states are shown with continuous and dashed lines, respectively, and they are separated by the Fermi energy, given by a red dashed line at constant frequency. The same vertical scale is used in both plots to ease the comparison. Momentum and energy axes, instead, are different.

Gorkov corrections is strongest at $\rho = 0.08\,\mathrm{fm}^{-3}$, and is less evident at larger densities. A detailed microscopic study of pairing in zero-temperature nuclear matter (momentum distributions, spectral functions, as well as pairing gaps) is outside the scope of this thesis, but is an interesting application of the SCGF formalism here developed, see e.g. [220, 228].

Finally, we compare our calculations with those performed with the coupled-cluster method at the level of the double (CCD) [126] [2]. The CCD method is a basis expansion technique that employs the same discretization of the continuum and the same model space as our ADC-SCGF (see also App. D.4). In Fig. 5.12, calculations performed with ADC(3) with Gorkov corrections (Gorkov-Cen) and CCD are shown for both NNLO$_{\mathrm{sat}}$ (450) (left) and ΔNNLO$_{\mathrm{go}}$ (394) (right) in PNM (top) and SNM (bottom). As in Fig. 5.6, correlation energies per particle are reported in the insets, where also MBPT(2) energies are plotted. A very close agreement between the two methods is found in PNM, while discrepancies are larger in SNM, of the order of 500 keV/A. In general, CCD provides a more repulsive correction to MBPT(2) than ADC(3). The latter occasionally lowers MBPT(2), as e.g. in SNM at and above saturation with ΔNNLO$_{\mathrm{go}}$ (394). In passing, it can be appreciated that correlation energies are much smaller for the ΔNNLO$_{\mathrm{go}}$ interactions and the convergence of many-body calculations is thus faster. Note that ADC(3) includes more correlations than CCD, and a more rightful comparison should be done with coupled-cluster including triples [CCD(T)] [126]. However, as these calculations are presently unavailable to us [3], this is left for future studies.

[2] We thank Weiguang Jiang for helping us in implementing the interactions and in checking our method, as well as providing us with the CCD results.

[3] We have written our own implementation of CCD following Refs. [14, 126] and benchmarked it successfully with the results by the Göteborg-Oak Ridge collaboration [106, 126]. However, a similar test for CCD(T) is still to be done.

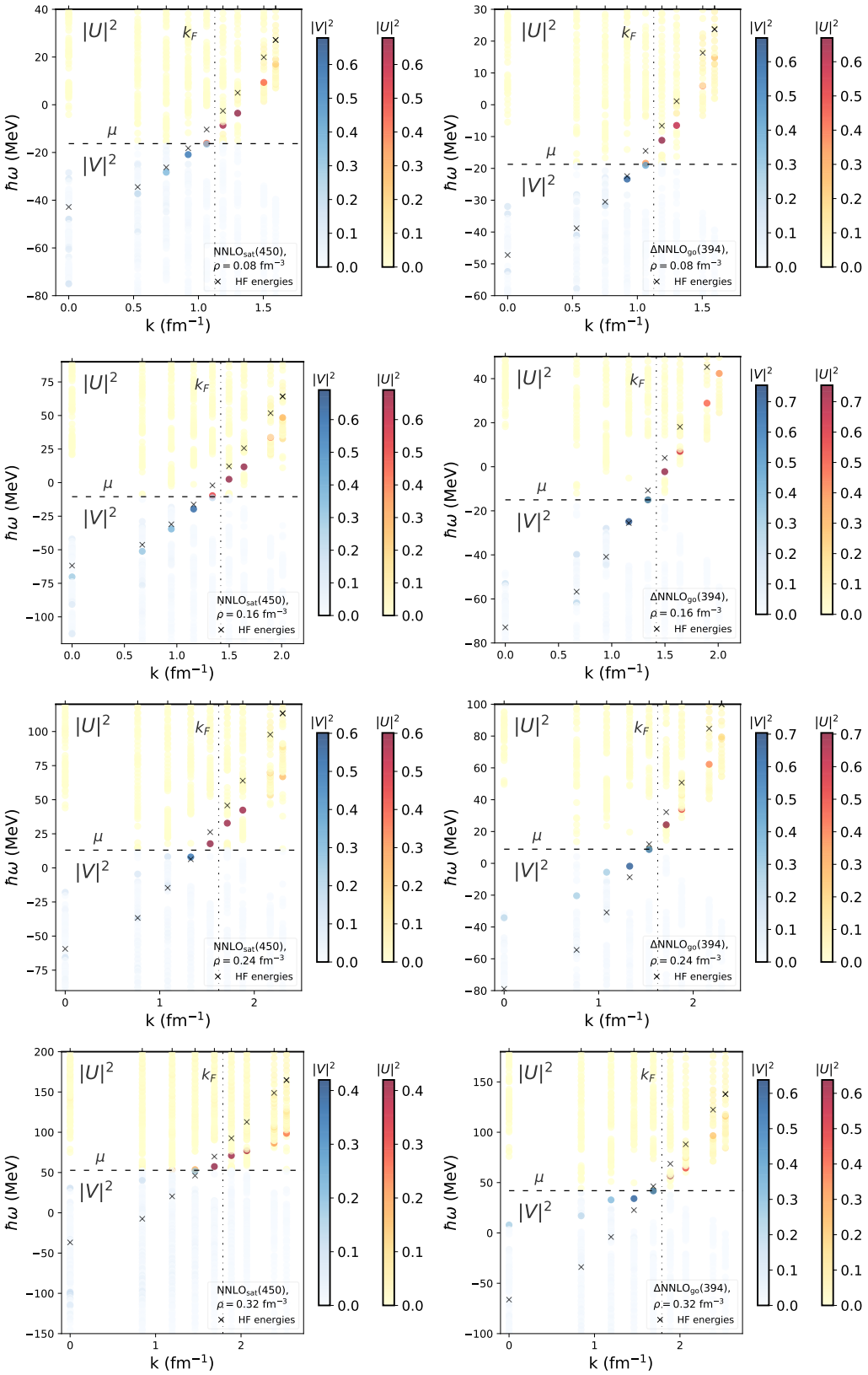

Figure 5.11: Gorkov spectral functions in SNM. The eight panels report a two-dimensional representation of the spectral functions from Gorkov-Cen ADC(3) calculations performed with the NNLO$_{\rm sat}$ (450) (left) and ΔNNLO$_{\rm go}$ (394) (right) potentials at four densities (from top to bottom: $\rho = 0.08, 0.16, 0.24, 0.32\,\mathrm{fm}^{-3}$). The momentum (energy) is reported on the horizontal (vertical) axis. The Fermi momentum k_F and the chemical potential μ are also shown as vertical (dash-dotted) and horizontal (dotted) lines, respectively. The squared amplitudes $|\mathcal{U}|^2$ and $|\mathcal{V}|^2$ are shown for the poles ($\epsilon_{\alpha,q}$) above and below the Fermi level, respectively. The color scale is found next to each plot. HF s.p. energies are represented by crosses.

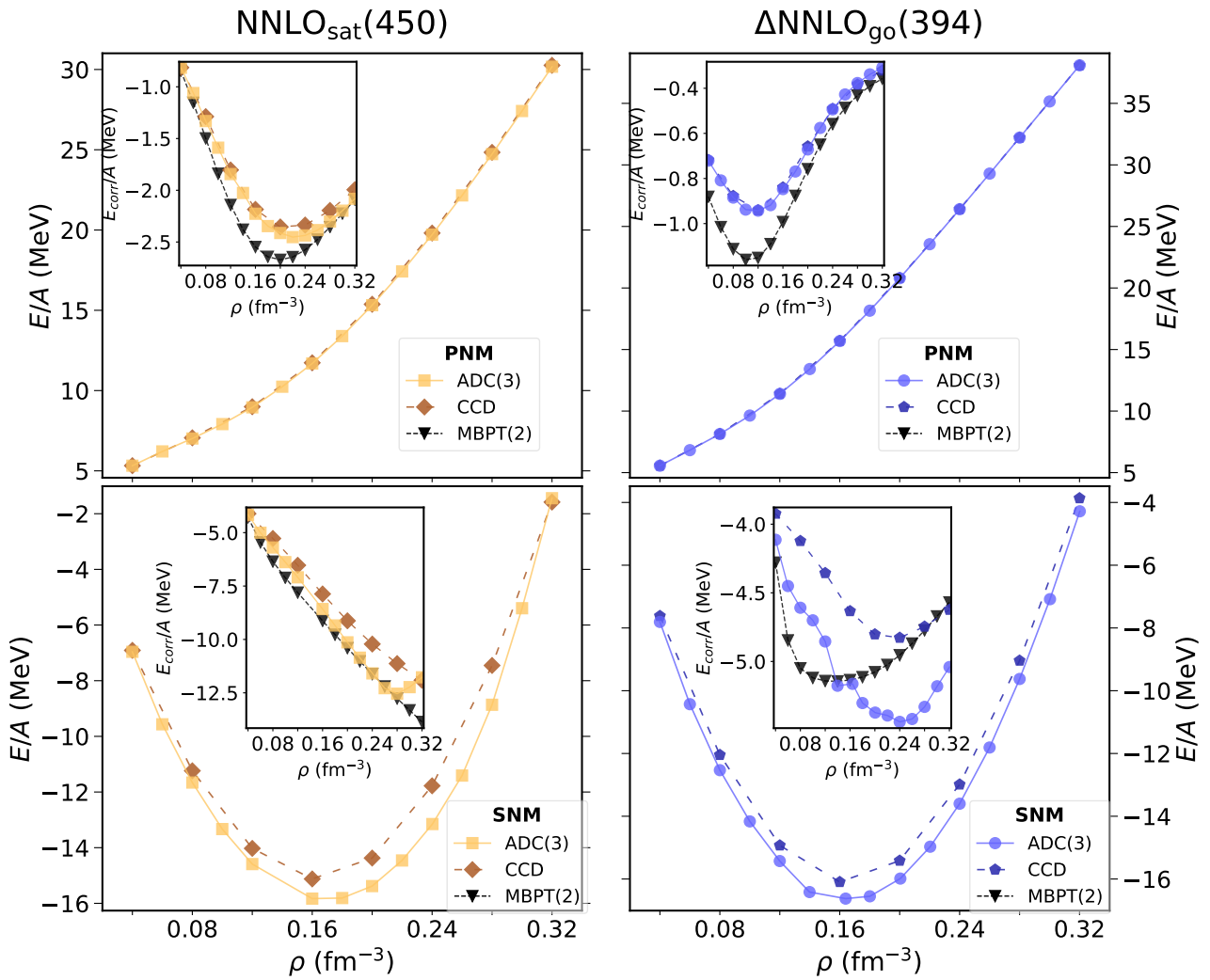

Figure 5.12: EOS in PNM (top) and SNM (bottom) with the NNLO$_{\text{sat}}$ (450) (left) and ΔNNLO$_{\text{go}}$ (394) (right) interactions. Results obtained with ADC(3) with Gorkov corrections (Gorkov-Cen) and with CCD are reported. Insets: correlation energy per particle. MBPT(2) energies are shown as black triangles. Lines are a guide to the eye.

CHAPTER 6

Results for *ab initio*-based EDFs

In this Chapter, we present the *ab initio*-constrained EDFs that are based on the nuclear matter EOS of Ch. 5 [1]. In particular, in Sec. 6.1 we discuss the LDA EDFs derived from the (2,3,4,5,6) and (2,5,6) parametrizations of the $\mathrm{NNLO_{sat}}$- and the AV4′+UIX$_c$-based EOS presented in Sec. 5.2 and 5.1, obtained respectively with the Finite-T SCGF method and AFDMC with $N = 66$ neutrons in PNM and $A = 76$ or $A = 132$ nucleons in SNM. Then, in Sec. 6.2 empirical gradient terms are introduced on top of LDA.

The energy functionals are applied to closed-subshell nuclei and compared to experimental values, taken from Refs. [229, 230], and to *ab initio* results. Full *ab initio* calculations were performed with AFDMC for a set of nuclei up to ^{90}Zr in the case of the AV4′+UIX$_c$ interaction, while in the case of $\mathrm{NNLO_{sat}}$ the SCGF method was used up to ^{54}Ca. Additionally, the densities for ^{90}Zr are available.

6.1 LDA EDFs

The discrepancy between theoretical predictions and experimental values for the energies per nucleon (top) and the charge radii (bottom) are shown in Fig. 6.1 for $\mathrm{NNLO_{sat}}$ and the (2,3,4,5,6) EDF, as well as the GA-E and GA-r EDFs introduced later on (Sec. 6.2). On the one hand, we can appreciate that the $\mathrm{NNLO_{sat}}$ predictions obtained with SCGF are very close to the experiment. On the other hand, the LDA EDF, although less precise, exhibits interesting trends, since it enables to reproduce heavier nuclei, especially from ^{90}Zr on, in a realistic way, with deviations smaller than 1 MeV/nucleon and 0.05 fm for the energies and radii, respectively. This is quite remarkable, as the LDA EDF incorporates only information on uniform matter. Also, it is unsurprising that light systems are less amenable to a local density treatment since surface effects are known to play a larger role at small A's.

For the case of the AV4′+UIX$_c$ interaction, we report two sets of EDFs that have been obtained using the SNM EOS computed with $A = 76$ (Fig. 6.2) and $A = 132$ nucleons (Fig. 6.3), respectively. In both cases, the outcome is somewhat puzzling, since, while the *ab initio* results are overall decent, the LDA EDF (2,5,6) is rather far from the experiment. In comparison to Ref. [68], the new fitting protocol allows us to find a better quantitative description, but qualitative considerations are unchanged. As a general trend, LDA overbinds nuclei with respect to both experiment and AFDMC. At the same time, it predicts too small radii, that differ by about 0.5 fm from the experimental values. In addition, we do not observe a significant improvement in the quality of the results as the mass number increases. This is at variance with the case of the $\mathrm{NNLO_{sat}}$ potential. The general features of the *ab initio*-based EDFs are the same whether they are based on either $A = 76$ or $A = 132$ calculations for the SNM EOS. A comparison between the two sets of models is reported in Fig. 6.4. At the scale of this plot, we can note that results based on the $A = 132$ EOS are slightly closer to the experiment. In particular, binding energies in nuclei with the $A = 132$-based EDF are higher, which is consistent with the SNM EOS, where energies obtained with $A = 132$ are higher than with $A = 76$ (see Fig. 5.1).

Number densities are then shown for the representative nuclei ^{40}Ca (Fig. 6.5), ^{48}Ca (Fig. 6.6) and ^{90}Zr (Fig. 6.7). In the top left panel, the $\mathrm{NNLO_{sat}}$ case is considered. One can appreciate that the (2,3,4,5,6) EDF density profile closely resembles the one obtained from *ab initio*, although it features slightly wider oscillation. The case of the AV4′+UIX$_c$ interaction (top right) is more problematic. (We are showing the EDFs based on the $A = 76$ SNM EOS.) In all three cases, LDA predicts too large densities in the interior of the nucleus compared to AFDMC. This is compensated by a sharp decrease of $\rho(r)$ at the surface, with the net effect of producing too small radii, as discussed above. Note also that AFDMC densities are numerically unstable at very short radial distances. As described in Sec. 3.1.3, $\rho(r)$ is estimated by counting the number of walkers that lie within a thin spherical shell around r. As the shell volume grows approximately as r^2, relatively few configurations are to be found at a small distance. Thus, large statistical fluctuations are expected to affect the density close to $r = 0$. In the bottom panels, the *ab initio* densities weighted by the squared radius, $r^2\rho(r)$, are compared. The r^2 factor emphasizes that AV4′+UIX$_c$ and $\mathrm{NNLO_{sat}}$ predict rather different density surfaces for ^{40}Ca and

[1] This chapter is partially based on our paper [68], that has been extended in two respects. AFDMC calculations with $A = 132$ nucleons in SNM have been added. Also, the EOS parametrization has been slightly changed, as the finite-A kinetic energy (2.13) is used when fitting the AFDMC EOS. This is somewhat more accurate than using the TL kinetic energy, as has been done in [68].

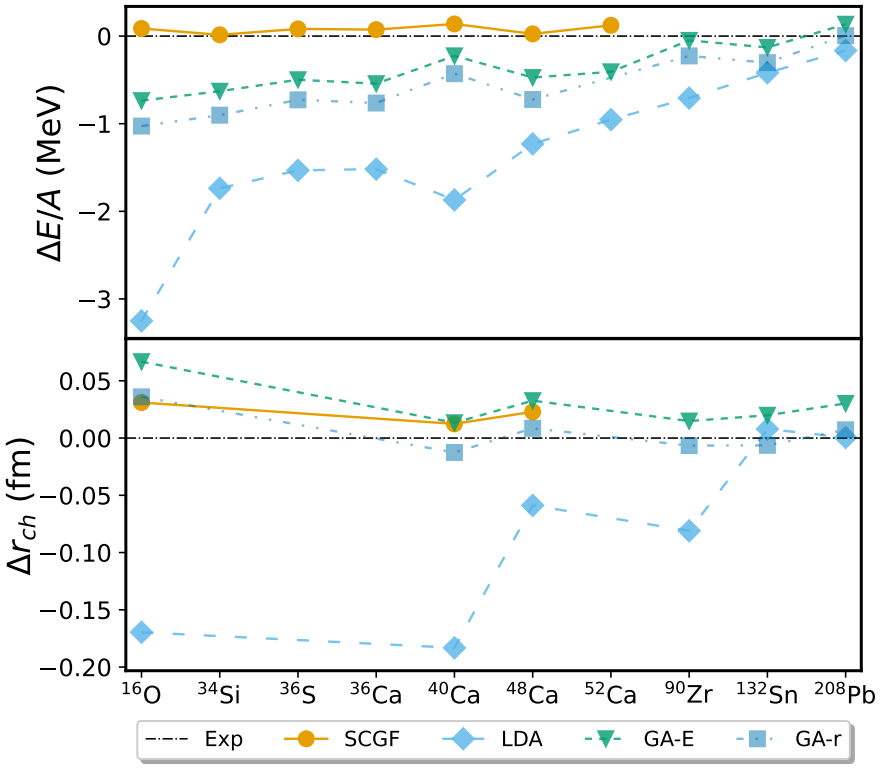

Figure 6.1: Discrepancy between the predicted energies per nucleon (top) and charge radii (bottom) and the corresponding experimental values for a set of closed subshell nuclei. Results obtained with the $\mathrm{NNLO_{sat}}$ interaction and with the LDA, GA-E and GA-r EDFs are shown. The LDA EDF is derived from the (2,3,4,5,6) model EOS. See text.

^{90}Zr, and in particular radii are smaller for the Argonne 4 interaction. Results are instead surprisingly similar for the case of ^{48}Ca. However, this is likely fortuitous, and in general, the radii predicted by Argonne 4 are smaller than the experimental ones.

6.2 GA EDFs

In this Section, we discuss the predictions that are obtained using the GA EDFs introduced in Sec. 2.2.2. These are defined complementing LDA with density-gradient and spin-orbit terms. Three parameters are introduces: two for the isoscalar ($C_0^{\Delta\rho}$) and isovector ($C_1^{\Delta\rho}$) gradient terms, and one (W_0) for the spin-orbit. The coefficients are tuned by grid-searching over physically reasonable intervals and the results for the four EDFs that yield the smallest rms errors on binding energies or charge radii, called GA-E and GA-r for short, are shown. The three parameters are measured in MeV fm^5; from now on, for simplicity the dimension is omitted.

In the case of the $\mathrm{NNLO_{sat}}$-based EDF (2,3,4,5,6), we have considered C_0^Δ and C_1^Δ in the intervals $[-45, 0]$ and $[0, 50]$ in steps of 5, while we have varied W_0 between 0 and 150 in steps of 10. The smallest rms error on the energy is obtained for ($C_0^\Delta = -35$, $C_1^\Delta = 10$, $W_0 = 140$), while charge radii are best reproduced for ($C_0^\Delta = -30$, $C_1^\Delta = 25$, $W_0 = 140$). The remarkable improvement over the LDA EDF can be appreciated by looking at energies and radii (Fig. 6.1). In Fig. 6.5, 6.6 and 6.7, the effect of the gradient terms on the number densities is made clear by the despite the oscillations which instead characterize the LDA densities. All considered, these GA EDFs are quite accurate, despite containing only three adjustable parameters, one of which (C_1^Δ) is of minor importance for the g.s. properties. The non-local part of the EDF is dominated by a single parameter, i.e. C_0^Δ, the isoscalar gradient term having a very strong impact on the orbitals and thus on all observables. Vice versa, C_1^Δ has a small impact on magic nuclei, whereas the choice of W_0 affects the binding energy in an almost perturbative way. A full-fledged optimization would be necessary to be truly competitive against the most sophisticated existing EDFs. However, the outcomes shown here are already encouraging.

In the case of AV4′+UIX$_c$-based EDFs, C_0^Δ, C_1^Δ and W_0 have been varied in the intervals $[-200, -60]$, $[0, 50]$ and $[0, 150]$. The best combination of parameters, which is optimal for both energies and radii, is the same for both $A = 132$ and $A = 76$, and is given by $C_0^\Delta = -150$, $C_1^\Delta = -50$, $W_0 = 0$. The corresponding PNM parameter is equal to $C_{PNM}^\Delta = -200$. We note that highly repulsive gradient contributions are favored. The GA EDFs perform significantly better than the LDA (2,5,6) EDFs. Surface terms are effective in improving the binding energies, which are brought less than 1 MeV/A from the experiment and quite close to AFDMC predictions

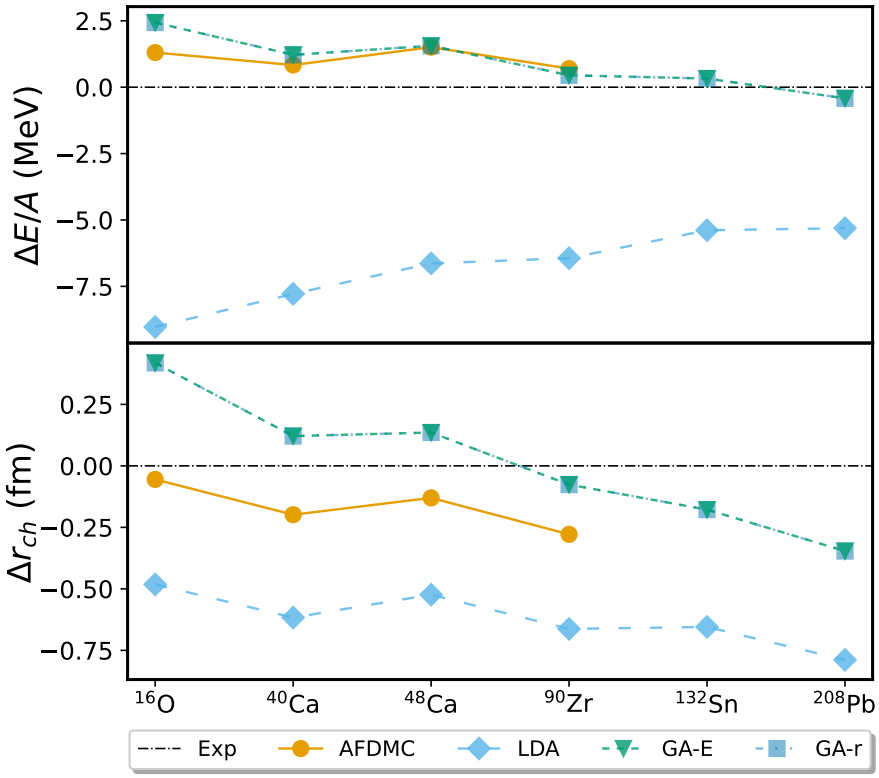

Figure 6.2: Same as Fig. 6.1, but for the AV4′+UIX$_c$ interactions. *Ab initio* calculations are performed with AFDMC, and the EOS on which the EDFs are based is obtained using $N = 66$ neutrons in PNM and $A = 76$ nucleons in SNM.

(top panel of Fig. 6.2). Note, however, that the scale is different from that of Fig. 6.1, and that NNLO$_{\rm sat}$-based EDF are nonetheless more accurate. Some problems persist, though, in particular concerning radii (bottom panel of Figs. 6.2 and 6.3), which are still inaccurate for the nuclear DFT standards. Also, peaks and minima in the number density cannot be reproduced by the EDFs, which are unable to describe the detailed shell structure of these nuclei. Finally, small differences are observed for the two different numbers of nucleons used to simulate SNM (Fig. 6.4). This is encouraging in perspective, as it implies that the finite-size effects on the EOS affect our methodology for *ab initio*-based EDFs mildly.

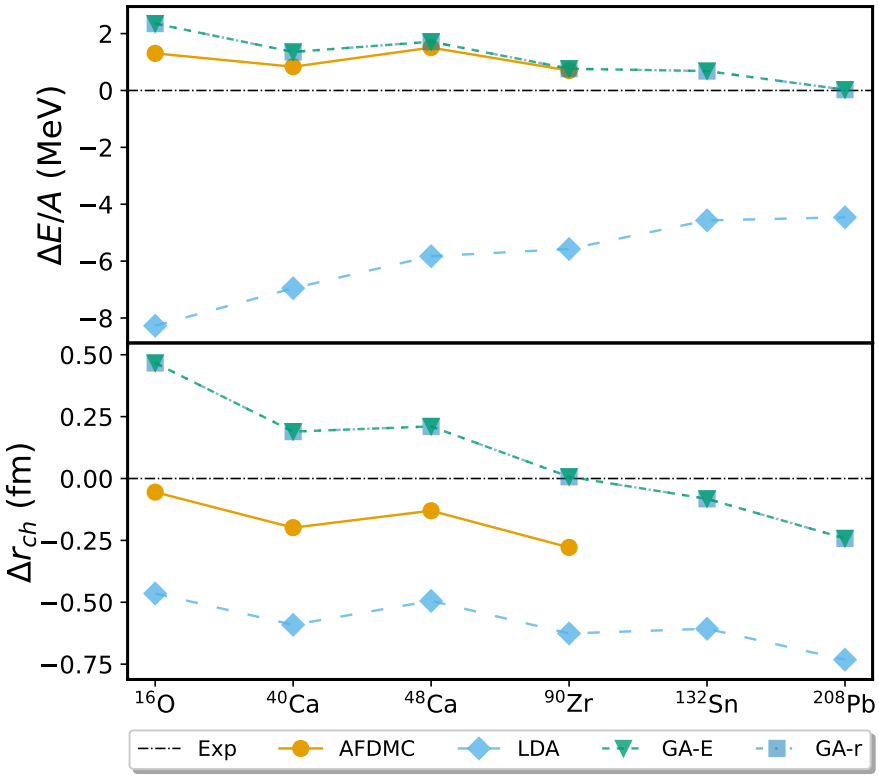

Figure 6.3: Same as Fig. 6.2, but in this case the SNM EOS has been obtained using $A = 132$ nucleons.

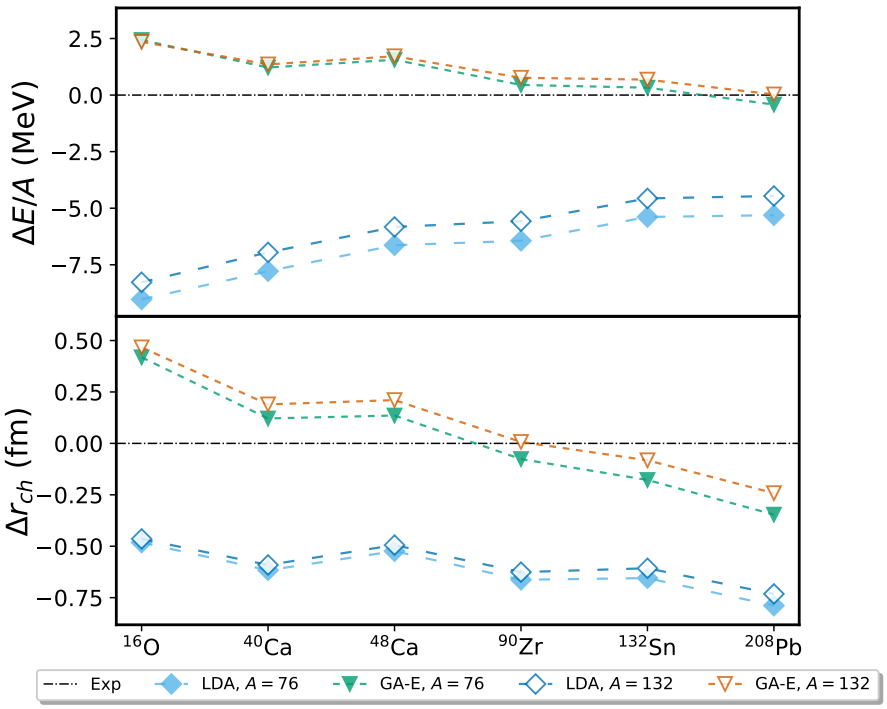

Figure 6.4: Same as Fig. 6.1, but in this case predictions by the LDA and GA-E EDFs based on the AV4′+UIX$_c$ EOS obtained in SNM with $A = 76$ or $A = 132$ are compared.

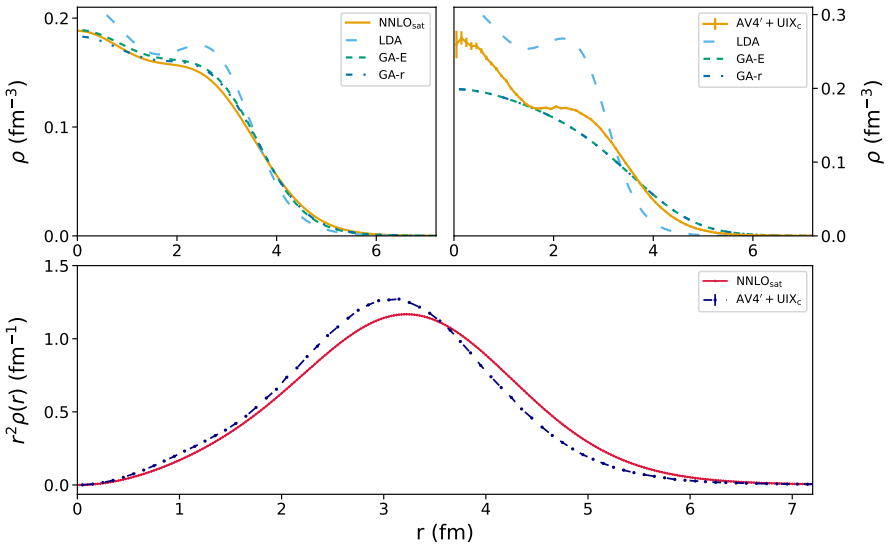

Figure 6.5: *Ab initio* and EDF (LDA, GA-E and GA-r) number densities, $\rho(r)$, for ^{40}Ca computed using the NNLO$_{\rm sat}$ (top left) and AV4′+UIX$_c$ (top right) Hamiltonians. See text for details. Note that for the AV4′+UIX$_c$ case the GA-E and GA-r curves overlap closely. Bottom: ab initio number densities times the squared radius, $r^2\rho(r)$, obtained with NNLO$_{\rm sat}$ (full line) and AV4′+UIX$_c$ (dotted). Taken from Ref. [68].

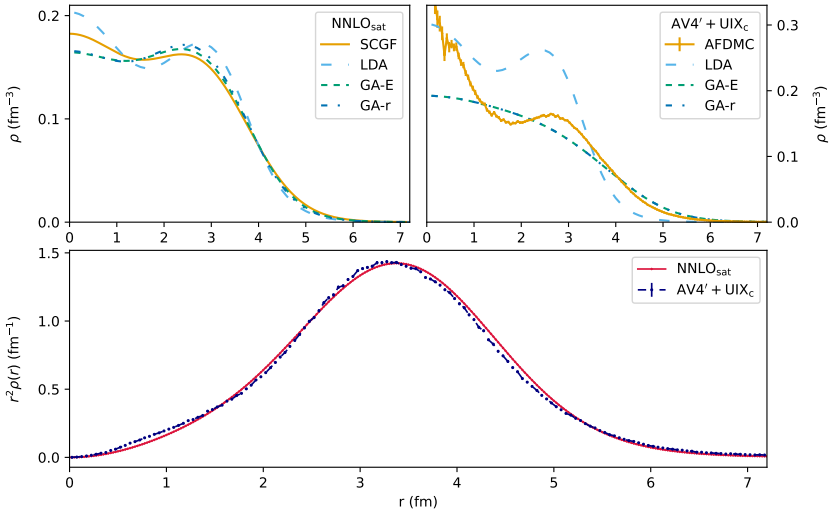

Figure 6.6: Same as Fig. 6.5, but for the ^{48}Ca nucleus. The EOS for the AV4′+UIX$_c$ interaction has been obtained using $A = 76$ nucleons in SNM.

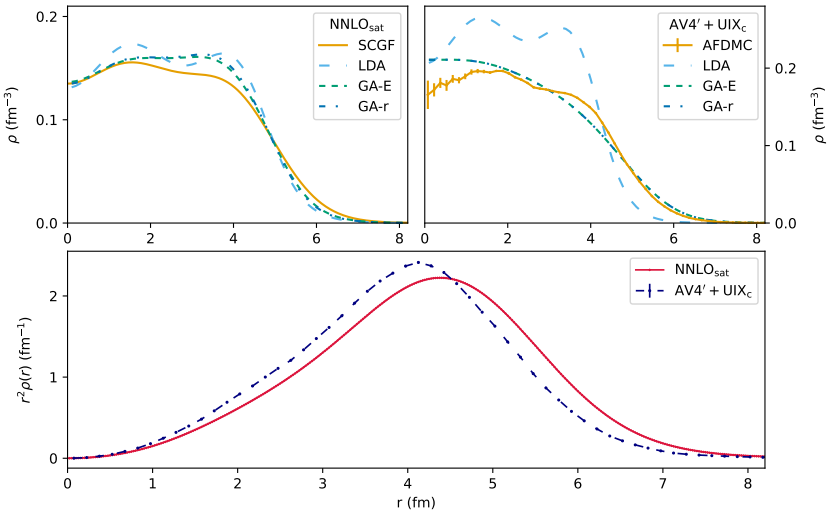

Figure 6.7: Same as Fig. 6.5, but for the ^{90}Zr nucleus.

CHAPTER 7

Results for perturbed nuclear matter within DFT

In this Chapter, the DFT method described in Sec. 2.3 is applied to calculate the EOS and the static response of infinite nuclear matter. The material presented is largely based on our paper Ref. [80].

The popular SLy4 EDF [43] is used when not stated otherwise, and examples of perturbed matter calculations are typically performed at a reference density of $\rho_0 = 0.16$ fm^{-3}. DFT energies are converged within a tolerance of 1 keV per nucleon. Perturbation strengths are measured in units of the Fermi energy of the corresponding system (v_q/E_F). We plot the static response function in the form $-\chi(q)/\rho_0$ (in MeV^{-1}), which is everywhere positive. Momenta are reported either in units of the Fermi momentum (q/q_F) or as integer multiples of the minimum allowed momenta ($q_{min} = 2\pi/L$).

The chapter is structured as follows. In Sec. 7.1, the nuclear matter EOS is studied. In Sec. 7.2, the static response of the free Fermi gas is considered. Finally, in Sec. 7.3 our method is applied to the study of the DFT response.

7.1 EOS

As a first application, the EOS is studied in both SNM (Fig. 7.1) and PNM (Fig. 7.2). The TL EOS is shown as a solid line, while calculations with $A = 132$, 16676 nucleons and N =66, 8338 neutrons, respectively, are reported as symbols. Multiples of 33 particles are commonly used in infinite matter studies, because the kinetic energy per particle of FG made of $33g$ particles is rather close to TL FG energy (see Ref. [75], Fig. 1). As a prototypical large-A system, we use a number of nucleons equal to 4169 times the spin/isospin degeneracy g, which corresponds to filling up all the momentum shells of the FG up to $n^2 = n_x^2 + n_y^2 + n_z^2 = 100$. Moreover, the insets in Figs. 7.1 and 7.2 show the relative difference (in percentage) between the finite-A and TL EOS as a function of the density ($\Delta e/|e| = (e_A - e_{TL})/|e_{TL}|$). Indeed, the results of the large-A calculations turn out to be practically indistinguishable from the TL curve and provide a strong check on the correctness of numerical calculations. It can also be appreciated that the $N = 66$ and $A = 132$ EOS give energies rather close to the TL EOS. Discrepancies amount to no more than 2 % in PNM over the considered range of densities. In SNM they remain within 2% up to $\rho = 0.26$ fm^{-3}, then they display a tendency to grow as the density further increases. At twice the saturation density, the difference has increased to roughly 6%. We suggest that the larger FS effects in SNM compared to PNM are a consequence of the stronger interactions in SNM. That is, choosing $A = 33g$ allows to approximate the TL kinetic energy effectively at all densities, but some FS effects on the potential energy persist and manifest themselves mostly in the highly correlated SNM in the high-density region. Nonetheless, the special usefulness of the "magic numbers" $N = 66$ and $A = 132$ is overall confirmed for DFT calculations.

7.2 Free response

A second study concentrates on the static response of the FG. The exact formula for $\chi_{0,N}$ [Eq. (1.23)] is applied in Fig. 7.3 for different numbers of neutrons and compared to the TL response (1.25). FS effects are rather strong at small or moderate momenta and manifest themselves as a non-monotonic behavior of $\chi_{0,N}(q)$ at finite N, while the TL response function is strictly decreasing in magnitude. For $q > 2q_F$, instead, the oscillations tend to disappear and the curves match rather well for all particle numbers. This qualitative change of behavior is due to geometric reasons, see e.g. the calculation of $\chi_0(q)$ in Ref. [115]: essentially, for $q > 2q_F$ any occupied momentum state can be scattered from the g.s. (the Fermi sphere) to an empty state and thus shell effects, that strongly affect the results at small q, are ineffective. The special role of $q = 2q_F$ is also signaled by the fact that the TL Lindhard function (1.25) is non-analytical at that point. Moreover, we note that the convergence to the TL as N is increased is relatively slow, and mild oscillations continue to persist up to very large N.

Then, the free response is computed numerically and compared to the analytical results. In particular, the FG response is determined by solving the Mathieu problem [75], i.e. the independent-particle problem of fermions subject to the external potential (2.26) (with the EDF potential terms turned off), for different momenta q and strengths v_q/E_F between 0.01 and 0.1 (with a step of 0.01). Then the energy differences δe_v

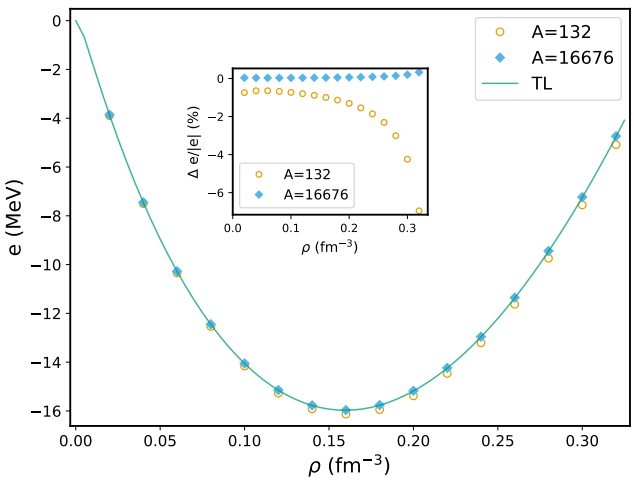

Figure 7.1: SNM EOS computed with the SLy4 EDF in the TL (line) and with a finite number of particles (symbols). Inset: relative difference (in percentage) between the finite-A and TL EOS as a function of the density.

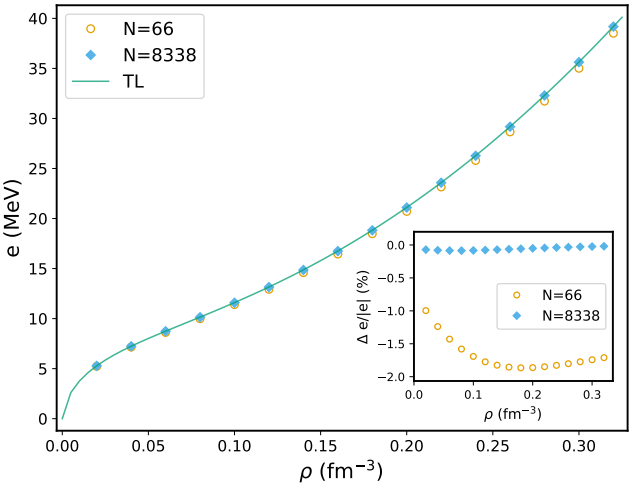

Figure 7.2: Same as Fig. 7.1, but for PNM.

are interpolated with the quartic formula (1.22) at each q. In Fig. 7.4, a comparison is drawn in the case of PNM with $N = 66$ neutrons between the exact response (filled squares) and the values obtained through the fitting procedure (empty diamonds). An almost perfect agreement is obtained, with a modest discrepancy only at the lowest momentum ($q/q_F \approx 0.5$). To better understand this deviation, in Fig. 7.5 we consider the ratio between the energy variation δe_v and the square of the perturbation strength v_q as a function of v_q/E_F. The exact response is shown as a hollow symbol at $v_q = 0$. If linear response theory were exact, at least in a certain range of small v_q, the ratio $\delta e_v/v_q^2$ would be constant. This is indeed verified for $q/q_{min} > 1$ over the whole interval considered, but at $q/q_{min} = 1$. a slight underestimation of the response is observed at all finite perturbations. This highlights that modest non-linear (fourth-order) contributions are present in the behavior of the system. Importantly, though, the ratio correctly converges to the exact response [$\delta e_v/v_q^2 \longrightarrow \chi_{0,N}(q)/\rho_0$] as $v_q \longrightarrow 0$.

7.3 Perturbed nuclear matter

Perturbed matter is now studied with the SLy4 EDF. First, a preliminary analysis of the convergence of the calculations with respect to the number of plane waves included in the basis is presented. Fig. 7.6, which reports calculations performed with $N = 66$ neutrons (density $\rho_0 = 0.16$ fm^{-3}) at $q/q_{min} = 1$ for a small ($v_q/E_F = 0.1$) and a moderate ($v_q/E_F = 0.25$) perturbation strengths, shows that in this case as few as 8 plane waves are sufficient to find energies converged within 0.1 keV or less. As a general rule, though, the number of plane waves required increases as a function of the momentum q of the perturbation and in practice we have found that a basis of 40 waves always yields converged results for 66 or 132 nucleons. When thousands of particles are considered, we raise the cutoff to 60 plane waves. Calculations remain very fast (a few seconds) even on a single processor. Then, the densities $\rho(z)$ as well as their Fourier components of PNM are shown in Figs. 7.7 and 7.8, respectively, for three perturbations that differ in strength and periodicity ($q/q_{min} = 1$ with strengths $v_q/E_F = 0.1$, 0.25 and $q/q_{min} = 2$ with $v_q/E_F = 0.1$). From the real space representation, one can appreciate that densities closely resemble cosine functions that oscillate around the unperturbed density with the same periodicity as that of the external perturbation [see Eq. (1.19)]. The Fourier analysis confirms that the response is essentially harmonic, as in all cases a single component at momentum q is clearly dominant with rather modest contributions beyond the linear regime. For completeness, the real-space densities (Fig. 7.9) and their Fourier components (Fig. 7.10) at reference density $\rho_0 = 0.16$ fm^{-3} are reported for SNM ($A = 132$) too. From a qualitative point of view, the behavior of SNM is the same as that of PNM, and the magnitude of the density fluctuation is very similar.

So far, we have always used particle numbers that correspond to a shell closure of the free Fermi gas and implicitly assumed that they are magic numbers for the perturbed system as well. This hypothesis proves true in general for weak potentials. Actually, its violation is a sign that the picture itself of a small perturbation of the homogeneous system is breaking down. In Fig. 7.11 the neutron level scheme of $N = 66$ PNM (same case as Fig. 7.7) is shown at two different perturbation strengths (both with momentum $q/q_{min} = 1$). We remind that the $\lambda = \pm 1$ energy eigenvalues are degenerate and we plot the s.p. energies only for $\lambda = +1$. The quantum numbers $\mathbf{n} = (n_x, n_y, n_z)$ ($0 \leq n_x \leq n_y$), and the number of nucleons corresponding to shell

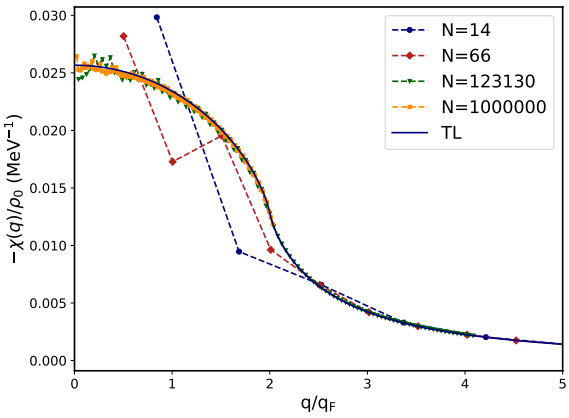

Figure 7.3: Dashed lines: free response function $-\chi_{0,N}(q)/\rho_0$ in PNM at ρ_0 =0.16 fm^{-3} as a function of q/q_F for different numbers of neutrons. Full line: response in the TL (Lindhard function).

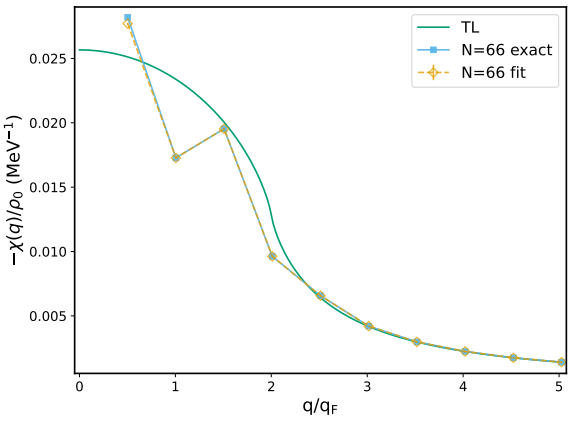

Figure 7.4: Static response $-\chi_{0,N}(q)/\rho_0$ of the FG as a function of q/q_F in PNM at a density $\rho_0 = 0.16$ fm^{-3}. The exact response (filled squares) and the response determined by a fit to the Mathieu energies (empty diamonds) are shown for $N = 66$ neutrons. For comparison, the TL response (Lindhard function) is also plotted.

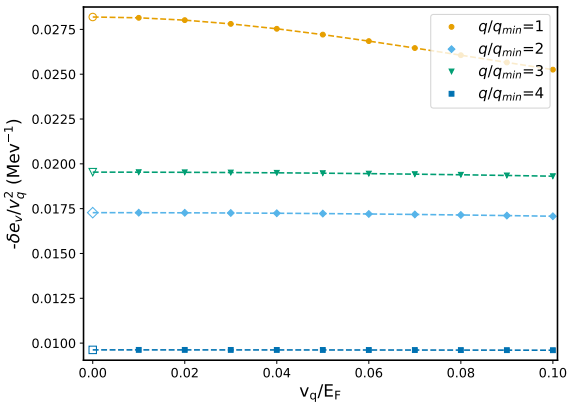

Figure 7.5: Ratio between the energy variation $-\delta e_v$ and the square of the perturbation strength v_q for the first four allowed moments (q/q_{min} between 1 and 4) for the same system as Fig. 7.4. Hollow symbols at $v_q = 0$ represent the exact value of -$\chi_{0,N}(q)/\rho_0$. Dashed lines are a guide to the eye.

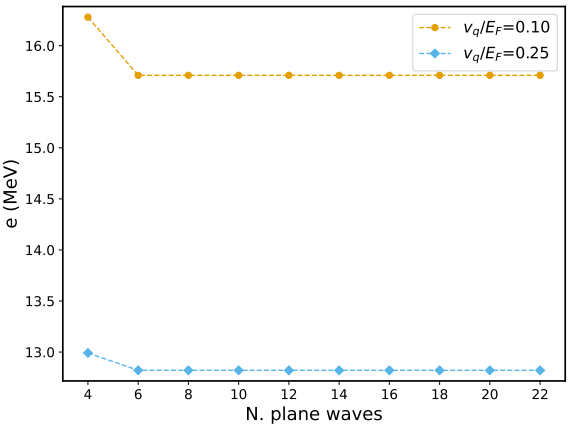

Figure 7.6: Energy per particle of PNM with $N = 66$ at $\rho_0 = 0.16$ fm^{-3} obtained with the SLy4 EDF as a function of the number of plane waves. Results are shown for the lowest momentum ($q = q_{min}$) for two different strengths of the external potential.

closures, are reported next to each level. Among the latter, the magic numbers of the FG are circled. In the case of the weaker potential, the effect of the perturbation is to partially lift the degeneracy of the free gas levels (as well as to lower the s.p. energies), as can be seen from the triplets or doublets of neighboring levels. The overall structure of the homogeneous system, though, is preserved and indeed all the FG magic numbers up to 33 are found in the perturbed system too. A markedly different picture appears for the stronger perturbation, where the level ordering of the FG is severely altered. One consequence is that a shell closure is found not for 33 nucleons but for 35. We suggest that the sudden changes in the slope of the energy as a function of the perturbation mentioned in Ref. [79] may be a side-effect of such 'shell-opening' effects. The key message is that care must be taken when studying perturbed finite-A matter and not only global properties (energy, density), but also the shell structure must be looked at. This was already noted in Ref. [74] concerning the AFDMC static response. For example, we warn that, if DFT or Mathieu orbitals are used to construct a reference state for Quantum Monte Carlo [75, 179], it is crucial to check that it be a closed-shell state, before embarking on expensive calculations.

Next, the static response function is discussed. The TL response of nuclear EDFs is known exactly [124] (App. C.3) and is now compared to the finite-A calculations in both SNM (Fig. 7.12) and PNM (Fig. 7.13). The numerical response functions for the large-A system are in very good agreement with the analytical predictions. The convergence to the TL is thus verified and we can appreciate by comparing to Fig. 7.3 that it is

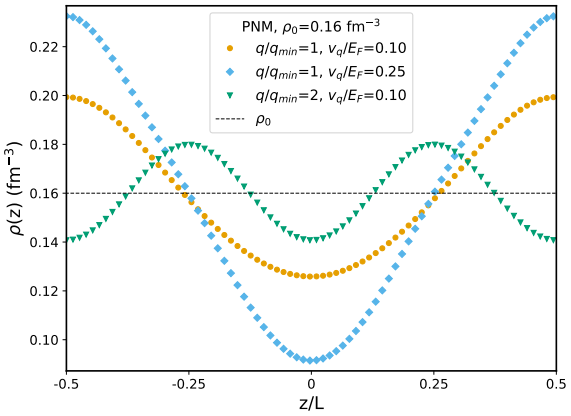

Figure 7.7: Densities $\rho(z)$ as a function of z/L in PNM ($N = 66$ neutrons) at a reference density $\rho_0 = 0.16$ fm^{-3} (dashed horizontal line). Densities for three perturbations, differing in strength and momentum (see legend), are shown as symbols.

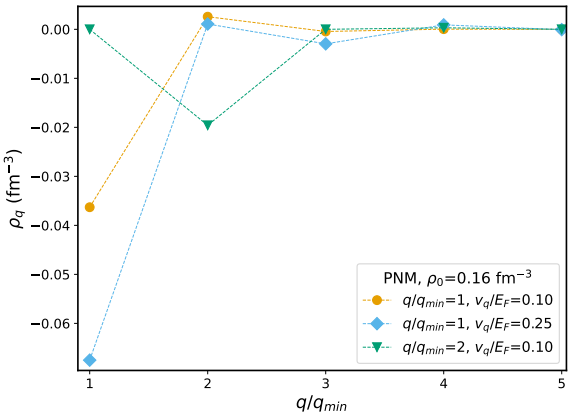

Figure 7.8: Fourier components ρ_q of the density fluctuations in the same cases as Fig. 7.7.

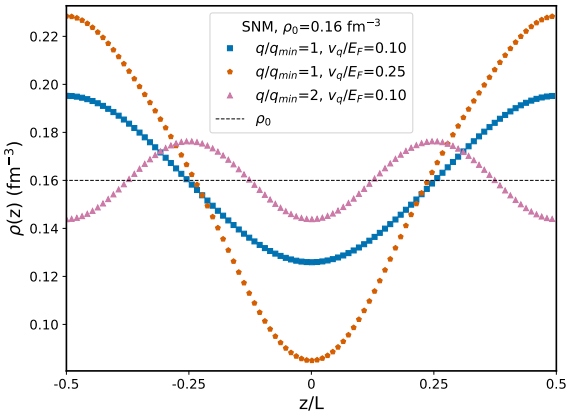

Figure 7.9: Same as Fig. 7.7, but for SNM with $A = 132$.

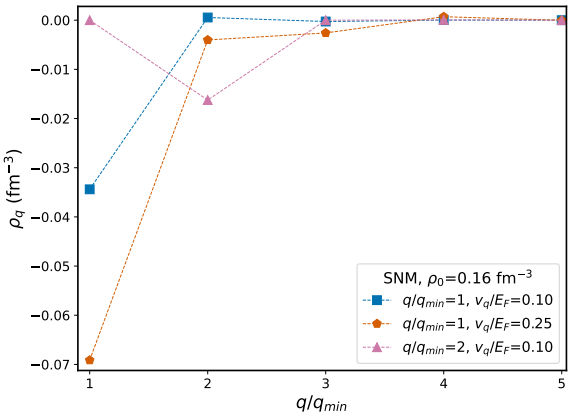

Figure 7.10: Same as Fig. 7.8, but for SNM with $A = 132$.

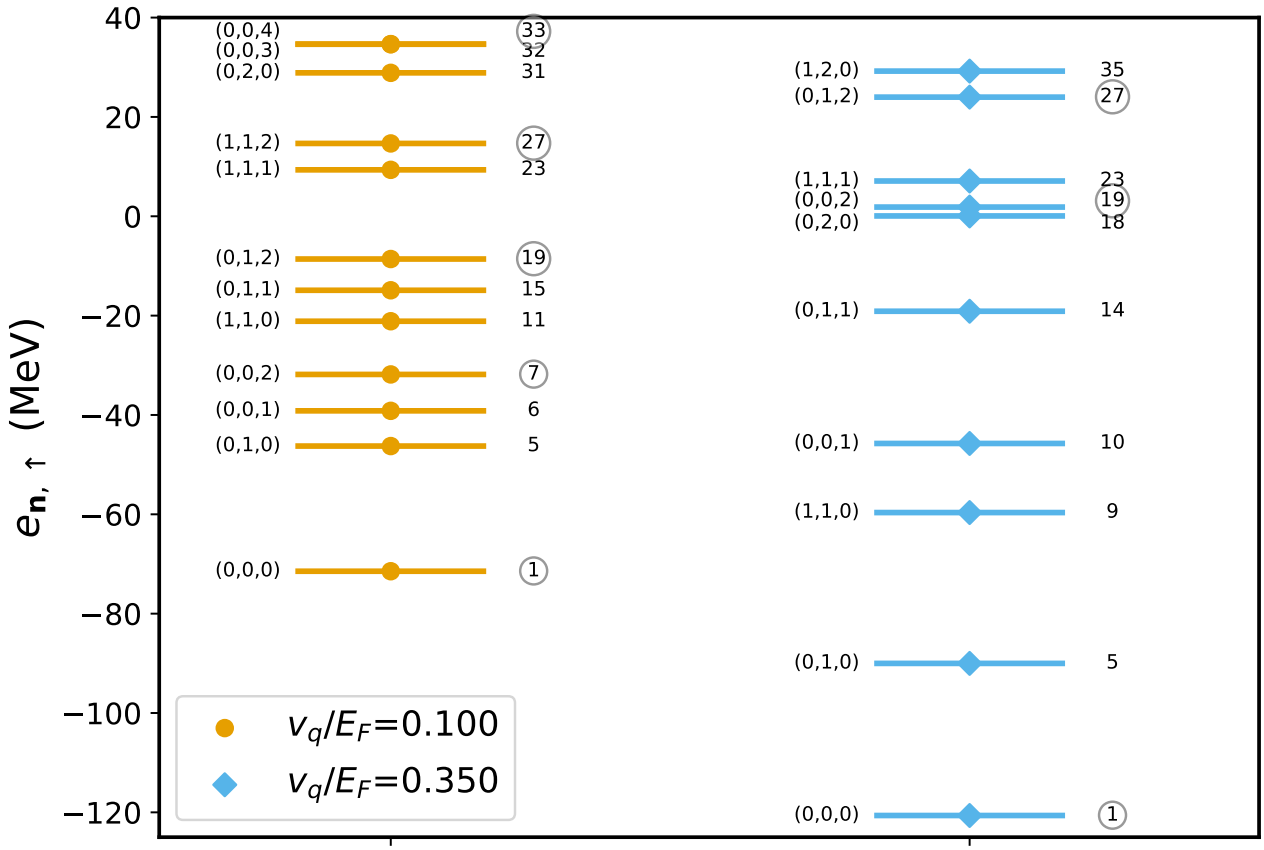

Figure 7.11: Level structure of $N = 66$ PNM. Two perturbation strengths (at momentum $q/q_{min} = 1$) are shown. The quantum numbers $\mathbf{n} = (n_x, n_y, n_z)$ of each level and the number of particles up to that shell are reported. Momentum-shell magic numbers of the FG are circled.

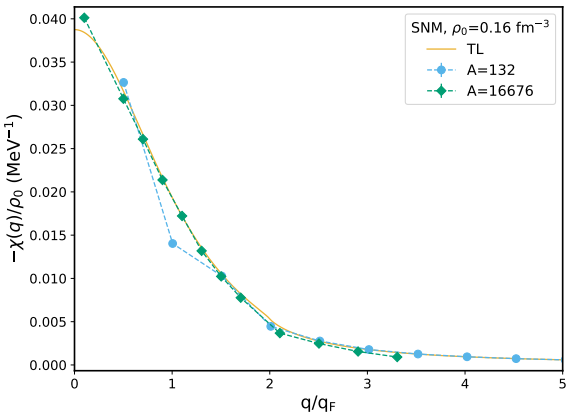

Figure 7.12: Static response of SNM at $\rho_0 = 0.16$ fm^{-3} obtained with the SLy4 EDF. The solid line represents the TL response, while symbols denote calculations for a finite number of particles ($A = 132$ and 16676).

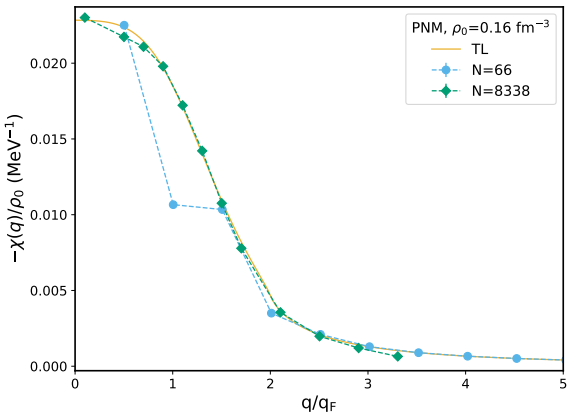

Figure 7.13: Same as Fig. 7.12, but for PNM. Calculations are performed with $N = 66$ and 8338 neutrons (symbols) and in the TL.

EDF	$C_0^{\nabla J}$	$C_1^{\nabla J}$	$C_{PNM}^{\nabla J}$
SLy4	-92.25	-30.75	-123
SkM*	-97.50	-32.5	-130
SkI3	-94.13	0	-94.13

Table 7.1: Spin-orbit coefficients for the SLy4, SkM* and SkI3 EDFs. All the parameters are measured in MeV fm^5.

definitely faster (as a function of the number of nucleons) in the interacting (DFT) system than for the FG. The small-A response, instead, is characterized by a non-monotonic behavior that is reminiscent of that of the free response, with marked fluctuations with respect to the TL function for $q < 2q_F$.

Lastly, we would like to understand the impact of the spin-orbit terms on the static response. Spin-orbit was neglected in Ref. [79] and its inclusion is one of the novelties of our work. The response computed with the full SLy4 EDF and for SLy4 with spin-orbit neglected, i.e. with $C^{\nabla J}$ set to zero, is reported for SNM (Fig. 7.14) and PNM (Fig. 7.15) both in the TL and for the usual $A = 132$ and $N = 66$ numbers of particles, respectively. One can appreciate that for the SLy4 EDF spin-orbit has the main effect of lowering the magnitude of $\chi(q)$ at all momenta, both in the TL and in the finite systems and, while in SNM it constitutes a small correction, in PNM it is a significant effect. While the qualitative picture of Ref. [79] is not altered fundamentally, quantitative results may change noticeably. In particular, it is important to incorporate spin-orbit terms if one aims at constraining the EDF parameters using *ab initio* information. It must be noted, however, that the importance of the spin-orbit terms on the response is dependent on the adopted EDF, as it is apparent in the TL. A systematic analysis is outside the scope of this work, and to demonstrate our previous assertion we show the TL response in SNM (Fig. 7.16) and PNM (Fig. 7.17) for three representative Skyrme models (SLy4 [43], SkM* [231], SkI3 [232]). While SLy4 and SkM* predict qualitatively similar response functions, SkI3 is markedly different in two respects. First, the PNM response is smaller by a factor of 2 compared to the other EDFs. The SNM response is comparable in all cases, as the isoscalar coefficients that determine the SNM response are more tightly constrained than the isovector ones that enter the PNM response [5] (App. C.2.1 and C.3). PNM properties can differ significantly according to the EDF, as we comment also in App. B.4. Second, in SLy4 and SkM* the spin-orbit term has a qualitative impact on the PNM response. In the SkI3, instead, it represents only a small quantitative correction in both PNM and SNM. To understand this, in Tab. 7.1 we have reported the isoscalar and isovector spin-orbit coefficients, as well as the PNM coefficient $C_{PNM}^{\nabla J} = C_0^{\nabla J} + C_1^{\nabla J}$ (App. C.2.1), for the three EDFs. Also, we note that the spin-orbit parameter enters the TL response quadratically in the denominator of Eq. (C.42), where $X_{so} \propto C^{\nabla J}$. Then, we observe that all three EDFs considered have roughly equal isoscalar spin-orbit coefficients. However, in SLy4 and SkM* $\left|C_{PNM}^{\nabla J}\right| > \left|C_0^{\nabla J}\right|$, while in SkI3 $C_{PNM}^{\nabla J} = C_0^{\nabla J}$. This may help explain why spin-orbit impacts PNM more strongly than SNM for the first two models.

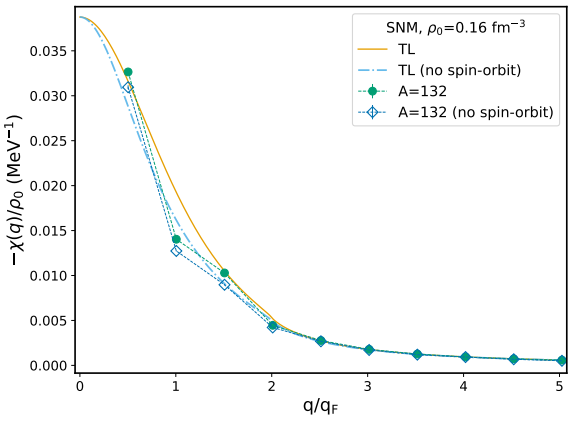

Figure 7.14: SNM static response obtained in the TL and for $A = 132$ nucleons with the full SLy4 EDF and SLy4 with spin-orbit terms neglected ('no spin-orbit' in the legend).

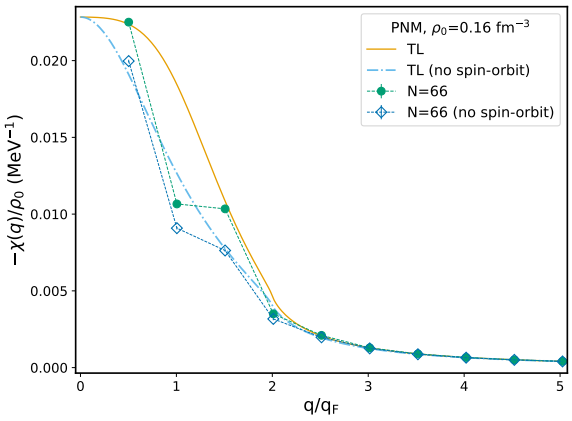

Figure 7.15: Same as Fig. 7.14, but for PNM with $N = 66$ neutrons.

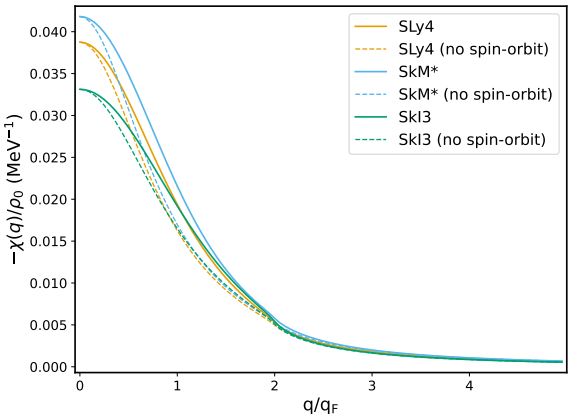

Figure 7.16: TL static response in SNM at density $\rho_0 = 0.16$ fm^{-3} obtained with three different EDFs, both with (solid line) and without (dashed line) spin-orbit terms.

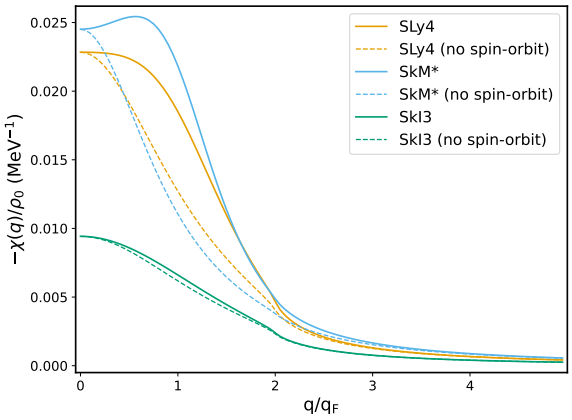

Figure 7.17: Same as Fig. 7.16, but for PNM.

CHAPTER 8

Results for perturbed nuclear matter within QMC

Perturbed nuclear matter studied with the *ab initio* AFDMC method is the subject of this Chapter. Calculations are presented, and their use as pseudo-data to tune the gradient terms of the nuclear EDF is discussed.

We summarize the strategy outlined in Sec. 2.2.2. First, the *ab initio* infinite matter EOS is used as input to construct a LDA EDF, see Ch. 5. Then, perturbed nuclear matter calculations are employed as the data to constrain the parameters of the GA EDFs built on top of LDA. SNM and PNM are essentially decoupled and can be studied separately. The isoscalar parameters of the GA EDF, i.e. $C_0^{\Delta\rho}$ and $C_0^{\nabla J}$, enter in SNM. PNM, instead, is sensitive to the sum of isoscalar and isovector coefficients, $C_{PNM}^{\Delta\rho} = C_0^{\Delta\rho} + C_1^{\Delta\rho}$ and $C_{PNM}^{\nabla J} = C_0^{\nabla J} + C_1^{\nabla J}$. The shorthand notation $C^{\Delta\rho}$, $C^{\nabla J}$ will be used in the following. Both $C^{\Delta\rho}$ and $C^{\nabla J}$ have units of MeV fm^5; in the following, the dimension is omitted for simplicity. We expect the density-gradient terms to provide a repulsive contribution to the energy (see e.g. App. B.2), thus we require $C^{\Delta\rho} < 0$.

To determine the optimal parameters of the GA EDF, then, we minimize a least-squares cost function that accounts for the difference between the AFDMC results and the DFT calculations of inhomogeneous matter (see Ch. 7). As the response properties are related to *differences* between the energies of perturbed and unperturbed matter ($\delta e_v = e(v) - e(v=0)$), we should aim at reproducing the *ab initio* energy variations (and not absolute energies) with our EDF models as best as possible.

This physical argument leads us to define the following cost function:

$$\chi^2(\mathbf{C}) = \sum_i \left(\frac{\delta e(x_i, \mathbf{C}) - \delta e_i}{\sigma_i} \right)^2 . \tag{8.1}$$

Here, δe_i denotes the energy differences in our *ab initio* data set; x_i is a shorthand, vector-like notation for the parameters that characterize the system [$x_i = (N_i, Z_i, \rho_{0,i}, q_i, v_{q,i})$], where N_i, Z_i are the neutron and proton numbers, $\rho_{0,i}$ the unperturbed densities, and $q_i, v_{q,i}$ the momenta and strengths of the external potential, respectively; $\mathbf{C} = (C^{\Delta\rho}, C^{\nabla J})$; and $\delta e(x_i, \mathbf{C})$ refers to the prediction of the EDF with parameters $\mathbf{C}$. We would like to stress that, while in general we could mix up results for different densities and/or nucleon numbers, in this work each fit is performed at a fixed reference density ρ_0 and number of fermions. σ_i represents the adopted error on the data points; we anticipate that we typically choose a uniform error $\sigma_i = \sigma = 100$ keV (independent of the strength and momentum of the external field). This value is somewhat larger than the typical AFDMC statistical error bars and is meant to take into account systematic uncertainties. We check that the results of the fit are unaffected by the precise values of σ.

As the optimization problem is highly non-linear, a scan of the parameter space is performed to identify reasonable initial parameters. Then, the fit is executed using the MINUIT library [166, 167]. In particular, a Nelder-Mead derivative-free algorithm (Simplex) is used in the first stage, and then the Migrad method is employed to refine the results. (A similar tactic was used e.g. in Ref. [233].) We expect $C^{\Delta\rho}$ to be the dominant parameter with respect to $C^{\nabla J}$. Moreover, while searching the parameter space we may find some unphysical combinations $\mathbf{C}$ for which the DFT solver struggles or fails to converge (see e.g. Ref. [234]). We have decided to simply drop not only non-convergent calculations, but also those cases where open-shell configurations are found (see Ref. [80]), as they typically lie well beyond the regime of linear response.

We first present original calculations for the static response of PNM with the AV4′+UIX$_c$ interaction (Sec. 8.1) and apply our method to this dataset. Then, a similar analysis is performed for the case of the PNM results obtained with the AV8′ + UIX interaction in Ref. [75] (Sec. 8.2). Finally, in Sec. 8.3 SNM is studied with the AV4′+UIX$_c$ potential; to our knowledge, these are the first *ab initio* calculations of the static response in symmetric matter.

8.1 Pure neutron matter with the Argonne 4 interaction

We have performed AFDMC calculations of perturbed PNM with the AV4′+UIX$_c$ interaction at the reference densities $\rho_0 = 0.16$ fm^{-3} and 0.10 fm^{-3}. In both cases, we have considered the first four allowed momenta of

the potential. The following strengths have been used in the $\rho_0 = 0.16$ fm^{-3} case: $v_q/E_F = 0.05, 0.1, 0.125, 0.15$. For $\rho_0 = 0.10$ fm^{-3}, we have considered $v_q/E_F = 0.1, 0.15, 0.2$ to ease the comparison with Argonne 8 calculations at the same density (Sec. 8.2). For each combination of q and v_q a full DMC computation has been performed. We have used the constrained propagation technique to mitigate the sign problem; this is deemed accurate for the Argonne 4 interaction, which does not include tensor or spin-orbit operators [127]. The trial wave function is made of a Slater determinant of Mathieu orbitals, on top of which central correlations, as well as linear correlations for the operators $\boldsymbol{\sigma}\cdot\boldsymbol{\sigma}$, $\boldsymbol{\tau}\cdot\boldsymbol{\tau}$ and $(\boldsymbol{\sigma}\cdot\boldsymbol{\sigma})(\boldsymbol{\tau}\cdot\boldsymbol{\tau})$, are included (see Sec. 3.3). In a typical run, about 2000 walkers are employed and 100 blocks of 50 steps each are sampled.

Our variational ansatz has been accurately tested. Mathieu orbitals have been generated with the DFT method detailed in Ch. 7, in the special case in which only the external potential (2.26) (but no mean field) is included, and extensively validated. Then, we verified that using Mathieu orbitals instead of plane waves allows to lower the VMC and DMC energies of the interacting system. In Fig. 8.1, a comparison between results obtained either using plane waves or Mathieu orbitals at the level of both VMC and DMC is reported. We can appreciate that the Mathieu ansatz improves the estimates of the energy significantly. The effect is evident also in DMC and tends to increase as the perturbation gets stronger.

A second interesting observable is the density $\rho(z)$ of perturbed matter (see Sec. 3.1.3). In Fig. 8.2, we compare in a representative case ($q/q_{min} = 1$, $v_q/E_F = 0.1$) the densities obtained at the VMC and DMC level of the Monte Carlo calculation, respectively. The trial wave function can capture the non-uniform behavior of the density already at the VMC level (empty circles). In particular, we can clearly recognize that $\rho(z)$ has the same periodicity as the external potential. This is the correct behavior when the perturbation is weak. The qualitative picture is consistent with the final DMC calculation (diamonds). The main effect of the diffusion process is to help reduce the statistical fluctuations that affect the density at different points, as it should be the case when a more accurate wave function is obtained. In light of these considerations, we are thus confident that our ansatz is adequate to properly treat perturbed matter.

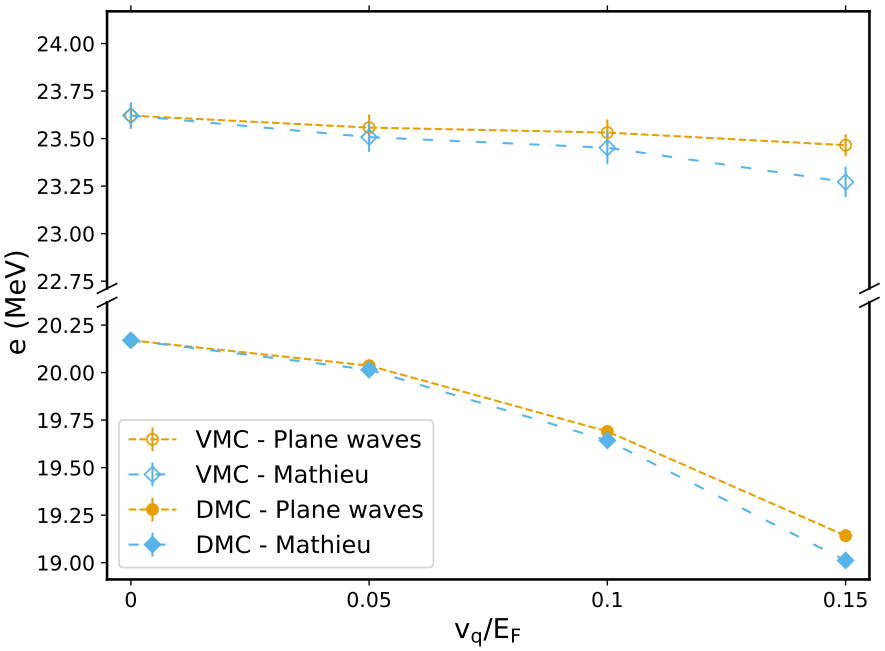

Figure 8.1: VMC (empty symbols) and DMC (full symbols) energies per particle, obtained starting from a reference Slater determinant of plane waves (circles) or Mathieu orbitals (diamonds), are shown as a function of the perturbation strength v_q/E_F. Calculations are performed in PNM at a reference density $\rho_0 = 0.16$ fm^{-3}. The external potential has momentum $q/q_{min} = 1$, and the AV4′+UIX$_c$ potential is used.

The fitting protocol has been described above. For each q and v_q, a DFT calculation has to be performed as described in Ch. 7. As mentioned before, we have assigned a uniform error σ =100 keV on the energies, independent of the strength and momentum of the external potential. Note that, in any case, the best-fit parameters are unaffected by the absolute value of the error.

We now present our results. AFDMC calculations and the predictions of the best GA EDF are reported for unperturbed densities of $\rho_0 = 0.16$ fm^{-3} and $\rho_0 = 0.10$ fm^{-3} in the left panels of Figs. 8.3 and 8.4, respectively. Solid (dashed) lines represent the predictions of the fits to the AFDMC (EDF) energies performed with Eq. (1.22) at each different q, which allows extracting of the static response $\chi(q)$ for $q \geq q_{min}$. The response functions $-\chi(q)/\rho_0$ thus obtained are shown in the right panels as a function of q/q_F. In that panel, error bars

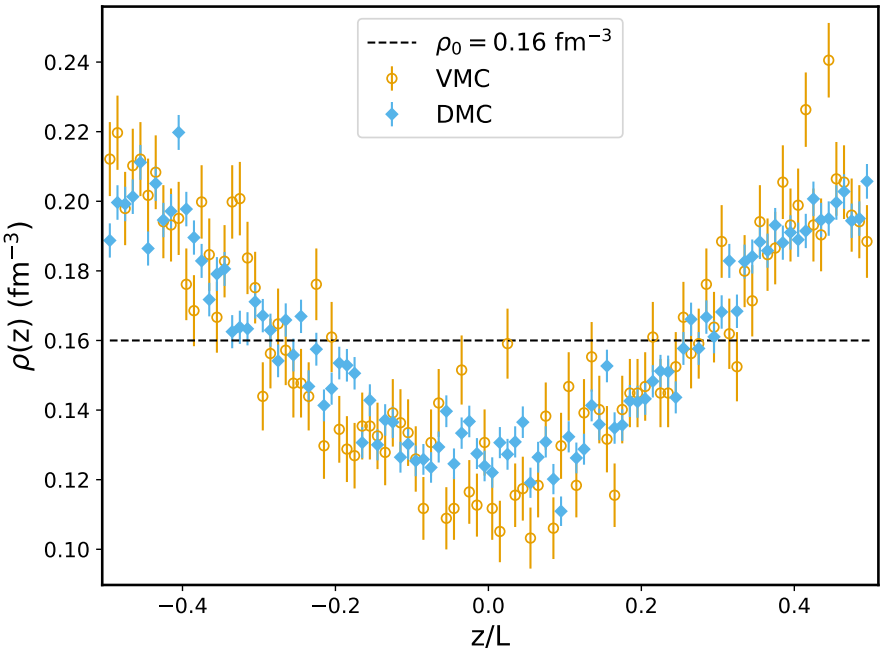

Figure 8.2: Density $\rho(z)$ as a function of the position z/L, where L is the box size, for PNM perturbed by a potential with momentum $q/q_{min} = 1$ and strength $v_q/E_F = 0.1$. The VMC (empty circles) and DMC (diamonds) results are shown. The unperturbed density is also reported as a dashed line. The AV4′+UIX$_c$ potential has been used.

represent the uncertainty on the fit parameters (note that in the EDF case they are smaller than the marker size). The response at zero momentum, instead, is derived from the parametrization of the EOS using the compressibility sum rule (CSR), see Eq. (B.54).

The results are unexpected, and the EDFs we obtain have unrealistic values of the coefficients. At $\rho_0 = 0.16$ fm^{-3}, we find for the best-fit model $C^{\Delta\rho} = -0.1 \pm 3$, $C^{\nabla J} = 30 \pm 40$. At $\rho_0 = 0.10$ fm^{-3}, we get $C^{\Delta\rho} = -45 \pm 5$, $C^{\nabla J} = 0 \pm 30$. Uncertainties, as provided by MINUIT tools, are rather large for the spin-orbit coefficient, which appears to be poorly constrained. This may be related either to the relatively small effect of the spin-orbit term on the perturbed matter energies or to the fact that the external perturbation couples to the density and does not probe the spin directly. However, issues mainly concern the $C^{\Delta\rho}$ coefficient. At $\rho_0 = 0.16$ fm^{-3}, it is compatible with zero. This is unacceptable on physical grounds, as it would mean that gradient corrections are not needed, and LDA is already the "best" EDF model, whereas this cannot be the case, as demonstrated by the results of Ch. 6. Rather, this fact shows that the information content of our perturbed matter data is insufficient to improve the LDA EDF. Note also that we have tried estimating the EDF parameters with different choices of the dataset (i.e. including only some periods of the perturbation or adding some higher-strength points), but with no impact on the conclusions. The value of the density-gradient parameter at $\rho_0 = 0.10$ fm^{-3} is larger, but still too small in relation to the study of empirical GA EDFs presented in Sec. 6.2. Also, the agreement with the *ab initio* response is not qualitatively better at $\rho_0 = 0.10$ fm^{-3}, as it is evident from Fig. 8.4. Furthermore, it is surprising to observe such a large difference for the $C^{\Delta\rho}$ parameters at the two different densities, since $C^{\Delta\rho}$ is usually taken constant in Skyrme EDFs.

The difficulties we have found call for some reflection. First, the unsatisfactory outcomes require to further investigate the QMC trial wave function, to rule out or confirm the possibility that the ansatz is not sufficiently rich. For this purpose, it is useful to compare our results with those obtained with other methods or wave functions. In particular, the trial states introduced by Lovato *et al.* in Ref. [188] [1] are among the most accurate available in AFDMC for PNM. The ansatz of [188] makes use of central Jastrow correlations parametrized by cubic splines, and the plane-wave Slater determinant is improved by including spin-dependent backflow correlations [197]. This is a rather sophisticated and flexible state that has proved very accurate in homogeneous matter. It does not contain information on the external potential, though. Thus, comparing the DMC results that are found starting from either "backflow" or "Mathieu" wave functions is useful to get an overall idea of the pros and limitations of the two models. This is done in Fig. 8.5, where the difference between perturbed and unperturbed energies, δe, is shown as a function of the perturbation strength v_q/E_F in the case of PNM at ρ_0= 0.16 fm^{-3}.

In light of Ref. [127], for the Argonne 4 interaction the constrained propagation is accurate, and thus no unconstrained propagation is performed. Note that we compare energy differences, since these determine the

[1] We thank Alessandro Lovato for sharing his calculations for the AV4′+UIX$_c$ interaction.

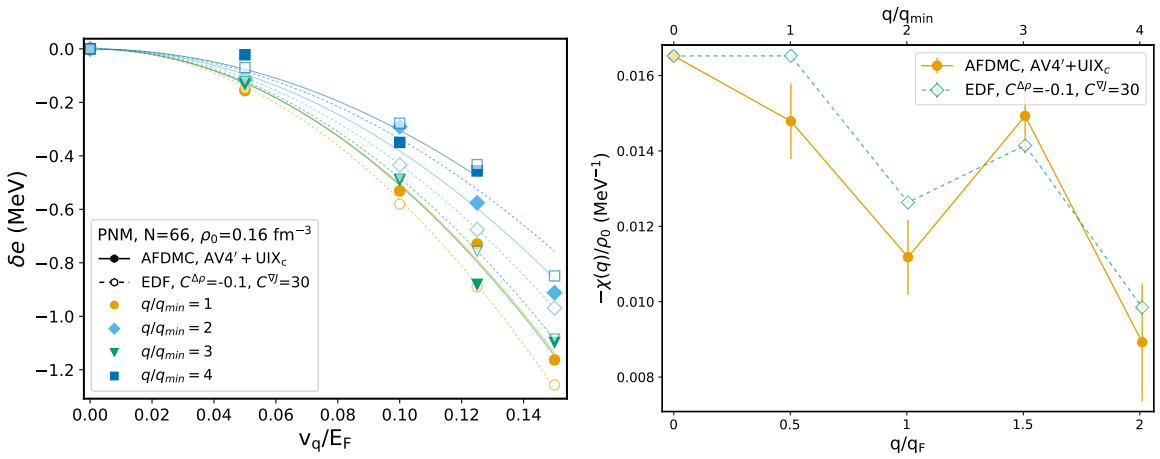

Figure 8.3: Left: AFDMC energies for the AV4′+UIX$_c$ interactions (solid markers) and predictions by the best-fit GA EDF (hollow markers) in PNM at a density $\rho_0 = 0.16$ fm^{-3} as a function of the strength of the external perturbation v_q/E_F for different values of the momentum q/q_{min}. The parameters $C^{\Delta\rho}$ and $C^{\nabla J}$ are reported in the legend. Solid (dashed) lines represent the predictions of fits to the AFDMC (EDF) perturbed energies, see Eq. (1.22).
Right: static response $-\chi(q)/\rho_0$ as a function of the momentum extracted from the AFDMC (filled markers) and EDF (empty markers) calculations. The momentum is expressed both in units of q_F (q/q_F, bottom) and in units of q_{min} (q/q_{min}, top). For $q/q_{min} \geq 1$, the response has been obtained by fitting the perturbed energies with Eq. (1.22). Error bars represent the uncertainty of the fit parameters. The response at zero momentum has been obtained using the CSR [Eq. (B.54)]. Lines are a guide to the eye.

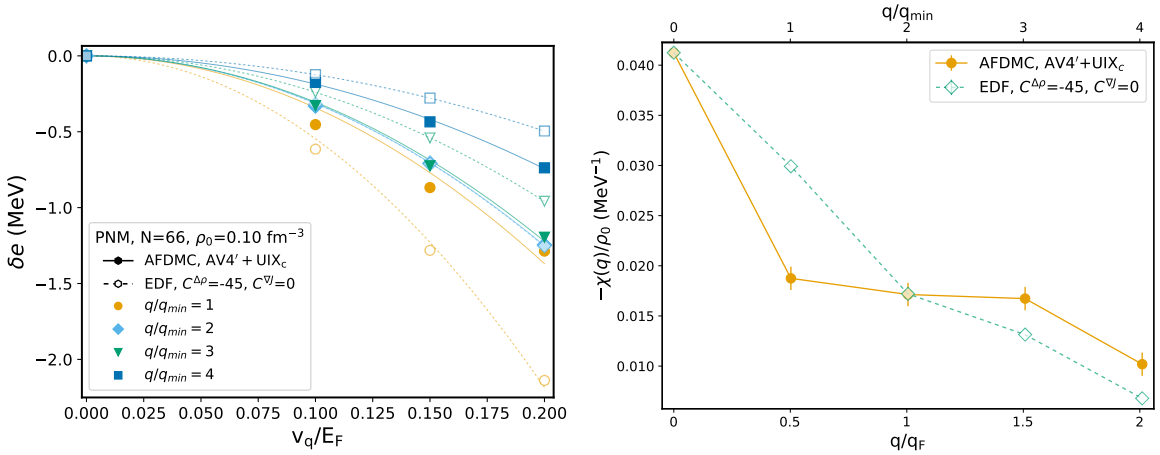

Figure 8.4: Same as Fig. 8.4, but for PNM at the unperturbed density $\rho_0 = 0.10$ fm^{-3}.

response properties; in the homogeneous system, the spline-based wave function yields a lower unperturbed energy. Also, a cancellation of errors is expected to make energy differences less sensitive to the details of the trial states. We appreciate that for modest intensities of the perturbation the two sets of calculations are compatible within the statistical error bars. At the highest strength shown ($v_q/E_F = 0.15$), instead, using Mathieu orbitals enhances the effects of the perturbation compared to the backflow wave function. Thus, our ansatz compares well with the recently introduced wave functions of Ref. [188] in the regime of almost uniform matter, where the latter are expected to be accurate, and, by incorporating the effect of the perturbation in its reference state, it improves upon it for stronger external potentials. We also comment that the ansatz used by Gezerlis *et al.* [75, 235] is slightly simpler than ours, as it lacks operator correlations. However, while these are rather important for SNM, they are expected to be of little impact in PNM in the case of the Argonne 4 potential [127].

This analysis suggests that our QMC ansatz is adequate for our problem. However, the static response is a delicate quantity, related to small energy differences, and we cannot exclude that deficiencies or missing correlations in the currently used trial states may affect the outcomes noticeably. Incorporating backflow correlation not only in plane waves, but also in Mathieu (or generic) orbitals could pave the way for more refined calculations of perturbed matter, and would be an interesting development for the future.

In principle, we could consider the possibility that the ansatz for the GA EDF is too simple. However, additional terms, such as e.g. fourth-order density gradients, are expected to be small corrections to the dominant

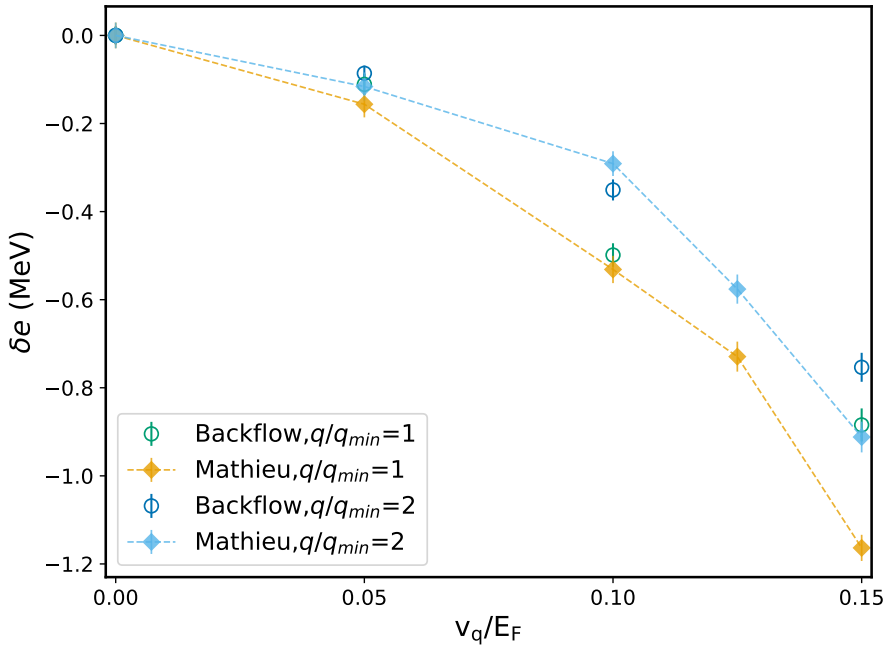

Figure 8.5: Difference between the energy of the perturbed system and the unperturbed energy, $\delta e = e(v) - e(v=0)$, as a function of the perturbation strength v_q/E_F in PNM, ρ_0= 0.16 fm^{-3}, with the AV4′+UIX$_c$ potential. Results are shown for the first two momenta of the external potential. The DMC results obtained using two different trial wave functions are compared. "Mathieu" (full symbols) refers to the ansatz presented in Sec. 3.3. "Backflow" (empty symbols) is the spline-based ansatz with spin-dependent backflow correlations described in the text and in Ref. [188]. Lines are a guide to the eye.

$\Delta\rho$ terms. Also, $\rho\tau$ terms have been neglected in this work, and thus the effective mass has been assumed to be equal to the bare mass. However, their effect on the EOS is mimicked by a richer density dependence in our EDFs than in the typical Skyrme models. Moreover, in light of Refs. [235, 236], the effective mass ratio, as deduced from the s.p. excitation spectrum, should be close to 1 in PNM.

We are thus led to conclude that our *ab initio* calculations are still too noisy to allow to constrain a DFT description. In Fig. 8.3 (right panel), error bars are rather large, so that uncertainties on the AFDMC data points are almost comparable to the variations of the response functions at low q. It is clear, then, that little information can be gained from the static response data at our disposal. From a different perspective, we can state that, while AFDMC calculations of the EOS may be under control, the same level of accuracy has not been achieved yet for perturbed matter computations. Energy differences are small quantities that may be sensitive to little inaccuracies or limitations of the *ab initio* method. We think that the Monte Carlo statistical errors, although they typically get somewhat underestimated, are not the major source of uncertainty. Rather, systematic biases of AFDMC, such as the approximate technique to control the sign problem or the propagation algorithm, which have been carefully investigated in homogeneous PNM [127, 188], should be characterized in detail also in the case of inhomogeneous matter.

For comparison, we would like to highlight that in Ref. [65] a similar conclusion about the currently available *ab initio* calculation was reached. In that work, finite nuclei perturbed by external 1B and 2B operators were studied with ADC(3)-SCGF, and their energies formed the *ab initio* data set to constrain the EDF coupling constants. Similar difficulties were faced, as theoretical errors, that can be estimated quite safely in the ground state, impact energy variations severely. In the case of [65], for instance, expectation values of 2B operators were evaluated using the 1B propagator in a rather approximate way. Therefore, we could state that *ab initio* techniques, while getting more and more powerful for g.s. properties, may still be somewhat immature as far as excited or perturbed nuclear states are concerned.

8.2 Pure neutron matter with the Argonne 8 interaction

In this Section, we apply our strategy to the case of PNM studied with the AV8′ + UIX interaction [89]. The calculations have been performed with the AFDMC method; the EOS is taken from Ref. [227] and the energies of perturbed nuclear matter are from Refs. [75, 76] [2]. In these works, a trial wave function made of a Slater determinant of Mathieu orbitals multiplied by Jastrow central correlations has been employed. The analysis

[2] We thank A. Gezerlis from providing us the perturbed matter results.

shall focus in particular on the case of PNM at an unperturbed density ρ_0 =0.10 fm^{-3}. As a caveat, we must mention, though, that Argonne 8 calculations should be checked in light of the findings of Refs. [127, 188], where it has been suggested that an unconstrained propagation would be required to get accurate AFDMC energies for potentials that include spin-orbit operators. The EOS of Ref. [227], in particular, may need to be revised. Energy differences should be less sensitive to specific details of the wave function than the energy itself (see also Sec. 8.1 above). Nevertheless, it would be interesting to perform unconstrained propagations in perturbed matter as well and compare with the outcomes of Refs. [75, 76].

The data for perturbed matter are obtained for the following momenta of the external potential: q/q_{min} = 1, 2, 3, 4, 6, 8, 10. For each q, calculations were done at the following strengths: v_q/E_F =0.125, 0.15, 0.175, 0.25. In light of Ch. 7, we exclude $v_q/E_F = 0.25$ as it already lies beyond the regime of linearity. Also, we have checked that the energies at $q/q_{min} = 8$ and 10 have essentially no effect on the parameters of the EDF, and we neglect them in the subsequent study. We stress that we are using here raw data for the $N = 66$ systems. We are not applying any of the finite-size corrections of Refs. [75, 76] to extrapolate to the TL.

The results of the fit are presented in Fig. 8.6. The energies of the perturbed system for several momenta q/q_{min} are shown as a function of the perturbation strength v_q/E_F. AFDMC results (solid symbols) are compared to the predictions of the best-fit GA EDF (empty smarkers). A small value of the $C^{\Delta\rho}_{PNM}$ parameter is

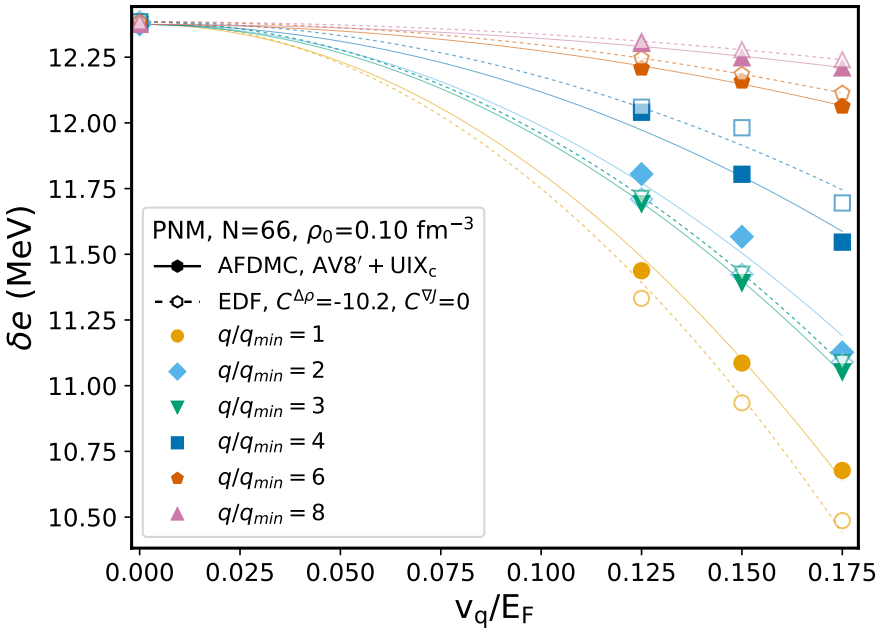

Figure 8.6: AFDMC energies for the AV8′+UIX interactions (solid markers) and predictions by the best-fit GA EDF (hollow markes) in PNM at a density ρ_0 =0.10 fm^{-3} as a function of the strength of the external perturbation v_q/E_F for different values of the momentum q/q_{min}. Solid (dashed) lines represent fits to the AFDMC (EDF) perturbed energies. The parameters $C^{\Delta\rho}$ and $C^{\nabla J}$ of the GA EDF are reported in the legend.

found ($C^{\Delta\rho} = -10.2 \pm 2$, $C^{\nabla J} = 0 \pm 35$), although the discrepancies with *ab initio* are smaller that for the Argonne 4 potential. The static response functions for the Argonne 8 interactions (triangles) and the GA EDF that best reproduces the AV8′+UIX data (empty diamonds), as well as the Argonne 4 response (circles), are then shown in Fig. 8.7. The response function has been determined at each momentum fitting the perturbed energies as in Ch. 7. For both Argonne potentials, we have decided not to apply any finite-size correction on the perturbed energies, and thus our predictions for the AV8′+UIX differ from the published results [76], that instead were extrapolated to the TL. The $q = 0$ values have been obtained using the CSR (B.51) on Argonne 4 EOS, while for Argonne 8 we have taken the CSR value from Ref. [76], Fig. 3.

Comparing the two Argonne models, we observe that the AV8′+UIX potential predicts a response stronger by about 50% than AV4′+UIX$_c$, although at $q = 0$ the difference is much smaller. This means that the curvature of the EOS, which determines the CSR, is similar for the two interactions, but the behavior in perturbed matter differs considerably. The agreement between AV8′+UIX and the GA EDF is somewhat better than what we have found in Sec. 8.1. Some discrepancies are evident, though, for example, a peculiar fact is that the GA EDF predicts almost degenerate responses for $q/q_{min} = 2$ and 3, while AFDMC does not. In addition, the density-gradient coefficient is too small to be accurate in finite nuclei (see below). This is clarified by comparing the values of $C^{\Delta\rho}$ in different EDFs. In Ref. [75], a study was performed, in which the *ab initio* pseudo-data were compared to the results of the Sly4 EDF, and the $C_1^{\Delta\rho}$ parameter of the latter was then tuned to reproduce the energy differences predicted by AFDMC for the AV8′ + UIX force. The method used in [75] is much simpler

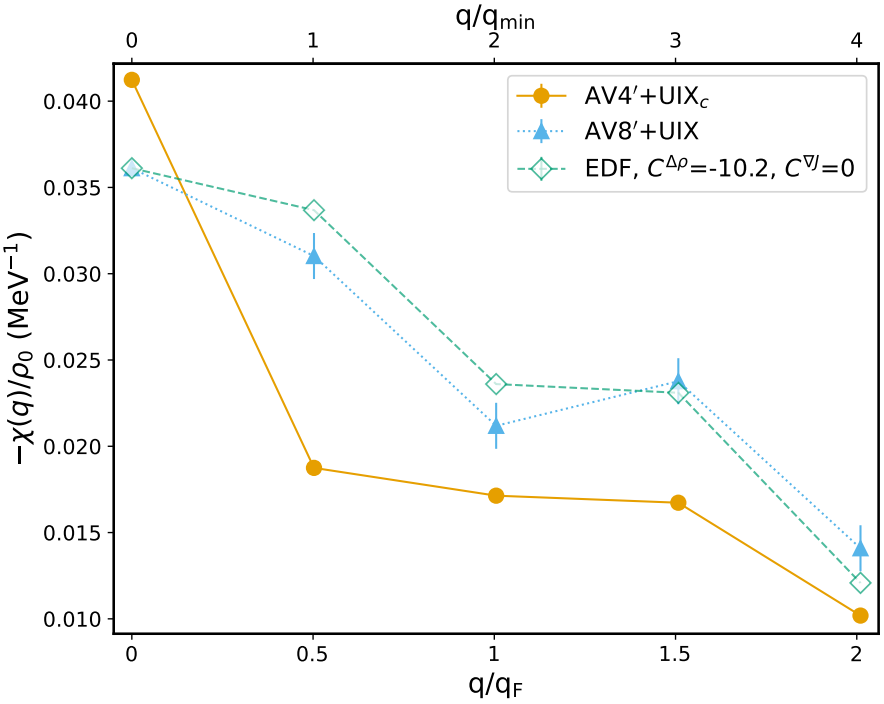

Figure 8.7: Static response function $-\chi(q)/\rho_0$ as a function of q/q_F computed with the AV4′+UIX$_c$ (circles) and AV8′+UIX (triangles) interactions in PNM at density ρ_0 =0.10 fm^{-3}, and with the EDF that best fits the Argonne 8 data (empty diamonds). The AV8′+UIX response has been derived from the raw energies of Ref. [75] to which no finite-size corrections have been applied. The $q = 0$ points have been obtained with the CSR. Lines are a guide to the eye. See text for details.

than ours, as in that case a single parameter of an empirical EDF was adjusted. In our case, the bulk terms of the EDF are already constrained to be consistent with the *ab initio* EOS. In addition, we take into account perturbations of several different wavelengths in our protocol, while in [75] parameters are estimated using data for $q/q_{min} = 2$ only. In Tab. 8.1 the $C^{\Delta\rho}$ coefficients are reported for the standard Sly4 EDF, the modified SLy4 model, adjusted to the AFDMC data for $\rho_0 = 0.10$ fm^{-3}, and our GA EDF fitted on perturbed matter at $\rho_0 = 0.10$ fm^{-3}, as well as on the EOS. The gradient coefficient is density-independent in Sly4, while in the two

EDF	$C_0^{\Delta\rho}$	$C_1^{\Delta\rho}$	$C_{PNM}^{\Delta\rho}$
Sly4	-76.996	15.657	-61.339
Sly4 (mod.)	-77	-29	-106
GA			-10.2

Table 8.1: Coefficients of the EDF density-gradient terms for the standard Sly4 EDF [43] and two EDFs constrained on the *ab initio* PNM response obtained with the AV8′ + UIX interaction at $\rho_0 = 0.10$ fm^{-3}. "Sly4 (mod.)" refers to the modified Sly4 EDF discussed in [75], in which the $C_1^{\Delta\rho}$ was adjusted, while the other parameters are the same as in Sly4. "GA" is our GA EDF model, in which both the bulk and gradient terms are constrained on the *ab initio* data. All coefficients are measured in MeV fm^5. See also text for details.

other models it is fitted on a specific ρ_0. (No SNM results are available with this interaction, thus only $C_{PNM}^{\Delta\rho}$ is shown for the GA EDF.) At this density, AFMDC is more repulsive than Sly4, and correspondingly a stronger (more negative) $C_{PNM}^{\Delta\rho}$ must be used in the modified Sly4 EDF. By contrast, our fit predicts a much smaller (in magnitude) coefficient, as well as a vanishing spin-orbit parameter.

The conclusions we draw are essentially the same as in the case of AV4′+UIX$_c$.

8.3 Symmetric nuclear matter with the Argonne 4 interaction

Calculations of SNM with the AV4′+UIX$_c$ at the reference density $\rho_0 = 0.16$ fm^{-3} are presented in this Section. We mention that these are, to our knowledge, the first *ab initio* calculations of the SNM static response. $A = 132$ nucleons have been used. The relative simplicity of the Argonne 4 interaction is instrumental in this respect. Indeed, the tensor component of the NN force, which is absent from AV4′, is rather strong in the $T = 0$ channel between neutrons and protons and makes SNM calculations delicate and computationally demanding

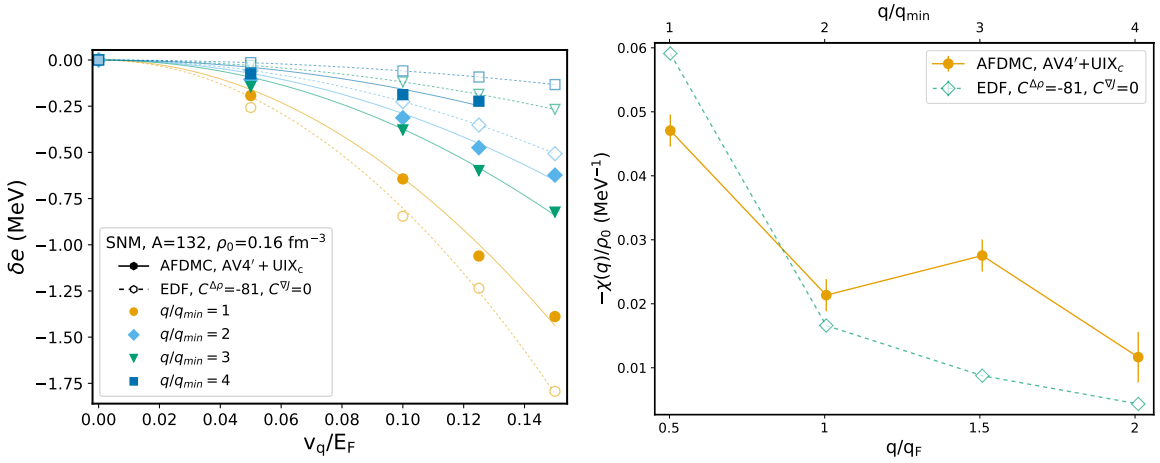

Figure 8.8: Same as Fig. 8.3, but for the AV4′+UIX$_c$ interaction in SNM at density ρ_0 =0.16 fm^{-3}.

for AFDMC [18, 87, 127]. For this reason, it is valuable to look at perturbed SNM results, even with a simple interaction.

In Fig. 8.8, the energies of the perturbed system (left panel) and the static response function (right panel) are shown. Unfortunately, the agreement of the GA EDF with AFDMC is unsatisfactory. Large discrepancies are observed for most data points, and qualitative features can not be reproduced by the DFT calculations. In particular, the curvature of the energies as a function of the perturbation strength for the AV4′+UIX$_c$ interaction is larger at $q/q_{min} = 3$ than at $q/q_{min} = 2$. The non-monotonic behavior of $\chi(q)$ is a peculiar FS effect that we had already pointed out in Ch. 7, see e.g. Figs. 7.3 and 7.13. However, the GA EDF is unable to catch this trend. We conclude that the same difficulties that we have in PNM are evident in SNM, too.

CHAPTER 9

Conclusions and perspectives

The overarching motivation of this work has been to develop the initial steps of a research program devoted to the construction of *ab initio*-constrained nuclear EDFs. Inspired by the "Jacob's ladder" program of electronic DFT, a hierarchy of EDFs of increasing complexity has been proposed, with the microscopic description of nuclear matter and its response playing a pivotal role in connecting *ab initio* calculations to the DFT description of nuclear systems.

The nuclear matter EOS has been studied with the Finite-T SCGF method applied in connection to the popular $\mathrm{NNLO_{sat}}$ chiral interaction and with AFDMC using the simplified AV4′+UIX$_c$ force. The EOS has been parametrized with a polynomial of the Fermi momentum, and a model selection procedure has been applied to select the best description of the *ab initio* data. Then, the fits to the EOS were employed as input for the LDA EDFs, which we used to predict binding energies and radii of magic nuclei. The results show that LDA is a reasonable approximation for heavy nuclei, where surface effects are subleading, when it is based on $\mathrm{NNLO_{sat}}$, while the models based on the Argonne 4 EOS overbind nuclei considerably. The different behaviors of $\mathrm{NNLO_{sat}}$ and Argonne 4 are likely because $\mathrm{NNLO_{sat}}$ predicts a saturation point in symmetric nuclear matter that is consistent with the empirical constraints, while Argonne 4 predicts saturation at a very high density and rather low energy.

This analysis has been complemented by an exploratory study of GA EDFs built on top of LDA, with the parameters of the surface terms tuned on selected empirical data. The $\mathrm{NNLO_{sat}}$-based GA EDFs are accurate and close to the quality of *ab initio* predictions. This gives us confidence that our approach is viable. The results for AV4′+UIX$_c$ are less satisfactory. Although gradient terms significantly improve the EDF predictions, some deficiencies, particularly in the charge radii, persist.

Subsequently, a strategy to determine the surface contributions of the EDF from *ab initio* has been devised. The cornerstone of our approach is to perturb nuclear matter through a static external potential to probe inhomogeneous matter. Then, the parameters of the GA EDF can be estimated by matching the energies of the perturbed system computed *ab initio* and in DFT. For this purpose, a DFT approach for perturbed matter has been developed, which simulates infinite matter by using a finite number of nucleons subject to periodic boundary conditions. Our method extends previous works by allowing to treat the spin-orbit term of the EDF and to study both PNM and SNM. The finite-A DFT code makes it possible to compare consistently the DFT predictions to those of *ab initio* methods that employ the same scheme, such as AFDMC and ADC-SCGF. Then, a fitting protocol that is based on minimizing a least-squares cost function has been implemented to find the optimal EDF parameters.

Accordingly, AFDMC has been extended to include the external potential, and calculations of the static response have been performed, including the first study of the SNM response in this context. The first full study of the GA EDFs constrained by the AV4′+UIX$_c$ energies has highlighted some inconsistencies, since the coefficients obtained with this procedure are incompatible with the empirical estimates. The source of these problems mainly resides in the significant systematic uncertainties of the AFDMC response, which limits the possibility of extracting information useful for fixing the nuclear EDFs. We believe that the difficulties encountered in the AFDMC static response might be remedied by further developments of the method, such as combining backflow correlations with generic (e.g. Mathieu or DFT) orbitals or using twist-averaged boundary conditions.

The need to overcome the limitations of AFDMC, related to the accuracy of the method and to the fact that the most sophisticated chiral interactions cannot be employed with it, has led us to develop the ADC-SCGF method for infinite nuclear matter. In particular, an effective way to include Gorkov pairing correlations on top of Dyson-ADC(3) has been introduced, and successful calculations of the EOS and momentum distributions of homogeneous matter have been reported. Importantly, this method is well-suited to treat the static and dynamic response, and studying the response with ADC-SCGF will be pursued as a natural development of this thesis.

In conclusion, in this work, a robust LDA scheme has been developed to ground the nuclear EDF into *ab initio* EOS. A methodology for the GA EDFs, that consists in constraining the surface terms on the *ab initio* nuclear matter response, has been proposed. Some of the pillars to carry on this approach have been realized,

namely a DFT framework for studying nuclear matter with a finite nucleon number, AFDMC calculations of the static response, and ADC-SCGF calculations of the EOS. Although some difficulties have been encountered, we deem that these could motivate further developments in *ab initio* theory.

This work will be extended in several directions. ADC-SCGF can be applied to many physical cases, including more detailed studies of the occupation numbers and the onset of superfluidity (pairing gaps, anomalous densities) in nuclear matter from a microscopic perspective. Further efforts are needed to make it possible for *ab initio* response calculations to reach the quality already achieved for the EOS, for which computations are at present quite well under control. Finally, combining DFT and *ab initio* can benefit from the use of advanced statistical and machine learning techniques, such as Bayesian analysis, which have greatly progressed in the last few years.

APPENDIX A

Overview of chiral interactions

This Appendix is devoted to the description of chiral NN and 3N forces [95, 97]. The purpose of this section is both to provide a general overview of the subject and to discuss some of the aspects that are involved in the implementation of the chiral forces for infinite nuclear matter calculations.

Sec. A.1 serves as a general introduction to chiral forces and discusses specifically NN forces, giving an overview of their structure with references to the literature. Sec. A.2 is devoted to chiral 3N interactions. The main expressions and the applications of regulators to the matrix elements are discussed. While the two previous sections cover essentially interactions derived in the framework of a chiral effective field theory (EFT) in terms of nucleons and pions (delta-less EFT), in Sec. A.3 we describe briefly delta-full forces [92], which are derived from an EFT that includes the Δ isobar degrees of freedom explicitly, and discuss the differences with delta-less forces.

In infinite matter, in particular, the plane wave basis is employed. Since chiral forces are formulated in momentum space, writing the matrix elements directly on this basis is relatively straightforward and computationally cheap, when an operator definition of the potential is available. This is the choice adopted in this work and used for all the SCGF calculations presented. For completeness, though, a section details, for the case of NN forces, the transformation that relates the momentum space matrix elements to the angular-momentum-coupled ones (Sec. A.4).

A.1 Chiral nucleon-nucleon interactions

In this Section, we briefly describe chiral NN interactions and outline their implementation. The subject is covered in great detail in e.g. Refs. [92, 93, 97–99].

Chiral forces provide a link between the underlying theory of the strong interaction, QCD, and the emergent nuclear interactions between nucleons. In short, chiral EFT allows to construct a low-energy Lagrangian that is formulated in terms of the low-energy degrees of freedom relevant for nuclear physics, i.e. nucleons and pions (and possibly Δ isobars), and that satisfies the same symmetries as QCD [99]. Besides the obvious symmetries, a key property of QCD in the approximation of massless quarks is the so-called chiral symmetry. The spontaneous breaking of this symmetry leads to the emergence of a triplet of light bosons, the pions. The EFT approach is based on constructing an order-by-order expansion of the chiral Lagrangian in terms of a small parameter. In the so-called Weinberg power counting, this is given by the ratio $Q = p/\Lambda_\chi$ between a typical momentum scale (p), of the order of the pion mass, and the breakdown scale (Λ_χ), that denotes a momentum at which the short-distance structure becomes important. Λ_χ is of the order of the mass of the ρ and ω mesons, about 700-800 MeV. Discussions about alternative power countings can be found in Refs. [93, 99, 237].

The NN potential is derived from the EFT Lagrangian as the sum of a finite number of Feynman diagrams that give irreducible contributions to the scattering amplitude for processes that involve two nucleons in the initial and final states [93]. (More generally, the A-body interaction is given by the amplitude for scattering processes involving A incoming and outgoing nucleons [99].) Power counting provides a way to organize the graphs according to their importance as powers of Q so that the potential at any given chiral order contains just a finite number of terms. Following a suggestion by Weinberg, the non-relativistic potential thus obtained perturbatively is then used in the Schrödinger or Lippmann-Schwinger equations, or their many-body equivalents, to determine the scattering amplitude or other observables [98, 99]. Long-range contributions to the interaction, mediated by the exchange of mesons, emerge naturally in this approach. In particular, the exchange of one pion determines the long-range attraction of the nuclear force, while the intermediate-range behavior of the nuclear interaction is governed by two-pion-exchange contributions. The short-range (high-energy) physics, instead, is encoded in the so-called contact terms, that need to be introduced to renormalize the theory and depend on a set of parameters, called low-energy constants (LECs). The LECs need to be constrained on experimental data, such as scattering phase shifts and the binding energy of the deuteron and possibly other light nuclei, or lattice QCD calculations [96].

Chiral potentials are expressed in momentum space. In the following, V has to be understood as a function of the momenta but as an operator in spin and isospin space [93]. We note that all c, $\hbar$ and volume factors

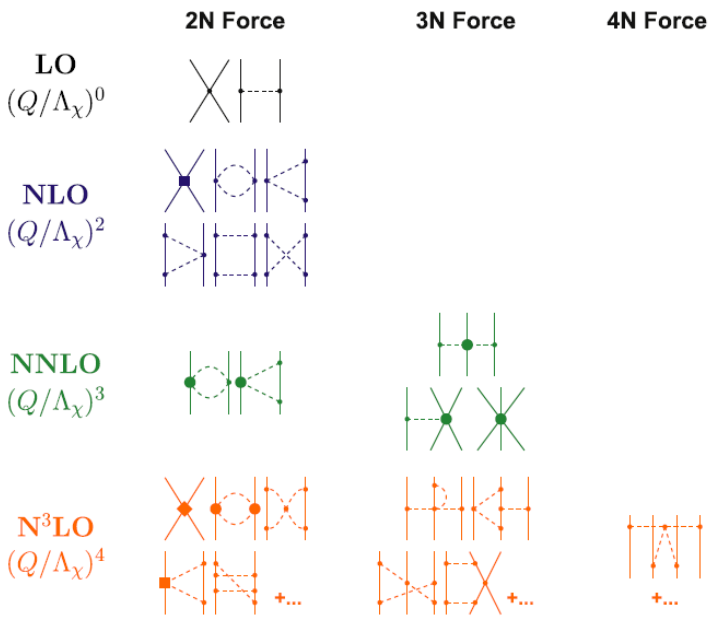

Figure A.1: Schematic representation of the diagrams that enter delta-less chiral interactions up to N3LO. Contribution to NN and 3N forces are shown. Dotted lines denote the exchange of pions. Adapted from Ref. [98], Fig. 1.

will be omitted in this section, and momenta and masses are all understood to have dimensions of energy. When the matrix elements of the interaction in the momentum basis are evaluated, the spin and isospin Pauli matrices need to be replaced by their corresponding elements. Also, one has to multiply the expression of the interaction by a constant factor $(\hbar c)^3/\Omega$, where $\Omega = L^3$ is the volume and L the size of the box (see e.g. [83, 130]).

NN interactions involve two incoming and two outgoing particles, whose momenta are labeled by $\mathbf{k}_1$,$\mathbf{k}_2$, $\mathbf{k}'_1$ and $\mathbf{k}'_2$. The total momentum must be conserved, i.e. $\mathbf{K} = \mathbf{k}'_1 + \mathbf{k}'_2 = \mathbf{k}_1 + \mathbf{k}_2$, and the potential must be independent from $\mathbf{K}$. Indeed, the potential is a function only of the initial and final relative momenta

$$\mathbf{p} = \frac{1}{2}(\mathbf{k}_1 - \mathbf{k}_2), \quad \mathbf{p}' = \frac{1}{2}(\mathbf{k}'_1 - \mathbf{k}'_2). \tag{A.1}$$

Thus $V = V(\mathbf{p}, \mathbf{p}')$. The momentum transfer $\mathbf{q} = \mathbf{p}' - \mathbf{p}$ and the average momentum (or momentum scale) $\mathbf{k} = \frac{1}{2}(\mathbf{p} + \mathbf{p}')$ are also introduced.

The structure of the chiral potential involves pion-exchange contributions and contact (zero-range) terms. The diagrams contributing to the chiral expansion at different orders in the parameter Q (in Weinberg power counting) are shown in Fig. A.1. The emergence of 3N forces is also depicted. For this section, our focus is on delta-less NN forces, that are structured as [14, 93]

$$V_{LO} = V_{1\pi}^{(0)} + V_{ct}^{(0)}, \tag{A.2}$$

$$V_{NLO} = V_{LO} + V_{1\pi}^{(2)} + V_{2\pi}^{(2)} + V_{ct}^{(2)}, \tag{A.3}$$

$$V_{NNLO} = V_{NLO} + V_{1\pi}^{(3)} + V_{2\pi}^{(3)}, \tag{A.4}$$

where the superscript denotes the chiral order ν. LO stands for the leading order ($\nu = 0$), NLO for next-to-leading-order ($\nu = 2$) and NNLO for next-to-next-to-leading-order ($\nu = 3$). All the contributions with $\nu = 1$ vanish due to parity and time-reversal invariance [95]. Higher-order contributions are described e.g. in Refs. [93, 97, 112]. 1π denotes the one-pion-exchange (OPE) contributions, 2π the two-pion-exchange (TPE) contributions and ct the contact terms. The axial-vector coupling constant $g_A = 1.29$, the pion decay constant $f_\pi = 92.4$ MeV and the pion mass m_π are universal constants entering the chiral forces [1]

At LO, the nuclear force is made of the well-known OPE potential, plus two momentum-independent contact terms. The OPE reads

$$V_{1\pi}^{(0)} = -\frac{g_A^2}{4f_\pi^2}\frac{\sigma_1 \cdot \mathbf{q}\,\sigma_2 \cdot \mathbf{q}}{q^2 + m_\pi^2}\tau_1 \cdot \tau_2, \tag{A.5}$$

[1] Note that different interactions may use slightly different values. This is the case e.g. of the delta-less NNLO$_{\rm sat}$ [105] and delta-full ΔNNLO$_{\rm go}$ [106] forces.

and it is evaluated at the average pion mass. The potential is thus charge-independent at LO. From NLO on, $V_{1\pi}$ is charge-dependent, i.e. the potential depends on the type of nucleons involved. The masses of the $\pi^{\pm}$ particles are equal, but are different from the mass of the neutral pion: $m_{\pi^{\pm}} = 139.5702$ MeV and $m_{\pi^0} = 134.9766$ MeV [105]. Following [98], the OPE for proton-proton (pp) and neutron-neutron (nn) scattering are given by

$$V_{1\pi}^{(pp)} = V_{1\pi}^{(nn)} = V_{1\pi}(m_{\pi^0}), \tag{A.6}$$

while for the proton-neutron (pn) part one has

$$V_{1\pi}^{(pn)} = -V_{1\pi}(m_{\pi^0}) + (-1)^{T+1}\, 2V_{1\pi}(m_{\pi^{\pm}}), \tag{A.7}$$

where T is the total isospin of the two-nucleon system, and

$$V_{1\pi}(m_\pi) = -\frac{g_A^2}{4f_\pi^2}\frac{\sigma_1\cdot\mathbf{q}\,\sigma_2\cdot\mathbf{q}}{q^2+m_\pi^2} \tag{A.8}$$

as a function of the pion mass. The NLO and NNLO orders do not introduce additional terms to the OPE, but renormalize the mass and the coupling constant. These effects are taken care of by working with the physical values, see [98].

The exchange of two or more pions always involves loop diagrams and consequently LECs appear [93]. In particular, the NNLO TPE term depends on three LECs, c_1, c_3 and c_4 [93]. The general operator structure of the two-pion-exchange sector of the interaction is written as

$$\begin{aligned} V_{2\pi}(p,p') &= V_C + \tau_1\cdot\tau_2 W_C + [V_S + \tau_1\cdot\tau_2 W_S]\sigma_1\cdot\sigma_2 + [V_{LS} + \tau_1\cdot\tau_2 W_{LS}](-i)\mathbf{S}\cdot(\mathbf{q}\times\mathbf{k}) \\ &+ [V_T + \tau_1\cdot\tau_2 W_T]\sigma_1\cdot\mathbf{q}\,\sigma_2\cdot\mathbf{q} + [V_{\sigma L} + \tau_1\cdot\tau_2 W_{\sigma L}]\sigma_1\cdot(\mathbf{q}\times\mathbf{k})\,\sigma_2\cdot(\mathbf{q}\times\mathbf{k}). \end{aligned} \tag{A.9}$$

$\mathbf{S}$ is the total spin, $\mathbf{S} = \frac{1}{2}(\sigma_1+\sigma_2)$. At NLO, the TPE terms contribute to W_C, V_T e V_S. At NNLO, contributions to the eight operators ($V_C, W_C, V_S, W_S, V_T, W_T, V_{LS}, W_{LS}$) appear. At N3LO, two further operators ($V_{\sigma L}, W_{\sigma L}$) are involved. The TPE NNLO potential, and in particular the isoscalar central potential V_C, is crucial as it provides an attractive contribution at intermediate range [93].

Finally, the contact terms are in general polynomials of the momenta $\mathbf{k}$ and $\mathbf{q}$. At LO, two LECs are required. Seven more contact LECs enter at NLO, while there are no new contacts at NNLO. The LECs are often provided in terms of partial waves: ${}^1S_0$ and ${}^3S_1$ at LO; ${}^1S_0$, ${}^3P_0$, ${}^1P_1$, ${}^3P_1$, ${}^3S_1$, ${}^3S_1 - {}^3D_1$, ${}^3D_1 - {}^3S_1$ and ${}^3P_2$ at NLO. A linear combination of them generates the constants C_S and C_T at LO and C_i, $i = 1,7$ at NNLO which enter the definition of the contact terms (Ref. [93], Eqs. 4.38-4.42). We report below the structure of the contact terms at LO and NLO:

$$V_{ct}^{(0)} = C_S + C_T\sigma_1\cdot\sigma_2, \tag{A.10}$$

$$\begin{aligned} V_{ct}^{(2)} &= C_1 q^2 + C_2 k^2 + (C_3 q^2 + C_4 k^2)\sigma_1\cdot\sigma_2 + C_5(-i)\mathbf{S}\cdot(\mathbf{q}\times\mathbf{k}) \\ &+ C_6\sigma_1\cdot\mathbf{q}\,\sigma_2\cdot\mathbf{q} + C_7\sigma_1\cdot\mathbf{k}\,\sigma_2\cdot\mathbf{k}. \end{aligned} \tag{A.11}$$

The expressions of all terms of the chiral potentials up to NNLO (and beyond) can be found in Refs. [93, 97, 98, 112, 238]. We summarize the contributions that appear in the different orders in Tab. A.1, where references to the relevant equations of the review [93] are also provided. Note that Ref. [93] on the one hand, and e.g. Refs. [98, 112, 238] on the other hand adopt different power countings, and expressions of the NNLO terms are different. Among the interactions from the Göteborg-Oak Ridge collaboration, for example, NNLO$_{\rm sat}$ [105] and NNLO$_{\rm opt}$ [239] follow the "Machleidt" power counting [93], while the delta-full ΔNNLO$_{\rm go}$ [106] force is based on the "Epelbaum" power counting of Ref. [238].

The interaction should also be multiplied by a relativistic correction ([95], p. 28), that reads (in the minimal relativity scheme)

$$\frac{M_N}{\sqrt{E(p)E(p')}}, \qquad E(p) = \sqrt{p^2 + M_N^2}, \tag{A.12}$$

where M_N is the nucleon mass and $E(p)$ its relativistic kinetic energy.

Nuclear interactions suffer from ultraviolet (UV) divergences that must be cured by the application of regularization and renormalization techniques [92, 99]. UV divergences in the loop integrals are treated by dimensional regularization (DR) or spectral function regularization (SFR). The two schemes differ from each other by an infinite series of higher-order contact interactions [238], and might be seen as two different conventions to define the high-energy, low-distance behavior of the interaction ([238], Fig. 6). SFR depends on an

Chiral order	Type	Eq.	Terms	N. terms	LECs	[GeV]^n
LO ($\nu=0$)	1π	4.5	Eq. (A.5)	1		
	ct	4.38-4.39	see Eq. (A.10)	2	C_S, C_T	-2
NLO ($\nu=2$)	1π	4.77-4.79	see Eq. (A.5)-(A.8)	1		
	2π	4.9-4.10	W_C, V_S, V_T	3		
	ct	4.40-4-42	see Eq. (A.11)	7	C_i, $i=1,7$	-4
NNLO ($\nu=3$)	1π	4.77-4.79	see Eq. (A.5)-(A.8)	1		
	2π	4.13-4.18, 4.21-4.24	V_C,W_C,V_S,W_S, V_T,W_T, V_{LS}, W_{LS}	8	c_1, c_3, c_4	-1

Table A.1: The contributions to the delta-less chiral NN potential are summarized. OPE (1π), TPE (2π) and contact (ct) terms at LO, NLO and NNLO are reported. References are given to the equations of the review [95] where the expression of the different terms are contained. With reference to the general expression Eq. (A.9), the operators to which two-pion-exchange terms contribute, as well as the number of terms of each of the three types of contributions that appear at a given chiral order, are listed. The OPE terms are given in Eqs. (A.5)-(A.8). For the contact terms, we refer to Eqs. (A.10) and (A.11) above. Finally, in the two last columns, the LECs that appear in a given term and their dimension as powers of GeV are reported. Note in Ref. [93] dimensional regularization is used. Also, relativistic corrections $\sim 1/M_N$ are already included in the terms of the interactions cited in the table. In other works, such as e.g. Refs. [98, 238], a different power counting is used, and these corrections are considered separately. See also the text for details.

additional cutoff Λ_{SFR} of the order of Λ_χ. Refs. [95, 240] use DR, while SFR is employed in e.g. Refs. [98, 112, 238].

Divergences manifest themselves also when the interaction is employed in the Schrödinger or Lippmann-Schwinger equations. To avoid this issue, the nuclear potential is multiplied by regulator functions that suppress the high-momentum components above a chosen cutoff scale [92, 93, 97]. A common choice for the NN regulator is the following non-local function:

$$f(p) = \exp\Big(-\left(p^2/\Lambda^2\right)^n\Big), \tag{A.13}$$

where Λ is the interaction cutoff, typically of the order of 500 MeV. A typical value for the exponent is $n=3$ at NNLO [110], although in some cases $n=4$ is used [106]. Local chiral interactions, such as those used in QMC, differ in the choice of the regulator, as well as the contact terms, but are not discussed here; we refer the reader to e.g. Refs. [92, 102]. The regularized potential is obtained multiplying $V(p,p')$ by the regulators evaluated at the incoming and outgoing relative momenta, namely

$$V^{reg}(p,p') = f(p)V(p,p')f(p'). \tag{A.14}$$

If n is large enough, then the low-p expansion of the regulator generates corrections that are of a higher order than the order of the chiral expansion. Thus, the effect of the regularization is to dampen the pathological high momentum terms, while the low-momentum matrix elements are barely changed.

Regularization introduces a dependence of the interaction matrix elements on the choice of the regularization scheme and the cutoff. The purpose of the renormalization procedure is to remove such dependencies [98]. This is realized in essence by properly tuning the LECs order by order. In principle, once the LECs are fixed the predictions of the EFT should be independent on the details of the theory [99].

A.2 Chiral three-nucleon forces

In this Section, an overview of chiral three-nucleon interactions is given. This topic is reviewed e.g. in Refs. [92, 241, 242]. Here we focus mostly on delta-less interactions, while in Sec. A.3 we will comment on delta-full forces.

3N forces appear naturally in the chiral expansion. In the delta-less EFT approach, 3N interactions give non-vanishing contributions starting from NNLO. At this order, three topologies appear (Fig. A.2): a long-range two-pion exchange term W_C, a one-pion exchange interaction W_D and a contact term W_E. W_C depends on the pion-nucleon LECs c_1, c_3 and c_4 that already enter the NN force at that order. W_D and W_E, instead, depend on two new LECs c_D and c_E, that describe the 3N physics and must be adjusted to properties of systems with $A \geq 3$. c_D and c_E are dimensionless constants. Also, for later convenience we define the constants $E = \frac{c_E}{f_\pi^4 \Lambda_\chi}$ and $D = \frac{c_D}{f_\pi^2 \Lambda_\chi}$, where Λ_χ=700 MeV is the chiral symmetry breaking scale. The following expressions hold in momentum space [241, 242]:

$$W_C = \frac{1}{2}\left(\frac{g_A}{2f_\pi}\right)^2 \sum_{\pi(ijk)} \frac{(\sigma_i \cdot \mathbf{Q}_i)(\sigma_j \cdot \mathbf{Q}_j)}{(Q_i^2+m_\pi^2)(Q_j^2+m_\pi^2)} F_{ijk}^{\alpha\beta} \tau_i^\alpha \tau_j^\beta, \tag{A.15}$$

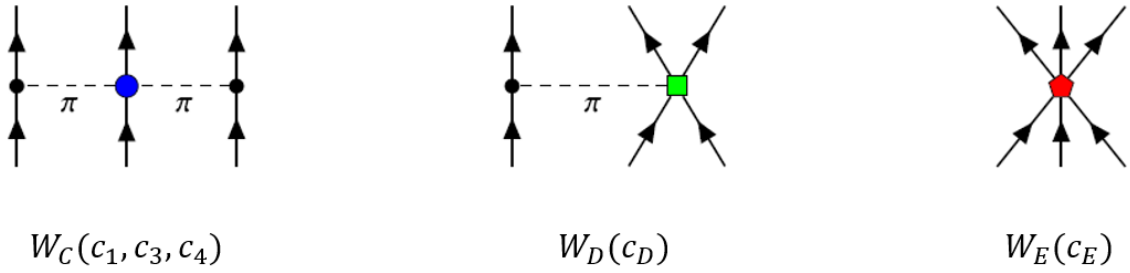

Figure A.2: 3N interactions at NNLO in the chiral expansion. The three topologies (from left to right: two-pion exchange, one-pion exchange and contact term) entering the 3N force and the LECs they depend on are shown. Adapted from Ref. [241].

$$W_D = -\frac{g_A^2}{8\pi^2} D \sum_{\pi(ijk)} \frac{\sigma_j \cdot \mathbf{Q}_j}{Q_j^2 + m_\pi^2} (\tau_i \cdot \tau_j)(\sigma_i \cdot \mathbf{Q}_j), \tag{A.16}$$

$$W_E = \frac{E}{2} \sum_{\pi(ijk)} \tau_i \cdot \tau_j, \tag{A.17}$$

and the tensor $F_{ijk}^{\alpha\beta}$ is defined as

$$F_{ijk}^{\alpha\beta} = \delta^{\alpha\beta}\left[-\frac{4c_1 m_\pi^2}{f_\pi^2} + \frac{2c_3}{f_\pi^2}\mathbf{Q}_i \cdot \mathbf{Q}_j\right] + \frac{c_4}{f_\pi^2}\sum_\gamma \epsilon^{\alpha\beta\gamma}\tau_k^\gamma \sigma_k \cdot (\mathbf{Q}_i \times \mathbf{Q}_j). \tag{A.18}$$

$\pi(ijk)$ denotes the six permutations of the indexes i, j, k, Greek letters denote the Cartesian components of the vectors σ_i and τ_i, and $\mathbf{Q}_i = \mathbf{k}_i' - \mathbf{k}_i$ are the momentum transfers.

To ease the notation, the index 1,2,3 are used now in place of i, j, k to refer to the three particles involved in the interaction. Next, we partition W_C as the sum of three expressions, $W_C = W_C^{(1)} + W_C^{(2)} + W_C^{(3)}$, where $W_C^{(1)}$ collects the contributions coming from the permutations (231) and (321) in the sum, $W_C^{(2)}$ those from (132) and (312), and finally $W_C^{(3)}$ those from (123) and (213). In this way, a more clear structure appears behind the 3NF, and both the numerical implementation and the application of local regulators are made simpler. It is straightforward to show that

$$W_D^{(1)} = -\frac{g_A^2}{8\pi^2} D\, \tau_2 \cdot \tau_3 \left[\frac{\sigma_2 \cdot \mathbf{Q}_2}{Q_2^2 + m_\pi^2}(\sigma_3 \cdot \mathbf{Q}_2) + \frac{\sigma_3 \cdot \mathbf{Q}_3}{Q_3^2 + m_\pi^2}(\sigma_2 \cdot \mathbf{Q}_3)\right], \tag{A.19}$$

$$W_E^{(1)} = E\, \tau_2 \cdot \tau_3. \tag{A.20}$$

To deal with the TPE term, we first write it in vector form, namely

$$W_C = \frac{g_A^2}{8 f_\pi^4} \sum_{\pi(ijk)} \frac{(\sigma_i \cdot \mathbf{Q}_i)(\sigma_j \cdot \mathbf{Q}_j)}{(Q_j^2 + m_\pi^2)(Q_i^2 + m_\pi^2)} \tag{A.21}$$
$$\left[\left(-4c_1 m_\pi^2 + 2c_3 \mathbf{Q}_i \cdot \mathbf{Q}_j\right)\tau_i \cdot \tau_j + c_4 ((\mathbf{Q}_i \times \mathbf{Q}_j) \cdot \sigma_k)((\tau_i \times \tau_j) \cdot \tau_k)\right].$$

Then, we observe that the expression is invariant under the exchange of i and j, so that the (231) and (321) contributions are equal. Therefore,

$$W_C^{(1)} = \frac{g_A^2}{4 f_\pi^4} \frac{(\sigma_2 \cdot \mathbf{Q}_2)(\sigma_3 \cdot \mathbf{Q}_3)}{(Q_2^2 + m_\pi^2)(Q_3^2 + m_\pi^2)} \tag{A.22}$$
$$\left[\left(-4c_1 m_\pi^2 + 2c_3 \mathbf{Q}_2 \cdot \mathbf{Q}_3\right)\tau_2 \cdot \tau_3 + c_4\, \sigma_1 \cdot (\mathbf{Q}_2 \times \mathbf{Q}_3)\, \tau_1 \cdot (\tau_2 \times \tau_3)\right].$$

The (2) and (3) contributions are obtained by cycling the indexes. The total 3N potential can then be written as

$$W = \sum_{i=1}^{3} W^{(i)} = \sum_{i=1}^{3}\left(W_C^{(i)} + W_D^{(i)} + W_E^{(i)}\right). \tag{A.23}$$

The 3N matrix elements can be readily evaluated in the momentum space basis used in infinite matter calculations, and such strategy is followed in this work. The partial-wave formalism for the 3N interaction is an alternative approach, for which we refer the reader to e.g. Refs. [223, 241, 243].

To check the correct implementation of part of the 3N interaction, we have found useful the following formula [225, 244]:

$$\frac{E_{c_E}^{(HF)}}{A} = -\frac{3}{16} E \rho^2, \tag{A.24}$$

that holds in SNM and gives analytically the HF energy per particle due to the contact term W_E. This relation is valid when no regularization is applied to the 3N term. We also mention that c_E is typically the dominant LEC [245]. Another check is that, when non-local regulators or no regulators at all are used, the PNM results depend only on the c_1 and c_3 constants, as the terms proportional to c_4, c_D and c_E vanish, as explained in Ref. [245].

As a final remark, when one evaluates the momentum basis matrix elements, a factor of $(\hbar c)^6/\Omega^2$ must be inserted to get the proper dimensions of energy.

A.2.1 Local regulators

A thorough discussion of the regularization of both NN and 3N interactions can be found e.g. in Refs. [93, 241, 246]. We summarize here only the main equations for treating 3N forces in the case of local regulators and, in the following section, non-local regulators.

A typical choice of local 3N regulator function is that of Ref. [247],

$$f_\Lambda(Q) = \exp\Big(-\big(Q^2/\Lambda^2\big)^2\Big) \tag{A.25}$$

where $\mathbf{Q}$ is a momentum transfer. Local regulators must be applied to the individual components of the 3N force, see Eq. (A.23). The regularized 3N matrix elements are given by [241]

$$W^{reg} = W^{(1)} f_\Lambda(Q_2) f_\Lambda(Q_3) + W^{(2)} f_\Lambda(Q_1) f_\Lambda(Q_3) + W^{(3)} f_\Lambda(Q_1) f_\Lambda(Q_2). \tag{A.26}$$

We are following the convention of Eq. (24.a) of Ref. [246], for which we multiply $W^{(1)}$, that is function of $\mathbf{Q}_2$ and $\mathbf{Q}_3$, by regulators evaluated at the same momenta.

The advantage of local regulators is that, since they are functions of the individual momentum transfers and do not depend on the momentum scale, when the locally-regulated matrix elements are Fourier-transformed they give rise to interactions that are function of the relative distance between nucleons only, and do not depend on the gradient with respect to the coordinates [92]. This makes local NN+3N chiral forces suitable to coordinate-space methods such as QMC [18, 92, 103]. It must be mentioned, however, that locally regulated forces are not symmetric under individual nucleon permutations [246]. As a consequence, the so-called Fierz rearrangement freedom is violated and ambiguities arise as far as the operator structure of the contact terms is concerned [92]. In the 3N sector, this means in particular that choosing the operators 1 or $\tau_i \cdot \tau_j$ in the c_E contact term, while in principle should make no difference, in practice affects the results significantly, as seen e.g. in Ref. [246] and in the QMC studies of Refs. [88, 248]. An example is the c_E contact term, which should be vanishing in PNM, but acquires a finite expectation value when local regulators are employed [244].

A.2.2 Non-local regulator

Non-local momentum-space regulators have been found successful in helping the convergence of nuclear matter calculations [126]. The idea of this class of regulators is to cutoff the matrix elements according to the value of the kinetic energy of the three-nucleon system [241], which is conveniently expressed in terms of the Jacobi momenta

$$\mathbf{p} = \frac{\mathbf{k}_1 - \mathbf{k}_2}{2}, \mathbf{q} = \frac{2\mathbf{k}_3 - (\mathbf{k}_1 + \mathbf{k}_2)}{3}. \tag{A.27}$$

The non-local regulator function is then defined as [110]

$$f(p,q) = \exp\left[-\left(\frac{4p^2 + 3q^2}{4\Lambda^2}\right)^n\right] \tag{A.28}$$

and represents a generalization of the standard regulator of the NN force Eq. (A.13), to which it reduces when $q = 0$. Typically, the same exponents n and cutoff Λ are used in the NN and 3N regulators (Eqs. (A.13),(A.28)), although this is not strictly required [246].

The regularized matrix elements are finally obtained by multiplying by the function (A.28) evaluated on the incoming and outgoing Jacobi momenta:

$$W^{reg} = f(p,q) W f(p',q'). \tag{A.29}$$

A.3 Delta-full chiral interactions

Delta-full chiral interactions are based on including explicitly in their construction the delta isobar degrees of freedom $\Delta(1232)$ (Fig. A.3). Delta-full potentials have attracted interest because they have been shown to improve the description of nuclei and nuclear matter simultaneously [106, 110]. Also, when delta excitations are included explicitly, the convergence of the chiral expansion improves considerably compared to delta-less interactions [92]. This is because in delta-less models the strength of some of the LECs c_i is "unnaturally" large, as the contributions of the delta resonance to the nuclear interaction are accounted for implicitly in this way (this is known as "resonance saturation"). By contrast, in delta-full theories a significant portion of these constants is removed and dealt with by diagrams that involve the explicit delta resonance. As a consequence, the c_i's are much smaller. Moreover, when introducing the new degree of freedom the power counting must be adjusted [241]. New contributions appear and some contributions of the delta-less chiral EFT are promoted to a lower order (see Ref. [127], Fig. 1). Namely, the central (V_C,W_C), spin (V_S,W_S) and tensor (V_T,W_T) operators already appear at NLO (see Tab. A.2 below).

In this Section, we comment on the modifications that have to be applied to the delta-less NN (App. A.1) and 3N (App. A.2) interactions. Recent reviews that cover this topic are Refs. [92, 241]. Original papers on this subject include Refs. [110, 249, 250].

When delta isobars are included, two new constants enter the nuclear interaction. One is the difference between the mass of the delta excitation and the nucleon mass, $\delta = M_\Delta - M_N \approx 293$ MeV, that acts as an additional small scale. The other is the $\pi N\Delta$ axial coupling $h_A = 1.40$. The introduction of the Δ isobars also leads to the appearance of additional terms in both the NN and 3N sectors. The leading contributions of the delta degrees of freedom to the NN force appear at NLO; subleading terms have to be included at NNLO. All the relevant expressions are reported in Ref. [249], which we here summarize. Following Ref. [110] and references therein, the subleading $\pi N\Delta$ contributions proportional to the additional LEC $b_3 + b_8$ can be neglected, provided that h_A and the subleading πN couplings $c_{2,3,4}$ are renormalized. Tab. A.2 reports the relevant terms that must be added to the delta-less potential of App. A.1, with references to Sec. 2.2 of [249]. Ref. [112] also discusses these expressions in the Appendix. In total, 16 terms have to be included.

As far as the 3N forces are concerned, in delta-full interactions a contribution appears already at NLO, the Fujita-Miyazawa term [92, 250]. This has the same topology as the delta-less TPE interaction W_C (A.15), but with different LECs. Indeed, the constants

$$c_3^\Delta = -2c_4^\Delta = -\frac{4h_A^2}{9\delta} \approx -2.97\,\mathrm{GeV}^{-1} \tag{A.30}$$

and $c_1 = 0$ have to be used in the expression of Eq. (A.15) for this term. At NNLO, no additional 3N terms appear. In practice, incorporating delta-full 3N interactions up to NNLO amounts simply to using in the 3N operators the LECs

$$c_1^{3NF} = c_1,\; c_3^{3NF} = c_3 + c_3^\Delta,\; c_4^{3NF} = c_4 + c_4^\Delta \tag{A.31}$$

where c_i denote the NN LECs [251] [2].

	Graph	Eq.	Terms	N. terms
NLO	Δ in triangle graph	2.5	W_C	1
NLO	single Δ in box graph	2.6	V_C,W_C,V_S,W_S,V_T,W_T	6
NLO	double Δ in box graph	2.7	V_C,W_C,V_S,W_S,V_T,W_T	6
NNLO	Δ in triangle graph	2.9	V_C, W_T, W_S	3

Table A.2: Additional contribution to the NN interaction in delta-full chiral EDF. We summarize here Sec. 2.2 of Ref. [249] and show schematically the terms that have to be added to the delta-less interactions of App. A.1. Leading (NLO) and subleading (NNLO) TPE contributions for different types of Feynman graphs are reported, together with the number of the equation in Ref. [249] that contains their expression. The terms of the potential (A.9) that receive contributions and the number of terms are also reported. Subleading terms proportional to $b_3 + b_8$ have been neglected, see Ref. [110]. In total, 16 extra terms need to be implemented.

A.4 Partial wave expansion of the NN matrix elements

The purpose of this Section is to determine the transformation that allows to express the antisymmetrized matrix elements of the NN interaction as a function of the relative angular-momentum-coupled matrix elements. Similar calculations can be found e.g. in Refs. [14, 83, 125, 252]. We follow Ref. [253] for the angular momentum theory and conventions.

[2] Sometimes, as e.g. in Ref. [251], a different convention is used in which $h_A \approx 2.8$ and $c_3^\Delta = -h_A^2/(9\delta)$.

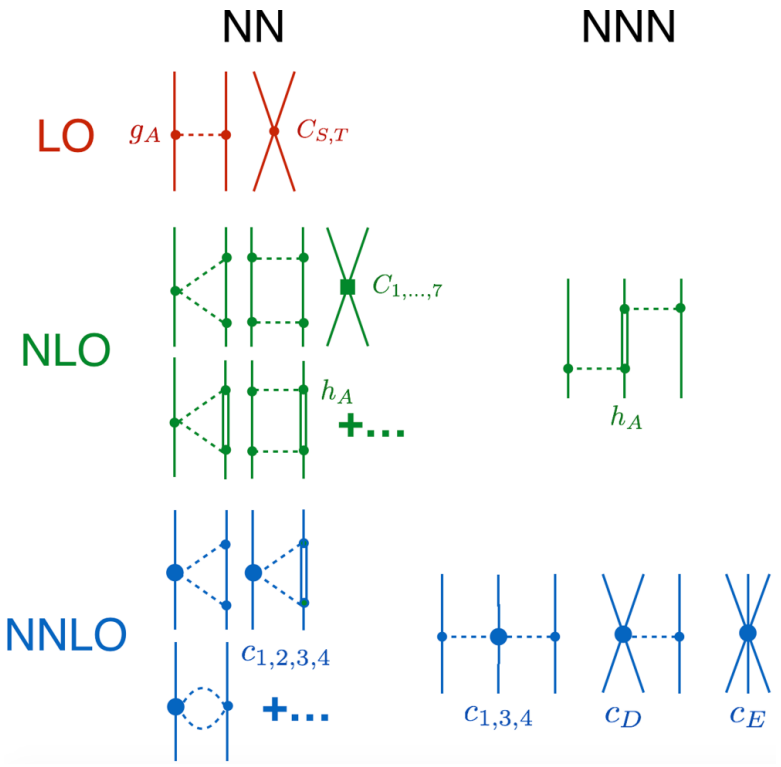

Figure A.3: Schematic representation of the diagrams that enter delta-full chiral interactions up to NNLO. Contribution to NN and 3N forces are shown. Dotted lines denote the exchange of pion. Double lines refer to the delta isobars. The LECs entering each term are reported. Taken from Ref. [110].

Chiral forces are naturally formulated in momentum space. Thus, it is efficient and relatively simple to evaluate the NN matrix elements in the momentum basis, implementing the operators directly in the s.p. basis, provided that an operator definition of the potential is available [125, 126]. Sometimes, however, this is inconvenient or even impossible. For example, it is common that the angular-momentum-coupled matrix elements are made available by groups specialized in the developments of nuclear interaction, and thus it is easier to simply transform them back to the s.p. basis of interest, as it often happens in finite nuclei (see e.g. Ref. [9]). Another example is the case of renormalization-group-evolved interactions [254, 255], where the matrix elements are defined only numerically and are provided already in partial waves. Therefore, it is strategic to have at our disposal the tools for performing the transformation of the NN angular-momentum-coupled matrix elements to the momentum basis. In passing, comparing the NN elements in the s.p. basis and those obtained using the partial wave expansion provides a useful check on the implementation of the former.

We use as s.p. states the momentum eigenstates

$$|\alpha\rangle = |\mathbf{k}_\alpha, s_\alpha, t_\alpha\rangle \tag{A.32}$$

and aim at relating the antisymmetrized matrix elements

$$\bar{v}_{\alpha\beta,\gamma,\delta} = \langle \alpha, \beta | V | \gamma\delta \rangle_A \,, \tag{A.33}$$

with $|\gamma\delta\rangle_A = |\gamma\delta\rangle - |\delta\gamma\rangle$, to the partial-wave matrix elements

$$\langle p | V_{LL'}^{JSTM_T} | p' \rangle \equiv \langle pJ(LS)TM_T | V | p'J(L'S)TM_T \rangle \,. \tag{A.34}$$

p and p' are the magnitudes of the relative momenta of the incoming and outgoing pairs of nucleons (see Eq. (A.1)),

$$\mathbf{p} = \frac{1}{2}\left(\mathbf{k}_\alpha - \mathbf{k}_\beta\right), \qquad \mathbf{p}' = \frac{1}{2}\left(\mathbf{k}_\gamma - \mathbf{k}_\delta\right). \tag{A.35}$$

We also introduce the total momentum of the nucleon pair,

$$\mathbf{K} = \mathbf{k}_\alpha + \mathbf{k}_\beta = \mathbf{k}_\gamma + \mathbf{k}_\delta. \tag{A.36}$$

We remember that the nuclear interaction conserves the total momentum $\mathbf{K}$, the total angular momentum J, the spin S, the isospin T and the isospin projection M_T of the nucleon pair. Moreover, it is independent of the

momentum projection M_J and of $\mathbf{K}$. However, it does not conserve the orbital angular momentum, as the non-central tensor interaction couples L to $L \pm 2$. Also, before delving into the calculation, we mention, following Ref. [95], that for a given M_T and partial wave J there are up to six matrix elements. These correspond to the following combinations of the S, L and L' quantum numbers: $S = 0$, $L = L' = J$ (singlet), $S = 1$, $L = L' = J$ (triplet), $S = 1$, $L = L' = J + 1$ (++), $S = 1$, $L = L' = J - 1$ (–), $S = 1$, $L = J + 1, L' = J - 1$ (+-) and $S = 1$, $L = J - 1, L' = J + 1$ (-+). The condition for having non-vanishing antisymmetric matrix elements (see below) reads

$$(-1)^{S+T+L} = -1 \tag{A.37}$$

and fixes the isospin T for given values of J and L [95].

The first step of the calculations consists of writing $|\alpha\beta\rangle$ in terms of the relative momentum $\mathbf{p}$, total spin and total isospin. To do this, we write

$$|\alpha\beta\rangle = |\mathbf{p}, \mathbf{K}; s_\alpha, t_\alpha, s_\beta, t_\beta\rangle \,. \tag{A.38}$$

Then, we couple the spin and isospin projections using the Clebsch-Gordan coefficients $(j_1 m_1; j_2, m_2|j, m_j) \equiv \langle j_1, m_1; j_2, m_2|j, m_j\rangle$

$$|\alpha\beta\rangle = \sum_{SM_S}\sum_{TM_T}\left(\frac{1}{2}s_\alpha, \frac{1}{2}s_\beta|S, M_S\right)\left(\frac{1}{2}t_\alpha, \frac{1}{2}t_\beta|T, M_T\right)|\mathbf{p}, \mathbf{Q}; S, M_S, T, M_T\rangle \tag{A.39}$$

The next step consists of performing an expansion of $|\mathbf{p}\rangle$ in terms of the eigenstates of the orbital momentum, labeled by $|LM_L\rangle$. Hence,

$$|\mathbf{p}\rangle = \sum_{LM_L}\langle pLM_L|\mathbf{p}\rangle\,|pLM_L\rangle = \sum_{LM_L} Y^*_{LM_L}(\hat{\mathbf{p}})\,|pLM_L\rangle \tag{A.40}$$

where Y_{LM_L} are the spherical harmonics, $p = |\mathbf{p}|$ and $\hat{\mathbf{p}}$ is the direction identified by $\mathbf{p}$. Thus

$$\begin{aligned}|\alpha\beta\rangle = &\sum_{SM_S}\sum_{TM_T}\sum_{LM_L}\left(\frac{1}{2}s_\alpha, \frac{1}{2}s_\beta|S, M_S\right)\left(\frac{1}{2}t_\alpha, \frac{1}{2}t_\beta|T, M_T\right)\\ &Y^*_{LM_L}(\hat{\mathbf{p}})\,|p, L, M_L, S, M_S, T, M_T\rangle\,|\mathbf{K}\rangle\,.\end{aligned} \tag{A.41}$$

Swapping α and β in Eq. (A.41) gives

$$\begin{aligned}|\beta\alpha\rangle = |-\mathbf{p}, \mathbf{K}; s_\beta, t_\beta, s_\alpha, t_\alpha\rangle = &\sum_{SM_S}\sum_{TM_T}\sum_{LM_L}(-1)^{S+T+L}\\ &\left(\frac{1}{2}s_\alpha, \frac{1}{2}s_\beta|S, M_S\right)\left(\frac{1}{2}t_\alpha, \frac{1}{2}t_\beta|T, M_T\right)Y^*_{LM_L}(\hat{\mathbf{p}})\,|p, L, M_L, S, M_S, T, M_T\rangle\,|\mathbf{K}\rangle\,.\end{aligned} \tag{A.42}$$

We have used the symmetry properties [253]

$$\left(\frac{1}{2}s_\beta, \frac{1}{2}s_\alpha|S, M_S\right) = (-1)^{S-1}\left(\frac{1}{2}s_\alpha, \frac{1}{2}s_\beta|S, M_S\right), \tag{A.43}$$

$$\left(\frac{1}{2}t_\beta, \frac{1}{2}t_\alpha|T, M_T\right) = (-1)^{T-1}\left(\frac{1}{2}t_\alpha, \frac{1}{2}t_\beta|T, M_T\right), \tag{A.44}$$

$$Y_{LM_L}(-\hat{\mathbf{p}}) = (-1)^L\,Y_{LM_L}(\hat{\mathbf{p}}). \tag{A.45}$$

Therefore, the antisymmetrized state $|\alpha\beta\rangle_A$ reads

$$\begin{aligned}|\alpha\beta\rangle_A = &\sum_{JM_J}\sum_{SM_S}\sum_{TM_T}\sum_{LM_L}\left[1-(-1)^{S+T+L}\right]\left(\frac{1}{2}s_\alpha, \frac{1}{2}s_\beta|S, M_S\right)\left(\frac{1}{2}t_\alpha, \frac{1}{2}t_\beta|T, M_T\right)\\ &(LM_L, SM_S|JM_J)\,Y^*_{LM_L}(\hat{\mathbf{p}})\,|p, L, M_L, S, M_S, T, M_T\rangle\,|\mathbf{K}\rangle\,,\end{aligned} \tag{A.46}$$

where the equalities $M_S = s_\alpha + s_\beta$, $M_T = t_\alpha + t_\beta$ and $M_J = M_S + M_L$ have to be satisfied.

Now, $\bar{v}_{\alpha\beta,\gamma,\delta}$ is conveniently expressed in terms of the doubly antisymmetric matrix elements as $\bar{v}_{\alpha\beta,\gamma,\delta} = 1/2\,{}_A\langle\alpha\beta|\,V\,|\gamma\delta\rangle_A$, which can be evaluated using the kets Eq. (A.46). Finally, we obtain the following formula [14, 83]:

$$\langle\alpha\beta|\,V\,|\gamma\delta\rangle_A = \frac{1}{2}\sum_{JM_J}\sum_{S}\sum_{T}\sum_{LM_L}\sum_{L'M'_L}\left[1-(-1)^{S+T+L}\right]\left[1-(-1)^{S+T+L'}\right] \tag{A.47}$$
$$\left(\frac{1}{2}s_\alpha,\frac{1}{2}s_\beta|S,M_S\right)\left(\frac{1}{2}t_\alpha,\frac{1}{2}t_\beta|T,M_T\right)(LM_L,SM_S|JM_J)$$
$$\left(\frac{1}{2}s_\gamma,\frac{1}{2}s_\delta|S,M'_S\right)\left(\frac{1}{2}t_\gamma,\frac{1}{2}t_\delta|T,M'_T\right)(L'M'_L,SM'_S|JM_J)$$
$$Y_{LM_L}(\hat{\mathbf{p}})Y^*_{L'M'_L}(\hat{\mathbf{p}}')\,\langle p|V^{JSTM_T}_{LL'}|p'\rangle$$

where it is understood that the total momentum and the isospin projection must be conserved, i.e.

$$\mathbf{k}_\alpha+\mathbf{k}_\beta=\mathbf{k}_\gamma+\mathbf{k}_\delta, \tag{A.48}$$
$$M_T=t_\alpha+t_\beta=t_\gamma+t_\delta, \tag{A.49}$$

and the angular momentum projections are understood as

$$M_S=s_\alpha+s_\beta, M'_S=s_\gamma+s_\delta, \tag{A.50}$$
$$M_L=M_J-M_S, M_L\prime=M_J-M'_S. \tag{A.51}$$

APPENDIX B

Details on the static response theory

The purpose of this Appendix is to complement and extend the discussion on the theory of the static response presented in Sec. 1.4. In Sec. B.1, we derive the equation (1.21), that relates the energy of a perturbed system to the static response function. In Sec. B.2, we present a formalism for defining the static response function within a DFT approach and show how the static response enters the gradient expansion of the EDF. This approach is applied in Sec. B.3.1 to derive RPA-like equations for the static response, and explicit expressions for $\chi(q)$ are obtained in the cases of LDA EDFs (Sec. B.3.1) and functionals with density-gradient terms (Sec. B.3.2). Then, in Sec. B.4 the compressibility sum rule, which relates $\chi(q=0)$ to the EOS, is discussed. Finally, in Sec. B.5 we show that, in the case of the DFT calculations of Ch. 7, the static response can be extracted fitting either the energy or the density of perturbed matter.

B.1 Perturbed energies and static response function

In this Section, we derive the key equation (1.21) that connects the energy of the perturbed system to the static response function. Starting from Eq. (1.15), the static response function can be defined in terms of the perturbed density as [60]

$$\chi(\mathbf{x},\mathbf{x}') = \left.\frac{\delta\rho(\mathbf{x})}{\delta v(\mathbf{x}')}\right|_{v=0}. \tag{B.1}$$

We now want to prove that the energy is quadratic with respect to the external perturbation. To show this, another useful identity is

$$\frac{\delta E}{\delta v(\mathbf{x})} = \rho(\mathbf{x}), \tag{B.2}$$

that can be easily understood noting that the potential can enter the total energy only with the term $\int d\mathbf{x} v(\mathbf{x})\rho(\mathbf{x})$. Differentiating Eq. (B.2) again,

$$\frac{\delta\rho(\mathbf{x})}{\delta v(\mathbf{x}')} = \frac{\delta^2 E}{\delta v(\mathbf{x})\,\delta v(\mathbf{x}')}. \tag{B.3}$$

Evaluating Eqs. (B.2) and (B.3) at $v=0$, we thus find

$$\rho_0 = \left.\frac{\delta E}{\delta v(\mathbf{x})}\right|_{v=0}, \qquad \chi(\mathbf{x},\mathbf{x}') = \left.\frac{\delta^2 E}{\delta v(\mathbf{x})\,\delta v(\mathbf{x}')}\right|_{v=0}. \tag{B.4}$$

Now, we perform a functional Taylor expansion of $E[v]$ around the unperturbed state [77] up to second order:

$$\begin{aligned} E[v] - E[0] = &\int d\mathbf{x} \left.\frac{\delta E}{\delta v(\mathbf{x})}\right|_{v=0} v(\mathbf{x}) + \\ &\frac{1}{2}\int d\mathbf{x}\int d\mathbf{x}' \left.\frac{\delta^2 E}{\delta v(\mathbf{x})\,\delta v(\mathbf{x}')}\right|_{v=0} v(\mathbf{x})v(\mathbf{x}'). \end{aligned} \tag{B.5}$$

Plugging Eq. (B.4) into the previous equation, we obtain

$$\begin{aligned} E[v] - E[0] = &\int d\mathbf{x} v(\mathbf{x})\rho_0 + \\ &\frac{1}{2}\int d\mathbf{x}\int d\mathbf{x}' \chi(\mathbf{x},\mathbf{x}')v(\mathbf{x})v(\mathbf{x}'), \end{aligned} \tag{B.6}$$

and we immediately see that the first-order term vanishes, v being periodic. A different argument is presented in Ref. [34], which proves the cancellation of the linear contribution in general terms. Thus, we have verified that the energy of the perturbed system is quadratic as a function of v. This is consistent with the picture of a small perturbation around an equilibrium state, i.e. the g.s. of the unperturbed Hamiltonian. Moreover, we remind that χ must be negative and the homogeneous matter response depends only on $\mathbf{x}-\mathbf{x}'$ due to translational invariance, i.e $\chi(\mathbf{x},\mathbf{x}')=\chi(\mathbf{x}-\mathbf{x}')$.

Then one can transform Eq. (B.6) to momentum space inserting the Fourier expansions

$$\delta\rho(\mathbf{x})=\sum_{\mathbf{k}}\rho_{\mathbf{k}}e^{i\mathbf{k}\cdot\mathbf{x}},\quad v(\mathbf{x})=\sum_{\mathbf{k}}v_{\mathbf{k}}e^{i\mathbf{k}\cdot\mathbf{x}} \tag{B.7}$$

$$\chi(\mathbf{x}-\mathbf{x}')=\frac{1}{\Omega}\sum_{\mathbf{k}}\chi(\mathbf{k})e^{i\mathbf{k}\cdot(\mathbf{x}-\mathbf{x}')}. \tag{B.8}$$

Then

$$E[v]-E[0]=\frac{\Omega}{2}\sum_{\mathbf{k}}v_{\mathbf{k}}\chi(\mathbf{k})v_{-\mathbf{k}}. \tag{B.9}$$

If the monochromatic potential (1.18) is considered in place of a generic perturbation, and if the relations $\rho_0=A/\Omega$ and $\chi=\chi(|\mathbf{q}|)$ that hold for uniform matter are employed, we find that the energy per particle of the perturbed system is given by [77]

$$\delta e_v=e_v-e_0=\frac{\chi(q)}{\rho_0}v_q^2. \tag{B.10}$$

Similarly, it follows from Eq. (B.7) that only the $\mathbf{k}=\pm\mathbf{q}$ components of $\delta\rho(\mathbf{x})$ are non-vanishing, and from the Fourier transform of Eq. (1.15) we find

$$\rho_q=\chi(q)v_q. \tag{B.11}$$

B.2 Connection between the static response function and the EDF

The static response function in the DFT framework and its connection to the gradient terms of the EDF are the subjects of this Section. We consider the case of the expansion around an unperturbed uniform state, and for simplicity neglect the the dependency on kinetic densities and spin-orbit densities. Also, we describe the system in terms of the total number density. This is sufficient to derive some key relations that allow to gain insights into the relevance of the static response. The formalism could also be extended easily to include different one-body densities.

For the sake of presentation, we write the total energy in the presence of the external potential as [155]

$$E[v]=F[\rho]+V_{ext}\Big|_{\rho=\rho[v]}, \tag{B.12}$$

where $F[\rho]$ denotes the internal (kinetic+potential) energy of the system [34],

$$F[\rho]=E_{kin}+E_{pot}, \tag{B.13}$$

and V_{ext} is the contribution due to the external potential,

$$V_{ext}=\int d\mathbf{x}\,v(\mathbf{x})\rho(\mathbf{x}). \tag{B.14}$$

As it will become apparent, it is important to stress that the density, and all terms in Eq. (B.12), must be ultimately considered as functionals of the potential v. $F[\rho]$ is, in essence, the EDF, and, to establish a connection between F and the energy as a functional of v, it is essential to apply the framework of the Legendre transform [256, 257]. This is similar to what is done to define the thermodynamical potentials. We remind that the unperturbed state is characterized by $v=0$ and, equivalently, $\rho(\mathbf{x})=\rho_0$. Also, we assume that ρ_0 is uniform (homogeneous matter).

Eq. (B.12) can also be written as

$$F[\rho]=E[v]-\int d\mathbf{x}\,v(\mathbf{x})\rho(\mathbf{x})\Big|_{v=v[\rho]}, \tag{B.15}$$

where both F and the r.h.s. are meant as functionals of the density. We evaluate the functional derivatives of F for later convenience. For the first-order derivative, using the chain rule and Eq. (B.2):

$$\frac{\delta F}{\delta\rho(\mathbf{x})} = \int d\mathbf{x}' \frac{\delta E}{\delta v(\mathbf{x}')}\frac{\delta v(\mathbf{x}')}{\delta\rho(\mathbf{x})} - v(\mathbf{x}) - \int d\mathbf{x}' \frac{\delta v(\mathbf{x}')}{\delta\rho(\mathbf{x})}\rho(\mathbf{x}') = -v(\mathbf{x}). \tag{B.16}$$

The second derivative, evaluated on the unperturbed states, then reads

$$K(\mathbf{x},\mathbf{x}') \equiv \frac{\delta^2 F}{\delta\rho(\mathbf{x})\,\delta\rho(\mathbf{x}')}\bigg|_{\rho(\mathbf{x})=\rho_0} = -\frac{\delta v(\mathbf{x})}{\delta\rho(\mathbf{x}')}\bigg|_{\rho(\mathbf{x})=\rho_0}, \tag{B.17}$$

where we have introduced the kernel $K(\mathbf{x},\mathbf{x}')$. There is a relation between K and the static response function, that we are now going to determine. We start from the identity

$$\int d\mathbf{y} \frac{\delta v(\mathbf{x})}{\delta\rho(\mathbf{y})}\frac{\delta\rho(\mathbf{y})}{\delta v(\mathbf{x}')} = \delta^{(3)}(\mathbf{x}-\mathbf{x}'), \tag{B.18}$$

we evaluate at $v=0$ and $\rho=\rho_0$, and the we insert Eqs. (B.17) and (B.2). Thus, we find that

$$\int d\mathbf{y} K(\mathbf{x},\mathbf{y})\chi(\mathbf{y},\mathbf{x}') = -\delta^{(3)}(\mathbf{x}-\mathbf{x}'). \tag{B.19}$$

This means that the kernel and the static response are, in a functional sense, the inverse of each other with opposite signs, and we can write synthetically

$$K\cdot\chi = -\mathbb{1}. \tag{B.20}$$

Note that, while χ is a function, the kernel is in general an operator, as we shall see. Eq. (B.20) does not hold by chance, but it is actually a general property of Legendre transforms [256], which is exploited e.g. in the effective action formalism of quantum field theory [55]. The importance of Eq. (B.20) can be understood if we Taylor-expand $F[\rho]$. By the same argument as before, the first-order term is null, and we are left with the second-order contribution,

$$\begin{aligned} F[\rho] - F[\rho_0] = \frac{1}{2}\int d\mathbf{x}\int d\mathbf{x}' K(\mathbf{x},\mathbf{x}')\delta\rho(\mathbf{x})\delta\rho(\mathbf{x}') = \\ -\frac{1}{2}\int d\mathbf{x}\int d\mathbf{x}' \chi^{-1}(\mathbf{x},\mathbf{x}')\delta\rho(\mathbf{x})\delta\rho(\mathbf{x}'). \end{aligned} \tag{B.21}$$

The expansion parameter is $\delta\rho = \rho - \rho_0$. Note that, at an intuitive level, this formula could have been found using $\rho = \chi v$ to replace v with ρ in Eq. (B.5). K is a positive function, so that the energy increases as the reference state is perturbed. This is consistent with the unperturbed state being a stable equilibrium point [34]. This argument was contained in essence already in the original paper by Hohenberg and Kohn [150], where a relation between the EDF kernel and the electronic polarizability was sought. This result states that the universal part of the EDF is intrinsically related to the response of a system to external perturbations, and it suggests that some information about the EDF may be gained by studying the response of homogeneous matter subject to a static perturbation. Applying the Fourier transform to Eq. (B.21), we get

$$F[\rho] - F[\rho_0] = \frac{\Omega}{2}\sum_{\mathbf{k}} \rho_{\mathbf{k}} K(\mathbf{k}) \rho_{-\mathbf{k}}. \tag{B.22}$$

Also, in momentum space Eq. (B.20) reads

$$K(k) = -\frac{1}{\chi(k)}. \tag{B.23}$$

It can be shown that $K = K(k)$ admits an expansion in powers of the wave number for small k, starting from k^2, namely $K(k) = K_0 + c_2 k^2 + c_4 k^4 + \ldots$. The coefficients, in principle, can be determined by studying the low-momentum behavior of the static response function $\chi(k)$ and using Eq. (B.23). Transforming back to real space, we can use the correspondence $q^2 \longrightarrow -\nabla^2$, so that at quadratic order the EDF has the form

$$F[\rho] - F[\rho_0] = -\frac{c_2}{2}\int d\mathbf{x} |\nabla\rho(\mathbf{x})|^2, \tag{B.24}$$

with $c_2 < 0$. Thus, the standard quadratic gradient corrections to the EDF have been derived, and the low-momentum static response of the reference system in principle allows us to fix the gradient term. This formal argument suggests that perturbed matter calculations, as well as the knowledge of the static response of homogeneous matter, may allow to get information on the EDF applicable to inhomogeneous systems.

B.3 Response equations in the EDF framework

We apply the formalism outlined in Sec. B.2 and derive the RPA equations for the static response function. We stress again that this is a somewhat simplified treatment, where only the dependence on a single number density is considered. Full studies of the response of nuclear matter in DFT can be found e.g. in Ref. [124] and references therein. A similar approach is also used in solid-state physics, see e.g. Refs. [34, 136].

The EDF $F[\rho]$ is broken down as the sum of kinetic and potential energy terms, Eq. (B.13). The kernel, and similarly the static response, are broken down as the sum of a free contribution K_0, χ_0 and a potential contribution K_{pot}, χ_{pot}. Thus,

$$K(\mathbf{x},\mathbf{x}') = K_0(\mathbf{x},\mathbf{x}') + K_{pot}(\mathbf{x},\mathbf{x}'), \tag{B.25}$$

where

$$K_0(\mathbf{x},\mathbf{x}') = \frac{\delta^2 E_{kin}}{\delta\rho(\mathbf{x})\,\delta\rho(\mathbf{x}')}, \tag{B.26}$$

$$K_{pot}(\mathbf{x},\mathbf{x}') = \frac{\delta^2 E_{pot}}{\delta\rho(\mathbf{x})\,\delta\rho(\mathbf{x}')}. \tag{B.27}$$

From Eq. (B.20), we have $\chi = -1/K$ and $\chi_0 = -1/K_0$. We can then multiply (in an operator sense) Eq. (B.20) to the left by χ and to the right by χ_0. Simple algebra allows to find the following familiar-looking equation [136]:

$$\chi = \chi_0 + \chi_0 K_{pot} \chi. \tag{B.28}$$

The functional derivative approach has allowed us to determine the RPA equations for the static response. The kernel K_{pot} can be interpreted as an effective interaction (or residual particle-hole interaction [124]) stemming from the EDF. In the case of homogeneous matter, and under our assumption that K_{pot} only depends on the number density, these can be immediately solved to give

$$\chi(q) = \frac{\chi_0(q)}{1 - \chi_0(q) K_{pot}(q)}. \tag{B.29}$$

In App. B.3.1 we calculate the interaction kernel for LDA EDFs, and in App. B.3.2 we evaluate it for EDFs including density-gradient terms. The full case where effective mass and spin-orbit terms are included, which is important for nuclear physics, is more complicated and is discussed in Ref. [124].

The response equations (B.28) hold for both finite and infinite systems. Clearly, the χ_0 and χ functions differ whether we are using a finite particle number or computing them in the TL, but it is important to stress that the equations remain valid in both scenarios. K_{pot} can be computed explicitly from Eq. (B.27) when E_{pot} is a functional of ρ only. Once we have determined the kernel, it is straightforward to find the resulting response function. The free response χ_0 for fermions is not an explicit function of the density, as the kinetic energy involves the kinetic density τ. However, it can be computed with second-order perturbation theory, and it amounts for finite-A systems to Eq. (1.23) and in the TL to the Lindhard function (1.25), see Sec. 1.4. For bosons, instead, it can be computed directly from the definition, and for completeness, we derive it in Sec. B.3.3.

We mention that formulas for extrapolating from the finite-A response to the TL response have been devised that exploit the fact that FS effects affect mostly the kinetic terms, while they are relatively smaller on the potential term, see e.g. Refs. [77, 133]. The idea, inspired by the EDF response, is to parametrize a set of calculations of the static response in the finite-A system, typically coming from *ab initio* (QMC), in the form (B.29), i.e.

$$\chi_A(q) = \frac{\chi_{0,A}(q)}{1 - \chi_{0,A}(q) K_{pot,A}(q)}, \tag{B.30}$$

where $K_{pot,A}(q)$ is extracted from $\chi_A(q)$. Similarly, for the TL one writes

$$\chi_{TL}(q) = \frac{\chi_{0,TL}(q)}{1 - \chi_{0,TL}(q) K_{pot,TL}(q)}. \tag{B.31}$$

Now, one makes the hypothesis that FS effects are mild on the kernel. This sounds reasonable, as K_{pot} describes short-range 2B interactions that should be only weakly affected by the shell structure of the system [1]. Thus,

[1] Nuclear interactions are indeed short-ranged. In electronic systems, slightly different equations are used, in which one focuses on the so-called local field correction(LFC) [77, 78]. The LFC describes the exchange and correlation effects, which are short-ranged, too.

we assume $K_{pot,TL}(q) \approx K_{pot,A}(q)$ and insert

$$K_{pot,TL}(q) = K_{pot,A}(q) = \frac{1}{\chi_{0,A}(q)} - \frac{1}{\chi_A(q)} \tag{B.32}$$

into the TL relation (B.31). Finally, we get the formula [133]

$$\chi_{TL}(q) = \frac{\chi_{0,TL}(q)}{1 + \chi_{0,TL}(q)\left[\frac{1}{\chi_A(q)} - \frac{1}{\chi_{0,A}(q)}\right]}. \tag{B.33}$$

This recipe has been applied in several studies of the electron gas to infer the TL response from finite-A results [77, 133, 172]. In nuclear physics, it has never been used, and unfortunately it is somewhat ineffective since it does not take into account the generalized densities. Other extrapolation recipes have been presented in Refs. [75, 76].

B.3.1 Response for LDA EDFs

We derive the explicit expression for the static response of LDA EDFs in infinite nuclear matter using the previously outlined formalism. Since the LDA EDF is a functional of just the number density, simple formulas that hold for both SNM and PNM can be determined. The LDA EDF (Sec. 2.2.1) contains just the density-dependent terms and reads, for the cases of SNM or PNM (i.e. single-component systems),

$$E_{LDA} = \int d\mathbf{x} \sum_\gamma c_\gamma \rho^{\gamma+1}(\mathbf{x}). \tag{B.34}$$

It is straightforward to find K_{pot} following its definition (B.27): we compute the second derivative of the energy and evaluate it on the constant density $\rho(\mathbf{x}) = \rho_0$,

$$K_{pot}(\mathbf{x}, \mathbf{x}') = \sum_\gamma c_\gamma \gamma(\gamma+1)\rho_0^{\gamma-1}\delta^{(3)}(\mathbf{x} - \mathbf{x}'). \tag{B.35}$$

The Fourier transform is momentum-independent,

$$K_{bulk} = \sum_\gamma c_\gamma \gamma(\gamma+1)\rho_0^{\gamma-1}, \tag{B.36}$$

and coincides with the K_{bulk} term of Eq. (C.42). The static response reads

$$\chi(q) = \frac{\chi_0(q)}{1 - K_{bulk}\chi_0(q)}. \tag{B.37}$$

It is easy to verify that this formula matches Eq. (C.42) when setting $C^{\nabla J} = C^{\Delta\rho} = C^\tau = 0$ and replacing χ_0 with the Lindhard function (1.25). However, Eq. (B.37) is more general as it is valid also in finite-A systems.

B.3.2 Response for EDFs with gradient corrections

We add to the LDA EDF (B.34) the gradient correction

$$E_{\Delta\rho} = C^{\Delta\rho}\int d\mathbf{x}\rho(\mathbf{x})\Delta\rho(\mathbf{x}) = -C^{\Delta\rho}\int d\mathbf{x}|\nabla\rho(\mathbf{x})|^2. \tag{B.38}$$

The corresponding kernel $K_{\Delta\rho}$ is now evaluated. The first functional derivative reads

$$\frac{\delta E_{\delta\rho}}{\delta\rho(\mathbf{x})} = 2C^{\Delta\rho}\nabla^2\rho(\mathbf{x}). \tag{B.39}$$

The second derivative is given by

$$\frac{\delta^2 E_{\delta\rho}}{\delta\rho(\mathbf{x})\,\delta\rho(\mathbf{x}')} = 2C^{\Delta\rho}\nabla^2_{\mathbf{x}}\delta^{(3)}(\mathbf{x} - \mathbf{x}') \tag{B.40}$$

Note that, correctly, local EDFs produce zero-range kernels. The Fourier transform reads

$$K_{\Delta\rho}(q) = -2C^{\Delta\rho}q^2 \tag{B.41}$$

and play the role of a repulsive momentum-dependent interaction ($C^{\Delta\rho} < 0$, as the contribution of Eq. (B.38) must be repulsive). Finally, the static response is given by

$$\chi(q) = \frac{\chi_0(q)}{1 - (K_{bulk} - 2C^{\Delta\rho}q^2)\chi_0(q)}. \tag{B.42}$$

Again, it is possible to verify that in the TL this is equal to Eq. (C.42) with $C^{\nabla J} = C^{\tau} = 0$. Unfortunately, with the approach here outlined we are unable to treat the response in the case of EDFs including effective mass and spin-orbit terms, as τ and $\mathbf{J}$ cannot be written as explicit functionals of the density.

B.3.3 Free response for bosons

We derive the free response function for a uniform system of bosons. The result is contained e.g. in Ref. [137], in the first term of Eq. (6) (with a different normalization). The wave function of non-interacting bosons at zero temperature is simply given by

$$\psi(\mathbf{x}) = \sqrt{\rho(\mathbf{x})}e^{i\theta}, \tag{B.43}$$

where θ is a global phase. Thus, the kinetic energy can be computed as

$$E_{kin}[\rho] = \frac{\hbar^2}{2m}\int d\mathbf{x}\left|\nabla\sqrt{\rho(\mathbf{x})}\right|^2 = \frac{\hbar^2}{2m}\int d\mathbf{x}\left|\frac{\nabla\rho(\mathbf{x})}{2\sqrt{\rho(\mathbf{x})}}\right|^2 = \frac{\hbar^2}{8m}\int d\mathbf{x}\frac{|\nabla\rho(\mathbf{x})|^2}{\rho(\mathbf{x})}. \tag{B.44}$$

E_{kin} is an explicit functional of the density, and we can thus determine the static response by first evaluating the kernel (B.26) using its definition. The first functional derivative reads

$$\begin{aligned}\frac{\delta E_{kin}}{\delta\rho(\mathbf{x})} &= \frac{\partial\mathcal{E}_{kin}}{\partial\rho} - \nabla\cdot\frac{\partial\mathcal{E}_{kin}}{\partial\nabla\rho} \\ &= \frac{\hbar^2}{8m}\left(-\frac{|\nabla\rho|^2}{\rho^2} - \nabla\cdot\left(2\frac{\nabla\rho}{\rho}\right)\right) \\ &= \frac{\hbar^2}{8m}\left(\frac{|\nabla\rho|^2}{\rho^2} - 2\frac{\nabla^2\rho}{\rho}\right).\end{aligned} \tag{B.45}$$

(B.46)

where we have used the Euler-Lagrange formula and $\mathcal{E}_{kin}$ is the energy density associated to E_{kin}

$$\mathcal{E}_{kin} = \frac{\hbar^2}{8m}\frac{|\nabla\rho(\mathbf{x})|^2}{\rho(\mathbf{x})}. \tag{B.47}$$

We now have to compute the second derivative and evaluate it for $\rho(\mathbf{x}) = \rho_0$. Since for ρ_0 is uniform, terms that contain gradients of the density do not contribute to K_0. In practice, only one term survives, and we get

$$K_0(\mathbf{x},\mathbf{x}') = -\frac{\hbar^2}{4m}\frac{\nabla^2}{\rho_0}\delta^{(3)}(\mathbf{x}-\mathbf{x}'). \tag{B.48}$$

It is convenient to transform to momentum space, so that $\nabla^2 \longrightarrow -q^2$. Thus,

$$K(q) = \frac{\hbar^2 q^2}{4m\rho_0} \tag{B.49}$$

Finally, we obtain the static response function for uniform matter of free bosons:

$$\chi(q) = -\frac{1}{K(q)} = -\frac{\rho_0}{\hbar^2q^2/(4m)}. \tag{B.50}$$

B.4 Compressibility sum rule

The compressibility sum rule (CSR), which has been discussed in detail in Refs. [76, 79], relates the static response at zero momentum to the properties of unperturbed matter:

$$-\frac{1}{\chi(0)} = \frac{1}{\rho}\frac{\partial P}{\partial\rho} = \frac{\partial^2}{\partial\rho^2}(\rho e). \tag{B.51}$$

EDF	L	K_0	K_{sym}	$-\chi(0)/\rho$ (SNM)	$-\chi(0)/\rho$ (PNM)
SLy4	45.94	229.91	−119.73	0.0391	0.0233
SkM*	45.78	216.61	−155.94	0.0415	0.0268
SkI3	100.53	258.19	73.04	0.0348	0.00963

Table B.1: Infinite nuclear matter coefficients L, K_0 and K_{sym} (in MeV) and CSR $-\chi(0)/\rho$ (in MeV^{-1}) in SNM and PNM for three EDFs. The coefficients are taken from Ref. [258].

We comment on how to evaluate the CSR. The r.h.s. of Eq. (B.51) is written as

$$\frac{\partial^2}{\partial\rho^2}(\rho e) = \frac{\partial^2}{\partial\rho^2}(\rho t) + \frac{\partial^2}{\partial\rho^2}(\rho v). \tag{B.52}$$

The kinetic energy per particle t is proportional to $k_F^2 \sim \rho^{2/3}$, thus

$$\frac{\partial^2}{\partial\rho^2}(\rho t) = \frac{10}{9}\frac{t}{\rho} \tag{B.53}$$

at fixed β, in both the TL and the finite-A system. Note that in the TL $\frac{\partial^2}{\partial\rho^2}(\rho t) = -1/\chi_0(q=0)$, where the limit for $q \longrightarrow 0$ can be taken directly in the Lindhard function χ_0, Eq. (1.25). In the finite systems, instead, as q is discrete it is impossible to evaluate the response directly at zero momentum, and one must necessarily resort to the previous formula. As for the potential term, we immediately get, using Eq. (2.16), that $\frac{\partial^2}{\partial\rho^2}(\rho v)$ is equal to K_{bulk}, Eq. (C.32). Therefore, in our case the CSR for a given EDF reads

$$-\frac{1}{\chi(0)} = \frac{10t}{9\rho} + K_{bulk}. \tag{B.54}$$

Next, we relate the CSR to the infinite matter parameters of an EDF, namely L, K_0 and K_{sym} (see Refs. [38, 258] and below). First, we write

$$-\frac{1}{\chi(0)/\rho} = 2\rho\frac{\partial e}{\partial\rho} + \rho^2\frac{\partial^2 e}{\partial\rho^2}. \tag{B.55}$$

Then, we use $\frac{\partial e}{\partial\rho} = 0$ and $K_0 = 9\rho^2\frac{\partial^2 e}{\partial\rho^2}$ in SNM, and $L = 3\rho\frac{\partial e}{\partial\rho}$ and $K_{PNM} = K_0 + K_{sym} = 9\rho^2\frac{\partial^2 e}{\partial\rho^2}$ in PNM. Finally,

$$-\frac{1}{\chi(0)/\rho} = \frac{K_0}{9} \qquad \text{(SNM)}, \tag{B.56}$$

$$-\frac{1}{\chi(0)/\rho} = \frac{2}{3}L + \frac{K_0 + K_{sym}}{9} \qquad \text{(PNM)}. \tag{B.57}$$

In Tab. B.1 we report the nuclear matter coefficients, taken from Ref. [258], and calculate the corresponding zero-momentum responses for the three representative EDFs discussed in Sec. 7.3. One can note that SNM values are consistent, while in SkI3 the PNM response is smaller by a value of 2 from that of the other two EDFs. This can be traced to SkI3 having a positive K_{sym} coefficient and a slope L twice as large as that of SLy4 and SkM*.

B.5 Static response from density and energy fits

The static response can be extracted either from the energies or the densities of the perturbed system. In the results presented in Sec. 7, $\chi(q)$ was obtained by energy changes. In this Section, we discuss fits of the density changes and show evidence that the two techniques give close outcomes.

In the linear response regime, the relation Eq.(1.20) holds and relates the Fourier component of the density fluctuation of the same momentum $\mathbf{q}$ as that of the external potential. If non-linear effects come into play, also higher-order harmonics are excited [259]. In order to extract $\chi(q)$, calculations are performed at a given momentum q for several strengths v_q and the corresponding densities $\delta\rho(z)$ are Fourier-transformed, i.e.

$$\rho_k = \frac{1}{L}\int dz\, \delta\rho(z) e^{-ikz}. \tag{B.58}$$

Then, the component with $k = q$ is selected. Other harmonics would be related to non-linear contributions and do not involve the function $\chi(q)$, as discussed in Ref. [259]. Finally, a linear fit to the amplitudes ρ_q as a function of v_q is performed.

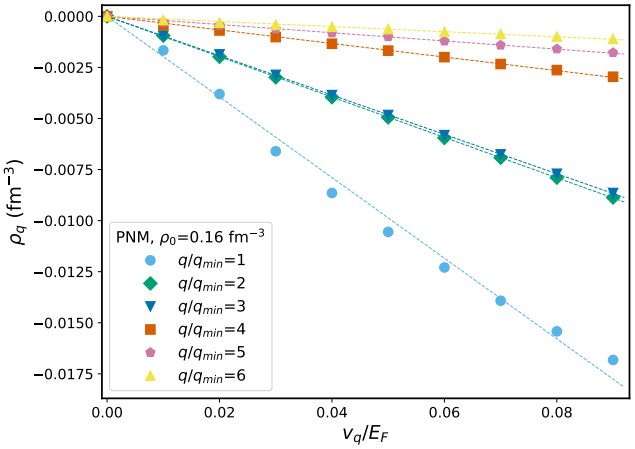

Figure B.1: Density amplitudes ρ_q as a function of the perturbation strength v_q/E_F in PNM (N=66 neutrons) at a reference density $\rho_0 = 0.16$ fm^{-3} for the SLy4 EDF for different moments q/q_{min}. Markers: results of the DFT calculations. Dashed lines: linear fits to the data points.

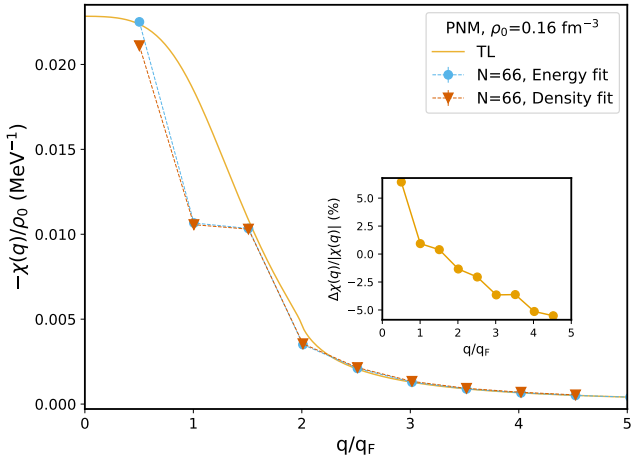

Figure B.2: Static response function $-\chi(q)/\rho_0$ extracted from fits to the energies (circles) and densities (triangles) of the perturbed system. The TL response is also shown for comparison. Inset: relative difference (in percentage) between the response function from density fits and energy fits ($\Delta\chi/|\chi|$).

.

We have studied the case of PNM with N=66 neutrons at a reference density $\rho_0 = 0.16$ fm^{-3} for the SLy4 EDF. Calculations for v_q/E_F between 0.01 and 0.1 have been performed. In Fig. B.1 the density amplitudes ρ_q are shown as a function of the perturbation strength for different momenta as markers. Dashed lines represent linear fits to the data. A distinct linear trend of the amplitudes can be noted in all cases, with some fluctuations appearing only for $q/q_{min} = 1$. Indeed, the response is strongest at $q/q_{min} = 1$ (about two times stronger than for $q/q_{min} = 2$, see Figs. 7.13 and B.2). As a consequence, non-linear effects are expected to play a relevant role in this case even for moderate perturbation strengths. In Fig. B.1, in particular, they manifest themselves in mild deviations of the amplitudes from the linear trend. These deviations are also similar to those observed in the energies per particle for $q/q_{min} = 1$ in the FG case (Fig. 7.5).

In Fig. B.2 we compare the response function extracted from fits to the density (triangles) and the energy (circles). In the inset, the relative discrepancy between the two fits, i.e.

$$\frac{\Delta\chi}{\chi} = \frac{-\chi_{Energy} + \chi_{Density}}{(\chi_{Energy} + \chi_{Density})/2}, \tag{B.59}$$

is shown. It can be appreciated that it remains within a modest 5% and, except the first allowed momentum $2\pi/L$, is much smaller for the momenta below $3k_F$. We conclude that the two ways to extract the response function essentially agree.

APPENDIX C

Details on Density functional theory

In this Appendix, details on nuclear DFT are provided. In Sec. C.1, the mean field and the rearrangement energy for the LDA and GA EDFs discussed in Sec. 2.2 are derived. Sec. C.2 complements Sec. 2.3 and gives details on the application of DFT to infinite nuclear matter(SNM and PNM specifically). Sec. C.3 reports the static response function of Skyrme-like EDFs in the TL.

C.1 Mean field and rearrangement energy of LDA and GA EDFs

In this Section, we derive the mean field and the rearrangement energy term for the LDA and GA EDFs described in Sec. 2.2.1 and 2.2.2.

C.1.1 LDA mean field potential

We derive the mean field potential $U_q(\mathbf{x})$ for the LDA EDF Sec. 2.2.1. By definition:

$$U_q(\mathbf{x}) = \frac{\delta E_{bulk}}{\delta \rho_q(\mathbf{x})} = \frac{\partial \mathcal{E}_{bulk}}{\partial \rho_q} = \frac{\partial \mathcal{E}_{bulk}}{\partial \rho} + \frac{\partial \beta}{\partial \rho_q}\frac{\partial \mathcal{E}_{bulk}}{\partial \beta} \tag{C.1}$$

with q=n, p. Using $\rho = \rho_n + \rho_p$ and $\beta = \frac{\rho_n - \rho_p}{\rho}$, the chain rule leads to the following contributions:

$$\begin{aligned} &\frac{\partial \beta}{\partial \rho_q} = \frac{1}{\rho}\frac{\partial}{\partial \rho_q}(\rho_n - \rho_p) + \\ &(\rho_n - \rho_p)\left(-\frac{1}{\rho^2}\right)\frac{\partial \rho}{\partial \rho_q} = \frac{\tau_z - \beta}{\rho}, \end{aligned} \tag{C.2}$$

$$\frac{\partial \mathcal{E}_{loc}}{\partial \rho} = \sum_\gamma (\gamma+1)\, c_\gamma(\beta)\rho^\gamma, \tag{C.3}$$

$$\frac{\partial \mathcal{E}_{loc}}{\partial \beta} = \sum_\gamma \frac{\partial c_\gamma(\beta)}{\partial \beta}\rho^\gamma = 2\beta \sum_\gamma c_{\gamma,1}\rho^{\gamma+1}, \tag{C.4}$$

where $\tau_z = +1$ for neutrons and $\tau_z = -1$ for protons. Therefore

$$\begin{aligned} U_q = \sum_\gamma (\gamma+1)c_\gamma(\beta)\rho^\gamma + (\tau_z - \beta)\, 2\beta \sum_\gamma c_{\gamma,1}\rho^\gamma = \\ \sum_\gamma \Big[(\gamma+1)\, c_\gamma(\beta)\rho^\gamma + 2\beta\,(\tau_z - \beta)\, c_{\gamma,1}\Big]\rho^\gamma, \end{aligned}$$

and finally

$$U_q(\mathbf{x}) = \sum_\gamma \Big[(\gamma+1)\, c_{\gamma,0} + 2\beta\,(\tau_z - \beta)\, c_{\gamma,1} + (\gamma+1)c_{\gamma,1}\beta^2\Big]\rho^\gamma,$$

which proves Eq. (2.20).

C.1.2 GA mean field potential

The mean field U_q^{surf} Eq. (2.24) is derived. By definition, $U_q^{surf}(\mathbf{x}) = \frac{\delta E_{surf}}{\delta \rho_q}$, where E_{surf} is conveniently written as the volume integral of the density:

$$\mathcal{E}_{surf} = \sum_{t=0,1}\left(-C_t^{\Delta\rho}|\nabla\rho_t|^2 + C_t^{\nabla J}\rho_t \nabla\cdot\mathbf{J}_t\right). \tag{C.5}$$

Then

$$\frac{\delta E_{surf}}{\delta \rho_q} = \frac{\partial \mathcal{E}_{surf}}{\partial \rho_q} - \nabla \cdot \left(\frac{\partial \mathcal{E}_{surf}}{\partial \left(\nabla \rho_q \right)} \right). \tag{C.6}$$

The first contribution is due to the spin-orbit part and is equal to

$$\frac{\partial \mathcal{E}_{surf}}{\partial \rho_q} = C_0^{\nabla J} \nabla \cdot \mathbf{J}_0 + C_1^{\nabla J} \nabla \cdot \mathbf{J}_1 \tau_z, \tag{C.7}$$

having used $\frac{\partial \rho_1}{\partial \rho_q} = \tau_z$. The second one is due to the gradient terms of the EDF. To compute it, we first insert $\rho_0 = \rho_n + \rho_p$ and $\rho_1 = \rho_n - \rho_p$ into the energy density:

$$\begin{aligned} \mathcal{E}_{surf} = &- \left(C_0^{\Delta} + C_1^{\Delta} \right) \left(\left| \nabla \rho_n \right|^2 + \left| \nabla \rho_p \right|^2 \right) + \\ &+ 2 \left(C_1^{\Delta} - C_0^{\Delta} \right) \nabla \rho_n \cdot \nabla \rho_p, \end{aligned}$$

and then take the derivative:

$$\begin{aligned} &- \nabla \cdot \left(\frac{\partial \mathcal{E}_{surf}}{\partial \left(\nabla \rho_q \right)} \right) = \\ &2 \left(C_0^{\Delta} + C_1^{\Delta} \right) \Delta \rho_q - 2 \left(C_1^{\Delta} - C_0^{\Delta} \right) \Delta \rho_{\bar{q}} = \\ &2 C_0^{\Delta} \left(\Delta \rho_q + \Delta \rho_{\bar{q}} \right) + 2 C_1^{\Delta} \left(\Delta \rho_q - \Delta \rho_{\bar{q}} \right) = \\ &2 C_0^{\Delta} \Delta \rho_0 + 2 C_1^{\Delta} \Delta \rho_1 \tau_z, \end{aligned} \tag{C.8}$$

where $\bar{q} = p$ if $q = n$ and viceversa. Summing Eqs. (C.7) and (C.8) concludes the derivation.

C.1.3 Rearrangement energy

In nuclear DFT, the total energy can be computed in two independent ways:

- As the space integral of the EDF evaluated on the ground state densities that one obtains by solving the mean field equations:

$$E = \int d\mathbf{x}\, \mathcal{E}(\mathbf{x}). \tag{C.9}$$

- With the Hartree-Fock (HF) formula for a density-dependent Hamiltonian [156]:

$$E = \frac{1}{2} \left(T + \sum_k \epsilon_k \right) + E_{rea}. \tag{C.10}$$

The extra term E_{rea} is called rearrangement energy. The equality of the two expressions for the binding energy is often used as a non-trivial test of the correctness of the implementation of a DFT or HF code.

Here, the rearrangement energy for the LDA EDF of Sec. 2.2.1 is derived. The following practical definition is employed:

$$E_{rea} = \int d\mathbf{x}\, \mathcal{E}_{bulk}(\mathbf{x}) - \frac{1}{2} \sum_q \int d\mathbf{x} U_q(\mathbf{x}) \rho_q(\mathbf{x}), \tag{C.11}$$

with the mean field $U_q(\mathbf{x})$ 2.20. Then:

$$\begin{aligned} &\sum_q U_q \rho_q = U_n \rho_n + U_p \rho_p = \\ &\left[U_n (1+\beta) + U_p (1-\beta) \right] \frac{\rho}{2} = \left[(U_n + U_p) + (U_n - U_p)\, \beta \right] \frac{\rho}{2}. \end{aligned}$$

We calculate $U_n + U_p$ and $U_n - U_p$ separately:

$$\begin{aligned} U_n + U_p &= 2 \sum_\gamma \left[(\gamma+1)\, c_{\gamma,0} - 2\beta^2 c_{\gamma,1} + (\gamma+1)\, \beta^2 c_{\gamma,1} \right] \rho^\gamma = \\ &= 2 \sum_\gamma \left[(\gamma+1)\, c_{\gamma,0} + (\gamma-1)\, \beta^2 c_{\gamma,1} \right] \rho^\gamma \end{aligned}$$

and

$$U_n - U_p = 4\beta \sum_\gamma c_{\gamma,1}\rho^\gamma$$

with $\tau_z = 1$ for neutrons and $\tau_z = -1$ for protons. Then:

$$\sum_q U_q \rho_q = \frac{\rho}{2}\, 2 \sum_\gamma \left[(\gamma+1)\, c_{\gamma,0} + (\gamma+1)\, \beta^2 c_{\gamma,1}\right] \rho^{\gamma+1}$$

Plugging into the definitions of E_{rea}:

$$\begin{aligned} E_{rea} = \int d\mathbf{x} \sum_\gamma \Big[&\left(c_{\gamma,0} + \beta^2 c_{\gamma,1}\right) \rho^{\gamma+1} + \\ &- \left(\frac{1+\gamma}{2}\right) \left(c_{\gamma,0} + \beta^2 c_{\gamma,1}\right) \rho^{\gamma+1} \Big], \end{aligned}$$

and finally:

$$E_{rea} = \int d\mathbf{x} \sum_\gamma \left(\frac{1-\gamma}{2}\right) \left(c_{\gamma,0} + \beta^2 c_{\gamma,1}\right) \rho_0^{\gamma+1}. \tag{C.12}$$

C.2 Nuclear EDFs in infinite nuclear matter

This Section complements Sec. 2.3 providing details on the EDF and the mean fields used in the DFT infinite matter calculations. We focus on PNM and SNM, which can be treated as two-component (spin up/down) fermionic systems. We adopt the convention for which C^τ stands for C_0^τ in SNM and $C_{nm}^\tau = C_0^\tau + C_1^\tau$ in PNM, and likewise for $C^{\Delta\rho}$, $C^{\nabla J}$ and the c_γ coefficients. The material is adapted from Ref. [80].

C.2.1 EDFs

The expression of the EDF $\mathcal{E}$ under the assumptions of Sec. 2.1 is the following:

$$\begin{aligned} \mathcal{E}(z) = \mathcal{E}_{kin}(z) + \mathcal{E}_{bulk}(z) + C^\tau \rho(z)\tau(z) + \\ C^{\Delta\rho}\rho(z)\rho''(z) - C^{\nabla J}\rho'(z)J_z(z) \end{aligned} \tag{C.13}$$

with

$$\mathcal{E}_{kin}(z) = \frac{\hbar^2}{2m}\tau(z), \tag{C.14}$$

$$\mathcal{E}_{bulk}(z) = \sum_\gamma c_\gamma \rho^{\gamma+1}(z). \tag{C.15}$$

The rearrangement term was computed in Ref. [68] and is given by

$$E_{rea} = L^2 \int dz \sum_\gamma \left(\frac{1-\gamma}{2}\right) c_\gamma \rho^{\gamma+1}(z). \tag{C.16}$$

The expressions for the mean field, effective mass and spin-orbit potential are also shown:

$$\frac{\hbar^2}{2m^*(z)} = \frac{\hbar^2}{2m} + C^\tau \rho(z), \tag{C.17}$$

$$U(z) = U^{bulk}(z) + C^\tau \tau(z) + 2C^{\Delta\rho}\rho''(z) + C^{\nabla J} J_z'(z) \tag{C.18}$$

with

$$U^{bulk} = \sum_\gamma c_\gamma \left(\gamma+1\right) \rho^\gamma(z), \tag{C.19}$$

and lastly

$$W_z(z) = -C^{\nabla J}\rho'(z). \tag{C.20}$$

C.2.2 Kinetic term

We derive the kinetic term of Eq. (2.36). First, the gradient and the Laplacian of $\psi_{\mathbf{n},\lambda}$ [Eq. 2.33] are reported:

$$\begin{aligned}\nabla\psi_{\mathbf{n},\lambda}(\mathbf{x}) = ik_x\psi_{\mathbf{n},\lambda}(\mathbf{x})\hat{\mathbf{x}} + ik_y\psi_{\mathbf{n},\lambda}(\mathbf{x})\hat{\mathbf{y}} \\ + \frac{1}{L}e^{i(k_x x+k_y y)}\chi_{n_x,n_y,\lambda}\phi'_{\mathbf{n},\lambda}(z)\hat{\mathbf{z}},\end{aligned} \tag{C.21}$$

$$\begin{aligned}\nabla^2\psi_{\mathbf{n},\lambda}(\mathbf{x}) = -\left(k_x^2+k_y^2\right)\psi_{\mathbf{n},\lambda}(\mathbf{x}) \\ + \frac{1}{L}e^{i(k_x x+k_y y)}\chi_{n_x,n_y,\lambda}\phi''_{\mathbf{n},\lambda}(z).\end{aligned} \tag{C.22}$$

Using these expressions, we elaborate on $-\nabla\cdot\left(\frac{\hbar^2}{2m(z)}\nabla\psi_{\mathbf{n},\lambda}\right)$ as follows:

$$\begin{aligned}&-\nabla\cdot\left(\frac{\hbar^2}{2m^*(z)}\nabla\psi_{\mathbf{n},\lambda}(\mathbf{x})\right) = \\ &-\frac{\hbar^2}{2m^*(z)}\nabla^2\psi_{\mathbf{n},\lambda}(\mathbf{x}) - \frac{d}{dz}\left(\frac{\hbar^2}{2m^*(z)}\right)\frac{\partial\psi_{\mathbf{n},\lambda}}{\partial z} = \\ &\frac{1}{L}e^{i(k_x x+k_y y)}\chi_{n_x,n_y,\lambda} \\ &\left[-\frac{d}{dz}\left(\frac{\hbar^2}{2m^*(z)}\phi'_{\mathbf{n},\lambda}(z)\right) + \frac{\hbar^2}{2m^*(z)}k^2_{n_x n_y}\phi_{\mathbf{n},\lambda}(z)\right].\end{aligned} \tag{C.23}$$

The constant spinor χ and the exponential appear in all terms in Eq. (2.6), thus they can be simplified and drop out of the the final equations (2.36).

C.2.3 Densities as a function of the orbitals

Number density, kinetic density and spin-orbit density may be computed from their definitions as functions of the occupied orbitals [6] applied to the wave functions (2.33). Eqs. (C.21) and (C.22) are also used to find

$$\rho(z) = \sum_j |\psi_j(\mathbf{x})|^2 = \frac{1}{L^2}\sum_{\mathbf{n},\lambda}|\phi_{\mathbf{n},\lambda}(z)|^2 \tag{C.24}$$

$$\begin{aligned}\tau(z) &= \sum_j |\nabla\psi_j(\mathbf{x})|^2 \\ &= \frac{1}{L^2}\sum_{\mathbf{n},\lambda}\left(\left|\phi'_{\mathbf{n},\lambda}\right|^2 + k^2_{n_x n_y}|\phi_{\mathbf{n},\lambda}|^2\right)\end{aligned} \tag{C.25}$$

$$\begin{aligned}J_z(z) &= \sum_j \psi_j^*(\mathbf{x})\,(-i)\,(\nabla\times\sigma)_3\,\psi_j(\mathbf{x}) \\ &= \sum_{\mathbf{n},\lambda}\psi^*_{\mathbf{n},\lambda}(\mathbf{x})K\psi_{\mathbf{n},\lambda}(\mathbf{x}) \\ &= \frac{1}{L^2}\sum_{\mathbf{n},\lambda}\lambda k_{n_x n_y}|\phi_{\mathbf{n},\lambda}(z)|^2\end{aligned} \tag{C.26}$$

where only the z component of **J** does not vanish and Eq. (2.34) has been used.

C.2.4 Hamiltonian in the plane waves basis

We derive the Hamiltonian matrix in the plane waves basis $\left(\tilde{h}_{\mathbf{n},\lambda}\right)_{k,k'}$ (Eq. (2.37)). We start from the real space DFT equations (2.36) and Fourier-expand the orbitals as $\phi(z) = \frac{1}{\sqrt{L}}\sum_{k'}c_{k'}e^{ik'z}$. Then, we project on the k plane wave by multiplying by $e^{-ikz}/\sqrt{L}$ and integrating over z for $-L/2 \le z \le L/2$. The multiplicative terms are simple to treat and one easily finds the Fourier transform

$$\begin{aligned}\tilde{U}(k-k') = \frac{1}{L}\int_{-L/2}^{L/2}dz\,e^{-i(k-k')z} \\ \left(U(z)+v(z)+\lambda k_{n_x n_y}W(z)+\frac{\hbar^2}{2m^*(z)}k^2_{n_x n_y}\right).\end{aligned} \tag{C.27}$$

The derivative term is slightly more involved and is discussed in detail. We simplify the notation by defining $B(z) = \frac{\hbar^2}{2m^*(z)}$ and dropping the subscripts $\mathbf{n}, \lambda$ and move on to compute

$$\frac{1}{\sqrt{L}} \int_{-L/2}^{L/2} dz e^{-ikz} \Big[- \frac{d}{dz} \big(B(z) \phi'(z) \big) \Big]. \tag{C.28}$$

An integration by parts, followed by inserting $\phi'(z) = \frac{i}{\sqrt{L}} \sum_{k'} k' c_{k'} e^{ik'z}$, gives

$$\begin{aligned} &\frac{1}{\sqrt{L}} \int dz B(z) \phi'(z) \frac{d}{dz} e^{-ikz} = \\ &- i \frac{k}{\sqrt{L}} \int dz\, B(z) \phi'(z) e^{-ikz} = \\ &k \sum_{k'} k' c_{k'} \frac{1}{L} \int dz B(z) e^{-i(k-k')z} = \\ &k \sum_{k'} \tilde{B}(k-k') k' c_{k'} \end{aligned} \tag{C.29}$$

where

$$\tilde{B}(k-k') = \frac{1}{L} \int_{-L/2}^{L/2} dz\, e^{-i(k-k')z} \frac{\hbar^2}{2m^*(z)}. \tag{C.30}$$

In case effective mass terms are absent, $m^*(z) = m$, $\tilde{B}(k-k')$ is simply equal to $\frac{\hbar^2}{2m} \delta_{k,k'}$ and one recovers in $\tilde{h}_{k,k'}$ the usual kinetic term $\frac{\hbar^2}{2m} k^2$. Summing the $\tilde{B}$ and $\tilde{U}$ terms, one finds the Hamiltonian matrix

$$\tilde{h}_{k,k'} = k \tilde{B}(k-k') k' + \tilde{U}(k-k'). \tag{C.31}$$

C.3 EDF response in the thermodynamic limit

The dynamic response of a large class of generalized Skyrme EDFs has been determined in the thermodynamic limit analytically in Ref. [124] and references therein. We summarize the main formulas here for the case of PNM and SNM. A slightly different notation is also introduced.

First, for later convenience we define K_{bulk} as

$$K_{bulk} = \sum_{\gamma} c_\gamma \gamma(\gamma+1) \rho^{\gamma-1}. \tag{C.32}$$

Then, the following W functions are defined as in Ref. [124], namely

$$W_1(q)/g = K_{bulk} - \left(2C^{\Delta\rho} + \frac{C^\tau}{2} \right) q^2 \tag{C.33}$$

$$W_2/g = C^\tau \tag{C.34}$$

$$W_{so}/g = C^{\nabla J}. \tag{C.35}$$

W_2 is a constant proportional to C^τ, while W_1 mixes the C^τ and C^δ coefficients and carries a momentum dependence through q^2. Lastly, W_{so} is a spin-orbit constant.

Now, we introduce adimensional functions X and insert them into $\chi(q)$ (eq. (67), Ref. [124]). With $k = q/2q_F$, we define $\tilde{\rho}$ as ρ in SNM and 2ρ in PNM. With this trick, the expressions for SNM [260] and PNM [261] are identical. The X functions are derived from the corresponding W functions using

$$X_1 = \frac{m^* c^2}{(\hbar c)^2} \tilde{\rho} \frac{W_1(q)}{q_F^2} \tag{C.36}$$

$$X_2 = \frac{m^* c^2}{(\hbar c)^2} \tilde{\rho} W_2 \tag{C.37}$$

$$X_{so} = \frac{m^* c^2}{(\hbar c)^2} \tilde{\rho} W_{so}. \tag{C.38}$$

We further elaborate on X_1 by splitting it as the sum or a bulk and a momentum-dependent contributions:

$$X_1(k) = X_{bulk} + X_{surf}(k) \tag{C.39}$$

with

$$X_{bulk} = g\frac{m^*c^2}{(\hbar c)^2}\frac{\tilde{\rho}}{q_F^2}K_{bulk} \tag{C.40}$$

$$X_{surf}(k) = -4g\left(2C^{\Delta\rho} + \frac{C^\tau}{2}\right)\frac{m^*c^2}{(\hbar c)^2}\tilde{\rho}k^2. \tag{C.41}$$

Finally, by using $\chi(q) = -\rho\, 2m_{-1}(q)/A$, with m_{-1} being the inverse energy-weighted sum rule of the strength function, and collecting some constant factors, one ends up with following formula for the TL response of a nuclear EDF:

$$\begin{aligned}\chi(q) = -3\frac{m^*c^2}{(\hbar c)^2}\frac{\rho}{q_F^2}f(k) \\ \Bigg[\left(1+\frac{3}{8}X_2\right)^2 + \frac{3}{4}\Big(X_1(k) + X_2(1-k^2)\Big)f(k) \\ -\frac{3}{64}X_2^2\left(2+\frac{26}{3}k^2+(1-k^2)f(k)\right)f(k) \\ -\frac{3}{8}k^2f(k)X_{so}^2\Big(1+3(1-k^2)f(k)\Big)\Bigg]^{-1}.\end{aligned} \tag{C.42}$$

with $f(k)$ defined in Eq. (1.26).

APPENDIX D

Details on Self-consistent Green's functions

We complement the exposition of SCGF theory (Sec. 4.1) and provide further details. Sec. D.1 reports the derivation of the matrix eigenvalue formulation of the Dyson equation. In Sec. D.2 the Lanczos algorithm that is employed to reduce the complexity of the diagonalization of the Dyson matrix is discussed. In Sec. D.3 the formulas that define the corrections to the energy in second- and third-order many-body perturbation theory are described. Sec. D.4 delves into some specific approximations of the ADC method, and highlights how these are connected to MBPT and coupled-cluster. The strict relation between ADC(2) and MBPT(2) (Sec. D.4.1) is first discussed. Then, an example is shown of how the ADC interaction matrices are related to MBPT at third and higher orders (Sec. D.4.2). Finally, we further motivate that the ADC coupling matrices generate an infinite sum of Feynman diagrams, and discuss how the ladder series for the ground state energy can be found either in the coupled-cluster approach (using the CC ladder approximation) or using the ADC method. Sec. D.5 provides details on the algorithm employed to determine the Fermi energy. In Sec. D.6, we comment on how the Gorkov approach generalized the Dyson formalism. Finally, in Sec. D.7 we summarize the parameters that have to be set to run a SCGF calculation.

D.1 Dyson equation as an eigenvalue problem

In this Section, we derive the formulation of the Dyson equation as an energy-independent matrix eigenvalue problem, following Refs. [81, 82]. As a first step, we select a pole ϵ^i of the dressed propagator, multiply the Dyson equation (4.13) by $(\omega - \epsilon^i)$ and take the limit $\omega \longrightarrow \epsilon^i$. ϵ^i is itself an unknown of the problem and will be determined as an eigenvalue of a Hermitian matrix, together with the eigenvectors $\mathcal{Z}^i$. Then, one finds

$$\mathcal{Z}^i_\alpha \left(\mathcal{Z}^i_\beta\right)^* = g^{(0)}_{\alpha\gamma}(\epsilon^i)\Sigma^{(\star)}_{\gamma\delta}(\epsilon^i)\mathcal{Z}^i_\delta \left(\mathcal{Z}^i_\beta\right)^*. \tag{D.1}$$

$\left(\mathcal{Z}^i_\beta\right)^*$ simplifies from the two sides of the previous equality. The following step consists in reminding that the unperturbed propagator is the Green's function (in a mathematical sense) of $\omega - \hat{H}_0$, i.e. $g^{(0)}(\omega) = (\hbar\omega\mathbb{1} - \hat{H}^{(0)})^{-1}$ or, making the matrix indexes explicit,

$$\left(\omega\delta_{\alpha\beta} - h^{(0)}_{\alpha\beta}\right) g^{(0)}_{\beta\gamma}(\omega) = \delta_{\alpha\gamma} \tag{D.2}$$

with $h^{(0)}_{\alpha\beta} = t_{\alpha\beta} + u_{\alpha\beta}$. Then, we now multiply Eq. (D.1) by $\epsilon^i - \hat{H}_0$ and find

$$\epsilon^i \mathcal{Z}^i_\alpha = [h^{(0)}_{\alpha\beta} + \Sigma^{(\star)}_{\alpha\beta}(\epsilon^i)]\mathcal{Z}^i_\beta = [t_{\alpha\beta} + \Sigma^{(\infty)}_{\alpha\beta} + \tilde{\Sigma}_{\alpha\beta}(\epsilon^i)]\mathcal{Z}^i_\beta. \tag{D.3}$$

The auxiliary vectors $\mathcal{W}$ and $\mathcal{V}$, defined in Eqs. (4.49) and (4.50), are introduced In Eq. (D.3) with $\omega = \epsilon^i$, so that we find

$$\epsilon^i \mathcal{Z}^i_\alpha = \left(t_{\alpha\beta} + \Sigma^{(\infty)}_{\alpha\beta}\right)\mathcal{Z}^i_\beta + M^\dagger_{\alpha r}\mathcal{W}^i_r + N_{\alpha s}\mathcal{V}^i_s. \tag{D.4}$$

Eqs. (D.4), (4.50) and (4.49) are now combined:

$$\epsilon^i \mathcal{Z}^i = \left(t + \Sigma^{(\infty)}\right)\mathcal{Z}^i + M^\dagger \mathcal{W}^i + N\mathcal{V}^i, \tag{D.5}$$

$$\epsilon^i \mathcal{W}^i = M\mathcal{Z}^i + \left(E^> + C\right)\mathcal{W}^i, \tag{D.6}$$

$$\epsilon^i \mathcal{V}^i = N^\dagger \mathcal{Z}^i + \left(E^< + D\right)\mathcal{V}^i. \tag{D.7}$$

The matrix eigenvalue problem (4.51) follows immediately.

D.2 Lanczos method

A crucial step in the solution of the Dyson problem is the use of the Lanczos method [26, 209, 262]. Due to the large dimension of the Dyson matrix, a full diagonalization of Eq. (4.51) is extremely demanding, and techniques for reducing the dimensionality of the problem are needed. The essence of the Lanczos algorithm consists of performing an orthogonal projection onto the so-called Krylov subspace that maps a Hermitian matrix H into a tridiagonal matrix T. The projection is realized iteratively and is rather efficient.

The Krylov subspace is defined as the vector space spanned by $\mathbf{q}_1, H\mathbf{q}_1, ..., H^n\mathbf{q}_1$ Starting from an initial vector $\mathbf{q}_1$, called pivot, the methods constructs an orthonormal basis $\{\mathbf{q}_1, ..., \mathbf{q}_n\}$ for the Krylov space. The theorem at the heart of the Lanczos algorithm is the following [262]: There exists a unitary matrix Q that maps a Hermitian matrix H into a tridiagonal real symmetric matrix T, i.e. $T_{i,i+1} = T_{i+1,i}$ and $T_{ij} \neq 0$ only for $j = i-1, i, i+1$, such that

$$HQ = QT. \tag{D.8}$$

The columns of the matrix Q are the orthonormal basis vectors $\mathbf{q}_i$. The Lanczos vectors and matrix elements of T are obtained by the simple recursive formulas

$$T_{ij} = \mathbf{q}_i^\dagger H \mathbf{q}_j, \tag{D.9}$$

$$T_{i,i+1}\mathbf{q}_{i+1} = (H - T_{ii})\,\mathbf{q}_i - T_{i,i-1}\mathbf{q}_{i-1}. \tag{D.10}$$

At each iteration, a new vector is constructed. To improve the numerical stability of the algorithm, it is suggested to orthogonalize the basis, e.g. with the Gram-Schmidt procedure, at each iteration [263]. The tridiagonal matrix is similar to the original matrix H, thus it shares the same eigenvalues and eigenvectors. As the number of iterations increases, T is slowly constructed, but crucially we do not need to determine the full matrix T. Indeed, since the convergence is best for the extreme (smallest and largest) eigenvalues of H, information on the spectrum can often be recovered with a limited number of iterations. Therefore, the Lanczos algorithm effectively projects the initial matrix into a much smaller one, while keeping its essential features. In methods such as the shell model [4], where the lowest-lying eigenvalues of the Hamiltonian are targeted, the resulting small tridiagonal matrix is then diagonalized fully at a moderate cost. In Green's function methods [26, 209], the interest of the Lanczos technique lies mainly in reducing the size of both the backward and (mostly) forward energy denominators separately, as we discuss below. A key point is that, as we want to conserve the structure of the self-energy close to the Fermi energy, the smallest eigenvalues of $E^> + C$ and the largest ones of $E^< + D$ have to be reproduced. Luckily, the Lanczos method works well also for the highest eigenvalues.

Note that a very large number of eigensolutions of the original Dyson matrix is needed to find a good representation of the propagator. That is the reason why pole search algorithms are expensive, as all eigenvalues must be searched one by one. Significant contributions to the sum rules come also from solutions far from the Fermi surface. In contrast, a small number (of the order of tens or hundreds at most) of Lanczos vectors allows to evaluate the energy and other observables accurately.

We expose the Lanczos method for the forward matrix $E^> + C$, but identical steps hold for the backward subspace. Using Eq. (D.8), we write

$$(E^> + C)Q^> = Q^> T^>, \tag{D.11}$$

where $T^>$ is a triangular matrix of dimension $N_{fw} \times N_{fw}$ and $Q^>$ is the matrix of dimension $N_{fw} \times N_{fw}$ whose columns are the Lanczos vectors. Consider now the ADC self-energy, Eq. (4.31), and insert the expression (D.8). Then, for the forward term we find

$$M^\dagger \left[\omega - (E^> + C) + i\eta\right]^{-1} M = M^\dagger Q^> \left[\omega - T^> + i\eta\right]^{-1} Q^{>,\dagger} M = \\ \tilde{M}^\dagger \left[\omega - T^> + i\eta\right]^{-1} \tilde{M} \tag{D.12}$$

having defined $\tilde{M} = Q^{>,\dagger} M$. The matrix elements of $\tilde{M}$ are obtained, one per iteration, as follows:

$$\tilde{M}_{l\alpha} = (Q^{>,\dagger})_{lr} M_{r\alpha} = (Q_{rl})^* M_{r\alpha} = (\mathbf{q}_l)_r^* M_{r\alpha}. \tag{D.13}$$

This means that, for each state α, the l-th element of $\tilde{M}$ is given by the inner product between the l-th Lanczos vector and M, namely

$$\tilde{\mathbf{M}}_\alpha = (\mathbf{q}_l)^* \cdot \mathbf{M}_\alpha. \tag{D.14}$$

If we perform similar passages for the backward part and define $\tilde{N} = Q^{<,\dagger}N$, we can write the self-energy as

$$\Sigma^{(\star)}(\omega) = -U_{\alpha\beta} + \Sigma^{(\infty)} + \tilde{M}^\dagger \frac{1}{\omega\mathbb{1} - T^> + i\eta}\tilde{M} + \tilde{N}\frac{1}{\omega\mathbb{1} - T^< - i\eta}\tilde{N}^\dagger \tag{D.15}$$

and the Dyson matrix as

$$\begin{pmatrix} T + \Sigma^{(\infty)} & \tilde{M}^\dagger & \tilde{N} \\ \tilde{M} & T^> & \\ \tilde{N}^\dagger & & T^< \end{pmatrix}. \tag{D.16}$$

All the steps performed so far are exact. The crucial point is that an excellent approximation of Eq. (D.16) can be obtained by summing over only the first few Lanczos elements N_{Lan}. In most cases, a few hundred Lanczos vectors at most are sufficient. For example, for the forward term we can write

$$\sum_{r,r'=1}^{N_{fw}} \tilde{M}^\dagger_{\alpha r}\Big(\frac{1}{\omega\mathbb{1} - T^> + i\eta}\Big)_{rr'}\tilde{M}_{r'\beta} \approx \sum_{l,l'=1}^{N_{Lan}} \tilde{M}^\dagger_{\alpha l}\Big(\frac{1}{\omega\mathbb{1} - T^> + i\eta}\Big)_{ll'}\tilde{M}_{l'\beta}. \tag{D.17}$$

Therefore, we can truncate all the matrices in Eq. (D.16), and the resulting Dyson matrix can be now diagonalized fully due to its small dimension. A key property of the Lanczos algorithm is that the extremal (largest and smallest) eigenvalues of the original matrix are best conserved by the method. This is of crucial importance, since the physical content of the Green's function concentrates on the poles close to the Fermi surface. Almost completely occupied (unoccupied) states at very low (high) energy are of limited interest, while the effects of the interactions are most prominent on the lowest-energy particle states and highest-energy hole states, i.e. the largest and smallest eigenvalues of $E^> + C$ and $E^< + D$, respectively, that are indeed well-reproduced by the Lanczos algorithm.

Before concluding, we mention that a full diagonalization of the matrices $E^> + C$ and $E^< + D$ is not strictly needed. Yet, the physical content of the ADC(3) self-energy is more transparent in its diagonal form. Also, this is useful e.g. for plotting $\Sigma^{(\star)}(\omega)$ [82] or for evaluating the sum rules of App. D.4. Let us call $\Lambda^> = \lambda_r\delta_{rr'}$ ($\Lambda^< = \lambda_s\delta_{ss'}$) the matrix of the eigenvalues of $E^> + C$ ($E^< + D$) and $U^>$ ($U^<$) the corresponding eigenvector matrix, i.e.

$$(E^> + C)U^> = U^>\Lambda^>, \quad (E^< + D)U^< = U^<\Lambda^<. \tag{D.18}$$

Also, we introduce the unitary-transformed coupling matrices

$$\bar{M} = U^{>,\dagger}M, \quad \bar{N} = U^<N \tag{D.19}$$

Reintroducing the s.p. indexes, the ADC(3) self-energy reads

$$\Sigma^{(\star)}_{\alpha\beta}(\omega) = -U_{\alpha\beta} + \Sigma^{(\infty)}_{\alpha\beta} + \sum_r \frac{\bar{M}^\dagger_{\alpha r}\bar{M}_{r\beta}}{\omega - \lambda_r + i\eta} + \sum_s \frac{\bar{N}_{\alpha s}\bar{N}^\dagger_{s\beta}}{\omega - \lambda_s - i\eta}. \tag{D.20}$$

In this form, the Lehmann representation is easily recognized, and the meaning of the interaction matrices can be understood. In ADC(2), where C and D vanish, the self-energy eigenvalues are simply the energies of the three-quasi-particle (3qp) configurations r and s (Eqs. (4.47),(4.41)). In ADC(3), the poles of $\Sigma^{(\star)}$ are instead shifted from their unperturbed value as an effect of the interactions, that induce a mixing of the 3qp configurations. Note that in numerical calculation, the $E^> + C$ and $E^< + D$ are always Lanczos-reduced first, and then diagonalized.

D.3 Many-body perturbation theory at second and third order

In this Section, we discuss the correction to the total energy in many-body perturbation theory (MBPT) at second and third order. Formulas can be found in Refs. [14, 125, 264].

The effect of 3N force is incorporated by using an effective 2B normal-ordered interaction [126, 265],

$$\tilde{v}_{\alpha\beta,\gamma\delta} = \tilde{v}_{\alpha\beta,\gamma\delta} + \sum_h \bar{w}_{\alpha\beta h,\gamma\delta h} \tag{D.21}$$

with h denoting the hole states. This formula can also be derived from Eq. (4.24) using a HF density matrix. Terms that depend explicitly on the 3N interaction are usually neglected in MBPT, as they are computationally expensive but expected to be small corrections.

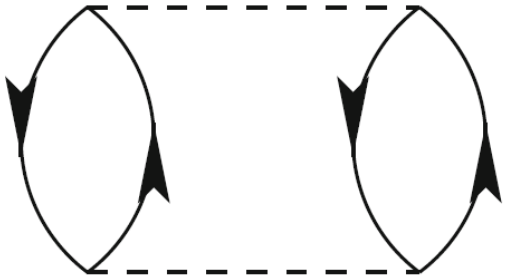

Figure D.1: MBPT diagram at second-order. The dotted lines represent the effective 2B interaction (D.21). The corresponding expression is given in Eq. (D.23). Adapted from Ref. [14].

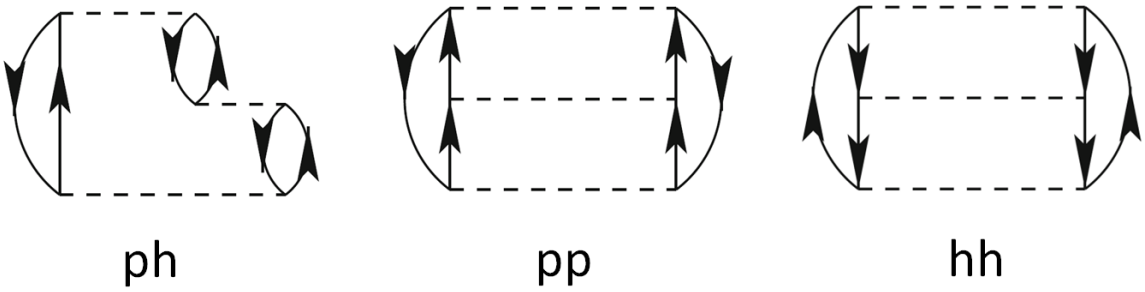

Figure D.2: MBPT diagrams at third order. The dotted lines represent the effective 2B interaction (D.21). From left to right, the three diagrams propagate ph [Eq. (D.25)], pp [Eq. (D.26)] and hh [Eq. (D.27)] excitations. Adapted from Ref. [14].

The unperturbed doublet amplitudes $t^{(0)}$ are defined as [14, 126]

$$t^{(0)}_{p_1p_2,h_1h_2} = \frac{\tilde{v}_{p_1p_2,h_1h_2}}{\epsilon_{h_1} + \epsilon_{h_2} - \epsilon_{p_1} - \epsilon_{p_2}}. \tag{D.22}$$

Eq. (D.22) is also found specializing Eq. (4.35) to a HF density.

The well-known second-order correction $E^{(2)}$ reads

$$E^{(2)} = \frac{1}{4} \sum_{\substack{p_1p_2 \\ h_1h_2}} t^{(0)}_{p_1p_2,h_1h_2} \tilde{v}_{h_1h_2,p_1p_2}. \tag{D.23}$$

MBPT(2) is typically evaluated at the beginning of SCGF or CC calculations, and $t^{(0)}$ is commonly used as an initial guess for the CC amplitude. The corresponding diagram is shown in Fig. D.1. For completeness, for this case only we report also the irreducible second-order contribution due to 3N forces [245]:

$$E^{(2,3N)} = \frac{1}{36} \sum_{\substack{p_1p_2p_3 \\ h_1h_2h_3}} \frac{|\tilde{w}_{p_1p_2p_3,h_1h_2h_3}|^2}{\epsilon_{h_1} + \epsilon_{h_2} + \epsilon_{h_3} - \epsilon_{p_1} - \epsilon_{p_2} - \epsilon_{p_3}}. \tag{D.24}$$

Three diagrams contribute to the third order (Fig. D.2), which propagate particle-particle (pp), particle-hole (ph) and hole-hole (hh) excitations, respectively [see Ref. [14], Eqs. (8.24)-(8.26)], and read

$$E^{(3,ph)} = \sum_{\substack{p_1p_2p_3 \\ h_1h_2h_3}} t^{(0)*}_{p_1p_2,h_1h_2} \tilde{v}_{p_2h_3,h_1p_3} t^{(0)}_{p_1p_3,h_2h_3}, \tag{D.25}$$

$$E^{(3,pp)} = \frac{1}{8} \sum_{\substack{p_1p_2p_3p_4 \\ h_1h_2}} t^{(0)*}_{p_1p_2,h_1h_2} \tilde{v}_{p_1p_2,p_3p_4} t^{(0)}_{p_3p_4,h_1h_2}, \tag{D.26}$$

$$E^{(3,hh)} = \frac{1}{8} \sum_{\substack{p_1p_2 \\ h_1h_2h_3h_4}} t^{(0)}_{p_1p_2,h_1h_2} \tilde{v}_{h_1h_2,h_3h_4} t^{(0)*}_{p_1p_2,h_3h_4}. \tag{D.27}$$

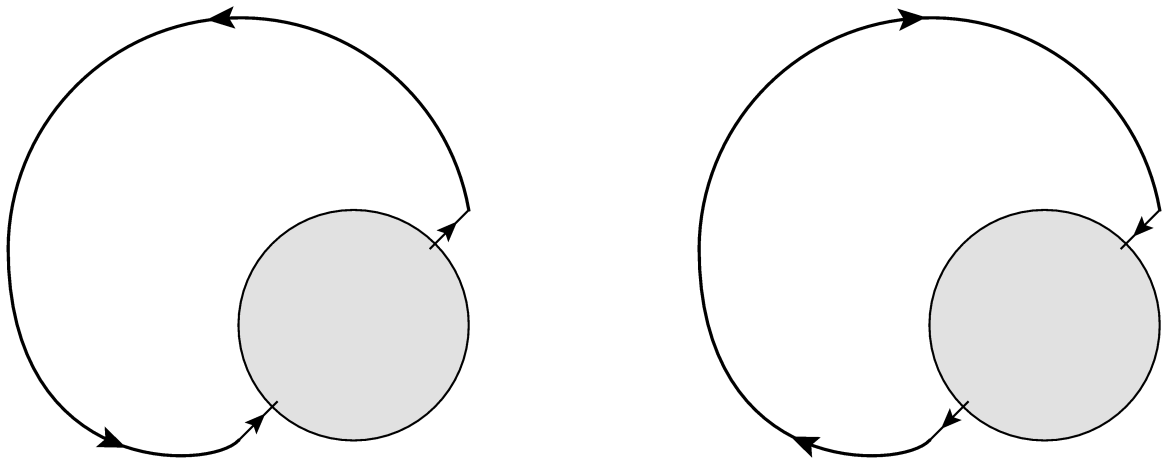

Figure D.3: Diagrammatic representation of the self-energy sum rules Eq. (D.30) (left) and (D.31) (right). The forward (backward) self-energy, represented as a grey circle, is contracted with an unperturbed hole (particle) GF that propagates backward-in-time (forward-in-time).

D.4 Connections between ADC, MBPT and coupled-cluster

In this Section, we discuss some specific cases of the ADC method and highlight the relations that exist between the ADC self-energy on the one hand, and MBPT and coupled-cluster on the other hand. This analysis has a twofold purpose, as it gives some intuition about how ADC-SCGF works and at the same time allows testing the implementation of the SCGF code.

We consider the forward-in-time and backward-in-time parts of the ADC dynamical self-energy,

$$\Sigma^{>} = M^{\dagger} \frac{1}{\hbar\omega \mathbb{1} - (E^{>} + C) + i\eta} M, \tag{D.28}$$

$$\Sigma^{<} = N \frac{1}{\hbar\omega \mathbb{1} - (E^{<} + D) - i\eta} N^{\dagger}. \tag{D.29}$$

The following two sum rules are then introduced:

$$E^{>} = \frac{1}{2} \int d\omega \, \Sigma^{>}_{\alpha\beta}[g_0](\omega) \, S^{h(0)}_{\beta\alpha}(\omega), \tag{D.30}$$

$$E^{<} = \frac{1}{2} \int d\omega \, \Sigma^{<}_{\alpha\beta}[g_0](\omega) \, S^{p(0)}_{\beta\alpha}(\omega), \tag{D.31}$$

where $\Sigma^{>}$ and $\Sigma^{<}$ are evaluated as a functional of the unperturbed propagator g_0, and $S^{p(0)}$ and $S^{h(0)}$ are the particle and hole HF spectral functions. These formulas resemble the expression for the Kadanoff-Baym functional $\Phi[g]$, see e.g. Refs. [84, 213, 214]. Diagramatically, they can be represented as closing a forward (backward) self-energy term with an unperturbed hole (particle) GF. In the case of infinite matter, the self-energy is diagonal and the spectral functions read

$$S^{h(0)}_{\beta\alpha}(\omega) = \sum_k \epsilon_k \delta(\hbar\omega - \epsilon_k)\delta_{\alpha\beta}\delta_{\alpha k}, \quad S^{p(0)}_{\beta\alpha}(\omega) = \sum_p \epsilon_p \delta(\hbar\omega - \epsilon_p)\delta_{\alpha\beta}\delta_{\alpha p}, \tag{D.32}$$

where ϵ_h and ϵ_p are the unperturbed s.p. energies. Thus, the sum rules (D.30) and (D.31) can be evaluated as follows:

$$E^{>} = +\frac{1}{2} \sum_h \Sigma^{>}_h(\epsilon_h), \tag{D.33}$$

$$E^{<} = -\frac{1}{2} \sum_p \Sigma^{<}_p(\epsilon_p). \tag{D.34}$$

Eqs. (D.31) and (D.30) are very useful as a test for the ADC method. We first choose what terms to include in the ADC matrices. Then, a direct evaluation of the sum rules or diagrammatic arguments produce a set of contributions that can be evaluated numerically. Alternatively, they can be obtained from SCGF by constructing the Dyson matrix from the unperturbed GF, then Lanczos-reducing it. If the value of the sum

rules as extracted from this procedure matches the expected value, then we can gain confidence in both the implementation of the ADC matrices and the correctness of the Lanczos algorithm.

Note that is convenient to diagonalize the self-energy, see Eq. (D.20) so that Eqs. (D.31) and (D.30) can be quickly evaluated as follows:

$$E^{>} = \frac{1}{2}\sum_{h}\sum_{r}\frac{\left|\tilde{M}_{rh}\right|^2}{\epsilon_h - \lambda_r}, \tag{D.35}$$

$$E^{<} = \frac{1}{2}\sum_{p}\sum_{s}\frac{\left|\tilde{N}_{ps}\right|^2}{\lambda_s - \epsilon_p}. \tag{D.36}$$

We discuss three examples. First, in Sec. D.4.1 we consider the connection between ADC(2) and MBPT(2). This is the simplest check on the ADC method. Then, in Sec. D.4.2 we include additional terms in the coupling matrices and show that third-order and fourth-order MBPT diagrams are obtained. Finally, in Sec. D.4.3 we combine the first-order ADC(2) coupling matrix and include the ladder terms, Eqs. (4.39) and (4.45), in the interaction matrices. This generates an infinite sum of contributions to the energy. We discuss how an equivalent all-order resummation is obtained in the ladder approximation of the coupled-cluster method [130].

D.4.1 ADC(2) and MBPT(2)

In ADC(2), the structure of the Dyson matrix is simple, as $C = D = 0$ and the M and N matrices are just matrix elements of the effective NN interaction (see Tab. 4.1). It is a simple exercise to show that

$$E^{>}_{ADC(2)} = E^{<}_{ADC(2)} = E^{(2)}, \tag{D.37}$$

where $E^{(2)}$ is the MBPT(2) energy correction.

We show the steps for $E^{>}_{ADC(2)}$. We start from Eq. (D.35), where $\lambda_r = E^{>}_r$ are the energies of the unperturbed 2p1h states. As $r = (n_1 < n_2, h_1)$ and $E^{>}_r = \epsilon_{n_1} + \epsilon_{n_2} - \epsilon_{h_1}$, with ϵ being the HF energies, we get

$$E^{>}_{ADC(2)} = \frac{1}{2}\sum_{h_2 r}\frac{\left|M^{(1)}_{rh_2}\right|^2}{\epsilon_{h_2} - E^{>}_r} = \frac{1}{4}\sum_{\substack{n_1 n_2\\ h_1 h_2}}\frac{\left|\tilde{v}_{n_1 n_2, h_1 h_2}\right|^2}{\epsilon_{h_1} + \epsilon_{h_2} - \epsilon_{n_1} - \epsilon_{n_2}}, \tag{D.38}$$

and, exploiting the antisymmetry of the matrix elements, we have made the replacement

$$\sum_{n_1 < n_2} \longrightarrow \frac{1}{2}\sum_{n_1 n_2}. \tag{D.39}$$

D.4.2 Connection with MBPT(3)

We consider now another limiting case. First of all, we set the coupling matrices to zero, $C = D = 0$. This implies that the self-energy contains a finite number of diagrams, as we shall explicitly show. To further simplify the study, we neglect the ring contribution to the coupling matrices and set $M = M^{(1)} + M^{(2,pp)}$ and $N = N^{(1)} + N^{(2,hh)}$. For the forward-in-time part of the self-energy, we get

$$\begin{aligned}\Sigma^{>}(\omega) = {} & M^{(1),\dagger}\frac{1}{\hbar\omega\mathbb{1} - E^{>}}M^{(1)} + M^{(1),\dagger}\frac{1}{\hbar\omega\mathbb{1} - E^{>}}M^{(2,pp)} \\ & + M^{(2,pp),\dagger}\frac{1}{\hbar\omega\mathbb{1} - E^{>}}M^{(1)} + M^{(2,pp),\dagger}\frac{1}{\hbar\omega\mathbb{1} - E^{>}}M^{(2,pp)}.\end{aligned} \tag{D.40}$$

We recognize the second-order term that already appears in ADC(2), two third-order contributions, and an additional fourth-order term. The corresponding energy contribution is obtained from the self-energy with Eq. (D.35). By directly plugging the expression of the interaction matrices (4.36) and (4.37), we find the following identity:

$$E^{>} = E^{(2)} + 2E^{(3,hh)} + E^{(4,pp-6h)}. \tag{D.41}$$

$E^{(2)}$ is the MBPT(2) contribution. The second and third terms in Eq. (D.40) produce two identical contributions to the energy, and it can shown that each of them coincides with the MBPT(3) diagram involving hh excitations,

Eq. (D.27). Finally, one specific MBPT(4) term appears [see Ref. [125], Eq. (33)], namely a diagram that propagates two particle and six hole intermediate states, that reads

$$E^{(4,pp-6h)} = \frac{1}{16} \sum_{\substack{n_1 n_2 \\ h_1 h_2 h_3 h_4 h_5 h_6}} t_{n_1,n_2;h_1,h_2} \tilde{v}_{h_1 h_2;h_3,h_4} \frac{1}{D_{h_3,h_4;n_1,n_2}} \tilde{v}_{h_3,h_4;h_5,h_6} t_{h_5,h_6;n_1,n_2}. \tag{D.42}$$

We have introduced the notation $t_{h_5,h_6;n_1,n_2} = t^*_{n_1,n_2;h_5,h_6}$ and $D_{h_1 h_2;n_1 n_2} = \epsilon_{h_1} + \epsilon_{h_2} - \epsilon_{n_1} - \epsilon_{n_2}$. Thus, we can evaluate the three terms in the r.h.s. directly, and compare to the result that we obtain computing the ADC self-energy matrices. Note that Eq. (D.42) can be evaluated efficiently by breaking down the sums as follows:

$$E^{(4,pp-6h)} = \frac{1}{16} \sum_{\substack{n_1 n_2 \\ h_3 h_4}} \left(\sum_{h_1,h_2} t_{n_1,n_2;h_1,h_2} \tilde{v}_{h_1 h_2;h_3,h_4} \right) \frac{1}{D_{h_3,h_4;n_1,n_2}} \left(\sum_{h_5,h_6} \tilde{v}_{h_3,h_4;h_5,h_6} t_{h_5,h_6;n_1,n_2} \right). \tag{D.43}$$

Also, restricted sums ($h_1 < h_2$, $n_1 < n_2$ etc.) can be used thanks to the matrix elements being antisymmetrized.

With the same steps, an identity can be obtained also for the backward-in-time part of the self-energy. We find

$$E^{<} = E^{(2)} + 2E^{(3,pp)} + E^{(4,hh-6p)}, \tag{D.44}$$

where $E^{(3,pp)}$ is the MBPT(3) pp ladder diagram, Eq. (D.26), and $E^{(4,hh-6p)}$ is the following MBPT(4) diagram involving sums over two hole and six particle states:

$$E^{(4,hh-6p)} = \frac{1}{16} \sum_{\substack{n_1 n_2 \\ h_3 h_4}} \frac{1}{D_{h_1 h_2,n_1 n_2}} \left(\sum_{n_3 n_4} \tilde{v}_{n_1 n_2,n_3 n_4} t_{n_3 n_4,h_1 h_2} \right) \left(\sum_{n_5 n_6} t_{h_1 h_2,n_5 n_6} \tilde{v}_{n_5 n_6,n_1 n_2} \right). \tag{D.45}$$

Such identities allow to check that the $M^{(2,pp)}$ and $N^{(2,hh)}$ are implemented correctly.

D.4.3 Ladder approximations in coupled-cluster and ADC

There exists an interesting connection between the ADC(ld,2) method (Sec. 4.2) and the coupled-cluster ladder approximation (CC-Ladd) [14, 130]. Both schemes give rise to an infinite sum of ladder diagrams that contribute to the ground-state energy.

The CC-Ladd scheme is defined by the following equations:

$$0 = \tilde{v}_{ab,ij} + (\epsilon_a + \epsilon_b - \epsilon_i - \epsilon_j) t_{ab,ij} + \frac{1}{2} \sum_{cd} \tilde{v}_{ab,cd} t_{cd,ij} + \frac{1}{2} \sum_{kl} t_{ab,kl} \tilde{v}_{kl,ij}, \tag{D.46}$$

where $a, b...$ and $i, j...$ denote particle and hole states, respectively. ϵ_α are the s.p. HF energies and the amplitude $t_{ab,ij}$ is the unknown. We also introduce the short-hand notation $D_{ab,ij} = \epsilon_i + \epsilon_j - \epsilon_a - \epsilon_b$. Rearranging Eq. (D.46) as

$$t_{ab,ij} = \frac{1}{D_{ab,ij}} \left(\tilde{v}_{ab,ij} + \frac{1}{2} \sum_{cd} \tilde{v}_{ab,cd} t_{cd,ij} + \frac{1}{2} \sum_{kl} t_{ab,kl} \tilde{v}_{kl,ij} \right) \tag{D.47}$$

immediately suggests an iterative method to solve these non-linear equations. Indeed, we start using the unperturbed amplitude $t^{(0)}$, Eq. (D.22), in the r.h.s. of (D.47), which provides on the l.h.s. a new estimate for the amplitude t. Then, we evaluate the CC energy correction contracting t with the 2N interaction [126],

$$E^{(CC)} = \frac{1}{4} \sum_{ab,ij} t_{ab,ij} \tilde{v}_{ij,ab}, \tag{D.48}$$

use the new t in Eq. (D.47), and so on, until the energy converges within a given tolerance.

The CC-Ladd approximation involves sums over intermediate pp and hh states. Two further simplifications are obtained including only either the hh or pp sums. These schemes are named CC hhLadd and CC ppLadd, respectively. The ppLadd approximation is similar to the well-known equations for the G-matrix [14]. From e.g. a diagrammatic analysis, it can be shown that these approximations generate for the energy the infinite series of the ladder diagrams propagating either only forward or backward excitations [199]. See also Fig. D.4, where the CC equations for the amplitude in the ppLadd approximations are represented in diagrammatic form.

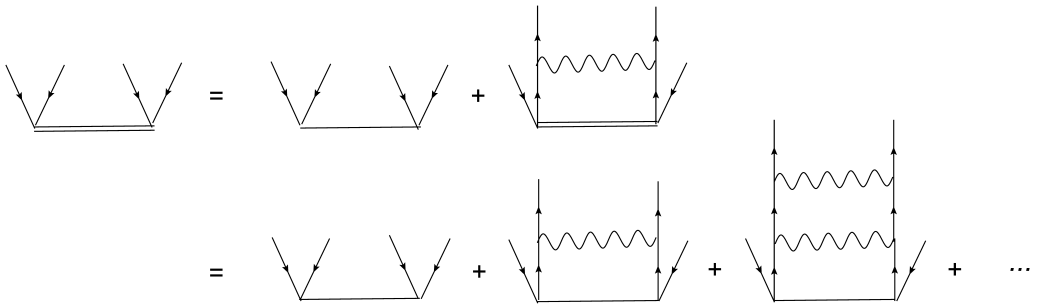

Figure D.4: Diagrammatic representation of the coupled-cluster equations for the amplitude (double line) in the particle-particle ladder approximation, see Eq. (D.46). Single straight lines denote the unperturbed amplitude $t^{(0)}$.

The ADC(ld,2) scheme, on the other hand, consists in using the ADC(2) coupling matrices $M^{(1)}$ and $N^{(1)}$, which simply amount to the interaction matrix elements, see Eq. (4.36) and (4.42), and the ladder interaction matrices $C^{(pp)}$ and $D^{(hh)}$. If we concentrate on the forward-in-time part of the self-energy and expand the energy denominator, we find

$$\Sigma^{>}(\omega) = V^{\dagger}\frac{1}{\hbar\omega\mathbb{1} - E^{>}}V + V^{\dagger}\frac{1}{\hbar\omega\mathbb{1} - E^{>}}C\frac{1}{\hbar\omega\mathbb{1} - E^{>}}V + ..., \tag{D.49}$$

where V is a compact notation for the interaction matrix elements $\tilde{v}_{n_1 n_2, \alpha k_3}$. Diagramatically, this is represented by Fig. D.5. Again, a ladder expansion can be recognized, with an infinite sum of terms with an increasing number of C insertions. If we close the forward self-energy diagram with an unperturbed fermion line, we find exactly the ladder expansion of the energy that was generated by CC in the ppLadd approximation. A similar argument holds for the hh case.

We conclude that the following identities must hold:

$$E^{>}_{ADC(ld,2)} = E^{(CC)}_{ppLadd}, \tag{D.50}$$

$$E^{<}_{ADC(ld,2)} = E^{(CC)}_{hhLadd}. \tag{D.51}$$

We have indeed verified that the previous equalities are satisfied to numerical accuracy.

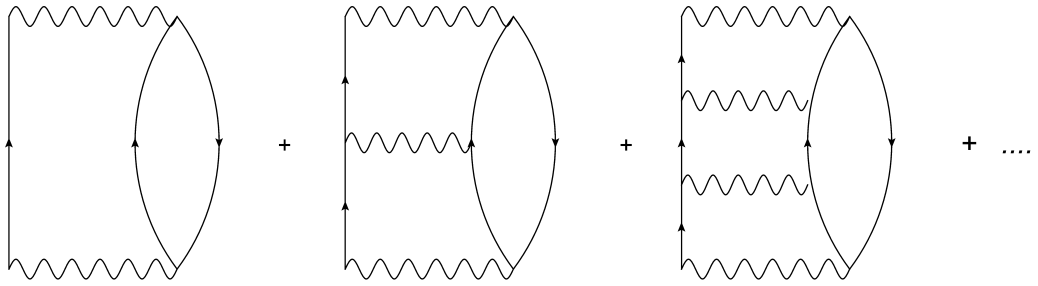

Figure D.5: Diagrams contributing to the ADC(ld,2) forward-in-time self-energy, Eq. (D.49).

D.5 Determination of the chemical potential

In this Section, we describe the algorithm to determine the chemical potential in the Gorkov formalism (see also Ref. [26]). The expectation value of the particle number, for each particle species i, is expressed as a function of the chemical potential, $A_i(\mu_i) = \langle\Psi_0|\hat{A}_i|\Psi_0\rangle$, by

$$A_i(\mu_i) = \sum_{\alpha}\rho_{\alpha\alpha} = \sum_{\alpha q}\left|\bar{\mathcal{V}}^{q}_{\alpha}\right|^2, \tag{D.52}$$

where Eq. (4.80) has been used. The amplitudes $\bar{\mathcal{V}}^{q}_{\alpha}$ are determined by solving the Gorkov equations (4.90) for that value of the chemical potentials. The Fermi energy is determined by fulfilling the condition on the particle number,

$$A_i(\mu_i) = A_i, \tag{D.53}$$

with A_i being the number of fermions of species i.

To solve the constraint (D.53), we exploit the fact that $A_i(\mu_i)$ is an increasing function of the chemical potential. Thus, the iterative bisection algorithm is well-suited to the root-finding problem (D.53). The monotonicity of $A(\mu)$, moreover, guarantees that a solution μ to the problem exists and is unique. For each particle species separately, a lower and an upper limit for the chemical potential are chosen that bracket the target particle number, i.e. $A_i(\mu_1) \leq A_i \leq A_i(\mu_2)$. Then, the number of particles is evaluated at the midpoint $\mu_m = (\mu_1 + \mu_2)/2$. If $A_i(\mu_m) > A_i$, then we perform the update $\mu_2 \longleftarrow \mu_m$; otherwise, $\mu_1 \longleftarrow \mu_m$. A new iteration is then started and so on until $|A_i(\mu_m) - A_i| \leq \epsilon_A$ for a given threshold ϵ_A. A few tens of iterations at most allow to reproduce the target particle number accurately. In infinite nuclear matter calculations, the procedure is relatively inexpensive from a computational point of view, since it essentially involves only several diagonalizations of the small Lanczos-reduced Gorkov matrix.

D.6 Relation between the Dyson and Gorkov propagators

In this Section, we further comment on the relation between the Dyson 1B GF and the normal propagator of Gorkov theory. A Dyson GF can always be mapped to a Gorkov propagator. Given a Dyson GF with N_{bk} and N_{fw} poles in the forward and backward parts, respectively, the corresponding Gorkov GF has $N_{poles} = N_{bk} + N_{fw}$ poles. The poles ω_q in the Gorkov representation are found as

$$\hbar\omega_q = \epsilon_n^+ - \mu \quad (q = n), \tag{D.54}$$

$$\hbar\omega_q = \mu - \epsilon_k^- \quad (q = k), \tag{D.55}$$

where μ is the chemical potential and n (k) label the quasi-particle (quasi-hole) Dyson states with excitation energies ϵ_n^+ (ϵ_k^-). The amplitudes are related as follows:

$$\mathcal{U}_\alpha^q = (\mathcal{X}_\alpha^n)^*, \; \bar{\mathcal{V}}_\alpha^q = 0 \quad (q = n), \tag{D.56}$$

$$\mathcal{U}_\alpha^q = 0, \; \bar{\mathcal{V}}_\alpha^q = \left(\mathcal{Y}_\alpha^k\right)^* \quad (q = k). \tag{D.57}$$

This implies, correctly, that the anomalous density (4.81) and the anomalous self-energy (4.87) vanish when a Dyson propagator, built on top of an HF state, is used.

In this case, the Gorkov matrix (4.89) reduces to

$$\begin{pmatrix} \mathcal{H} - \mu\mathbb{1} & 0 \\ 0 & -\left(\mathcal{H}^\dagger - \mu\mathbb{1}\right) \end{pmatrix} \begin{pmatrix} \mathcal{A}^q \\ \bar{\mathcal{B}}^q \end{pmatrix} = \hbar\omega_q \begin{pmatrix} \mathcal{A}^q \\ \bar{\mathcal{B}}^q \end{pmatrix}, \tag{D.58}$$

that decouples into

$$\mathcal{H}\mathcal{A}^q = (\mu + \hbar\omega_q)\mathcal{A}^q, \tag{D.59}$$

$$\mathcal{H}\mathcal{B}^q = (\mu - \hbar\omega_q)\mathcal{B}^q. \tag{D.60}$$

These are two copies of the Dyson eigenvalue problem (D.1) that contain the solution with energies above (below) the Fermi surface. No coupling is induced, and we find again the Dyson solution. Therefore, if we want to find a superfluid solution, it is essential to start with a propagator that generates a non-vanishing anomalous part, i.e. there must exist values of q for each both $\mathcal{U}_\alpha^q$ and $\bar{\mathcal{V}}_\alpha^q$ are non-vanishing. A simple choice is to start a sc0 cycle with a propagator with uniform amplitudes

$$\mathcal{U}_\alpha^q = \bar{\mathcal{V}}_\alpha^q = \frac{1}{\sqrt{2N_{poles}}}. \tag{D.61}$$

D.7 Parameters of a SCGF calculation

This Section summarizes the main parameters that are set in SCGF calculations.

The model space is determined by the cutoff N_{max}^2. We have found that $N_{max}^2 = 25$ is sufficient to obtain well-converged results in all cases considered, see Sec. 5.3.

The following tolerances are set for the convergence of the energies per particle. The overall convergence of a SCGF calculation is determined by the tolerance on OpRS energies, which we set to $\epsilon_{OpRS} = 10$ keV. For the sc0 iterations, we use $\epsilon_{sc0,Gorkov} = 10$ keV in Gorkov-sc0. The Dyson-sc0 cycle is much faster and we typically ask for convergence within $\epsilon_{sc0,Gorkov} = 1$ keV. In most cases, 10 OpRS iterations or less are sufficient. We limit the number of sc0 iterations to 20, although often about 10 are enough.

The number of Lanczos vectors is another parameter. We use 100 Lanczos iterations in both the forward and backward self-energies, that are sufficient to approximate the solution at excellent accuracy.

Bibliography

[1] A. Obertelli and H. Sagawa, *Modern nuclear physics : from fundamentals to frontiers / alexandre obertelli, hiroyuki sagawa*, Unitext for physics (Springer, Singapore, 2021).

[2] V. Somà, Eur. Phys. J. Plus **133**, 434 (2018).

[3] P. Möller and A. Sierk, International Journal of Mass Spectrometry **349-350**, 100 years of Mass Spectrometry, 19–25 (2013).

[4] E. Caurier, G. Martınez-Pinedo, F. Nowacki, A. Poves, and A. P. Zuker, Rev. Mod. Phys. **77**, 427–488 (2005).

[5] G. Colò, Advances in Physics: X **5**, 1740061 (2020).

[6] N. Schunck, ed., *Energy density functional methods for atomic nuclei*, 2053-2563 (IOP Publishing, 2019).

[7] H. Hergert, Frontiers in Physics **8**, 379 (2020).

[8] M. Hjorth-Jensen, M. Lombardo, and U. van Kolck, *An advanced course in computational nuclear physics: bridging the scales from quarks to neutron stars* (2017).

[9] R. Roth, "Ab initio approaches to nuclear structure", in *The euroschool on exotic beams, vol. vi*, edited by S. M. Lenzi and D. Cortina-Gil (Springer International Publishing, Cham, 2022), pp. 87–139.

[10] A. Ekström, C. Forssén, G. Hagen, G. R. Jansen, W. Jiang, and T. Papenbrock, Frontiers in Physics **11** (2023).

[11] M. Piarulli, E. Epelbaum, and C. Forssén, Frontiers in Physics **11** (2023).

[12] B. R. Barrett, P. Navrátil, and J. P. Vary, Progress in Particle and Nuclear Physics **69**, 131–181 (2013).

[13] G. Hagen, T. Papenbrock, M. Hjorth-Jensen, and D. J. Dean, Reports on Progress in Physics **77**, 096302 (2014).

[14] J. G. Lietz, S. Novario, G. R. Jansen, G. Hagen, and M. Hjorth-Jensen, "Computational nuclear physics and post hartree-fock methods", in *An advanced course in computational nuclear physics*, Vol. 936, Lecture Notes in Physics (Springer International Publishing, Cham, 2017), pp. 293–399.

[15] H. Hergert, S. Bogner, T. Morris, A. Schwenk, and K. Tsukiyama, Physics Reports **621**, Memorial Volume in Honor of Gerald E. Brown, 165–222 (2016).

[16] A. Tichai, R. Roth, and T. Duguet, Frontiers in Physics **8** (2020).

[17] J. Carlson, S. Gandolfi, F. Pederiva, S. C. Pieper, R. Schiavilla, K. E. Schmidt, and R. B. Wiringa, Rev. Mod. Phys. **87**, 1067–1118 (2015).

[18] S. Gandolfi, D. Lonardoni, A. Lovato, and M. Piarulli, Frontiers in Physics **8** (2020).

[19] V. Somà, Frontiers in Physics **8**, 340 (2020).

[20] A. Rios, Frontiers in Physics **8** (2020).

[21] T. D. Morris, J. Simonis, S. R. Stroberg, C. Stumpf, G. Hagen, J. D. Holt, G. R. Jansen, T. Papenbrock, R. Roth, and A. Schwenk, Phys. Rev. Lett. **120**, 152503 (2018).

[22] S. R. Stroberg, J. D. Holt, A. Schwenk, and J. Simonis, Phys. Rev. Lett. **126**, 022501 (2021).

[23] P. Arthuis, C. Barbieri, F. Pederiva, and A. Roggero, Phys. Rev. C **107**, 044303 (2023).

[24] T. Miyagi, S. R. Stroberg, P. Navrátil, K. Hebeler, and J. D. Holt, Phys. Rev. C **105**, 014302 (2022).

[25] B. Hu, W. Jiang, T. Miyagi, Z. Sun, A. Ekström, C. Forssén, G. Hagen, J. D. Holt, T. Papenbrock, S. R. Stroberg, and I. Vernon, Nature Physics **18**, 1196–1200 (2022).

[26] V. Somà, C. Barbieri, and T. Duguet, Phys. Rev. C **89**, 024323 (2014).

[27] A. Tichai, P. Demol, and T. Duguet, arXiv e-prints, arXiv:2307.15619, arXiv:2307.15619 (2023).

[28] P. Arthuis, C. Barbieri, M. Vorabbi, and P. Finelli, Physical Review Letters **125** (2020).

[29]S. Gandolfi, A. Gezerlis, and J. Carlson, Annual Review of Nuclear and Particle Science **65**, 303–328 (2015).

[30]N. Rocco, Frontiers in Physics **8** (2020).

[31]B. Acharya, S. Bacca, F. Bonaiti, S. S. Li Muli, and J. E. Sobczyk, Frontiers in Physics **10** (2023).

[32]M. Bender, P.-H. Heenen, and P.-G. Reinhard, Rev. Mod. Phys. **75**, 121–180 (2003).

[33]G. Colò, European physical journal plus **133**, 1–21 (2018).

[34]G. Giuliani and G. Vignale, *Quantum theory of the electron liquid* (Cambridge University Press, 2005).

[35]T. Nakatsukasa, K. Matsuyanagi, M. Matsuo, and K. Yabana, Rev. Mod. Phys. **88**, 045004 (2016).

[36]H. Liang and E. Litvinova, "Model for collective vibration", in *Handbook of nuclear physics* (Springer Nature Singapore, 2022), pp. 1–35.

[37]G. Colo', *Theoretical methods for giant resonances*, arXiv: 2201.04578 (2022) [nucl-th].

[38]X. Roca-Maza and N. Paar, Progress in Particle and Nuclear Physics **101**, 96–176 (2018).

[39]G. Burgio, H.-J. Schulze, I. Vidaña, and J.-B. Wei, Progress in Particle and Nuclear Physics **120**, 103879 (2021).

[40]N. Schunck and L. Robledo, Reports on Progress in Physics **79**, 116301 (2016).

[41]M. Bender, R. Bernard, G. Bertsch, S. Chiba, J. Dobaczewski, N. Dubray, S. A. Giuliani, K. Hagino, D. Lacroix, Z. Li, P. Magierski, J. Maruhn, W. Nazarewicz, J. Pei, S. Péru, N. Pillet, J. Randrup, D. Regnier, P.-G. Reinhard, L. M. Robledo, W. Ryssens, J. Sadhukhan, G. Scamps, N. Schunck, C. Simenel, J. Skalski, I. Stetcu, P. Stevenson, S. Umar, M. Verriere, D. Vretenar, M. Warda, and S. Åberg, Journal of Physics G: Nuclear and Particle Physics **47**, 113002 (2020).

[42]D. Vretenar, A. Afanasjev, G. Lalazissis, and P. Ring, Physics Reports **409**, 101–259 (2005).

[43]E. Chabanat, P. Bonche, P. Haensel, J. Meyer, and R. Schaeffer, Nuclear Physics A **627**, 710–746 (1997).

[44]J. Dobaczewski, Journal of Physics: Conference Series **312** (2010).

[45]J. Erler, N. Birge, M. Kortelainen, W. Nazarewicz, E. Olsen, A. M. Perhac, and M. Stoitsov, Nature (London) **486**, 509–512 (2012).

[46]A. Afanasjev, S. Agbemava, D. Ray, and P. Ring, Physics Letters B **726**, 680–684 (2013).

[47]A. Ravlić, E. Yüksel, T. Nikšić, and N. Paar, Nature Communications **14**, 4834–4834 (2023).

[48]M. Kortelainen, J. McDonnell, W. Nazarewicz, E. Olsen, P.-G. Reinhard, J. Sarich, N. Schunck, S. M. Wild, D. Davesne, J. Erler, and A. Pastore, Phys. Rev. C **89**, 054314 (2014).

[49]P.-G. Reinhard, X. Roca-Maza, and W. Nazarewicz, Phys. Rev. Lett. **129**, 232501 (2022).

[50]J. Piekarewicz, Phys. Rev. C **104**, 024329 (2021).

[51]E. Yüksel and N. Paar, Physics Letters B **836**, 137622 (2023).

[52]J. Drut, R. Furnstahl, and L. Platter, Progress in Particle and Nuclear Physics **64**, 120–168 (2010).

[53]J. Dobaczewski, Journal of Physics G: Nuclear and Particle Physics **43**, 04LT01 (2016).

[54]M. Grasso, Progress in Particle and Nuclear Physics **106**, 256–311 (2019).

[55]R. J. Furnstahl, The European Physical Journal A **56** (2020).

[56]R. Navarro Pérez, N. Schunck, A. Dyhdalo, R. J. Furnstahl, and S. K. Bogner, Phys. Rev. C **97**, 054304 (2018).

[57]L. Zurek, E. A. Coello Pérez, S. K. Bogner, R. J. Furnstahl, and A. Schwenk, Phys. Rev. C **103**, 014325 (2021).

[58]L. Zurek, S. K. Bogner, R. J. Furnstahl, R. N. Pérez, N. Schunck, and A. Schwenk, *Optimized nuclear energy density functionals including long-range pion contributions*, arXiv: 2307.13568 (2023) [nucl-th].

[59]T. Duguet, J.-P. Ebran, M. Frosini, H. Hergert, and V. Somà, The European physical journal. A, Hadrons and nuclei **59** (2023).

[60]A. Boulet and D. Lacroix, Phys. Rev. C **97**, 014301 (2018).

[61]A. Boulet, G. Wlazłowski, and P. Magierski, Phys. Rev. A **106**, 013306 (2022).

[62]J. Bonnard, M. Grasso, and D. Lacroix, Phys. Rev. C **98**, 034319 (2018).

[63]J. Bonnard, M. Grasso, and D. Lacroix, Phys. Rev. C **101**, 064319 (2020).

[64]C. J. Yang, W. G. Jiang, S. Burrello, and M. Grasso, Phys. Rev. C **106**, L011305 (2022).

[65]G. Salvioni, J. Dobaczewski, C. Barbieri, G. Carlsson, A. Idini, and A. Pastore, Journal of Physics G: Nuclear and Particle Physics **47**, 085107 (2020).

[66]J. P. Perdew and K. Schmidt, AIP Conference Proceedings **577**, 1–20 (2001).

[67]M. G. Medvedev, I. S. Bushmarinov, J. Sun, J. P. Perdew, and K. A. Lyssenko, Science **355**, 49–52 (2017).

[68]F. Marino, C. Barbieri, A. Carbone, G. Colò, A. Lovato, F. Pederiva, X. Roca-Maza, and E. Vigezzi, Phys. Rev. C **104**, 024315 (2021).

[69]J. Stone and P.-G. Reinhard, Progress in Particle and Nuclear Physics **58**, 587–657 (2007).

[70]M. Baldo, P. Schuck, and X. Viñas, Physics Letters B **663**, 390–394 (2008).

[71]M. Baldo, L. M. Robledo, P. Schuck, and X. Viñas, Phys. Rev. C **87**, 064305 (2013).

[72]J. P. Perdew, K. Burke, and M. Ernzerhof, Phys. Rev. Lett. **77**, 3865–3868 (1996).

[73]S. Gandolfi, J. Carlson, and S. C. Pieper, Phys. Rev. Lett. **106**, 012501 (2011).

[74]M. Buraczynski and A. Gezerlis, Phys. Rev. Lett. **116**, 152501 (2016).

[75]M. Buraczynski and A. Gezerlis, Phys. Rev. C **95**, 044309 (2017).

[76]M. Buraczynski, S. Martinello, and A. Gezerlis, Physics Letters B **818**, 136347 (2021).

[77]G. Senatore, S. Moroni, and D. M. Ceperley, "Static response of homogeneous quantum fluids by diffusion monte carlo", in *Quantum monte carlo methods in physics and chemistry*, edited by M. Nightingale and C. J. Umrigar (Springer Netherlands, 1999).

[78]T. Dornheim, S. Groth, and M. Bonitz, Physics Reports **744**, 1–86 (2018).

[79]M. Buraczynski, S. Martinello, and A. Gezerlis, Phys. Rev. C **105**, 025807 (2022).

[80]F. Marino, G. Colò, X. Roca-Maza, and E. Vigezzi, Phys. Rev. C **107**, 044311 (2023).

[81]F. Raimondi and C. Barbieri, Phys. Rev. C **97**, 054308 (2018).

[82]C. Barbieri and A. Carbone, "Self-consistent green's function approaches", in *An advanced course in computational nuclear physics: bridging the scales from quarks to neutron stars*, edited by M. Hjorth-Jensen, M. P. Lombardo, and U. van Kolck (Springer International Publishing, Cham, 2017), pp. 571–644.

[83]C. Mcilroy, "Self-consistent green's function studies of modern hamiltonians in finite and infinite systems.", PhD thesis (University of Surrey, 2020).

[84]V. Somà, T. Duguet, and C. Barbieri, Phys. Rev. C **84**, 064317 (2011).

[85]A. Roggero, A. Mukherjee, and F. Pederiva, Phys. Rev. C **92**, 054303 (2015).

[86]S. K. Bogner, R. J. Furnstahl, H. Hergert, M. Kortelainen, P. Maris, M. Stoitsov, and J. P. Vary, Phys. Rev. C **84**, 044306 (2011).

[87]S. Gandolfi, A. Lovato, J. Carlson, and K. E. Schmidt, Phys. Rev. C **90**, 061306 (2014).

[88]D. Lonardoni, I. Tews, S. Gandolfi, and J. Carlson, Phys. Rev. Res. **2**, 022033 (2020).

[89]R. B. Wiringa and S. C. Pieper, Phys. Rev. Lett. **89**, 182501 (2002).

[90]J. E. Lynn and K. E. Schmidt, Phys. Rev. C **86**, 014324 (2012).

[91]J. E. Lynn, "Quantum monte carlo calculations of light nuclei with non-local potentials", PhD thesis (Arizona State University, 2013).

[92]M. Piarulli and I. Tews, Frontiers in Physics **7** (2020).

[93]R. Machleidt and D. Entem, Physics Reports **503**, 1–75 (2011).

[94]R. B. Wiringa, V. G. J. Stoks, and R. Schiavilla, Phys. Rev. C **51**, 38–51 (1995).

[95]R. Machleidt, Phys. Rev. C **63**, 024001 (2001).

[96]I. Tews, Z. Davoudi, A. Ekström, J. D. Holt, K. Becker, R. Briceño, D. J. Dean, W. Detmold, C. Drischler, T. Duguet, E. Epelbaum, A. Gasparyan, J. Gegelia, J. R. Green, H. W. Grießhammer, A. D. Hanlon, M. Heinz, H. Hergert, M. Hoferichter, M. Illa, D. Kekejian, A. Kievsky, S. König, H. Krebs, K. D. Launey, D. Lee, P. Navrátil, A. Nicholson, A. Parreño, D. R. Phillips, M. Płoszajczak, X.-L. Ren, T. R. Richardson, C. Robin, G. H. Sargsyan, M. J. Savage, M. R. Schindler, P. E. Shanahan, R. P. Springer, A. Tichai, U. van Kolck, M. L. Wagman, A. Walker-Loud, C.-J. Yang, and X. Zhang, Few-Body Systems **63**, 67, 67 (2022).

[97]E. Epelbaum, H.-W. Hammer, and U.-G. Meißner, Rev. Mod. Phys. **81**, 1773–1825 (2009).

[98]R. Machleidt and F. Sammarruca, Physica Scripta **91**, 083007 (2016).

[99]H.-W. Hammer, S. König, and U. van Kolck, Rev. Mod. Phys. **92**, 025004 (2020).

[100]C. Drischler, W. Haxton, K. McElvain, E. Mereghetti, A. Nicholson, P. Vranas, and A. Walker-Loud, Progress in Particle and Nuclear Physics **121**, 103888 (2021).

[101]C. McIlroy, C. Barbieri, T. Inoue, T. Doi, and T. Hatsuda, Phys. Rev. C **97**, 021303 (2018).

[102]A. Gezerlis, I. Tews, E. Epelbaum, S. Gandolfi, K. Hebeler, A. Nogga, and A. Schwenk, Phys. Rev. Lett. **111**, 032501 (2013).

[103]D. Lonardoni, S. Gandolfi, J. E. Lynn, C. Petrie, J. Carlson, K. E. Schmidt, and A. Schwenk, Phys. Rev. C **97**, 044318 (2018).

[104]A. Rios, A. Carbone, and A. Polls, Phys. Rev. C **96**, 014003 (2017).

[105]A. Ekström, G. R. Jansen, K. A. Wendt, G. Hagen, T. Papenbrock, B. D. Carlsson, C. Forssén, M. Hjorth-Jensen, P. Navrátil, and W. Nazarewicz, Phys. Rev. C **91**, 051301 (2015).

[106]W. G. Jiang, A. Ekström, C. Forssén, G. Hagen, G. R. Jansen, and T. Papenbrock, Phys. Rev. C **102**, 054301 (2020).

[107]F. Sammarruca and R. Millerson, Phys. Rev. C **102**, 034313 (2020).

[108]D. Lonardoni and F. Pederiva, *Medium-mass hypernuclei and the nucleon-isospin dependence of the three-body hyperon-nucleon-nucleon force*, arXiv: 1711.07521 (2017) [nucl-th].

[109]D. Lonardoni, "From hypernuclei to hypermatter: a quantum monte carlo study of strangeness in nuclear structure and nuclear astrophysics", PhD thesis (Universitá di Trento, 2013).

[110]A. Ekström, G. Hagen, T. D. Morris, T. Papenbrock, and P. D. Schwartz, Phys. Rev. C **97**, 024332 (2018).

[111]A. Carbone, Phys. Rev. Research **2**, 023227 (2020).

[112]Y. Nosyk, D. R. Entem, and R. Machleidt, Phys. Rev. C **104**, 054001 (2021).

[113]V. Somà, P. Navrátil, F. Raimondi, C. Barbieri, and T. Duguet, Phys. Rev. C **101**, 014318 (2020).

[114]T. Hüther, K. Vobig, K. Hebeler, R. Machleidt, and R. Roth, Physics Letters B **808**, 135651 (2020).

[115]A. L. Fetter and J. D. Walecka, *Quantum theory of many-particle systems* (McGraw-Hill, Boston, 1971).

[116]T. M, C. Sfienti, J. Piekarewicz, C. J. Horowitz, and M. Vanderhaeghen, Journal of Physics G: Nuclear and Particle Physics **46**, 093003 (2019).

[117]G. F. Burgio and I. Vidaña, Universe **6** (2020).

[118]P. Haensel, A. Y. Potekhin, and D. G. Yakovlev, *Neutron stars 1: Equation of state and structure*, Vol. 326 (Springer, New York, USA, 2007).

[119]J. Piekarewicz, *The nuclear physics of neutron stars*, arxiv: 2209.14877 (2022) [nucl-th].

[120]*The physics and astrophysics of neutron stars*, eng, 1st ed. 2018., Astrophysics and Space Science Library, 457 (Springer International Publishing, Cham, 2018).

[121]A. Bulgac, M. M. Forbes, and P. Magierski, "The unitary fermi gas: from monte carlo to density functionals", in *The bcs-bec crossover and the unitary fermi gas*, Lecture Notes in Physics (Springer Berlin Heidelberg, Berlin, Heidelberg, 2011), pp. 305–373.

[122]D. Blaschke and N. Chamel, "Phases of dense matter in compact stars", eng, in *Arxiv.org* (Cornell University Library, arXiv.org, Ithaca, 2018).

[123]J. Keller, K. Hebeler, and A. Schwenk, Phys. Rev. Lett. **130**, 072701 (2023).

[124]A. Pastore, D. Davesne, and J. Navarro, Physics Reports **563**, 1–67 (2015).

[125]C. Drischler, "Nuclear matter from chiral effective field theory", PhD thesis (Technische Universität Darmstadt, 2017).

[126]G. Hagen, T. Papenbrock, A. Ekström, K. A. Wendt, G. Baardsen, S. Gandolfi, M. Hjorth-Jensen, and C. J. Horowitz, Phys. Rev. C **89**, 014319 (2014).

[127]M. Piarulli, I. Bombaci, D. Logoteta, A. Lovato, and R. B. Wiringa, Phys. Rev. C **101**, 045801 (2020).

[128]I. Tews, Frontiers in Physics **8** (2020).

[129]P. Maris, J. P. Vary, S. Gandolfi, J. Carlson, and S. C. Pieper, Phys. Rev. C **87**, 054318 (2013).

[130]G. Baardsen, A. Ekström, G. Hagen, and M. Hjorth-Jensen, Phys. Rev. C **88**, 054312 (2013).

[131]Buraczynski, M., Dawkins, W., Ismail, N., and Gezerlis, A., EPJ Web Conf. **182**, 02044 (2018).

[132]S. Moroni, D. M. Ceperley, and G. Senatore, Phys. Rev. Lett. **75**, 689–692 (1995).

[133]S. Groth, T. Dornheim, and M. Bonitz, The Journal of Chemical Physics **147**, 164108 (2017).

[134]C. Lin, F. H. Zong, and D. M. Ceperley, Phys. Rev. E **64**, 016702 (2001).

[135]L. Riz, F. Pederiva, D. Lonardoni, and S. Gandolfi, Particles **3**, 706–718 (2020).

[136]S. Lundqvist and N. H. March, eds., *Theory of the inhomogeneous electron gas* (Springer, Boston, MA, 1983).

[137]F. Dalfovo, A. Lastri, L. Pricaupenko, S. Stringari, and J. Treiner, Phys. Rev. B **52**, 1193–1209 (1995).

[138]J. Carlson, S. Gandolfi, and A. Gezerlis, Progress of Theoretical and Experimental Physics **2012**, 01A209 (2012).

[139]D. Davesne, A. Pastore, and J. Navarro, Progress in Particle and Nuclear Physics **120**, 103870 (2021).

[140]R. N. Bisset, P. B. Blakie, and S. Stringari, Phys. Rev. A **100**, 013620 (2019).

[141]B. Mihaila, *Lindhard function of a d-dimensional fermi gas*, arXiv: 1111.5337 (2011) [cond-mat.quant-gas].

[142]R. M. Martin, *Electronic structure : basic theory and practical methods*, 2. ed (Cambridge university press, Cambridge, 2020).

[143]P. Hohenberg and W. Kohn, Phys. Rev. **136**, B864–B871 (1964).

[144]R. G. Parr and W. Yang, *Density-functional theory of atoms and molecules (international series of monographs on chemistry)* (Oxford University Press, USA, 1994).

[145]K. Burke, The Journal of Chemical Physics **136**, 150901 (2012).

[146]A. D. Becke, The Journal of Chemical Physics **140**, 18A301 (2014).

[147]L. Guo, D. Lacroix, N. Schunck, C. Simenel, and P. Stevenson, Frontiers in Physics **8** (2021).

[148]C. J. Horowitz, A. Arcones, B. Côté, I. Dillmann, W. Nazarewicz, I. U. Roederer, H. Schatz, A. Aprahamian, D. Atanasov, A. Bauswein, T. C. Beers, J. Bliss, M. Brodeur, J. A. Clark, A. Frebel, F. Foucart, C. J. Hansen, O. Just, A. Kankainen, G. C. McLaughlin, J. M. Kelly, S. N. Liddick, D. M. Lee, J. Lippuner, D. Martin, J. Mendoza-Temis, B. D. Metzger, M. R. Mumpower, G. Perdikakis, J. Pereira, B. W. O'Shea, R. Reifarth, A. M. Rogers, D. M. Siegel, A. Spyrou, R. Surman, X. Tang, T. Uesaka, and M. Wang, Journal of Physics G: Nuclear and Particle Physics **46**, 083001 (2019).

[149]S. A. Giuliani, G. Martınez-Pinedo, and L. M. Robledo, Phys. Rev. C **97**, 034323 (2018).

[150]P. Hohenberg and W. Kohn, Phys. Rev. **136**, B864–B871 (1964).

[151]P. Chomaz and K. Hasnaoui, *From energy-density functionals to mean field potentials: a systematic derivation*, arXiv: 0610027v2 (2009) [nucl-th].

[152]D. Vautherin and D. M. Brink, Phys. Rev. C **5**, 626–647 (1972).

[153]T. Nikšić, D. Vretenar, and P. Ring, Progress in Particle and Nuclear Physics **66**, 519–548 (2011).

[154]G. Colò, L. Cao, N. V. Giai, and L. Capelli, Computer Physics Communications **184**, 142–161 (2013).

[155]A. Liardi, F. Marino, G. Colò, X. Roca-Maza, and E. Vigezzi, Phys. Rev. C **105**, 034309 (2022).

[156]P. Ring and P. Schuck, *The nuclear many-body problem* (Springer-Verlag, New York, 1980).

[157]J. Margueron, R. Hoffmann Casali, and F. Gulminelli, Phys. Rev. C **97**, 025805 (2018).

[158]P. Papakonstantinou, T.-S. Park, Y. Lim, and C. H. Hyun, Phys. Rev. C **97**, 014312 (2018).

[159]A. Bulgac, M. M. Forbes, S. Jin, R. N. Perez, and N. Schunck, Phys. Rev. C **97**, 044313 (2018).

[160]U. Garg and G. Colò, Progress in Particle and Nuclear Physics **101**, 55–95 (2018).

[161]N. Kaiser, S. Fritsch, and W. Weise, Nuclear Physics A **697**, 255–276 (2002).

[162]R. Andrae, T. Schulze-Hartung, and P. Melchior, *Dos and don'ts of reduced chi-squared*, arXiv: 1012.3754 (2010) [astro-ph.IM].

[163]T. Hastie, R. Tibshirani, and J. Friedman, *The elements of statistical learning: data mining, inference and prediction*, 2nd ed. (Springer, 2009).

[164]P. Mehta, M. Bukov, C.-H. Wang, A. G. Day, C. Richardson, C. K. Fisher, and D. J. Schwab, Physics Reports **810**, 1–124 (2019).

[165]F. Pedregosa, G. Varoquaux, A. Gramfort, V. Michel, B. Thirion, O. Grisel, M. Blondel, P. Prettenhofer, R. Weiss, V. Dubourg, J. Vanderplas, A. Passos, D. Cournapeau, M. Brucher, M. Perrot, and E. Duchesnay, Journal of Machine Learning Research **12**, 2825–2830 (2011).

[166]H. Dembinski and P. O. et al., 10.5281/zenodo.3949207 (2020).

[167]F. James and M. Roos, Comput. Phys. Commun. **10**, 343–367 (1975).

[168]X. Roca-Maza, G. Colò, and H. Sagawa, Phys. Rev. C **86**, 031306 (2012).

[169]J. Carlson and S. Gandolfi, Phys. Rev. A **90**, 011601 (2014).

[170]G. Rupak and T. Schäfer, Nuclear Physics A **816**, 52–64 (2009).

[171]M. M. Forbes, *The Unitary Fermi Gas in a Harmonic Trap and its Static Response*, arXiv: 1211.3779 (2012) [cond-mat.quant-gas].

[172]T. Dornheim, J. Vorberger, S. Groth, N. Hoffmann, Z. A. Moldabekov, and M. Bonitz, The Journal of Chemical Physics **151**, 194104 (2019).

[173]Z. Moldabekov, 1. Vorberger, and T. Dornheim, Journal of Chemical Theory and Computation **18**, 2900–2912 (2022).

[174]Z. A. Moldabekov, X. Shao, M. Pavanello, J. Vorberger, F. Graziani, and T. Dornheim, arXiv: 2304.11169 (2023) [physics.comp-ph].

[175]P. Danielewicz and J. Lee, Nuclear Physics A **818**, 36–96 (2009).

[176]J. Izaac, *Computational quantum mechanics*, 1st ed. 2018., Undergraduate Lecture Notes in Physics (Springer International Publishing, Cham, 2018).

[177]W. M. C. Foulkes, L. Mitas, R. J. Needs, and G. Rajagopal, Rev. Mod. Phys. **73**, 33–83 (2001).

[178]F. Pederiva, A. Roggero, and K. Schmidt, "Variational and diffusion monte carlo approaches to the nuclear few- and many-body problem", English (US), in *Lecture notes in physics*, Vol. 936, Lecture Notes in Physics (Springer Verlag, Germany, 2017), pp. 401–476.

[179]J. Lynn, I. Tews, S. Gandolfi, and A. Lovato, Annual Review of Nuclear and Particle Science **69**, 279–305 (2019).

[180]R. M. Martin, L. Reining, and D. M. Ceperley, "Stochastic methods", in *Interacting electrons: theory and computational approaches* (Cambridge University Press, 2016).

[181]D. M. Ceperley and B. J. Alder, Phys. Rev. Lett. **45**, 566–569 (1980).

[182]B. M. Austin, D. Y. Zubarev, and W. A. J. Lester, Chemical Reviews **112**, PMID: 22196085, 263–288 (2012).

[183]L. Pollet, Reports on Progress in Physics **75**, 094501 (2012).

[184]F. Becca and S. Sorella, *Quantum monte carlo approaches for correlated systems* (Cambridge University Press, 2017).

[185]C. Adams, G. Carleo, A. Lovato, and N. Rocco, Phys. Rev. Lett. **127**, 022502 (2021).

[186]A. Lovato, C. Adams, G. Carleo, and N. Rocco, Phys. Rev. Res. **4**, 043178 (2022).

[187]G. Pescia, J. Han, A. Lovato, J. Lu, and G. Carleo, Phys. Rev. Res. **4**, 023138 (2022).

[188]A. Lovato, I. Bombaci, D. Logoteta, M. Piarulli, and R. B. Wiringa, Phys. Rev. C **105**, 055808 (2022).

[189]S. Gandolfi, F. Pederiva, S. Fantoni, and K. E. Schmidt, Phys. Rev. Lett. **98**, 102503 (2007).

[190]M. Baldo, A. Polls, A. Rios, H.-J. Schulze, and I. Vidaña, Phys. Rev. C **86**, 064001 (2012).

[191]M. Piarulli, L. Girlanda, R. Schiavilla, A. Kievsky, A. Lovato, L. E. Marcucci, S. C. Pieper, M. Viviani, and R. B. Wiringa, Phys. Rev. C **94**, 054007 (2016).

[192]J. E. Lynn, J. Carlson, E. Epelbaum, S. Gandolfi, A. Gezerlis, and A. Schwenk, Phys. Rev. Lett. **113**, 192501 (2014).

[193]M. Piarulli, A. Baroni, L. Girlanda, A. Kievsky, A. Lovato, E. Lusk, L. E. Marcucci, S. C. Pieper, R. Schiavilla, M. Viviani, and R. B. Wiringa, Phys. Rev. Lett. **120**, 052503 (2018).

[194]A. Roggero, A. Mukherjee, and F. Pederiva, Phys. Rev. B **88**, 115138 (2013).

[195]A. Roggero, A. Mukherjee, and F. Pederiva, Phys. Rev. Lett. **112**, 221103 (2014).

[196]D. Logoteta, The European physical journal. A, Hadrons and nuclei **54** (2018).

[197]A. Sarsa, S. Fantoni, K. E. Schmidt, and F. Pederiva, Phys. Rev. C **68**, 024308 (2003).

[198]L. Contessi, A. Lovato, F. Pederiva, A. Roggero, J. Kirscher, and U. van Kolck, Physics Letters B **772**, 839–848 (2017).

[199]R. D. Mattuck, *A guide to Feynman diagrams in the many-body problem*, European physics series (pub-MCGRAW-HILL, pub-MCGRAW-HILL:adr, 1967), pp. xii + 294.

[200]W. Dickhoff and C. Barbieri, Progress in Particle and Nuclear Physics **52**, 377–496 (2004).

[201]C. Barbieri, T. Duguet, and V. Somà, Phys. Rev. C **105**, 044330 (2022).

[202]W. H. Dickhoff and D. V. Neck, *Many-body theory exposed!* (World Scientific Publishing, 2004).

[203]A. Carbone, A. Cipollone, C. Barbieri, A. Rios, and A. Polls, Phys. Rev. C **88**, 054326 (2013).

[204]J. Schirmer and G. Angonoa, The Journal of Chemical Physics **91**, 1754–1761 (1989).

[205]J. Schirmer, *Many-body methods for atoms, molecules and clusters* (Jan. 2018).

[206]C. Barbieri, D. Van Neck, and W. H. Dickhoff, Phys. Rev. A **76**, 052503 (2007).

[207]C. Barbieri, D. Van Neck, and M. Degroote, Phys. Rev. A **85**, 012501 (2012).

[208]V. Somà, C. Barbieri, and T. Duguet, Phys. Rev. C **87**, 011303 (2013).

[209]H.-G. Weikert, H.-D. Meyer, L. S. Cederbaum, and F. Tarantelli, The Journal of Chemical Physics **104**, 7122–7138 (1996).

[210]C. Barbieri and M. Hjorth-Jensen, Phys. Rev. C **79**, 064313 (2009).

[211]F. Raimondi and C. Barbieri, Phys. Rev. C **99**, 054327 (2019).

[212]G. Baym and L. P. Kadanoff, Phys. Rev. **124**, 287–299 (1961).

[213]G. Baym, Phys. Rev. **127**, 1391–1401 (1962).

[214]A. Rios, A. Polls, A. Ramos, and H. Müther, Phys. Rev. C **74**, 054317 (2006).

[215]R. M. Martin, L. Reining, and D. M. Ceperley, "Many-body green's function methods", in *Interacting electrons: theory and computational approaches* (Cambridge University Press, 2016).

[216]S. Gandolfi, G. Palkanoglou, J. Carlson, A. Gezerlis, and K. E. Schmidt, Condensed Matter **7**, 10 . 3390 / condmat7010019 (2022).

[217]D. J. Dean and M. Hjorth-Jensen, Rev. Mod. Phys. **75**, 607–656 (2003).

[218]E. Garrido, P. Sarriguren, E. Moya de Guerra, and P. Schuck, Phys. Rev. C **60**, 064312 (1999).

[219]Sedrakian, Armen and Clark, John W., Eur. Phys. J. A **55**, 167 (2019).

[220]Drissi, Mehdi and Rios, Arnau, Eur. Phys. J. A **58**, 90 (2022).

[221]L. G. Cao, U. Lombardo, and P. Schuck, Phys. Rev. C **74**, 064301 (2006).

[222]D. Ding, A. Rios, H. Dussan, W. H. Dickhoff, S. J. Witte, A. Carbone, and A. Polls, Phys. Rev. C **94**, 025802 (2016).

[223]A. Carbone, A. Rios, and A. Polls, Phys. Rev. C **90**, 054322 (2014).

[224]M. Pini, P. Pieri, and G. C. Strinati, Phys. Rev. B **99**, 094502 (2019).

[225]A. Carbone, A. Polls, and A. Rios, Phys. Rev. C **88**, 044302 (2013).

[226]A. Rios, A. Polls, and I. Vidaña, Phys. Rev. C **79**, 025802 (2009).

[227]Gandolfi, S., Carlson, J., Reddy, S., Steiner, A. W., and Wiringa, R. B., Eur. Phys. J. A **50**, 10 (2014).

[228]A. Rios, A. Polls, and W. Dickhoff, Journal of Low Temperature Physics **189**, 234–249 (2017).

[229]I. Angeli and K. Marinova, Atomic Data and Nuclear Data Tables **99**, 69–95 (2013).

[230]M. Wang, G. Audi, F. G. Kondev, W. Huang, S. Naimi, and X. Xu, Chinese Physics C **41**, 030003 (2017).

[231]J. Bartel, P. Quentin, M. Brack, C. Guet, and H.-B. Håkansson, Nuclear Physics A **386**, 79–100 (1982).

[232]P.-G. Reinhard and H. Flocard, Nuclear physics. A **584**, 467–488 (1995).

[233]X. Roca-Maza, G. Colò, and H. Sagawa, Phys. Rev. C **86**, 031306 (2012).

[234]R. Bollapragada, M. Menickelly, W. Nazarewicz, J. O'Neal, P.-G. Reinhard, and S. M. Wild, Journal of Physics G: Nuclear and Particle Physics **48**, 024001 (2020).

[235]M. Buraczynski, N. Ismail, and A. Gezerlis, Eur. Phys. J. A **56**, 112 (2020).

[236]M. Buraczynski, N. Ismail, and A. Gezerlis, Phys. Rev. Lett. **122**, 152701 (2019).

[237]H. W. Griesshammer, Eur. Phys. J. A **56**, 118 (2020).

[238]E. Epelbaum, Progress in Particle and Nuclear Physics **57**, 654–741 (2006).

[239]A. Ekström, G. Baardsen, C. Forssén, G. Hagen, M. Hjorth-Jensen, G. R. Jansen, R. Machleidt, W. Nazarewicz, T. Papenbrock, J. Sarich, and S. M. Wild, Phys. Rev. Lett. **110**, 192502 (2013).

[240]N. Kaiser, R. Brockmann, and W. Weise, Nuclear Physics A **625**, 758–788 (1997).

[241]K. Hebeler, Physics Reports **890**, 1–116 (2021).

[242]E. Epelbaum, A. Nogga, W. Glöckle, H. Kamada, U.-G. Meißner, and H. Witała, Phys. Rev. C **66**, 064001 (2002).

[243]C. Drischler, K. Hebeler, and A. Schwenk, Phys. Rev. C **93**, 054314 (2016).

[244]A. Lovato, O. Benhar, S. Fantoni, and K. E. Schmidt, Phys. Rev. C **85**, 024003 (2012).

[245]K. Hebeler and A. Schwenk, Phys. Rev. C **82**, 014314 (2010).

[246]A. Dyhdalo, R. J. Furnstahl, K. Hebeler, and I. Tews, Phys. Rev. C **94**, 034001 (2016).

[247]P. Navratil, Few-Body Systems **41**, 117–140 (2007).

[248]D. Lonardoni and I. Tews, PoS - Proceedings of Science **317** (2020).

[249]H. Krebs, E. Epelbaum, and U.-G. Meissner, Eur. Phys. J. A **32**, 127–137 (2007).

[250]E. Epelbaum, H. Krebs, and U.-G. Meißner, **806**, 65–78 (2008).

[251]D. Logoteta, I. Bombaci, and A. Kievsky, Phys. Rev. C **94**, 064001 (2016).

[252]A. Lacour, J. A. Oller, and U. .-. Meissner, Annals Phys. **326**, 241–306 (2011).

[253]D. M. Brink and G. R. Satchler, *Angular momentum, 3rd edition* (Oxford Science Publications, 1993).

[254]H. Hergert, S. K. Bogner, J. G. Lietz, T. D. Morris, S. Novario, N. M. Parzuchowski, and F. Yuan, Lect. Notes Phys. **936**, 477–570 (2017).

[255]B. Zhu, R. Wirth, and H. Hergert, Phys. Rev. C **104**, 044002 (2021).

[256]R. K. P. Zia, E. F. Redish, and S. R. McKay, American Journal of Physics **77**, 614–622 (2009).

[257]W. Kutzelnigg, English, Journal of Molecular Structure **768**, 163–173 (2006).

[258]M. Dutra, O. Louren ço, J. S. Sá Martins, A. Delfino, J. R. Stone, and P. D. Stevenson, Phys. Rev. C **85**, 035201 (2012).

[259]T. Dornheim, M. Böhme, Z. A. Moldabekov, 1. Vorberger, and M. Bonitz, Phys. Rev. Research **3**, 033231 (2021).

[260]A. Pastore, D. Davesne, Y. Lallouet, M. Martini, K. Bennaceur, and J. Meyer, Phys. Rev. C **85**, 054317 (2012).

[261]A. Pastore, M. Martini, V. Buridon, D. Davesne, K. Bennaceur, and J. Meyer, Phys. Rev. C **86**, 044308 (2012).

[262]J. Izaac and J. Wang, *Computational quantum mechanics*, eng, 1st ed. 2018., Undergraduate Lecture Notes in Physics (Springer International Publishing, Cham, 2018).

[263]V. Somà, A. Cipollone, C. Barbieri, P. Navrátil, and T. Duguet, Phys. Rev. C **89**, 061301 (2014).

[264]I. Shavitt and R. J. Bartlett, *Many-body methods in chemistry and physics: mbpt and coupled-cluster theory*, Cambridge Molecular Science (Cambridge University Press, 2009).

[265]S. Bogner, R. Furnstahl, and A. Schwenk, Progress in Particle and Nuclear Physics **65**, 94–147 (2010).

List of publications

As of December 2023

The work reported in this thesis is partially based on the following peer-reviewed publications:

1. **F. Marino**, C. Barbieri, A. Carbone, G. Colò, A. Lovato, F. Pederiva, X. Roca-Maza, and E. Vigezzi, Phys. Rev. C **104**, 024315 (2021)
2. A. Liardi, **F. Marino**, G. Colò, X. Roca-Maza, and E. Vigezzi, Phys. Rev. C **105**, 034309 (2022)
3. **F. Marino**, G. Colò, X. Roca-Maza, and E. Vigezzi, Phys. Rev. C **107**, 044311 (2023)

Acknowledgements

At the end of this journey, I want to thank first of all my supervisor, Gianluca Colò, to whom I am indebted for his constant support and guidance, both from a scientific and human point of view.

A great thank goes also to my co-supervisor, Francesco Pederiva, for his encouragement and many insightful discussions.

I am grateful to the referees Alexandros Gezerlis and Jérôme Margueron for carefully reading my manuscript and providing useful feedback, and to Laura Elisa Marcucci and Vittorio Somà for accepting to be part of my PhD defense committee.

During my PhD, I have been lucky to have the opportunity to collaborate with several people. I would like to thank the members of the theory group in Milano, Carlo Barbieri, Xavier Roca-Maza, and Enrico Vigezzi. Their help and support were very important on countless occasions. Carlo played a very important role in the second half of my doctorate, and I thank him for teaching me so much about Green's functions. I also enjoyed the (mostly) long-distance collaboration with Alessandro Lovato.

I am also happy to acknowledge Arianna Carbone, for her contribution to my first paper, Alex Gezerlis, for sending me his results for the neutron matter response, Arnau Rios, for inviting me to give a seminar in Barcelona, and Alessandro Roggero, for sharing his CIMC code. Also, I thank Andrea Zanzani for his essential support on the administrative matters of the PhD. A special thanks goes to Weiguang Jiang, for providing part of the routines for the chiral interaction matrix elements and for his help in debugging the SCGF code and comparing it to the coupled-cluster method.

A collective thank goes to the nuclear physics group for welcoming me, and especially to the young colleagues with whom I shared a part of this adventure. Lastly, I would like to thank my family.